UNIVERSITY OF AMSTERDAM

UvA-DARE (Digital Academic Repository)

Zooming-in on the sources of fast radio transients

Nimmo, K.

Publication date
2022
Document Version
Final published version

Link to publication

Citation for published version (APA):
Nimmo, K. (2022). *Zooming-in on the sources of fast radio transients*. [Thesis, fully internal, Universiteit van Amsterdam].

General rights
It is not permitted to download or to forward/distribute the text or part of it without the consent of the author(s) and/or copyright holder(s), other than for strictly personal, individual use, unless the work is under an open content license (like Creative Commons).

Disclaimer/Complaints regulations
If you believe that digital publication of certain material infringes any of your rights or (privacy) interests, please let the Library know, stating your reasons. In case of a legitimate complaint, the Library will make the material inaccessible and/or remove it from the website. Please Ask the Library: https://uba.uva.nl/en/contact, or a letter to: Library of the University of Amsterdam, Secretariat, Singel 425, 1012 WP Amsterdam, The Netherlands. You will be contacted as soon as possible.

UvA-DARE is a service provided by the library of the University of Amsterdam (https://dare.uva.nl)

Download date:10 Mar 2023

Kenzie Nimmo

Zooming-in on the sources of fast radio transients

Zooming-in on the sources of fast radio transients

Kenzie Nimmo

Zooming-in on the sources of fast radio transients

Kenzie Nimmo

© 2022, Kenzie Nimmo
contact: nimmokenzie@gmail.com

Zooming-in on the sources of fast radio transients
PhD Thesis, Anton Pannekoek Institute, Universiteit van Amsterdam

Cover by Daniëlle Futselaar (https://artsource.nl/)
Printed by Gildeprint

UNIVERSITY OF AMSTERDAM

The research included in this thesis was carried out at the Anton Pannekoek Institute for Astronomy (API) of the University of Amsterdam and ASTRON, the Netherlands Institute for Radio Astronomy. Research by the AstroFlash group at University of Amsterdam, ASTRON and JIVE is supported in part by an NWO Vici grant (PI Hessels; VI.C.192.045). Support was also occasionally provided by the Leids Kerkhoven-Bosscha Fonds (LKBF).

Zooming-in on the sources of fast radio transients

ACADEMISCH PROEFSCHRIFT

ter verkrijging van de graad van doctor
aan de Universiteit van Amsterdam
op gezag van de Rector Magnificus
prof. dr. G. T. M. ten Dam
ten overstaan van een door het College voor Promoties ingestelde
commissie, in het openbaar te verdedigen in de de Aula der Universiteit
op vrijdag 16 september 2022, te 11:00 uur

door

Kenzie Nimmo

geboren te Bellshill

Promotiecommissie:

Promotor:	prof. dr. J. W. T. Hessels	Universiteit van Amsterdam & ASTRON
Copromotores:	dr. Z. Paragi	Joint Institute for VLBI ERIC
	dr. B. Marcote	Joint Institute for VLBI ERIC
Overige leden:	dr. N. D. Degenaar	Universiteit van Amsterdam
	prof. dr. A. L. Watts	Universiteit van Amsterdam
	dr. S. G. M. Toonen	Universiteit van Amsterdam
	dr. B. A. Rowlinson	Universiteit van Amsterdam
	prof. dr. R. A. M. J. Wijers	Universiteit van Amsterdam
	prof. dr. D. R. Lorimer	West Virginia University
	prof. dr. B. W. Stappers	The University of Manchester

Faculteit der Natuurwetenschappen, Wiskunde en Informatica

“You’ll never do a whole lot unless you’re brave enough to try.”
– Dolly Parton

Contents

Chapter 1

Introduction

Short-duration radio transients are astrophysical sources that emit at radio wavelengths and whose brightness varies on timescales of less than about 1 second. Neutron stars are known to be prolific emitters of short-duration radio transients. Rotation-powered radio pulsars (Hewish et al., 1968; Lorimer & Kramer, 2004) produce beams of radio light near the neutron star's magnetic poles which, as the star rotates, can sweep past an observer's line-of-sight in a periodic manner. Pulsars have been observed to rotate with periods from as slow as 23.5 seconds (Tan et al., 2018)[1] to as fast as 1.39 ms (Hessels et al., 2006). Typically the duration of the pulsed emission is a few percent of the period, up to tens of percent. Some young pulsars and rapidly spinning millisecond pulsars exhibit sporadic giant pulses (e.g. Staelin & Reifenstein 1968; Cognard et al. 1996), which in addition to having luminosities much higher than the average pulse emission, also sometimes have shorter durations ($\sim$ µs), and have been observed to vary on timescales down to nanoseconds (Hankins et al., 2003). In addition, some pulsars are visible not through their periodic emission, but through bright, isolated pulses (McLaughlin et al., 2006). These sources are known as Rotating RAdio Transients (RRATs).

Neutron stars are exceptionally magnetic objects with typical surface magnetic field strengths of $\sim 10^{8-12}$ G. These magnetic field strengths can reach as high as 10^{15-16} G for a category of neutron stars called magnetars (Kaspi & Beloborodov, 2017). Magnetars produce a wide range of magnetically powered emission types from X-ray burst storms, to short-duration flares spanning the electromagnetic spectrum. To date, 5 of the $\sim$ 30 known magnetars have been observed to produce millisecond-duration radio transients (Camilo et al., 2006, 2007; Levin et al., 2010; Eatough et al., 2013; CHIME/FRB Collaboration et al., 2020; Bochenek et al., 2020). The radio emission from magnetars shows phenomenological differences compared to rotation-powered pulsar emission, including comparatively flatter spectra and bursts that can occur at a wide range of rotational phases (Camilo et al., 2006).

[1] It is worth noting the recent discovery of a 75.9 s period neutron star, although whether or not the emission process is the same as pulsars is debated (Caleb et al., 2022a).

1

All of the known radio pulsars and magnetars reside within the Milky Way (at distances of a few kpc) and Small and Large Magellanic Clouds (at $\sim$ 50 kpc; Manchester et al. 2005; Crawford et al. 2001). This thesis focuses on radio observations of *extragalactic* fast radio transients (distances of Mpc–Gpc), which we introduce in §1.1, followed by an overview of observational results on individual sources in §1.2 and population studies in §1.3. The nature of these extragalactic fast radio transients is currently unknown, but the observational similarities with Galactic pulsars and magnetars suggest that extragalactic neutron stars could be responsible for these extreme transients, as we briefly discuss in §1.4. Not only does the large energy release in a short time span indicate that this is an extreme astrophysical process, but the transient signal itself is imprinted with a signature of the ionised material and magnetic field it interacts with on its journey to Earth. Extragalactic fast radio transients therefore carry valuable clues about some of the otherwise invisible material in the Universe as well as cosmic magnetism, as we briefly discuss in §1.5. In §1.6 we describe the radio telescopes and observing strategies used throughout this thesis to probe fast radio transients at the highest-possible temporal and spatial resolutions, before summarising the work presented in this thesis in §1.7.

1.1 Fast radio bursts

The first-discovered fast radio burst (FRB) was found in archival data from a radio pulsar survey (Lorimer et al., 2007). Since pulsars are known to produce millisecond-duration radio transients, pulsar survey data have sufficient time and frequency resolution to resolve fast radio transients, and distinguish them from human-made terrestrial interference. Astrophysical fast radio transients are strongly affected by dispersion: a frequency-dependence on the group velocity of the electromagnetic waves (Keith et al., 2013). This effect is not observed in human-made terrestrial signals, and thus provides a useful way to distinguish genuinely astrophysical signals[2]. As radio waves propagate through ionised material, e.g. the Milky Way's interstellar medium (ISM; Rand 1996; Haffner et al. 2003), the lower frequencies are delayed with respect to the higher frequencies. The more free electrons that the radio waves interact with on their journey to Earth, the larger the delay Δt. The integrated column density of free electrons on the path from the radio transient source (at luminosity distance $d_{\rm L}$) to Earth is defined as the dispersion measure DM,

$$\mathrm{DM} = \int_0^{d_{\rm L}} n_e dl, \tag{1.1}$$

and the time delay between the two frequencies ν_1 and ν_2 can be computed by

$$\Delta t = C \left(\frac{1}{\nu_1^2} - \frac{1}{\nu_2^2} \right) \mathrm{DM}, \tag{1.2}$$

[2] Note, however, that *some* human-made signals, e.g. air plane altimeters, are relatively broadband and frequency-swept, which can sometimes cause confusion.

for dispersion constant $C = 1/(2.41 \times 10^{-4})\,\mathrm{MHz^2 pc^{-1} cm^3 s}$ (Manchester & Taylor, 1972)[3], and the DM in units of $\mathrm{pc\,cm^{-3}}$ (Lorimer & Kramer, 2004).

The quadratic frequency sweep is visible in Figure 1.1, showing the dynamic spectrum (flux as a function of radio frequency and time) of the first-discovered FRB, which is colloquially named the "Lorimer burst" (Lorimer et al., 2007).

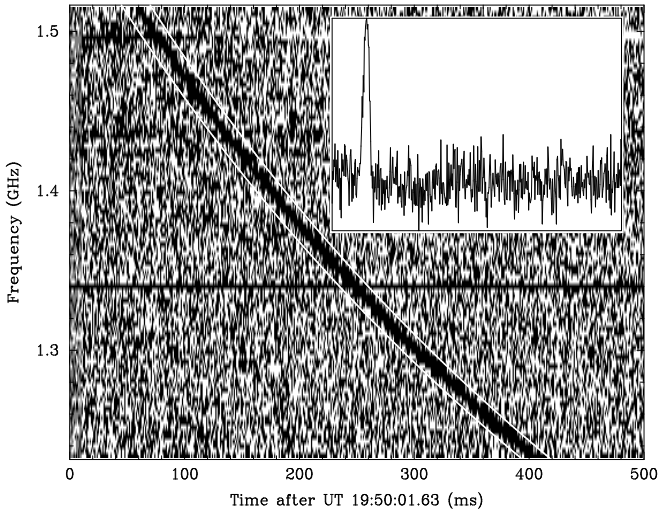

Figure 1.1: The dynamic spectrum (flux as a function of radio frequency and time) of the first-discovered FRB, FRB 010724 (Lorimer et al., 2007). The delay from the arrival of the highest frequencies to the arrival of the lowest frequencies is due to a propagation effect called dispersion (see §1.1). The inset shows the frequency-averaged burst profile after shifting the frequency channels to correct for the dispersive delay. Figure from Lorimer et al. (2007).

All known pulsars are located in the Milky Way or in the Small and Large Magellanic Clouds (Manchester et al., 2005; Crawford et al., 2001), and have been used to map the Galactic electron distribution (Cordes & Lazio, 2002; Yao et al., 2017). This allows for predictions of the DM contribution per line-of-sight from the ISM. From the dispersive sweep of the Lorimer burst (Figure 1.1), the DM was measured to be $375\,\mathrm{pc\,cm^{-3}}$, approximately $350\,\mathrm{pc\,cm^{-3}}$ in excess of the Galactic ISM contribution. If we assume a conservative Milky Way halo DM contribution of $100\,\mathrm{pc\,cm^{-3}}$ (Prochaska & Zheng, 2019)[4], and $\sim 200\,\mathrm{pc\,cm^{-3}}$ local DM contribution from the source's environment and putative host galaxy, then the redshift of the FRB source can be approximated as

$$z \approx \frac{\mathrm{DM_e}}{1000\,\mathrm{pc\,cm^{-3}}} \sim 0.05, \tag{1.3}$$

[3] This constant is often used by convention in the pulsar/FRB fields, but a formal definition is derived as $C = e^2 \times 1\mathrm{pc}/(2\pi m_e c)$, for electron charge e, mass m_e, speed of light c and parsec in SI units pc (Kulkarni, 2020).

[4] This is "conservative" since it is a relatively high estimate of the halo contribution. It has been argued that $\sim$40 $\mathrm{pc\,cm^{-3}}$ is more appropriate, on average (Yamasaki & Totani, 2020).

(Ioka, 2003; Inoue, 2004) where $\mathrm{DM_e}$ is the remaining DM contribution from the ionised material in the intergalactic medium (IGM; Sciama 1964). This redshift corresponds to a luminosity distance of $d_\mathrm{L} \sim 220\,\mathrm{Mpc}$ (assuming a flat Universe, Λ Cold Dark Matter cosmology with Hubble constant $H_0 = 70\,\mathrm{km\,s^{-1}\,Mpc^{-1}}$, and the fraction of the Universe's total energy density that is matter $\Omega_M = 0.3$ and dark matter $\Omega_\Lambda = 0.7$; Wright 2006). Using this inferred distance (d_L) with the Lorimer burst's observed flux density, $F = 30\,\mathrm{Jy}$ (Lorimer et al., 2007), the isotropic-equivalent spectral luminosity[5] can be estimated:

$$L_\mathrm{iso} = 4\pi F d_\mathrm{L}^2 \sim 2 \times 10^{33} \mathrm{erg\,s^{-1}\,Hz^{-1}}. \tag{1.4}$$

This calculation is relatively conservative since we have assumed high DM contributions from the Milky Way halo and host galaxy, placing the source closer to us than if we were to assume lower DM contributions. In Lorimer et al. (2007), they place an upper limit on the luminosity distance to the FRB source of 1 Gpc, which would, of course, imply a luminosity more than an order-of-magnitude higher.

One of the youngest pulsars known is the Crab pulsar, PSR B0531+21 (Staelin & Reifenstein, 1968), so-called since this pulsar resides within and powers the famous Crab nebula. The average Crab pulsar emission has a flux density of 0.014 Jy, on millisecond timescales, at an observing frequency of 1.4 GHz (Lorimer et al., 1995). If the Lorimer burst were to have been emitted from the close proximity of the Crab pulsar ($\sim$ 2 kpc; Staelin & Reifenstein 1968), it would have been detected with a flux density of $\sim 3.6 \times 10^{11} \times \left(\frac{d_L}{220\,\mathrm{Mpc}}\right)^2$ Jy, a 13 orders-of-magnitude jump in luminosity compared with Crab pulsar emission on comparable timescales. Although the FRB duration and measured brightness resemble phenomena seen from Galactic pulsars (Lorimer & Kramer, 2004), the large inferred distance of the Lorimer burst implies a burst luminosity $\sim$13 orders of magnitude brighter than *typical* pulsar emission. The short-duration radio transient phase space is shown in Figure 1.2, highlighting the comparable timescales of FRBs and pulsar emission, and their drastically different luminosities.

Since the discovery of the Lorimer burst, hundreds of FRBs are now known (e.g. CHIME/FRB Collaboration et al. 2021)[6], but the type(s) of astrophysical objects and physical processes capable of producing FRB emission remain a mystery. One of the most compelling progenitor models for the production of FRBs are magnetars since they have a huge amount of available energy stored in their magnetic field, and are capable of producing fast radio transients. One magnetar, SGR 1935+2154, has even produced a millisecond-duration radio transient with luminosity only 1–2 orders of magnitude weaker than the least luminous extragalactic FRBs (with the exception of FRB 20200120E, which we discuss in this thesis; see § 1.2.4, § 1.2.5, Figure 1.2; CHIME/FRB Collaboration et al. 2020; Bochenek et al. 2020), showing that at least a fraction of the observed FRBs are coming from extragalactic magnetars. To probe the nature of FRBs, one can study the properties of the FRB population as a whole to explore the possibility of multiple physical origins: similar to the identification of two distinct physical

[5] While we expect that FRBs are likely beamed, we do not know the value of the beaming angle, and hence assume isotropic emission for simplicity.

[6] All known and published FRBs can be found on the Transient Name Server: https://www.wis-tns.org/

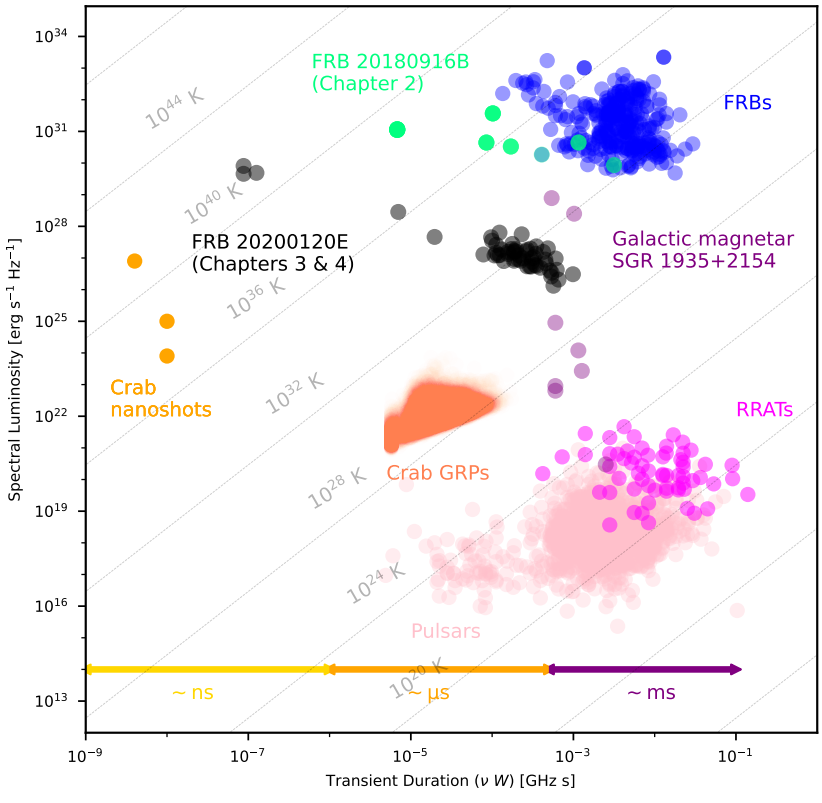

Figure 1.2: The transient phase space for fast radio transients. The y-axis is isotropic-equivalent spectral luminosity, which is used instead of luminosity to account for the fact that observations differ in their available frequency bandwidth and the spectra of short-duration radio transients also differ (some are broadband, some are narrow-band). The x-axis shows the transient duration multiplied by the emission frequency ν. The reason for quoting durations in this manner is because there are effects which cause the transient width to be larger as the frequency drops (e.g. scattering), so this allows for the comparison between vastly different observing frequencies. Figure made by K. Nimmo, adapted from Nimmo et al. (2022a).

origins of gamma-ray bursts based on their transient duration and distinct environments (Gehrels et al., 2009). When I began my PhD in 2018, however, there were only a few dozen FRBs reported in the literature. Another method for developing our understanding of these mysterious transients is to study a few sources in detail, to identify important observables to challenge progenitor theories: this is the main focus of the work presented in this thesis.

1

1.2 Detailed studies of individual FRBs

1.2.1 The first-discovered repeating FRB: FRB 20121102A

In the early days of the FRB field, there was great debate about the astrophysical origin of these extreme transients (Burke-Spolaor et al., 2011; Keane et al., 2012). The discovery of 4 more FRBs in 2013 by Thornton et al. (2013) alleviated the concern that FRBs were non-astrophysical signals. The discovery of a repeating FRB in 2016, FRB 20121102A (Spitler et al., 2014, 2016), further aided in the support of an astrophysical origin of FRBs. Not only that, but repetition rules out any progenitor models invoking a catastrophic event, such as the collapse of a supramassive neutron star (Falcke & Rezzolla, 2014).

Repeating FRBs are particularly valuable as they allow for follow-up observations to: probe the immediate environments in which FRBs live (e.g., Chatterjee et al. 2017; Tendulkar et al. 2017; Marcote et al. 2017; Bassa et al. 2017), characterise the range of burst properties, such as energies and burst temporal separations (e.g., Gourdji et al. 2019; Li et al. 2021), and explore the evolution of burst properties with time and observing frequency (e.g., Michilli et al. 2018b; Hilmarsson et al. 2021a; Majid et al. 2020).

The repetition of FRB 20121102A allowed for the first precision localisation of an FRB (Chatterjee et al., 2017; Tendulkar et al., 2017; Marcote et al., 2017). Using the Very Large Array (VLA), a radio interferometer located in New Mexico, Chatterjee et al. (2017) created radio images at the times of 9 FRB 20121102A bursts (one image is shown in Figure 1.3i) from which an average sky position was measured to 0.1 arcsecond accuracy. This precision was sufficient to pinpoint the FRB to its host galaxy, and identify a coincident persistent radio counterpart to the transient source (Figure 1.3ii; Chatterjee et al. 2017; Tendulkar et al. 2017).

Follow-up observations with the European Very Long Baseline Interferometry (VLBI) Network (EVN) improved the localisation precision by an order-of-magnitude (Figure 1.4i; Marcote et al. 2017). The improvement in localisation precision arises due to the much longer baselines (separation of elements of the array) afforded by VLBI, where the maximum image resolution achievable is

$$\theta \approx 1.22 \frac{\lambda}{b} \, [\mathrm{rad}], \tag{1.5}$$

for observing wavelength λ and maximum baseline length b (Condon & Ransom, 2016). VLBI instruments typically have maximum baselines of thousands of km, while the VLA has a maximum baseline of 36 km (in A configuration: the highest resolution configuration of the VLA). The VLBI technique is used extensively throughout this thesis (Chapters 5, 6, 7) and an introduction to VLBI can be found in §1.6.2.

With VLBI precision, the exact position of the FRB *within* the host galaxy can be determined (at a level that surpasses the resolution of even the *Hubble Space Telescope*), as well as the relative position of the FRB source and the persistent radio emission (Figure 1.4; Marcote et al. 2017; Bassa et al. 2017). FRB 20121102A was found to reside close to a star-forming region inside a dwarf host galaxy (total stellar mass $\sim 4 - 7 \times 10^7 \, \mathrm{M}_\odot$; Tendulkar et al. 2017) at a redshift of $z \sim 0.19273 \pm 0.00008$ (Tendulkar et al., 2017; Bassa et al., 2017).

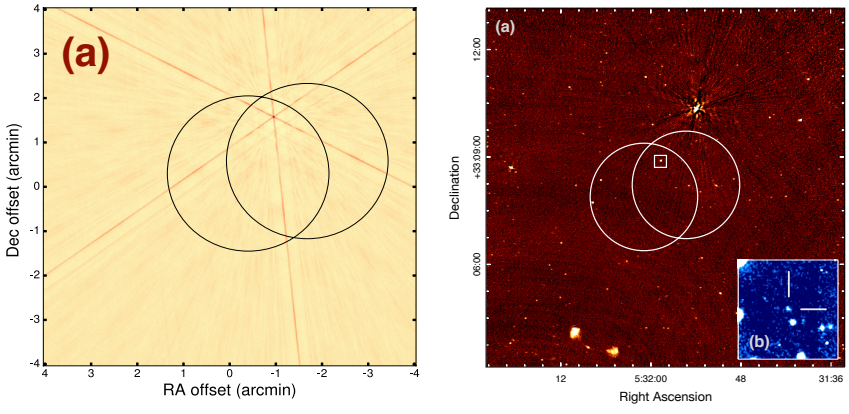

(i) (ii)

Figure 1.3: (i): Very Large Array (VLA) snapshot image at 3 GHz at the time of a burst from FRB 20121102A. The black circles represent positional uncertainty regions from bursts detected with the Arecibo telescope. **(ii)**: VLA 3 GHz image of the entire dataset at the position of FRB 20121102A searching for persistent radio emission. The white circles are the same as the black circles in sub-figure (i). The white box highlights a longer-lived radio source which appears to coincide with the burst position in sub-figure (i). The inset shows a Gemini r-band image of the field around FRB 20121102A, showing the host galaxy. Figures from Chatterjee et al. (2017).

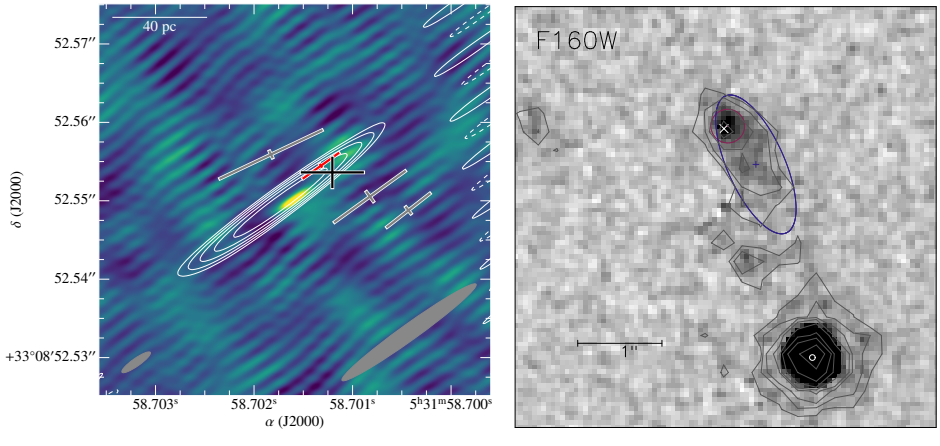

(i) (ii)

Figure 1.4: (i): EVN image at 5 GHz (with 1.7 GHz overplotted as white contours). The sythesised beam for 1.7 GHz and 5 GHz are shown at the bottom right and left of the figure, respectively. The grey and red crosses represent individual burst positions from FRB 20121102A (red is the highest S/N burst in the sample), and the black cross represents the S/N weighted average burst position. There is a systematic uncertainty on the burst positions that is not represented in the error bars here. This uncertainty is arising due to the strong sidelobes in the individual burst images, meaning that it is ambiguous which lobe is the correct burst position. Figure from Marcote et al. (2017). **(ii)**: *Hubble Space Telescope* image of the dwarf host galaxy of FRB 20121102A. The white cross represents the EVN position of FRB 20121102A (black cross on sub-figure (i)), which coincides with a star-forming region in the host galaxy (red circle). The blue contours are used to highlight the extent of the galaxy. Figure from Bassa et al. (2017).

This represents the first direct evidence that FRBs are indeed extragalactic in origin, as suggested by their anomalously high DMs (see §1.1). The FRB position is coincident with the persistent radio source to within $\sim$ 40 pc (transverse offset), which was found to be unresolved in the EVN image of the FRB 20121102A sky position (Figure 1.4i; Marcote et al. 2017). Similar to the FRB itself, the origin of the compact persistent emission is also unknown. The size of the persistent radio source is constrained to be less than 0.7 pc (Marcote et al., 2017), and the observed brightness does not vary by more than $\sim$ 10% on month-to-year timescales (Plavin et al., 2022). The lack of variation shows that the persistent radio source is not a decaying blast wave from, e.g., a supernova or gamma-ray burst, as seen in the case of FIRST J141918.9+394036 (Law et al. 2017; Chapter 7). There are two leading hypotheses on the nature of the persistent emission: either a nebula powered by a central neutron star (although the luminosity is 4–5 orders of magnitude brighter than the Crab nebula; Chatterjee et al. 2017; Eftekhari et al. 2019), or a low-luminosity accreting massive black hole (Marcote et al., 2017; Reines et al., 2020).

The transient emission itself also holds valuable clues about the environment of FRB 20121102A. Generally, bursts from repeating FRBs, including FRB 20121102A, are highly linearly polarised (e.g., Gajjar et al. 2018, Chapter 2). As these polarised radio waves (of wavelength λ) propagate through a magnetised plasma, with a magnetic field component parallel to the wave propagation ($B_{||}$ in μG), the angle of linear polarisation is rotated by (Smith, 1968; Lorimer & Kramer, 2004)

$$\Delta\phi = \lambda^2 \mathrm{RM}, \tag{1.6}$$

with rotation measure, RM, defined as

$$\mathrm{RM} = 0.81 \int_0^{d_\mathrm{L}} n_e B_{||} dl. \tag{1.7}$$

Michilli et al. (2018b) measure an extremely large RM of $\sim 10^5$ rad m^{-2} for FRB 20121102A (Figure 1.5), which is highly variable and has dropped in amplitude by $\sim$ 15% per year on average (Hilmarsson et al., 2021a). This, combined with the comparatively low DM variations (Michilli et al., 2018b; Hessels et al., 2019), indicates that FRB 20121102A lives in an extreme magneto-ionic local environment (Michilli et al., 2018b). The large and highly variable RM is comparable to that measured for the Galactic centre magnetar, PSR J1745−2900, with an RM of -67000 rad m^{-2} which dropped in amplitude by $\sim$ 5% in one year (Eatough et al., 2013), perhaps indicating that FRB 20121102A is also living in the vicinity of a massive black hole (Michilli et al., 2018b; Hilmarsson et al., 2021a).

Although at higher frequencies (e.g., 4–8 GHz; Gajjar et al. 2018) FRB 20121102A emission is 100% linearly polarised, the linear polarisation fraction drops to 0% going down to 1.4 GHz (Li et al., 2021; Plavin et al., 2022). This behaviour is seen in other repeating FRBs, and has been attributed to scattering of the radio waves close to the FRB source, further adding complexity to the local environment of FRB 20121102A (Feng et al., 2022). This effect is most pronounced in FRB 20121102A and FRB 20190520B, colloquially called FRB 20121102A's "twin" due to its strikingly similar observational qualities: e.g., dwarf host

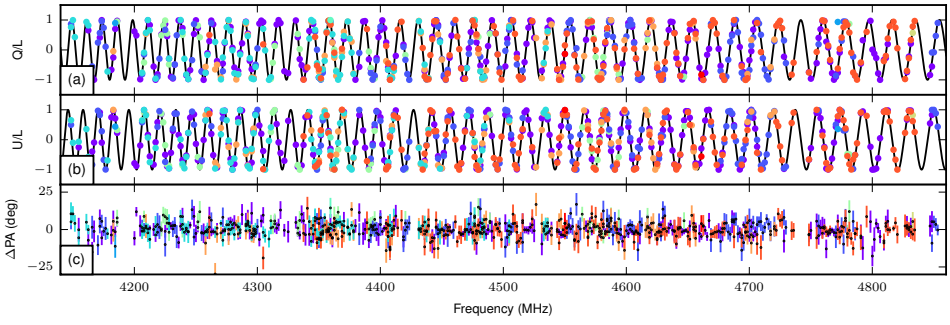

Figure 1.5: Faraday rotation in the bursts from FRB 20121102A. Panels (a) and (b) show the spectra of Stokes parameters Q and U, respectively, normalised by the linear polarisation (L= $\sqrt{Q^2 + U^2}$). The oscillation is a signature of Faraday rotation, which wraps quicker as the frequency decreases (see Equation 1.6). The different colours represent data points from individual bursts in the Michilli et al. (2018b) burst sample. The black line is the best fit Faraday rotation model. Panel (c) shows the residual polarisation angle values after subtracting the model. Figure from Michilli et al. (2018b).

galaxy origin, large RM that is also highly variable, and associated persistent radio counterpart (Niu et al., 2021; Anna-Thomas et al., 2022). These FRBs sharing comparably extreme magnetised local environments could indicate that they are both young sources (Feng et al., 2022).

1.2.2 The periodic repeating FRB: FRB 20180916B

FRB 20121102A is no longer a singular source: there are now $>$ 20 repeating FRBs identified, with a range of activity behaviour (CHIME/FRB Collaboration et al., 2019a,c; Fonseca et al., 2020; CHIME/FRB Collaboration et al., 2021; Niu et al., 2021). The majority of FRBs in the literature were discovered by the Canadian Hydrogen Intensity Mapping Experiment (CHIME) telescope's FRB detection system (CHIME/FRB; CHIME/FRB Collaboration et al. 2018). CHIME is a transit radio telescope in British Columbia, Canada, operating at a relatively low radio frequency of 400–800 MHz. Some of the CHIME/FRB-discovered repeaters have produced only 2 bursts over the span of multiple years of observation (CHIME/FRB Collaboration et al., 2019c; Fonseca et al., 2020), while others have been seen to produce hundreds to even thousands of bursts in follow-up observations using more sensitive telescopes (e.g., Xu et al. 2021). Interestingly, Li et al. (2021) report more than 1600 bursts from FRB 20121102A discovered within a few months of observing at 1.4 GHz with the FAST radio telescope in China, while CHIME/FRB has only ever detected FRB 20121102A once (Josephy et al., 2019). While there is a large sensitivity difference between FAST and CHIME/FRB, this is likely only partially the reason for the difference in activity rates.

FRB 20180916B is a CHIME/FRB-discovered repeating FRB, whose burst activity has been observed to vary periodically, on a cycle of 16.35$\pm$0.15 days with an active window of $\sim$ 5 days (Chime/Frb Collaboration et al., 2020). In Chapters 2 and 6, we report the detection of 4 bursts from FRB 20180916B at 1.4 GHz, and reveal the properties of those

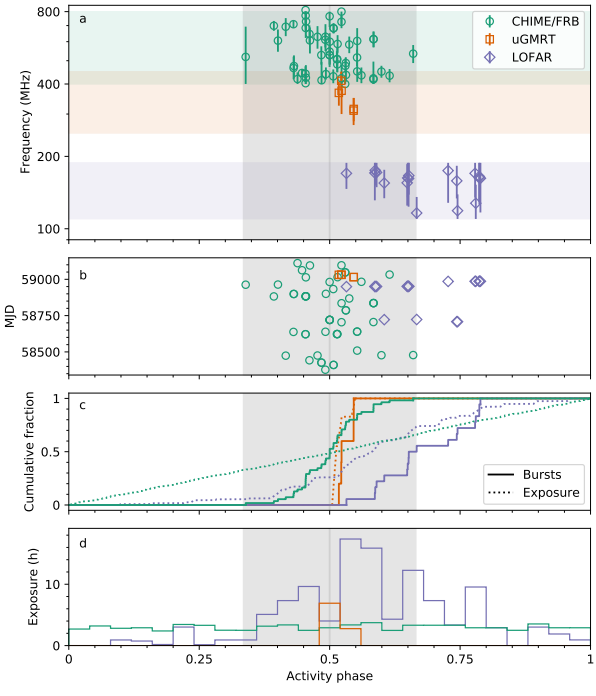

Figure 1.6: The activity phases, after folding using the measured period of 16.35 days (CHIME/FRB Collaboration et al., 2019b), of FRB 20180916B bursts detected by CHIME/FRB (600 MHz; in green), the upgraded Giant Metrewave Radio Telescope (uGMRT; 350 MHz; in orange), and the Low-Frequency Array (LOFAR; 150 MHz; in purple). Panel (a) shows the activity phase versus the central frequency of the burst, where the error bars show the spectral burst extent. The colour shaded region shows the observing bandwidth per telescope. The lower frequencies lag in phase with respect to the higher frequencies. Panel (b) shows the activity phase as a function of burst time of arrival. Panel (c) shows a comparison of the cumulative fraction of bursts through activity phase, with the telescope exposure to each activity phase. Finally, a histogram of the exposure is shown in panel (d). Figure from Pleunis et al. (2021b).

bursts at high time and spatial resolution, respectively. These higher-frequency bursts were found to occur earlier in the activity phase than CHIME/FRB's lower-frequency bursts, hinting at a frequency-dependence on the activity (Chime/Frb Collaboration et al., 2020). In further support of a relationship between activity and observing frequency: in 17.6 hr of 1.4 GHz observations with the 100-m Effelsberg telescope specifically targeting when FRB 20180916B was expected to be active, we detected no bursts despite CHIME/FRB discovering 2 contemporaneous with our observations (Chime/Frb Collaboration et al., 2020). This frequency-dependence was later confirmed with observations spanning from 1.4 GHz down to 100 MHz, where the lower frequencies arrive later in activity phase than the higher frequencies (Figure 1.6; Pleunis et al. 2021b; Pastor-Marazuela et al. 2021). This periodic activity and relationship with frequency must be explained in the progenitor models for FRB 20180916B. Models invoking a binary system (either interacting objects or absorption from the surrounding plasma; e.g., Zhang 2017; Lyutikov et al. 2020), ultra-long-period ro-

tation (e.g., Beniamini et al. 2020) and precessing neutron stars (e.g., Zanazzi & Lai 2020) have been introduced to explain FRB 20180916B's activity behaviour.

Following the discovery of FRB 20180916B's periodic activity, a tentative $\sim$ 160 day period has been observed for FRB 20121102A (Rajwade et al., 2020; Cruces et al., 2021), but a few more activity cycles are required to formally confirm this activity behaviour. Not only is the activity behaviour comparable between FRB 20180916B and FRB 20121102A, but the burst properties (e.g., morphology, polarimetry, etc.) are shared between the sources, and in general differ from observations of non-repeating FRBs (see Chapter 2 for a discussion; Pleunis et al. 2021a).

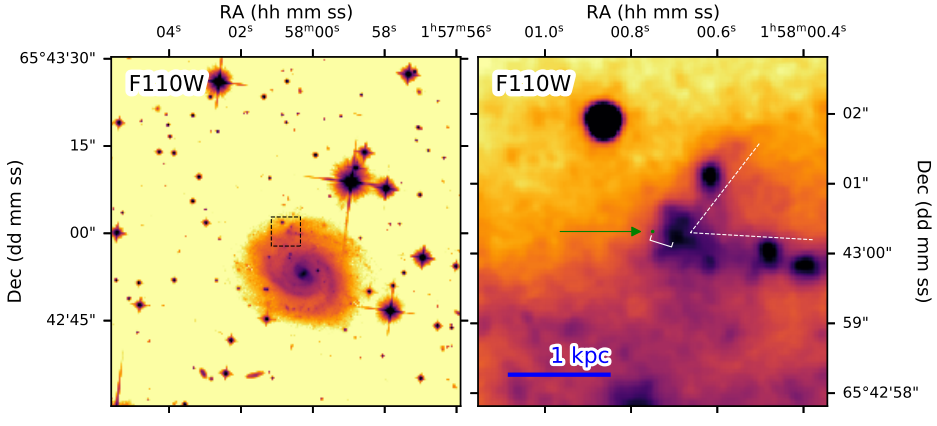

Figure 1.7: *Hubble Space Telescope* images of FRB 20180916B's Milky Way-like spiral host galaxy (left) and a zoom-in on the "v-shaped" star-forming region near where FRB 20180916B resides (right). This peculiar "v-shaped" feature has been modelled as arising due to a previous minor merger of galaxies (Kaur et al., 2022). The dashed box in the left panel indicates the extent plotted on the right zoom-in panel. The green marker and arrow on the right indicate the EVN position of FRB 20180916B (from Chapter 6). The white marker shows the $\sim$ 250 pc separation between the FRB position and the peak of the nearby Hα region. Figure from Tendulkar et al. (2021).

Despite the many similarities between FRB 20180916B and FRB 20121102A, we show in Chapter 6 that they live in very different environments. FRB 20180916B is living in a massive Milky Way-like spiral galaxy (total stellar mass $\sim 10^{10}\,\mathrm{M}_{\odot}$; Chapter 6), $\sim$ 250 pc offset from a star-forming region (Figure 1.7; Tendulkar et al. 2021), and has no persistent radio counterpart. This is in contrast to FRB 20121102A which is embedded in a star-forming region of a dwarf host galaxy (although still $\sim$ 200 pc offset from the peak of star-formation; Bassa et al. 2017) and is found associated with a persistent radio source (see § 1.2.1). If one assumes that the magnetar was born at the peak of star-formation, a typical natal kick velocity (Hobbs et al., 2005; Bray & Eldridge, 2016) and the 250 pc offset for FRB 20180916B would imply a magnetar age of $\sim 10^6$ yr (and therefore not a young, age $\sim 10^3$–10^5 yr, magnetar). It is possible that the massive star progenitor of the magnetar travelled outside of the star-forming region before collapsing to a neutron star. However, Tendulkar et al. (2021) argue that this is unlikely since only a small fraction ($\sim$1–10%) of the massive star population are considered "runaway" stars (Fujii & Portegies Zwart, 2011), and magnetars are a

small fraction (∼10%) of the neutron star population (Kaspi & Beloborodov, 2017). These results are more consistent with the interacting binary scenario (Tendulkar et al., 2021). Perhaps FRB 20180916B and FRB 20121102A are both interacting binaries (e.g. a massive star with an ionised stellar wind interacting with the highly magnetised neutron star companion; Zhang 2017; Tendulkar et al. 2021) living in different environments, or conversely maybe the difference in living conditions is informing us of the different physical origins of repeating FRBs.

1.2.3 The highly active FRB: FRB 20201124A

After more than 2 years of apparent quiescence (burst rate is constrained to be $< 3.4\,\mathrm{day}^{-1}$; Lanman et al. 2022) prior to discovery in 2020 (Chime/Frb Collabortion, 2021), FRB 20201124A entered a period of heightened activity in early 2021 (Figure 1.8; Lanman et al. 2022), showing some of the highest average burst rates measured from any repeating FRB, to date ($45.8^{+7.8}_{-8.2}\,\mathrm{hr}^{-1}$; Xu et al. 2021).

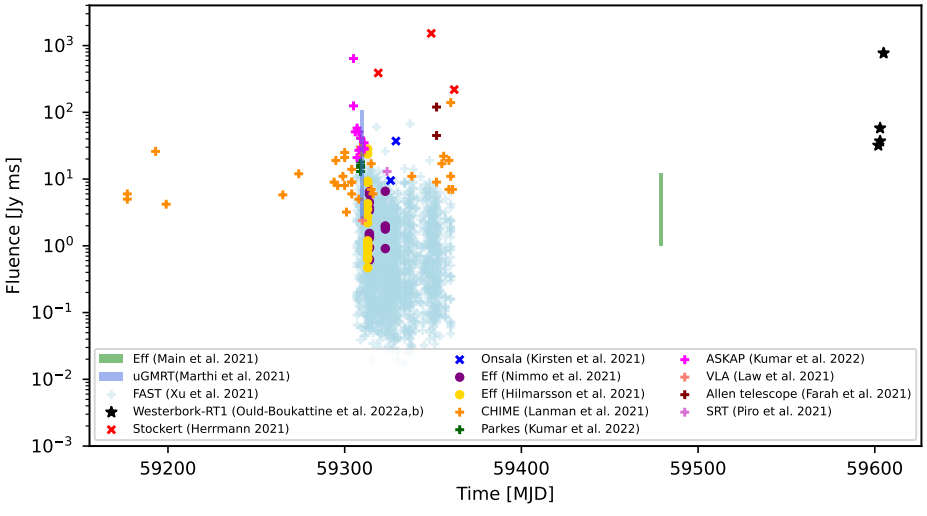

Figure 1.8: FRB 20201124A burst detections in the literature, from the original discovery by CHIME/FRB in November 2020 (Lanman et al., 2022), through to the most recent detection using the Westerbork-RT1 25-m telescope in January 2022 (Ould-Boukattine et al., 2022). FRB 20201124A went into a period of heightened activity in April 2021, where thousands of bursts were detected by many different telescopes over the span of a few weeks (Xu et al., 2021; Kirsten et al., 2021a; Herrmann, 2021; Kumar et al., 2022; Law et al., 2021; Farah et al., 2021; Piro et al., 2021; Lanman et al., 2022; Hilmarsson et al., 2021b), before entering a quiescent period for months. Figure made by K. Nimmo.

Telescopes all over the world detected bursts from FRB 20201124A within a time span of weeks-to-months, before FRB 20201124A entered another spell of quiescence (Figure 1.8). This period of heightened activity and consequently large number of detections of bursts from FRB 20201124A allowed for some interesting insights. FRB 20201124A was precisely localised to a massive star-forming galaxy at a redshift of $z = 0.0979 \pm 0.0001$ (stellar mass

$2 \times 10^{10}\,M_{\odot}$; Fong et al. 2021; Ravi et al. 2022). Initial observations with both the VLA (Ricci et al., 2021) and the upgraded Giant Metrewave Radio Telescope (uGRMT; Wharton et al. 2021a) find an unresolved radio source, potentially similar to the persistent radio counterpart of FRB 20121102A (see § 1.2.1). Increasing the spatial resolution with VLBI observations (Chapter 5, Ravi et al. 2022), however, showed that this radio source was not compact, implying that it was most likely associated with star-formation in the host galaxy. High radio frequency (22 GHz) imaging with the VLA resolved the radio source, further supporting the star-formation origin (Piro et al., 2021). With the VLBI position measured in Chapter 5, we show that the FRB source is embedded within the star-forming region, and this extremely high accuracy on the FRB position will allow us to measure the proximity to nearby knots of star-formation with upcoming *Hubble Space Telescope* observations (e.g., Bassa et al. 2017 for FRB 20121102A, and Tendulkar et al. 2021 for FRB 20180916B).

FRB 20201124A's burst polarimetric properties deviate from the characteristic description that is emerging for the polarimetric properties of repeating FRBs – i.e. strong linear polarisation, no circular polarisation, and constant polarisation angle during and between bursts (see discussion in Chapter 2) – FRB 20201124A bursts are sometimes strongly circularly polarised (Hilmarsson et al., 2021b; Kumar et al., 2022). This has been interpreted as extrinsic propagation effects from the local environment distorting the observed polarimetric properties, introducing measurable circular polarisation in the bursts.

The lack of a compact persistent radio counterpart is puzzling: the high burst activity and apparent propagation effects in the polarimetric properties of FRB 20201124A suggest that it is a young source in a high-density, turbulent plasma environment. Why does it then not show a persistent radio counterpart like FRB 20121102A and FRB 20190520B?

From a technical perspective, the high activity of FRB 20201124A allowed for multi-epoch VLBI observations with a range of participating telescopes, burst brightnesses and burst spectra, which all influence the accuracy of the derived FRB position (see Chapter 5). This presented the opportunity to explore the robustness of the VLBI technique for FRB localisation, an invaluable exercise for the future of VLBI FRB localisations (see §1.3).

1.2.4 The Galactic FRB from SGR 1935+2154

As discussed earlier, Galactic neutron stars are prolific emitters of fast radio transients: pulsars and RRATs are known for their periodic, but sometimes sporadic radio pulses (Hewish et al., 1968; McLaughlin et al., 2006); some pulsars produce occasional giant pulses with brightness greater than an order of magnitude higher than the average regular pulses (Cordes et al., 2004); and a handful of known magnetars in the Milky Way have been seen to produce both periodic and sporadic radio pulses that can occur at various rotational phases (Camilo et al., 2006, 2007; Levin et al., 2010; Eatough et al., 2013). But the luminosity of this emission is orders of magnitude weaker than measured for FRBs (Figure 1.2).

On 28 April 2020, an exceptionally high-fluence, millisecond-duration radio flare was detected from the Galactic magnetar SGR 1935+2154, simultaneously by both CHIME/FRB (at 600 MHz; CHIME/FRB Collaboration et al. 2020) and the STARE2 experiment (at

1.4 GHz; Bochenek et al. 2020). Not only is this the first time radio emission was observed from SGR 1935+2154, but the inferred isotropic-equivalent spectral luminosity of $\sim 10^{29}$ erg s^{-1} Hz^{-1}, is the highest luminosity fast radio transient ever seen from the Milky Way, and many orders of magnitude brighter than typical magnetar radio emission (Camilo et al., 2006; Caleb et al., 2022b). This luminosity, however, is still $\sim$ 1–2 orders of magnitude weaker than the weakest burst reported from FRB 20180916B which, until recently, was the closest-known extragalactic FRB (Chapter 6).

In the days and weeks following this discovery, a much lower-luminosity radio burst, more representative of typical radio emission from magnetars, was discovered from SGR 1935+2154 (Zhang et al., 2020), followed by 2 radio bursts with luminosities almost directly in between (Kirsten et al., 2021b). This highlights that SGR 1935+2154 can produce radio emission spanning roughly 8 orders of magnitude in luminosity, and, as yet, the distinction between FRB-like emission and less luminous fast radio transients from magnetars is not clear. Future studies of SGR 1935+2154 and other Galactic magnetars will shed light on the possibility of multiple physical processes creating these transients, or whether a single emission model can accommodate the huge range of observed luminosities.

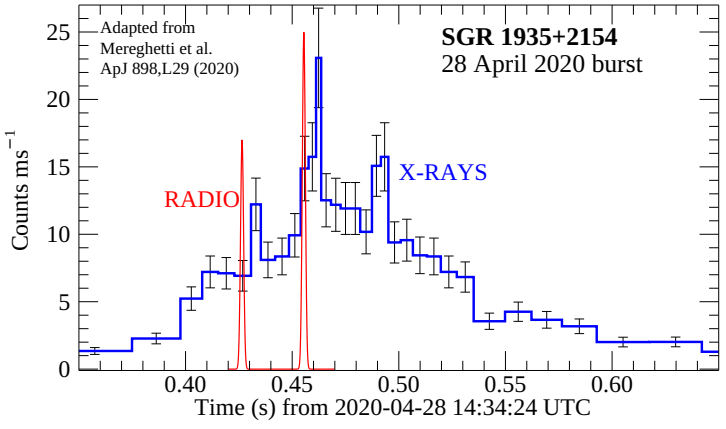

Figure 1.9: *INTEGRAL* detection of an atypical hard X-ray burst from SGR 1935+2154 (blue; Mereghetti et al. 2020) contemporaneous with the FRB-like radio burst (red; CHIME/FRB Collaboration et al. 2020; Bochenek et al. 2020). Figure from Petroff et al. (2022), adapted from Mereghetti et al. (2020).

Contemporaneous with the bright FRB-like burst on April 28 2020, many X-ray instruments detected an atypical hard X-ray flare (Figure 1.9; Mereghetti et al. 2020; Li et al. 2020; Ridnaia et al. 2020; Tavani et al. 2020). Storms of X-ray bursts are sometimes observed from magnetars (e.g. Younes et al. 2020), and SGR 1935+2154's X-ray activity was observed to rapidly ramp up only hours before the FRB-like burst (Fletcher & Fermi GBM Team, 2020; Palmer, 2020; Younes et al., 2020). The contemporaneous X-ray flare, however, observationally stands out from the typical X-ray magnetar emission: its spectrum is harder than typical X-ray bursts from SGR 1935+2154 (note SGR is an acronym for *Soft* Gamma-ray Re-

peater), and the spiky morphology of the burst (Figure 1.9) is also atypical compared with the sharp rise and slow decay that is often seen (Huppenkothen et al., 2015). This represents the first and, to date, *only* time an FRB has been observed accompanied by a high-energy burst. Compared with typical FRB distances of gigaparsecs, FRB 20180916B (§1.2.2) is relatively nearby: only $\sim$ 149 Mpc from Earth (see Chapter 6). Despite FRB 20180916B being relatively nearby, there is no evidence for any multi-wavelength signature (neither prompt nor persistent; Scholz et al. 2020; Pilia et al. 2020). Assuming the same ratio of radio to X-ray fluence for FRB 20180916B as measured for the FRB-like event from SGR 1935+2154 ($\sim 10^{-5}$; Mereghetti et al. 2020), prompt X-ray emission would not be detectable at the distance of FRB 20180916B given the sensitivities of current instruments.

1.2.5 The extremely nearby FRB: FRB 20200120E

Until recently, there was a huge gap in space and knowledge between the FRB-like event from SGR 1935+2154, and the relatively nearby repeating FRB 20180916B. That was until Bhardwaj et al. (2021a) discovered a repeating FRB, FRB 20200120E, coming from the direction of the grand design spiral galaxy M81 at a distance of *only* 3.6 Mpc (Freedman et al., 1994; Karachentsev et al., 2002). With the localisation precision afforded by CHIME/FRB, Bhardwaj et al. (2021a) identified 4 astrophysical sources potentially related to FRB 20200120E (Figure 1.10i): an M81 HII region (Patterson et al., 2012), an unidentified X-ray source (Sell et al., 2011), a globular cluster in M81 (Perelmuter & Racine, 1995; Perelmuter et al., 1995), and an unidentified radio source (Gordon et al., 2020). Using the EVN, we pinpointed FRB 20200120E to the M81 globular cluster [PR95] 30244 (Perelmuter & Racine, 1995; Perelmuter et al., 1995), approximately 2 pc from the globular cluster's centre of optical light (Figure 1.10ii; Kirsten et al. 2022).

FRB 20200120E living in an older stellar population, a globular cluster, is in stark contrast to the relatively close proximity to active star-formation in the case of other well-localised repeating FRBs: FRB 20121102A (§1.2.1), FRB 20180916B (Chapter 6, §1.2.2), and FRB 20201124A (Chapter 5, §1.2.3). This important discovery challenges FRB progenitor models which invoke a magnetar that was created through the typical core-collapse supernova formation route, and instead requires the magnetar to be created through a more exotic formation process such as accretion-induced collapse of a white dwarf or the merger of compact objects (Kremer et al., 2021; Kirsten et al., 2022; Lu et al., 2022).

Perhaps FRB 20200120E is not a magnetar, but instead a millisecond pulsar or an interacting binary system, both of which are found in abundance in globular clusters (Pooley et al., 2003; Heinke et al., 2003; Ablimit & Li, 2015; Hessels et al., 2015; Ye et al., 2019). The relative proximity of FRB 20200120E provides the unique opportunity to bridge the understanding of Galactic neutron stars to the extremely distant extragalactic FRBs. This is the main focus of Chapters 3 and 4 of this thesis, where we show that FRB 20200120E is observationally connecting Galactic neutron stars and extragalactic FRBs (black markers in Figure 1.2). FRB 20200120E burst luminosities are lower than the weakest FRBs by $\sim$ 2 orders of magnitude, and even lower than the FRB-like event from SGR 1935+2154 by an or-

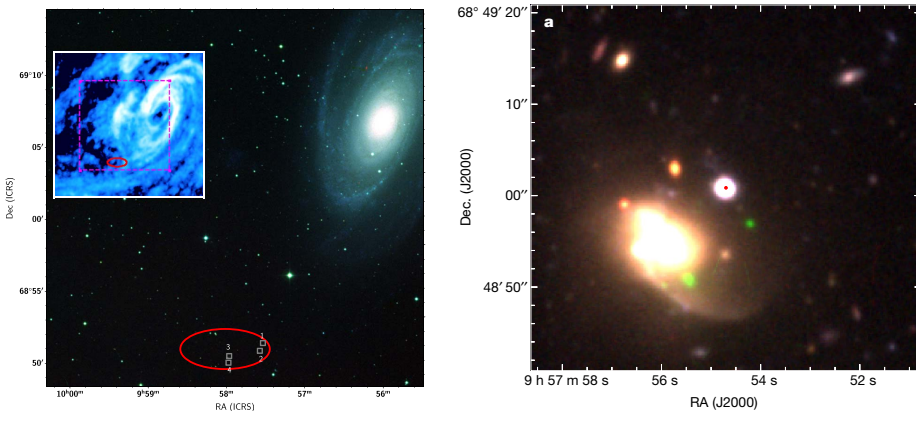

(i) (ii)

Figure 1.10: (i): The red ellipse shows the CHIME/FRB localisation region for FRB 20200120E in the outskirts of the M81 galaxy (Bhardwaj et al., 2021a) overplotted on the Digital Sky Survey RGB image of the field. Within the error ellipse are four numbered sources: 1. an M81 HII region (Patterson et al., 2012); 2. an unidentified X-ray source (Sell et al., 2011); 3. an M81 globular cluster (Perelmuter & Racine, 1995; Perelmuter et al., 1995); and 4. an unidentified radio source (Gordon et al., 2020). The inset shows the M81 circumgalactic material through 21-cm emission, highlighting that FRB 20200120E is in the outskirts of M81. Figure from Bhardwaj et al. (2021a). **(ii)**: EVN localisation of FRB 20200120E (red marker is the 10 σ uncertainty on the FRB position) to Source 3 from the left panel, i.e. the M81 globular cluster [PR95] 30244. The image is a g', r' and i' band optical image using Subaru's Hyper Suprime-cam. The FRB is found $\sim$ 2 pc from the centre of optical light of the globular cluster. Figure from Kirsten et al. (2022).

der of magnitude (see §1.2.4 and Figure 1.2). Furthermore, the FRB 20200120E timescales span from $\sim$100 µs down to $\sim$ 60 ns, atypically narrow compared with other well-studied FRBs, but comparable to the phenomena seen in Crab pulsar giant pulses (Hankins & Eilek, 2007). Despite the timescales and luminosities differing from other FRBs, the burst morphology, polarimetric properties, activity behaviour and energetics resemble those of other repeating FRBs. Observationally, FRB 20200120E is sitting in the middle of these different sources of fast radio transients. This highlights the importance of nearby sources for our understanding of the origins of these fast transients spanning across a broad range of phase space (Figure 1.2).

1.3 The FRB population

The FRB field has advanced significantly since I began my PhD; this is mostly a result of the rapid rise in the number of known FRBs from a few dozen in 2018 to now exceeding 600, of which $\sim$ 4% are known to repeat (as of May 2022; e.g. CHIME/FRB Collaboration et al. 2021). Continuing to study interesting individual FRB sources, those that seem to observationally stand-out from the general population (e.g., FRB 20201124A's suddenly high activity, or the so far non-repeating FRB 20191221A which shows a $\sim$ 217 ms periodicity between sub-bursts; The CHIME/FRB Collaboration et al. 2021) will continue to unveil im-

portant insights into the nature of FRBs. We are now also entering the regime of having sufficient numbers to explore the population statistics.

Since the discovery of the first repeating FRB, FRB 20121102A (see §1.2.1; Spitler et al. 2016), there has been debate about whether repeating and non-repeating FRBs come from different types of astrophysical objects, or whether the only difference is the activity rate: perhaps if one observes for long enough a non-repeater will produce more bursts. Recently, however, using the first CHIME/FRB catalog of 536 FRB sources (CHIME/FRB Collaboration et al., 2021), Pleunis et al. (2021a) show that, in general, repeating FRB bursts are temporally wider, and spectrally narrower than the non-repeating FRBs. Additionally, the burst morphology appears to differ between repeaters and non-repeaters: broadband, "simple" bursts are common morphological types of non-repeating FRBs (Type 1 in Figure 1.11; Pleunis et al. 2021a), but are never seen in the case of repeaters, while almost all repeating FRBs exhibit narrowband bursts (Type 2 in Figure 1.11; Gourdji et al. 2019), and downward-drifting sub-bursts (Type 4 in Figure 1.11; Hessels et al. 2019; Pleunis et al. 2021a). Already sub-populations appear to be forming, and future additions of polarimetry, extremely high time resolution studies, as well as precision localisations of this large scale will further advance our knowledge of the different FRB types, and what this means for their progenitor and emission physics.

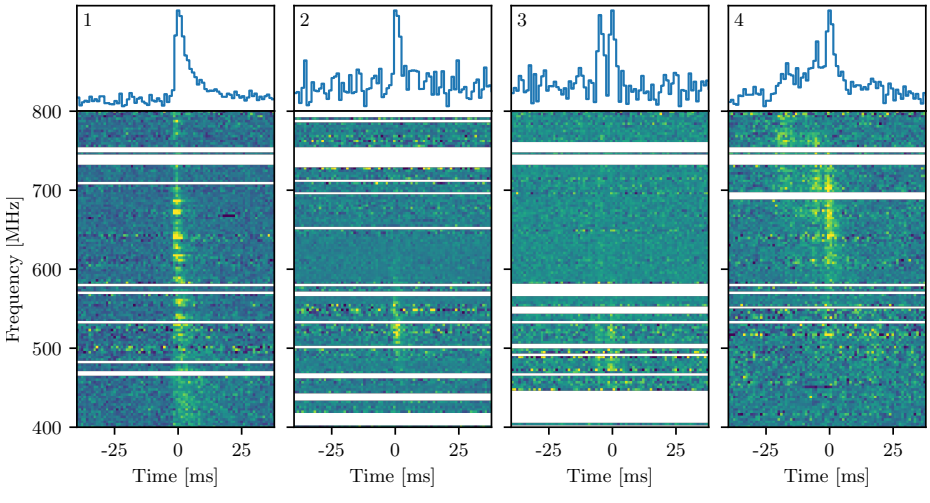

Figure 1.11: Four identified FRB morphological types. Dispersion has been corrected for in the burst dynamic spectra (flux as a function of frequency and time) and profiles (frequency-averaged). Type 1 shows a broadband "simple" burst with scatter broadening creating an exponential tail to the FRB profile. Type 2 is a narrowband "simple" burst. Type 3 shows multiple burst components that share a similar spectral extent. Lastly, Type 4 shows the downward-drifting sub-bursts, often termed the "sad-trombone" effect, of repeating FRBs (Hessels et al., 2019). Note that the white bands in the dynamic spectra are data that have been masked due to the presence of radio frequency interference. Figure from Pleunis et al. (2021a).

To date, there are $\sim$ 20 FRBs localised to host galaxies[7], 7 of which are repeating FRBs (Chapters 5 and 6; Chatterjee et al. 2017; Marcote et al. 2017; Bannister et al. 2019; Ravi et al. 2019; Prochaska et al. 2019; Bhardwaj et al. 2021b; Macquart et al. 2020; Heintz et al. 2020; Law et al. 2020; Bhandari et al. 2020; Niu et al. 2021; Kirsten et al. 2022; Bhandari et al. 2022). As is clear from the work presented in this thesis and discussion throughout §1.2, repeating FRBs live in a diversity of environments. Some are found in close proximity to active star-formation, while others are found in galaxies with low star-formation rates. They are sometimes found well within the galactic disk of their host and, conversely, sometimes in the outskirts of the host galaxy (Bhandari et al., 2022). Despite only having a small number of localised FRBs, some trends are emerging: e.g., FRBs preferentially avoid massive red galaxies; the host properties are consistent with hosts of core-collapse supernovae; and the offsets of FRBs from their host galaxy centres are inconsistent with the Milky Way's neutron star population[8] (Bhandari et al., 2022). Currently the CHIME/FRB telescope (see §1.6) is being outfitted with sister telescopes separated at large distances to be used as a very-long-baseline interferometer (CHIME/Outrigger project). The prospects for this experiment are incredibly promising, with expectations of a few FRBs precisely localised *daily*. Depending on the available optical follow-up resources, this will provide a large sample of FRBs with known host galaxy properties in the near future. Soon there will be hundreds-to-thousands of precisely localised FRBs, providing valuable insight into the question of the FRB origin(s).

1.4 FRB progenitor and emission models

Following the discovery of pulsars (Hewish et al., 1968), the existence of short-duration radio transients bright enough to be detected from extragalactic distances have been proposed since the 1970s: coming from, e.g., an expanding supernova shock ploughing into surrounding material (Colgate & Noerdlinger, 1971; Colgate, 1975) or from the final evaporation of black holes through the release of Hawking radiation (Rees, 1977). The list of possible progenitors capable of producing FRBs has expanded drastically since their discovery in 2007 (Lorimer et al., 2007; Platts et al., 2019): ranging from isolated compact objects (e.g., Rees 1977; Cordes & Wasserman 2016; Metzger et al. 2017), interacting and colliding compact objects (e.g., Lyutikov 2013; Gu et al. 2016; Zhang 2016, 2017) to more exotic models such as superconducting cosmic strings (e.g., Vachaspati 2008).

At least some FRBs have been seen to repeat (e.g., Spitler et al. 2016) meaning that a cataclysmic origin of the burst emission is ruled out for these sources. These repeating FRB sources have huge energy budgets of $\sim 10^{47}$–10^{49} erg (Margalit et al., 2020). One of the most compelling progenitor models, to date, are magnetars. The reasons for this are, firstly, magnetars have ultra-strong, multi-polar magnetic fields (10^{14}–10^{15} G), which can be considered a huge energy reservoir, from which the energy in the FRBs can be drawn (e.g., during outbursts in which the magnetic field topology reconfigures; Lyutikov & Popov 2020; Lyutikov 2021). Additionally, as described throughout Chapter 1, neutron stars are prolific producers

[7] https://frbhosts.org/

[8] Although it is worth noting that the current localised FRB sample may be biased by radio and optical observational selection effects (Seebeck et al., 2021).

of radio transients on millisecond timescales (albeit typically at much lower luminosities), and, to date, one Galactic magnetar has produced a radio transient closely resembling the FRB phenomenon in terms of its duration, spectrum and luminosity (§1.2.4; CHIME/FRB Collaboration et al. 2020; Bochenek et al. 2020).

However, a number of FRB observations challenge the simple hypothesis of an isolated magnetar. SGR 1935+2154 is an isolated magnetar with a spin period of 3.245 s (Israel et al., 2016). Longer periods of hundreds of days have been claimed for the activity behaviour of SGR 1935+2154 (Grossan, 2021), however this remains to be conclusively shown and therefore it is unclear whether an isolated magnetar like SGR 1935+2154 could be responsible for the observed 16-day and tentative 160-day activity cycles of FRB 20180916B (§1.2.2) and FRB 20121102A (§1.2.1), respectively. Perhaps a binary system is required to introduce such a long activity period (e.g., Zhang 2017; Lyutikov 2020), however ultra-long period magnetars (e.g., Beniamini et al. 2020) and precession (e.g., Zanazzi & Lai 2020) have also been suggested to explain this phenomenon.

SGR 1935+2154 has also only been seen to produce a single bright FRB-like transient in the last 3–4 years (the time span over which the transit telescope CHIME/FRB has been operational, although note that CHIME can only see SGR 1935+2154 for at most a few hours per day)[9]. Some repeating FRBs, however, have been seen to produce hundreds-to-thousands of FRBs in time spans of weeks and months, despite their much larger distances (Li et al., 2021; Hewitt et al., 2021; Jahns et al., 2022; Xu et al., 2021). Can this drastic difference in activity rate arise due to the physical conditions of the magnetar (e.g., age, magnetic field strength and magnetic field topology)? Or does the difference arise due to propagation effects in the local environment?

Magnetar progenitor models are broadly divided into two categories: magnetospheric (e.g., Lu et al. 2019), where the emission arises from within the neutron star's magnetosphere, or non-magnetospheric (e.g., Metzger et al. 2019), where the emission originates from much larger radial distances. In magnetospheric models, the FRB emission is thought to be emitted by either reconfiguration of the magnetic field lines (Lyutikov & Popov, 2020; Lyutikov, 2021) or acceleration of charged particles along magnetic field lines close to the neutron star surface emitting curvature radiation (Kumar et al., 2019). For the FRB origin to be at large radial distances from the central neutron star, Metzger et al. (2019) suggest an outward propagating shock from, e.g., a magnetar flare, interacting with the surrounding material to produce the FRB emission.

The host galaxy properties of the $\sim$ 20 well-localised FRBs are consistent with magnetars created through core-collapse of a massive star, with the exception of FRB 20200120E found living in a globular cluster (§1.2.5; Kirsten et al. 2022). Although stellar core-collapse is the most likely way to create a magnetar, they can be created by other formation channels such as accretion-induced collapse of a white dwarf (e.g., Nomoto & Kondo 1991; Tauris et al. 2013) or the merger of compact objects (e.g., Rosswog et al. 2003; Zhong & Dai 2020). Future studies of individual *interesting* FRB sources, Galactic neutron stars, and the FRB

[9] CHIME/FRB did report some subsequent lower-luminosity radio bursts from SGR 1935+2154, detected about 6 months after the FRB-like event (Good & Chime/Frb Collaboration, 2020).

population as a whole will shed light on whether isolated magnetars are responsible for the phenomena observed, whether a binary companion must be introduced to explain a subset of the FRB population, or perhaps even whether some other non-magnetar progenitor is required to explain all of the emission types observed.

1.5 FRBs as probes

Having large numbers of well-localised and well-characterised FRBs will shed light on their progenitor and emission properties. But even in the absence of knowledge about the FRB origin, and as with pulsars, FRBs have huge potential as astrophysical and cosmological probes.

Short-duration radio transients are highly affected by propagation effects such as dispersion (see §1.1). As mentioned in §1.1, pulsars have been used to map the ionised material in the Milky Way. Since FRBs are much more distant than the known pulsar population, their signals interact with not only the ionised material in the Milky Way, but also any ionised material in the host galaxy, any intervening galaxy, and additionally the medium *between* galaxies. The material in the IGM is difficult to probe using methods such as absorption line spectroscopy since it is not sensitive to 100% of the baryons and there are uncertain assumptions used. In contrast, an FRB's DM is essentially a count of every baryon along the line-of-sight from the FRB source to Earth, and therefore can be used to probe this otherwise invisible material (Macquart et al., 2020). The baryonic content in the IGM is related to redshift through the relationship (Deng & Zhang, 2014; Zhou et al., 2014; Petroff et al., 2022)

$$\mathrm{DM_{IGM}} = \Omega_B \frac{3H_0 c}{8\pi G m_p} \int_0^{z_{\mathrm{FRB}}} \frac{(1+z) f_{\mathrm{IGM}} [\frac{3}{4} X_{\mathrm{H}}(z) + \frac{1}{8} X_{\mathrm{He}}(z)]}{[\Omega_M (1+z)^3 + \Omega_\Lambda (1+z)^{3(1+w(z))}]^{1/2}} dz, \tag{1.8}$$

for Hubble constant H_0, baryonic Ω_B, matter Ω_M, and dark energy Ω_Λ densities, relative to the critical density $\rho = 3c^2 H_0^2 / 8\pi G$, speed of light c, gravitational constant G, proton mass m_p, dark energy equation-of-state parameter w, fraction of baryons remaining in the IGM from the Big Bang f_{IGM} and the ionisation fractions of hydrogen X_{H} and helium X_{He}. Having a large number of FRBs with known redshifts and IGM dispersion contributions will independently constrain the cosmological parameters, e.g., the Hubble constant $\mathrm{H_0}$ and the baryonic density Ω_B. The prediction is that 500 FRBs are required to constrain the Hubble constant to the few percent level (Hagstotz et al., 2022), which could relieve the tension between the cosmic microwave background (Planck Collaboration et al., 2020) and type Ia supernovae methods (Riess et al., 2019)[10]. The variance in this DM–z relationship also contains valuable insight into the structure of baryonic matter in galactic halos along the line-of-sight (McQuinn, 2014).

While dispersion is used to probe the amount of ionised material along the line-of-sight, Faraday rotation (see §1.2.1) can be used to probe the magnetisation of the material in

[10] We add the caveat that these are early-time and late-time measurements of $\mathrm{H_0}$, so if there is evolution of $\mathrm{H_0}$ with redshift then one should expect a difference in these measurements.

other galaxies and between galaxies. Another propagation effect we have not discussed yet is scintillation, which describes the distribution of the ionised material along the line-of-sight, i.e. how clumpy the material is (Figure 1.12). Scintillation studies on a large sample of FRBs can be used to probe the turbulence in the IGM (Xu & Zhang, 2020).

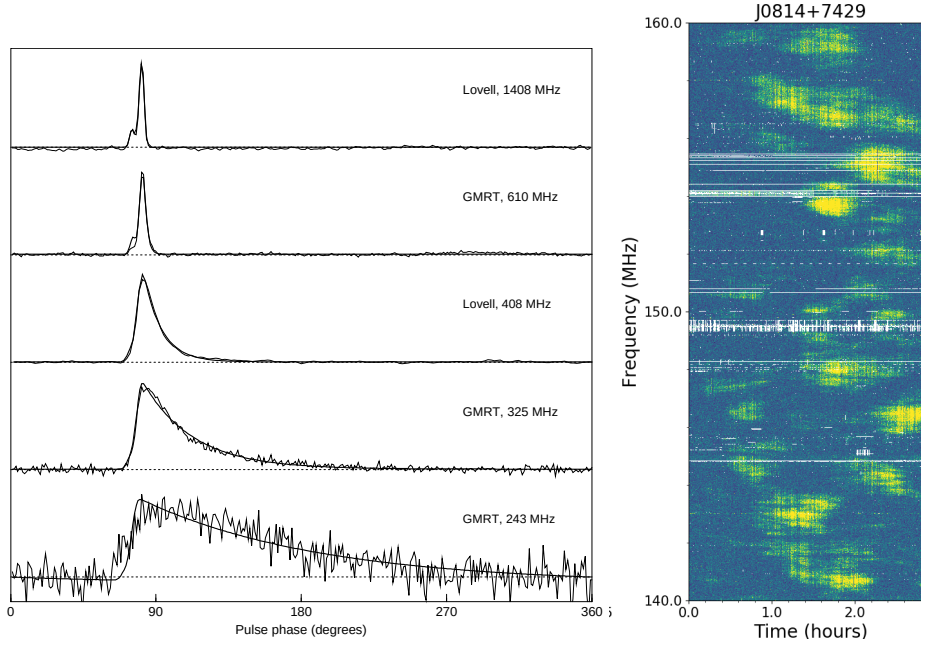

Figure 1.12: (i): Refractive scintillation is caused by large physical scale fluctuations in the density of the ISM. This scatters the radio waves creating an exponential scattering tail which becomes more prominent as the observing frequency decreases. The example shown here is the pulse profile of pulsar PSR B1831−03, and a similar effect is seen in extragalactic FRBs (a nice example can be found in Thornton et al. 2013). Figure from Lorimer & Kramer (2004). **(ii)**: Diffractive scintillation caused by small physical scale fluctuations in the ISM density, creating a diffraction pattern due to interference of the radio waves. This is viewed as "scintles", bright patches in frequency that change on timescales of seconds to hours. Shown here is the dynamic spectrum over a timescale spanning many pulse rotations of the pulsar J0814+7429, showing the scintillation pattern. The white horizontal and vertical stripes are data that have been masked due to the presence of radio frequency interference. Again this effect is sometimes seen in extragalactic FRBs, for example the bursts presented in Chapter 3 show bright scintles in their dynamic spectra (Figure 3.2). Figure from Wu et al. (2022).

1.6 Radio observations of fast transients

The FRB sources studied in this thesis, and the majority of the FRB sources in the literature to date, were all originally discovered via the CHIME/FRB project (CHIME/FRB Collaboration et al., 2018). The design of the CHIME telescope is four large cylindrical reflectors aligned North-to-South (Figure 1.13i), each cylinder focuses to a line made up of 256 individual dual-polarisation receivers which measure the electric field. CHIME is a transit telescope

and has no moving parts. The powerful signal processing does the work: it digitises the incoming signal and splits it into $n_{\rm chan} \sim 16000$ frequency channels between 400 MHz and 800 MHz, before spatially fast Fourier transforming to create 1024 pointed beams (Ng et al., 2017). This provides a combined field of view of $\sim$ 200 square degrees, with a sampling time of 1 ms.

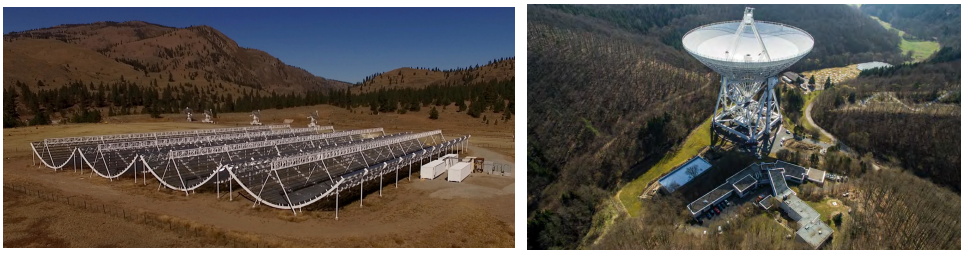

(i) (ii)

Figure 1.13: (i): Photograph of the CHIME telescope located at the Dominion Radio Astrophysical Observatory (DRAO) in Canada. The four cylindrical reflectors are clearly visible, with the containers housing the backend system to search for FRBs found next to the right-most cylinder. Figure from CHIME/FRB Collaboration et al. (2018). **(ii)**: Photograph of the 100-m Effelsberg telescope in Germany. Figure from Ros et al. (2018).

Although the design of CHIME (large field of view and wide frequency coverage) was chosen with the original science goal of mapping the hydrogen intensity at redshifts of $z \sim 0.8$ – 2.5 to measure the Universe's expansion, it also has proven to be an incredible FRB finding machine, discovering FRBs at a rate of 2–3 daily (CHIME/FRB Collaboration et al., 2021)[11].

To search for FRBs, the total intensity signals from each of the sky pointings are analysed in parallel. This *real-time* analysis pipeline includes cleaning the data of any terrestrial radio signals that interfere with the search, shifting the frequency channels with respect to some reference frequency to correct for dispersion (at various trial DM values), before finally searching for peaks over a range of possible widths in the frequency-averaged time series (CHIME/FRB Collaboration et al., 2018). The data products of this initial burst search pipeline are total intensity only, with 1 ms time samples. However, if an FRB is discovered within 35.5 s of the data being recorded, the voltage data (also referred to as "baseband" data) from the 1024 dual-polarisation pointings can be saved to disk, providing the opportunity to, e.g., extract polarisation information and explore sub-millisecond timescales (Michilli et al., 2021). Relevant for the work presented in this thesis is the localisation precision improvement gleaned from this raw data product compared with the total-intensity search data: from $\sim$10s of arcminutes to $\sim$arcminutes using the phase information of the voltage data to create pointed beams (Michilli et al., 2021). The field of view of a relatively large (100-m) radio telescope is $\sim$ 10 arcminutes at 1.4 GHz (using Equation 1.5 with the telescope diameter instead of b), therefore this localisation improvement is critical for the burst searches that we conducted with the Effelsberg 100-m radio telescope (Figure 1.13ii).

[11] https://www.chime-frb.ca/voevents

For FRB sources which are identified to repeat and are localised to within the field-of-view of Effelsberg, we conducted follow-up observations with Effelsberg as a single-dish, as well as connecting Effelsberg and many other radio dishes across the world as a very long baseline interferometer (Figure 1.14): a telescope called the European VLBI Network (EVN).

1.6.1 Effelsberg 100-m radio telescope

The power collected by a radio telescope is proportional to the effective collecting area and the signal intensity. Therefore, the larger the radio telescope (the more collecting area), the higher the sensitivity, although aperture efficiency and system temperature also significantly impact the sensitivity of a radio telescope. The Effelsberg radio telescope in Germany is one of the largest steerable radio telescopes in the world, and is therefore one of the most sensitive single-dish radio telescopes.

Effelsberg has a number of receivers with observing frequencies in the wide range from $\sim$ 300 MHz to $\sim$100 GHz. In this thesis, the 7-beam 1.4 GHz receiver is used. One of the unique advantages of Effelsberg for observing FRBs is its suite of high-time-resolution backend systems: the PSRIX (Lazarus et al., 2016) which we used until replaced by the Effelsberg Direct Digitisation backend (EDD). These systems have a "baseband mode", which records the high time resolution total intensity search data and simultaneously the voltages measured in both polarisation hands of the receiver. This is similar to CHIME saving the raw data products when they detect a burst, however, with Effelsberg we store the raw data for the *entire* observation. This provides full polarisation information, as well as an exceptionally high time resolution of $\sim$ 1 ns.

1.6.2 European VLBI Network

One of the main limitations of single-dish radio telescopes is their angular resolution. As described above (see Equation 1.5), the angular resolution is inversely proportional to the aperture diameter. The largest single-dish radio telescope, to date, is the 500-m FAST telescope in China (Nan et al., 2011), with an effective illuminated diameter of 300 m. This results in an angular resolution of $\sim$ 3 arcminutes at 1.4 GHz. For distant FRBs, there could be 10s to 1000s of galaxies within this field-of-view that could host the FRB source. In order to pinpoint FRBs to their host galaxies, $\sim$arcsecond precision is required at minimum (Eftekhari & Berger, 2017). But cost and engineering limit the ability to build bigger single-dish radio telescopes.

To achieve higher angular resolution, interferometry is used (Ryle & Vonberg, 1946). An interferometer combines the signals from separate array elements to obtain spatial information about the signal, where the resolution is dictated by the maximum separation of the elements in the array (Equation 1.5). The precision with which a signal can be localised on the sky is of course proportional to the angular resolution: the higher the angular resolution, the higher the localisation accuracy. But it also depends on the array configuration,

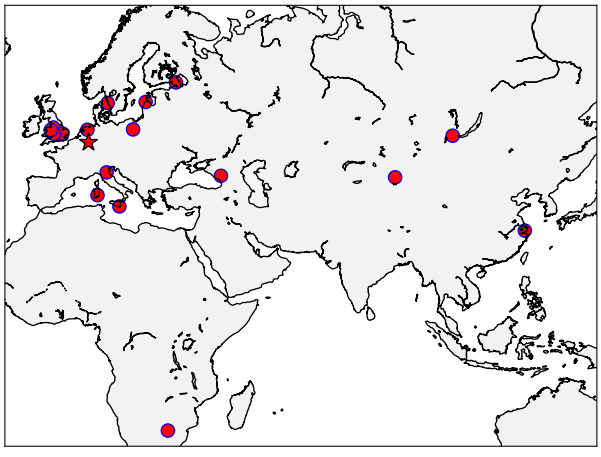

Figure 1.14: Map of the EVN telescopes used to create interferometric arrays for the work presented in Chapters 5, 6, 7 and Kirsten et al. (2022). The star marker highlights Effelsberg, which is used as the "burst finder" telescope for interferometric work since it is one of the most sensitive telescopes in the EVN.

total time integrated and quality of the calibration[12]. Additionally, the localisation precision is also proportional to the signal-to-noise ratio of the signal: i.e. brighter signals can be localised more accurately. There are limitations to this, arising from the uncertainties on the positions of calibrator sources, as well as the shape and size of the source.

VLBI is interferometry using array elements distributed globally, with separations of 100s-to-1000s of kilometres. The EVN is a global network of radio telescopes, whose data are correlated at the Joint Institute for VLBI ERIC (JIVE) in the Netherlands to achieve extremely high spatial resolution images of the radio sky. We use the EVN in Chapters 5, 6 and 7 of this thesis (Figure 1.14) to pinpoint FRBs on the sky to *milliarcsecond precision*, as well as to study a persistent radio source with observational properties similar to the persistent radio source associated with FRB 20121102A (see §1.2.1). With milliarcsecond precision, not only can we identify the host galaxy of an FRB, but we can probe ∼pc scales around the FRB giving valuable clues about the FRB's local environment.

[12] The spatial frequencies you are sampling with an interferometer is called the *uv*-coverage, and depends on the array configuration, radio observing frequency and source position. Allowing the Earth to rotate with time, i.e. allowing the projected array configuration to rotate, adds to the *uv*-coverage. Generally, the more "filled" your *uv*-coverage is, the better your final interferometric image will be.

1.7 Thesis summary

This thesis is focused on exploring the nature of FRB emission by studying the burst properties and local environments in detail. The main science questions considered are:

- What types of astrophysical objects are capable of producing fast radio transients?
- Are repeating and non-repeating FRBs coming from the same type of sources, but with varying levels of activity?
- Are all repeating FRBs the same type of object?
- What is the physical mechanism behind the FRB emission?

The thesis is divided into two parts. The first, "Zooming-in in time", details work using extremely high time resolution (from 30 ns to μs) single-dish Effelsberg observations (see §1.6.1) of repeating FRB sources. In the second, "Zooming-in in space", we use the EVN (see §1.6.2) to pinpoint repeating FRBs to milliarcsecond precision, identifying their host galaxies, probing their immediate surroundings and we study a radio transient with a potential link to FRBs on spatial scales of $\sim$ pc.

Zooming-in in time

In Chapter 2 we probe 1.4 GHz FRB 20180916B (§1.2.2) burst properties down to microsecond timescales using raw voltage data recorded with the 100-m Effelsberg telescope. We show that the bursts exhibit a range of timescales from milliseconds down to 3–4μs (Figure 2.1). These short timescales cast doubt on the non-magnetospheric emission models (§1.4), since they imply a small emission region ($\sim$km ignoring relativistic effects). Following Beniamini & Kumar (2020), the minimum observable timescale is

$$\delta t = \frac{r\epsilon^2}{2c\gamma^2}, \tag{1.9}$$

which gives $\delta t \sim 10\mu$s for radial distance $r = 10^5$ km, radiative efficiency $\epsilon = 0.1$ and Lorentz factor $\gamma = 10$ (Kumar et al., 2017). Therefore, the microsecond burst structure we observed is most *naturally explained* in magnetospheric models (radial distance $< 10^5$ km). Additionally, we observe polarimetric properties akin to that of FRB 20121102A, but differing from the general non-repeater polarimetric properties, suggesting that repeating FRBs could have a characteristic polarimetric description. Specifically, FRB 20180916B bursts at 1.4 GHz are $\sim$ 100% linearly polarised, and $\sim$ 0% circularly polarised, with a constant polarisation angle during and *between* bursts (Figure 2.5).

Diffractive scintillation in the Milky Way ISM causes scatter broadening on a timescale of $\sim$ 2.7 μs at 1.4 GHz along the line-of-sight to FRB 20180916B. This means that we are unable to probe timescales shorter than a few microseconds in the case of FRB 20180916B at 1.4 GHz. FRB 20200120E, however, is at much higher Galactic latitude than FRB 20180916B, meaning that the path through the Milky Way is "cleaner" and does not induce as large a scatter broadening effect on bursts from FRB 20200120E (Figure 3.6). In Chapter 3 we exploit this fact and probe down to timescales of tens of nanoseconds. Typically the bursts have

durations of 100 μs, which is exceptionally narrow compared with other repeating FRBs. In one burst we see strong micro-structure which resolves down to 60 ns isolated shots of emission (Figure 3.1), analogous to the "micro-bursts" and "nano-shots" phenomenology seen from Crab pulsar giant pulses (Hankins & Eilek, 2007). The observed 60 ns timescales further constrain the size of the emission region to be on the order of 10 m (ignoring relativistic effects). Not only are the timescales generally shorter than typical for FRBs, but we find the luminosities to be a few orders-of-magnitude lower than the weakest FRBs (and even 1–2 orders of magnitude weaker than the FRB-like burst from SGR 1935+2154; see §1.2.4). The range of timescales and luminosities we measure from FRB 20200120E is bridging the gap in the transient phase space between Galactic neutron stars and extragalactic FRBs (Figure 1.2). In this work, we are probing a relatively unexplored parameter space in the extremely short-duration (ns–μs), high-luminosity regime. This highlights that potentially there are *ultra*-fast transients populating this parameter space that current FRB searches are insensitive to.

In addition to FRB 20200120E exhibiting atypically narrow burst durations and low luminosities, FRB 20200120E lives in a nearby globular cluster (in M81, with distance 3.63 Mpc; Kirsten et al. 2022), which is in stark contrast to the other well-localised repeating FRBs found in relative proximity to star-formation (see §1.2). However, we show in Chapter 3 that the bursts exhibit polarimetric properties which match the characteristic description for repeating FRBs described in Chapter 2. Furthermore, in Chapter 4 we present the first-detected "burst storm" (53 bursts discovered in a 40 minute time window) from FRB 20200120E, resembling the activity behaviour of other repeating FRBs (Figure 4.12). With a large burst sample, we also show that the burst energy distribution is consistent with a power law (with index -2.39 ± 0.12; Figure 4.16), the time *between* consecutive bursts follow a bi-modal distribution (Figure 4.13), and there is no underlying periodicity in the burst arrival times, all characteristic of repeating FRBs. Whether FRB 20200120E is the same type of object as these other highly active repeating FRBs is still up for discussion, but Chapters 3 and 4 highlight the importance of FRB 20200120E and other local Universe (< 100 Mpc) sources of fast radio transients to bridge our knowledge from Galactic sources to the extremely distant FRBs.

Zooming-in in space

As mentioned in §1.6.2, the localisation precision with VLBI depends on the maximum separation of array elements, as well as the array configuration (number **and** orientation of array elements), time on source, the source's signal-to-noise ratio and how well calibrated the data is. FRBs, however, are ∼millisecond-duration transients, which is essentially a "snapshot" in VLBI (no time integration). The advantage of repeating FRBs is that they produce multiple bursts, so combining the data from multiple bursts improves the localisation accuracy (especially if they are separated by sufficient time such that the Earth has rotated causing the projected array configuration to significantly change)[13].

[13] Though with a large number of telescopes, optimally oriented, and good calibration, even single bursts can be localised to milliarcsecond precision using VLBI.

Due to the extremely high activity of FRB 20201124A (§1.2.3), we detected a total of 18 bursts during our VLBI campaign, at two separate observing epochs (Chapter 5). Using the full sample we determined the FRB position to 2.7 mas accuracy ($1\,\sigma$). Having such a large burst sample provided the opportunity to explore the astrometric accuracy as a function of burst brightness and number of telescopes, while having detections at multiple epochs allowed for an independent calibration to limit any systematic calibration uncertainties on the final FRB position. We find that for $\geq$ 7 array elements, single bursts can be localised to milliarcsecond precision, and that this drops to 0.1–1 arcsecond precision for 4 array elements. This is promising given that arcsecond localisation precision is sufficient to identify the FRB's host galaxy, while increasing to milliarcsecond precision will strongly constrain the local environment properties.

With the 2.7 mas localisation precision (Figure 5.2), we find that FRB 20201124A is embedded in a star-forming region (Piro et al., 2021) in a massive star-forming galaxy at a redshift of $z = 0.0979 \pm 0.0001$ (Fong et al., 2021; Ravi et al., 2022). It is interesting to consider whether FRB 20201124A's high bursting activity (compared with other repeaters) is related to its close proximity to active star formation. FRB 20121102A (§1.2.1) is also living within a star-forming region (Bassa et al., 2017) and has relatively high bursting activity (Li et al., 2021). The notable difference between FRB 20121102A and FRB 20201124A is that the former has a compact persistent radio counterpart, while we show in Chapter 5 that FRB 20201124A does not, down to a limit of 25 μJy beam^{-1} (a factor of $\sim$ 60 times weaker than the radio counterpart to FRB 20121102A; Figure 5.2). This work further establishes the fact that repeating FRBs live in a diversity of host galaxy types and local environments, a fact first established by the work presented in Chapter 6.

In Chapter 6 we precisely localise FRB 20180916B to a massive (stellar mass 10^{10} M$_\odot$) Milky Way-like spiral galaxy using the EVN (Figure 6.5). Not only does this host galaxy highlight that the low-metallicity dwarf galaxy origin of FRB 20121102A is not a requirement for a repeating FRB, but the lack of a comparably bright persistent radio source, and relatively low RM, shows that their environments differ greatly. Using the 8-m Gemini-North telescope, we determine a spectroscopic redshift of FRB 20180916B's host galaxy, $z = 0.0337 \pm 0.0002$ (luminosity distance 149.0 ± 0.9 Mpc), which, at the time of publication, was by far the closest FRB known (compared with the typical $\sim$Gpc FRB distances). Additionally, using Gemini-North, we determine that FRB 20180916B is living at the apex of a "v-shaped" star-forming region[14]. This work shows that FRBs live in a diverse range of host galaxy types and local environments. Perhaps this could mean that different types of astrophysical objects can produce FRBs, or that a single FRB progenitor can live in many different environments.

Although Chapter 6 shows that not all repeating FRBs have luminous persistent radio sources, a second repeating FRB, FRB 20190520B, was found with a persistent radio counterpart, and other strikingly similar qualities to FRB 20121102A (§1.2.1; Niu et al. 2021). This highlights that FRB 20121102A is not a red herring, but instead that some repeating FRBs are associated with a persistent radio counterpart. As discussed in §1.2.1, the nature of the persistent

[14] By increasing the spatial resolution in optical follow-up using the *Hubble Space Telescope*, Tendulkar et al. (2021) show that FRB 20180916B is offset from the peak of a nearby star-forming knot by $\sim$ 250 pc (Figure 1.7).

emission is not yet understood, nor is the relationship between the FRB source and the persistent emission. Law et al. (2022) predict that as much as 1% of the compact radio sources in the local Universe could be these FRB persistent radio sources. In Chapter 7, we study a radio source, FIRST J141918.9+394036, sharing properties with the persistent radio counterpart of FRB 20121102A: specifically, host galaxy type, proximity to star-formation and luminosity (Ofek, 2017). Using the EVN, we measure the radio source to be 1.6 ± 0.3 pc in extent (Figure 7.2), which implies an expansion velocity of $(0.10 \pm 0.02)c$, assuming an explosion date in 1993 (from the first reported detection of FIRST J141918.9+394036; Law et al. 2018b). The slowly-decaying nature of the radio source, mildly relativistic expansion and lack of detected radio bursts in high-time-resolution observations (using both the 100-m Effelsberg telescope and the 110-m Green Bank Telescope) supports the hypothesis that FIRST J141918.9+394036 is related to jet expansion from a long gamma-ray burst, and disfavours the competing model of a magnetar wind nebula. Nonetheless, there is evidence for magnetar creation in some long gamma-ray bursts (Stratta et al., 2018), so perhaps radio bursts can be detected from FIRST J141918.9+394036 with sufficient follow-up time and sensitivity. The behaviour of the longer-lived radio emission (expanding in size, and decaying in luminosity), however, points at a fundamentally different origin from the FRB persistent radio emission (Plavin et al., 2022).

In this thesis we show that FRBs come in a variety of "shapes and sizes" in their timescales, luminosities and local environments. This diversity must be accommodated for in the progenitor and emission models of fast radio transients.

ZOOMING-IN IN TIME

Chapter 2

Highly polarized microstructure from the repeating FRB 20180916B

K. Nimmo, J. W. T. Hessels, A. Keimpema, A. M. Archibald, J. M. Cordes, R. Karuppusamy, F. Kirsten, D. Z. Li, B. Marcote, Z. Paragi

Nature Astronomy, 2021, 5, 594

Abstract

Fast radio bursts (FRBs) are bright, coherent, short-duration radio transients of as-yet unknown extragalactic origin. FRBs exhibit a variety of spectral, temporal and polarimetric properties, which can unveil clues into their emission physics and propagation effects in the local medium. Here we present the high-time-resolution (down to 1 μs) polarimetric properties of four 1.7-GHz bursts from the repeating FRB 20180916B, which were detected in voltage data during observations with the European VLBI Network (EVN). We observe a range of emission timescales spanning three orders of magnitude, with the shortest component width reaching 3–4 μs (below which we are limited by scattering). This is the shortest timescale measured in any FRB, to date. We demonstrate that all four bursts are highly linearly polarised ($\gtrsim 80\%$), show no evidence for significant circular polarisation ($\lesssim 15\%$), and exhibit a constant polarisation position angle (PPA) during and *between* bursts. On short timescales ($\lesssim 100$ μs), however, there appear to be subtle (few degree) PPA variations across the burst profiles. These observational results are most naturally explained in an FRB model where the emission is magnetospheric in origin, as opposed to models where the emission originates at larger distances in a relativistic shock.

2.1 Introduction

Many FRBs (Petroff et al., 2019; Cordes & Chatterjee, 2019) show complex burst morphology and, to date, both repeaters and apparent non-repeaters have shown temporal structure, 'sub-bursts', as short as 20–30 μs (Farah et al., 2018; Michilli et al., 2018b; Cho et al., 2020). Probing shorter timescales is a powerful way to constrain emission models because of the limits that such temporal structures place on the instantaneous size of the emitting region: 1 μs corresponds to 300 m, though special relativistic effects cause the light-travel size to be smaller than the actual size.

Voltage data allow access to such timescales, but several practical challenges remain: e.g., scattering due to multi-path propagation can limit the effective time resolution (especially at low radio frequencies); the signal-to-noise (S/N) on short timescales may be too low; there may be limitations on the precision with which the dispersion measure (DM) can be determined, such that it is impossible to ensure that the DM smearing is less than the time resolution; and, if the bursts are composed of a forest of closely spaced (sub-)μs sub-bursts, then confusion may limit our ability to identify individual structures. For example, in the case of FRB 20181112A (Cho et al., 2020), the effective time resolution is limited by scattering, despite available voltage data.

Ultra-high-time-resolution studies are more powerful if they include full polarisation information. In general, FRBs show a variety of polarimetric properties. FRBs have been observed to exhibit linear polarisation fractions from 0% to 100% (e.g. Masui et al. 2015; Michilli et al. 2018b; Caleb et al. 2018; Day et al. 2020). Some FRBs show significant circular polarisation (Petroff et al., 2015), though most so far show very little (Ravi et al., 2016; Caleb et al., 2018). Some sources show a flat PPA across the burst profile (Michilli et al., 2018b; CHIME/FRB Collaboration et al., 2019c; Day et al., 2020), whereas others show a PPA variation (Masui et al., 2015; Luo et al., 2020).

Both FRB 20121102A, the first discovered repeating FRB (Spitler et al., 2014, 2016), and the repeating FRB 20190711A (Day et al., 2020; Kumar et al., 2021), show remarkably similar polarisation properties. FRB 20121102A bursts (in the frequency range 4–8 GHz; Gajjar et al. 2018; Michilli et al. 2018b) and FRB 20190711A bursts (detected at 1.3 GHz; Day et al. 2020; Kumar et al. 2021) are highly linearly polarised (approximately 80–100%), show no sign of circular polarisation, and exhibit a flat PPA across the burst profile. For FRB 20121102A, the absolute PPA value is approximately equal between bursts (Michilli et al., 2018b). In contrast, bursts from the repeating FRB 180301 (detected at 1.25 GHz; Luo et al. 2020), exhibit lower linear polarisation fractions (approximately 30–80%), and some bursts show a PPA swing across the burst profile.

The only other repeating FRB with published polarisation information from multiple bursts is FRB 20180916B (CHIME/FRB Collaboration et al., 2019c; Chawla et al., 2020). Bursts from FRB 20180916B, measured at both 600 MHz (CHIME/FRB Collaboration et al., 2019c) and 350 MHz (Chawla et al., 2020), exhibit approximately 100% linear polarisation, show no evidence for circular polarisation, and show a flat PPA over the burst duration. This is consistent with observations of FRB 20121102A and FRB 20190711A. The polarisation properties

of FRB 20180916B, measured at 110–188 MHz, are similar to those at higher frequencies, but also show significant depolarisation down to lowest observed frequencies (Pleunis et al., 2021b). This is likely the result of scattering, though investigation into whether this is due to Faraday conversion (Gruzinov & Levin, 2019; Vedantham & Ravi, 2019) is underway (Pleunis et al., 2021b). FRB 20180916B's polarimetric properties have not previously been investigated at radio frequencies > 1 GHz, where most FRB 20121102A studies have been conducted, and previous studies have been limited by the temporal resolution of the data.

Here we present an analysis of four FRB 20180916B bursts whose spectro-temporal properties were previously presented (Marcote et al., 2020). In the present work, we provide a higher-time-resolution, full polarimetric analysis of this sample. Throughout this paper we use the nomenclature Bn for the bursts, following Marcote et al. (2020). Additionally, we introduce the nomenclature B4-sb$n$ for the three clear sub-bursts in burst B4. In §2.2 we describe the data, in §2.3 we present the high-time-resolution and polarimetry results, and thereafter discuss the consequences for our understanding of repeating FRBs in §2.4.

2.2 The data

The data were acquired as part of an EVN campaign on 2019 June 19 (experiment code: EM135C) at a central radio frequency of 1.7 GHz. Using SFXC (Keimpema et al., 2015), we created two data products. Firstly, we converted the voltage data from the 100-m Effelsberg telescope into full-polarisation (circular basis) filterbank data with time and frequency resolutions of 1 μs and 0.5 MHz, respectively. Secondly, we produced full-polarisation filterbank data with time and frequency resolutions of 16 μs and 62.5 kHz, respectively. The data were coherently dedispersed to a dispersion measure (DM) of 348.76 $\mathrm{pc\ cm^{-3}}$, which is the best-fit DM that maximises S/N for burst B4 at 16 μs time resolution (Marcote et al., 2020). Using PSRCHIVE (van Straten & Bailes, 2011), we created archive files containing each burst from the filterbank files at the native time and frequency resolution. The archive files are incoherently dedispersed to a refined DM using the 1 μs data (see Methods §2.5). We manually mask frequency channels that are contaminated by radio frequency interference (RFI), and artefacts at the sub-band edges.

2.3 Results

In our previous characterisation of these bursts (Marcote et al., 2020), we found that B3 and B4 show several sub-bursts with widths ranging from 60–700 μs. Here, we probe order-of-magnitude shorter timescales by studying the burst temporal properties at higher time resolution. Additionally, we study the bursts' full polarisation properties.

2.3.1 High time resolution

In Figure 2.1, we present the four FRB 20180916B burst profiles at both 16 μs and 1 μs resolution. In the case of bursts B1 and B2, the increase in time resolution does not reveal any shorter-timescale structure, and the burst widths are consistent with those measured

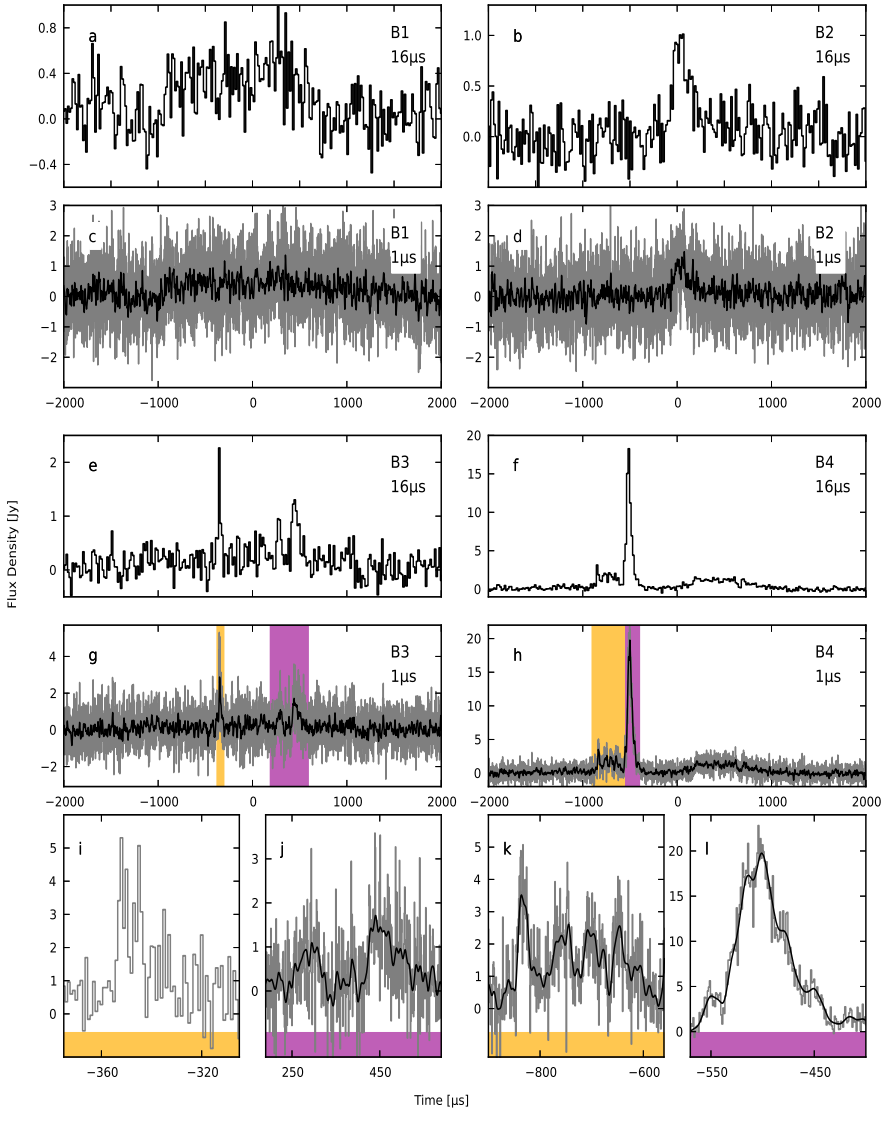

Figure 2.1: Burst profiles at 16 μs and 1 μs time resolution for four 1.7 GHz bursts from FRB 20180916B. The burst name (B1–B4) and time resolution used for plotting is shown in the top right of each panel. Bursts B3 and B4 show complex temporal structure. Panels i and j are zoomed-in 1 μs resolution data around the B3 burst components highlighted by the orange and purple bars in panel g, respectively. Similarly for burst B4, panels k and l are zoomed-in 1 μs resolution data around the B4 burst components highlighted by the orange and purple bars in panel h, respectively. Overplotted on panels j, k and l is a smoothed profile using a Blackman window function with a window length of 19 bins.

Table 2.1: Results of power spectrum fitting

Burst	Power law slope (α)	Goodness of fit p-value[a]	Posterior predictive p-value[b]	Residual outlier p-value[c]
B4-sb2	1.58 ± 0.02	0.44	0.44	0.37
B3	1.38 ± 0.01	0.33	0.74	0.06

[a]Goodness of fit of the power law red noise model described by Equation 2.2.
[b]Model comparison of power law red noise model, versus a power law plus Lorentzian (to describe a quasi-periodic oscillation). See text for details.
[c]p-value of the highest outlier in the residuals of the power spectrum divided by the best fit power law slope.

previously (1.86 ± 0.13 ms and 0.24 ± 0.02 ms for B1 and B2, respectively; Marcote et al. 2020). Bursts B3 and B4 show structure in the 16 μs resolution data. By increasing the time resolution to 1 μs, we see clear 10–20 μs structure in burst B4 (panel k, Figure 2.1), and the bright component of B4 does not appear to be a simple Gaussian envelope; instead, it exhibits 10–20 μs fluctuations on the broader envelope (panel l, Figure 2.1). B3 exhibits 50–100 μs components (panel j, Figure 2.1), and even components that are a few μs wide (panel i, Figure 2.1). We note that the two 3–4 μs components shown in panel i, Figure 2.1, are detected across our 128 MHz band. The 3–4 μs shots of emission are consistent with the estimated Galactic scattering time (2.7 μs; Marcote et al. 2020) for FRB 20180916B.

In addition to B4-sb2's 10–20 μs structure (panel l, Figure 2.1), there also appear to be narrower spikes on top of the burst envelope. We fit the burst envelope and remove it from the data, in order to test the statistical significance of any outliers (see Methods §2.5). We find no significant outliers in this burst, implying that the narrow features are consistent with amplitude-modulated noise (Figure 2.2). This is further supported by our measurement of a S/N-weighted correlation coefficient < 0.2 (panel f; Figure 2.2), where we would expect a value of 1/3 if each time bin is perfectly correlated (and the scattering time is greater than the bursts' separation; Cordes et al. 2004). Due to the large scatter, we cannot distinguish between a constant or slightly decreasing correlation coefficient as a function of lag. Thus, based on the data in hand, we can rule out that B4 is comprised of a few well-separated bright (sub-)μs shots of emission.

By eye, B4-sb1 (panel k, Figure 2.1) appears to fluctuate quasi-periodically. There are other examples of FRBs showing this diffraction-pattern-like temporal behaviour (Hessels et al., 2019), which potentially can be explained by self-modulation breaking the burst into 'pancakes' (Sobacchi et al., 2021), or by plasma lensing (Cordes et al., 2017). To test this, we computed the autocorrelation function (ACF; using Equation 1 in Marcote et al. (2020), but considering time lag instead of frequency lag), and the power spectrum (see Methods §2.5 and Figure 2.3). We find no statistically significant evidence for quasi-periodic emission in the power spectrum of B4-sb1 or B3 (see Table 2.1). We conclude that bursts B4-sb1 and B3 are consistent with red noise, with a power-law index of $\alpha = 1.58 \pm 0.02$ and $\alpha = 1.38 \pm 0.01$, respectively. Typically, magnetar X-ray bursts show steeper red noise spectra ($\alpha \approx 2$–5; Huppenkothen et al. 2013).

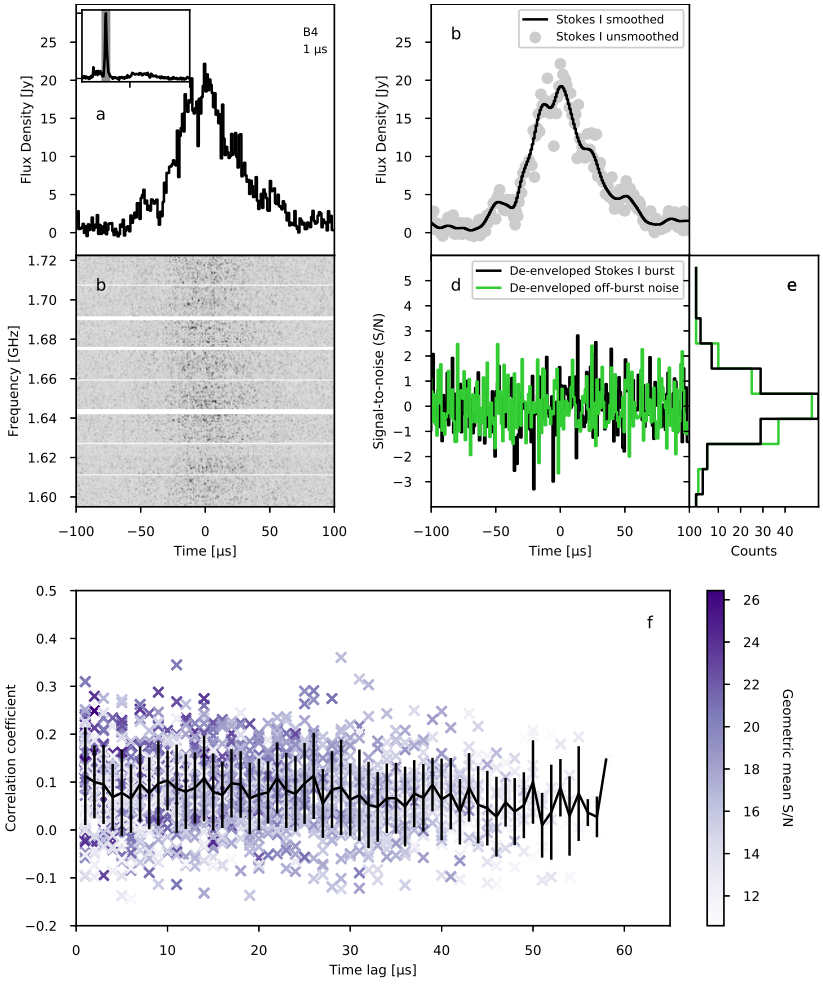

Figure 2.2: Microsecond structure in B4-sb2 consistent with amplitude-modulated noise. Stokes I burst profile of the bright component of burst B4 (B4-sb2) sampled at 1 μs resolution (panel a). The inset of panel a shows the profile of B4 at 16 μs resolution, with the shaded region indicating the extent of the profile shown in the panel. The dynamic spectrum is shown in panel b. Panel c shows the profile again, overplotted with a smoothed profile using a Blackman window function with a window length of 19 bins. The burst profile was "de-enveloped" by dividing out the smoothed profile, and the residuals are shown in black in panel d. Also shown in panel d is the de-enveloped off-burst time series in green, for comparison. In panel e, we show the histogram of the on-burst and off-burst residuals. Panel f shows the correlation coefficient of the spectra of bins with S/N $>$ 10 in the main peak of B4, as a function of time between the spectra (in μs). The colour bar represents the geometric mean S/N of the two time bins that have been correlated, with the darker purple representing a higher S/N. Overplotted in black is the weighted mean and standard deviation per time lag.

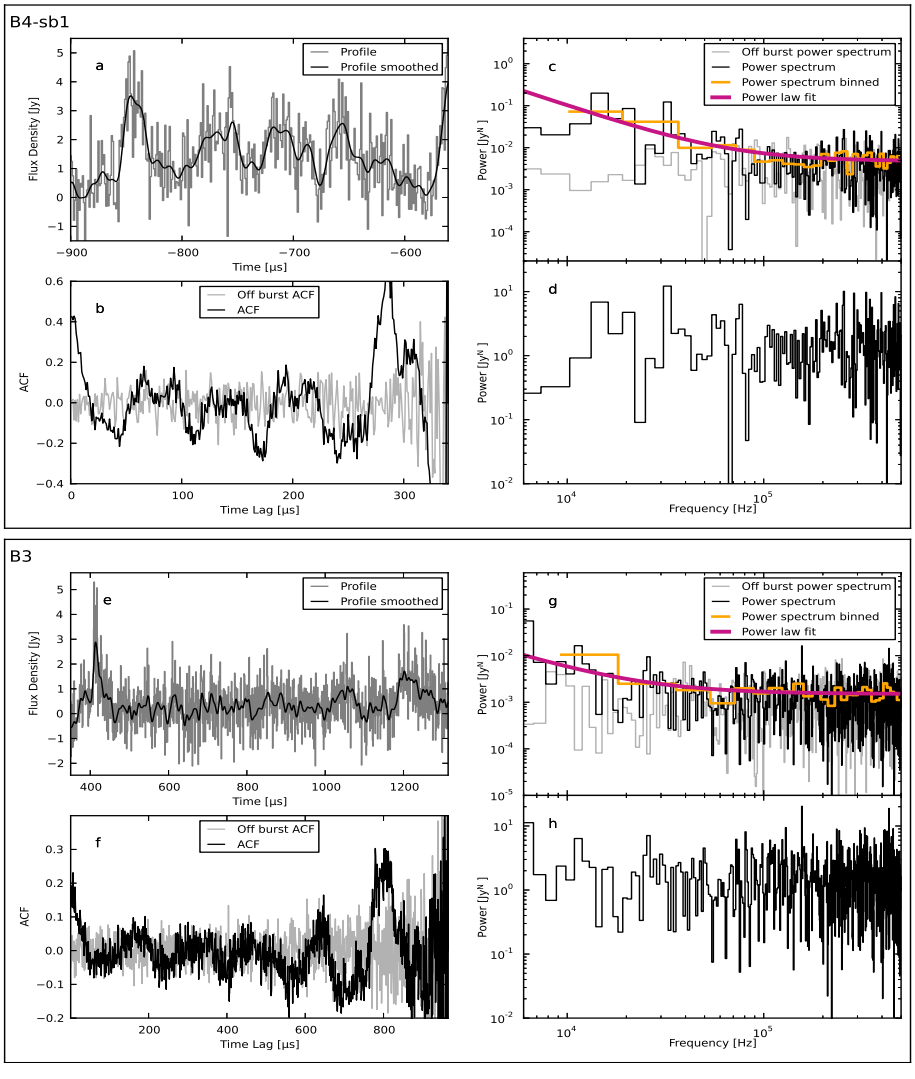

Figure 2.3: Autocorrelation functions (ACFs) and power spectra for B4-sb1 and B3. The temporal profiles of bursts B4-sb1 (top frame) and B3 (bottom frame) are shown in the top left of each frame (panels a and e). The corresponding ACF of these temporal profiles are shown in panels b and f. The corresponding power spectra of the temporal profiles are shown in panels c and g, and the orange line is the power spectrum downsampled in frequency by a factor of 3. Overplotted in pink on the power spectrum is the best fit power law plus white noise component. Panels d and h are the residuals (2×power spectrum/best fit model).

2.3.2 Polarimetry

As described in §2.5, the polarimetric data were calibrated using the test pulsar PSR B2111+46 (Figure 2.4).

For the highest-S/N burst in our sample, B4, we measure the rotation measure (RM) to be $-104 \pm 20\,\mathrm{rad\,m^{-2}}$ (see Methods §2.5), where the large fractional error arises due to covariances between the Q-U fit parameters and instrumental delay between the two polarisation channels, which is not independently constrained. We find the RM to be consistent with previous measurements (CHIME/FRB Collaboration et al., 2019c; Chawla et al., 2020).

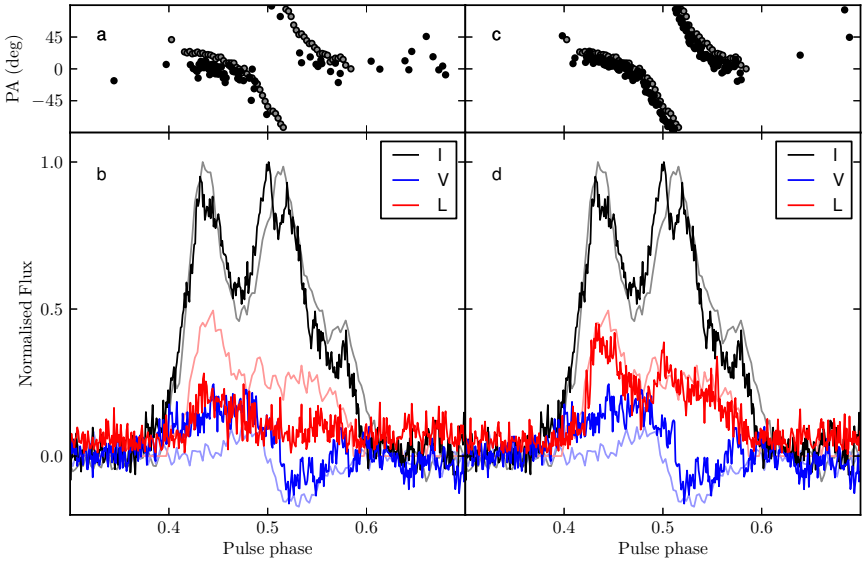

Figure 2.4: Before and after calibrating the polarisation data of PSR B2111+46. The average polarisation profiles (panels b and d) and polarisation position angle (panels a and c) of PSR B2111+46. Black represents the Stokes I profile, red is the unbiased linear polarisation profile (defined in Everett & Weisberg (2001), and rewritten here in Equation 1), and blue is the circular polarisation (Stokes V) profile. Panels a and b show the polarisation profile and position angle after Faraday-correcting to the true rotation measure (Force et al., 2015) of PSR B2111+46 ($-218.7\,\mathrm{rad\,m^{-2}}$); here we are not correcting for the instrumental delay between polarisation hands. Panels c and d are Faraday-corrected with the rotation measure determined using the PSRCHIVE tool rmfit, which, in essence, accounts for the instrumental delay. For comparison, we plot the profile and position angle from the literature using more transparent colours (Gould & Lyne, 1998). This illustrates the calibration we applied to the bursts from FRB 20180916B.

Figure 2.5 shows the Faraday-derotated profiles for the four FRB 20180916B bursts. We use the rmfit-determined RM for B4 (see Methods §2.5) to correct all four bursts, since B4 has the highest S/N, and we assume the RM does not change between bursts separated

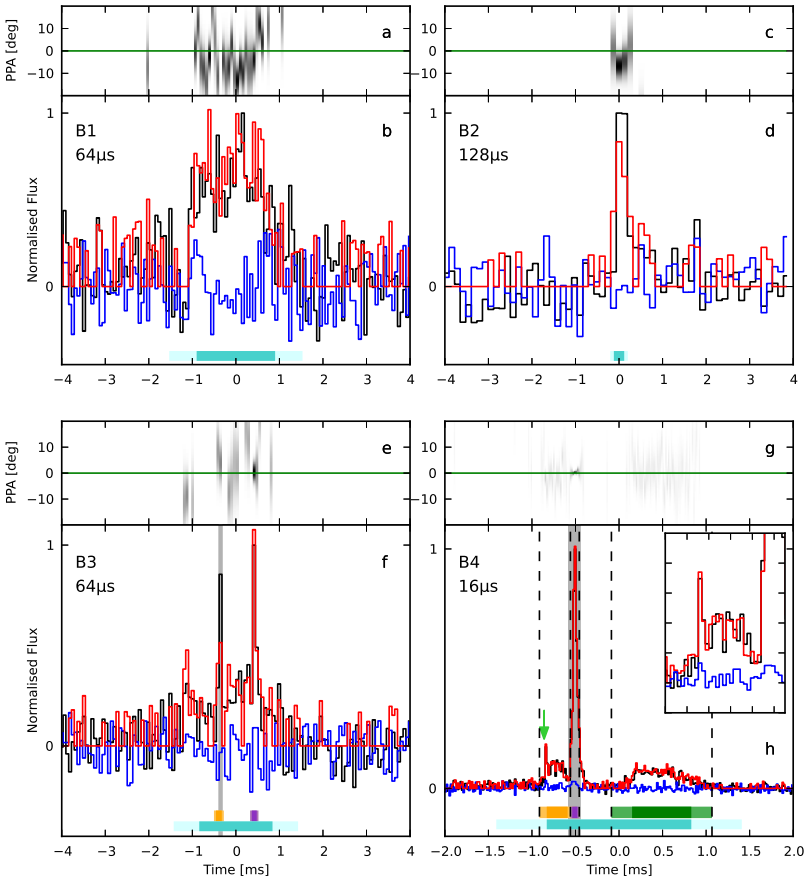

Figure 2.5: Polarimetric burst profiles and PPAs for four 1.7 GHz bursts from FRB 20180916B. Polarimetric profiles (lower panels of each sub-figure) and PPAs (top panels of each sub-figure). In the bottom panels, the total intensity (Stokes I) profile is shown in black, the unbiased linear polarisation (Equation 2.1) is shown in red, and circular polarisation (Stokes V) is shown in blue. For B1, B2 and B3, we plot 8 ms around the burst, and for B4 we plot 4 ms. The time is referenced to the mean of the Gaussian fit to the burst envelope discussed in Marcote et al. (2020). The inset in panel h shows a zoom-in on the profile at the leading edge, highlighting a narrow, approximately 30 μs, spike, also highlighted by the green arrow. The top left of each lower panel shows the burst name, Bn, used to define the bursts in this work (ordered according to their arrival time), and the time resolution used for plotting. Also shown in the lower panels are the Gaussian full-width at half-maximum (FWHM) of each burst illustrated by the dark cyan bar. The light cyan bar represents the 2-σ region. Bursts B3 and B4 show multiple sub-bursts indicated by the orange, purple and green bars in panels f and h (the FWHM is shown in the dark colour, and the 2-σ region shown in the lighter colour). For burst B4, we also show dotted lines indicating the extent of the three sub-bursts: B4-sb1 (orange), B4-sb2 (purple) and B4-sb3 (green). The top panel shows the PPA, defined as $\mathrm{PPA} = 0.5 \tan^{-1}(\mathrm{U/Q})$. The greyscale represents the probability distribution of the PPA following Everett & Weisberg (2001), the darker shading representing higher polarised S/N. The PPA has been shifted by the best-fit flat PPA of the four bursts, weighted by their unbiased linear polarisation S/N. Thus, the weighted PPA of the four bursts is set to zero, as is illustrated by the green line. The shaded region of the profile of B3 and B4 highlights the timescale plotted in Figure 2.6 for each burst.

by approximately 4 hours. We plot the unbiased linear polarisation, $L_{\rm unbias}$, profile in red, following Everett & Weisberg (2001), where

$$L_{\rm unbias} = \begin{cases} \sigma_I \sqrt{\left(\frac{L_{\rm meas}}{\sigma_I}\right)^2 - 1}, & \text{if} \frac{L_{\rm meas}}{\sigma_I} \geq 1.57 \\ 0, & \text{otherwise} \end{cases} \tag{2.1}$$

where $L_{\rm meas} = \sqrt{Q^2 + U^2}$, and σ_I is the standard deviation in the off-burst Stokes I data.

The PPA, corrected for parallactic angle variations (see Methods §2.5), is shown in the top panel of each sub-figure in Figure 2.5. We performed a least-squares fit of a horizontal line to the PPA of the four bursts together, weighted by their 1-σ errors. Note that for all PPA fits, we consider only additive noise in the determination of the variance. The weighted χ^2-statistic for this global fit is 175.5, with 125 degrees of freedom. We have shifted the absolute value of the PPA by this best-fit value, -89.2°. We note that, due to imperfect calibration, this value is not the absolute PPA and should not be used for comparison with bursts from other FRB 20180916B studies. We performed individual least-square fits for each burst (Table 2.2). For the fits, we only included PPAs within the Gaussian-fit 2-σ temporal width region (illustrated by the light cyan bars shown in Figure 2.5) that also satisfied $L_{\rm unbias}/\sigma_I > 3$. We find that the PPAs of the four bursts are consistent with being constant across the burst duration. We do, however, see slight PPA variations between burst components (most evident in B1 and B3).

We find that all four bursts are highly linearly polarised ($> 80\%$), and show no evidence for circular polarisation ($< 15\%$; Table 2.2). Additionally, the PPAs are consistent with being flat across the burst duration, with the absolute PPA within approximately 7° between bursts. The second spike in B3's profile (orange bar in Figure 2.5) appears to have a lower linear polarisation fraction than the rest of the burst. We see that the observed linear polarisation fraction increases when viewed in the 1 μs data (Figure 2.6). As shown in §3.1, this component is only a few μs wide (Figure 2.1). Therefore, the low polarisation fraction in the 16 μs data can be attributed to this component being unresolved. This highlights another importance of studying the burst properties at high time resolution.

In addition, we show B4-sb2's PPA and polarisation profile at 1 μs resolution in the lower subfigure of Figure 2.6. At this resolution, there are small (few degrees) variations in the PPA across this bright burst component. To test the significance of these variations, we performed a weighted least-squares fit of a flat PPA to the 1 μs resolution PPAs across the bright burst component of B4. The measured reduced-χ^2 of this fit is 3.7, compared with a reduced-χ^2 ≈1 for the 16 μs resolution data. Thus, the variations are significant.

2.4 Discussion

Neutron stars are prodigious generators of short-duration radio bursts, including canonical radio pulsar emission (Lorimer & Kramer, 2004), giant pulses (Hankins et al., 2003; Hankins & Eilek, 2007), and radio pulses from magnetars (Camilo et al., 2006). The Crab pulsar shows various emission features at different radio frequencies (Hankins et al., 2015),

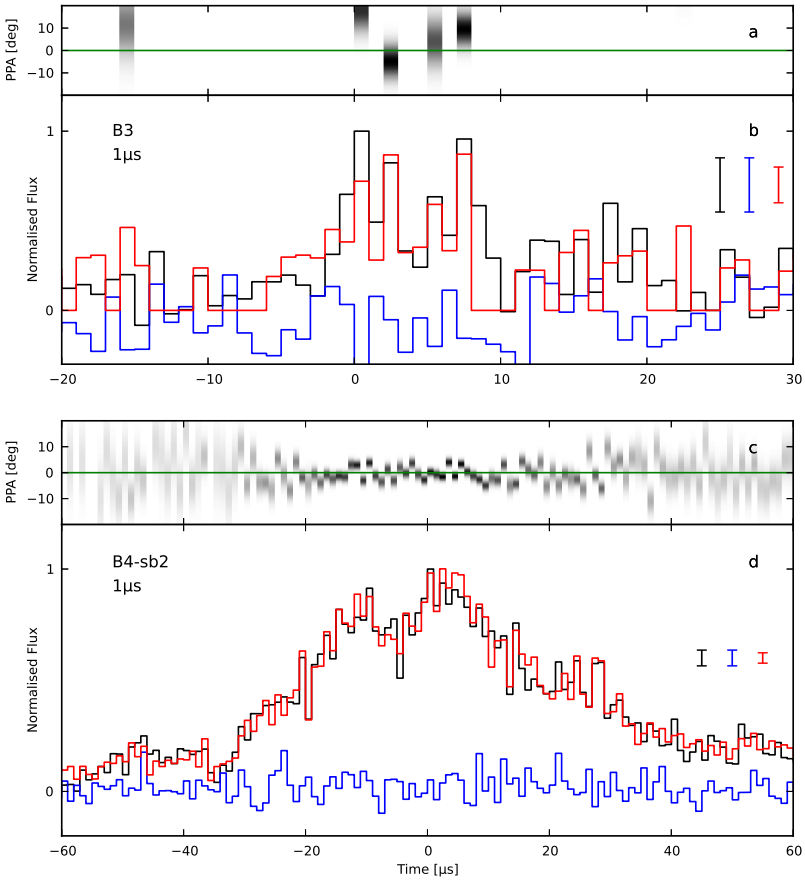

Figure 2.6: Microsecond resolution burst polarisation profiles and PPAs for B3 and B4. Polarisation profiles (panels b and d) and polarisation position angle (PPA; panels a and c) of burst components of B3 (top figure) and B4 (bottom figure), plotted at 1 µs time resolution. The shaded regions of the burst profiles shown in Figure 2.5 highlight the timescales plotted here. On the right of the bottom panels, the off burst standard deviation is shown. As is also done in Figure 2.5, the PPA has been shifted by the best-fit flat PPA of the four bursts weighted by their S/N. The weighted PPA of the four bursts is thus set to zero, as illustrated by the green line.

Table 2.2: Burst polarisation properties and polarisation position angle fit results.

Burst	MJD[a]	Fluence [Jy ms][a,b]	S/N [a]	$L_{unbiased}/I$ [%][c,d,e]	V/I [%][d,e]	PPA offset [deg][d]	χ^2	Degrees of freedom
B1	58653.0961366466	0.72	9.87	112 ± 14	-1 ± 12	-2.96	49.7	25
B2	58653.1112573504	0.20	9.61	88 ± 20	-4 ± 20	-5.85	0.91	2
B3	58653.1465969404	0.62	9.78	99 ± 14	-15 ± 14	0.30	25.55	14
B4	58653.2785078914	2.53	65.42	103 ± 4	5 ± 4	0.02	92.83	81
B4-sb2 (1 µs)	-	-	-	-	-	-0.50	445.77	121

[a]For details on the determination of these values see Marcote et al. (2020)
[b]A conservative fractional error of 30% is taken for the derived fluences.
[c]Removing the baseline can result in the condition $I^2 \geq Q^2 + U^2 + V^2$ not being satisified, which can lead to apparent linear polarisation fractions $> 100\%$.
[d]The fractional polarisations and PPA values are measured over the Gaussian-fit 2-σ region of the burst profile,
[e]The quoted uncertainties are statistical 2-σ errors assuming the errors in the Stokes parameters are independent of each other, and the errors in the time bins are independent of each other.
The uncertainties do not contain the calibration uncertainty nor do they encapsulate the effect of removing the baseline.

each with their own characteristic spectro-tempo-polarimetric properties (Hankins et al., 2016). Hessels et al. (2019) commented on the similar phenomenology seen when comparing FRB 20121102A with the high-frequency interpulses (HFIPs) produced by the Crab pulsar. Like FRB 20121102A and FRB 20180916B, the Crab pulsar HFIPs typically show high (approximately 80–90%) linear polarisation, weak (approximately 10–20%) or undetectable circular polarisation, and non-varying PPA within and between bursts (Hankins et al., 2016). Since HFIPs are observed to be highly polarised, this implies that the emission region is spatially localised (Hankins et al. 2016, as opposed to coming from an extended region from the neutron star surface to the light cylinder, which would lead to depolarisation; Dyks et al. 2004). Additionally, the flat PPAs between HFIPs suggest that the magnetic field direction is stable during each observational epoch. However, there are examples of HFIPs that deviate from this, either showing significant circular polarisation, weaker linear polarisation and/or a significant PPA variation across the burst profile (Hankins et al., 2016).

Simply comparing phenomenology with the Crab pulsar ignores the fact that FRB 20180916B and other repeaters produce bursts that are orders-of-magnitude longer duration and higher luminosity. Indeed, Lyutikov (2017) argue that the established extragalactic distances of FRBs preclude rotational energy and support magnetic energy as the power source for the bursts. Many theories have invoked a magnetar central engine (see Platts et al. 2019 for a catalogue of FRB theories). The recent discovery of an exceptionally bright (kJy–MJy) millisecond-duration radio burst from the Galactic magnetar SGR 1935+2154 adds compelling evidence for such a scenario (CHIME/FRB Collaboration et al., 2020; Bochenek et al., 2020). SGR 1935+2154 has been observed to produce sporadic radio bursts spanning more than 7 orders-of-magnitude in fluence (Kirsten et al., 2021b), though it is unclear whether these all arise from the same physical mechanism.

Magnetar FRB models come in various flavours. First, there is debate about whether the radio burst emission originates within or close to the magnetosphere (e.g. Kumar et al., 2017), or whether it is generated in a relativistic shock produced by an explosive energy release from the central engine (e.g. Metzger et al., 2019). Secondly, one can consider whether the magnetar is isolated, or whether an external plasma stream stimulates its activity (e.g. Zhang, 2018a).

As with pulsars, the polarimetric properties of magnetar radio bursts show diversity (Kramer et al., 2007; Lower et al., 2020). Nonetheless, high ($> 80\%$) linear polarisation fractions are common (Kaspi & Beloborodov, 2017), though not ubiquitous (Kramer et al., 2007; Kirsten et al., 2021b).

The high linear polarisation observed for FRB 20180916B is expected in both magnetospheric magnetar models (Lu et al., 2019) and synchrotron maser shock models (e.g. Metzger et al., 2019). The magnetospheric model described in Lu et al. (2019) additionally predicts small PPA variations between bursts from a repeating FRB, with the burst-to-burst variability following the magnetar's rotation period. Relativistic shock models, where the FRB emission originates much farther from the magnetar, naturally predict constant PPA within and between bursts (e.g. Metzger et al., 2019). However, small variations can be explained by invoking clumpiness in the medium into which the shock front propagates, or could alternatively come from the maser emission itself.

In this work, we observe the shortest-timescale structure seen in any FRB to date ($3 - 4\,\mu$s), *and* see that there is a range of timescales from a few μs to a few ms. In the literature, there are bursts detected from FRB 20180916B with total envelope widths of up to 6 ms (at 300–800 MHz; CHIME/FRB Collaboration et al. 2019c; Chawla et al. 2020). Note that there are larger burst widths reported at 110–188 MHz (Pleunis et al., 2021b), but at these low frequencies, scattering dominates. Note, there appears to be a frequency dependence on burst width, therefore comparison of temporal structure across different frequencies should be done with caution. The observed shortest timescales of a few μs, and range of timescales have implications for magnetar progenitor FRB models. Assuming a magnetar progenitor, temporal fluctuations strongly constrain where the emission originates (i.e. within the magnetosphere or well outside the magnetosphere). The ratio of fluctuations to total burst duration, in our case, is approximately $4\,\mu\text{s} / 2\,\text{ms} = 0.002 << 1$, which is most naturally explained by invoking emission originating within the magnetosphere (Beniamini et al., 2020). The short-timescale structure observed in FRB 20180916B implies that the emission region is on the order of 1 km. In the case of FRB emission originating from a relativistic shock at large distances from the magnetar, this implies a very small area of the total shock front dominating. Nonetheless, the temporal fluctuations could be explained by invoking clumpiness in the medium where the shock front propagates or, potentially, propagation effects.

Additionally, we find that the bright component of B4 (B4-sb2) at 1 μs resolution exhibits fluctuations of 10–20 μs. We conclude that this sub-burst is not comprised of a few well-separated, bright (sub-)μs shots of emission, but possibly the envelope is made of many closely spaced (sub-)μs shots of comparable amplitude. This has been predicted in models of magnetospheric burst emission to explain the observed flux densities (Cordes & Wasserman, 2016).

The consistent PPA between bursts from FRB 20180916B has direct implications regarding the precessing neutron star models (Zanazzi & Lai, 2020; Levin et al., 2020) created to explain the 16.35 day periodicity (Chime/Frb Collaboration et al., 2020). During precession, the line-of-sight inevitably sweeps across a much larger angular area on the neutron star surface compared to a non-precessing case. Therefore, the model not only expects PPA variation

as a function of the rotational phase, but also precession phase. We observe only a small PPA variation between bursts, which strongly suggests that the emission angle is greatly tilted from the direction of the magnetic pole in this scenario. Precession is thus disfavoured given that we require a very specific geometry to explain the constant PPA between bursts (which is also observed for FRB 20121102A; Michilli et al. 2018b).

Based on the observed offset from the nearest star forming regions in the host galaxy, Tendulkar et al. (2021) discuss a model in which FRB 20180916B is a neutron star in an interacting high-mass X-ray binary system. In this scenario, the neutron star magnetosphere is 'combed' by the ionised wind of the stellar companion (Ioka & Zhang, 2020), and creates a magnetic tail and a clear funnel where FRBs can be seen. Low-frequency detections of FRB 20180916B indicate that the line-of-sight to the neutron star must be relatively clean (Pleunis et al., 2021b). Our results from microsecond polarimetry of FRB 20180916B are consistent with the bursts being produced near the neutron star in a magnetic tail. Nonetheless, it also remains possible that FRB 20180916B's observed periodic activity is due to rotation(Beniamini et al., 2020); this case can also accommodate the results we present here.

There is, arguably, a characteristic observational picture emerging for repeating FRBs (for a detailed comparison of FRB 20180916B with other FRBs, see Methods §2.5). Specifically, repeaters exhibit the downward drifting, so-called 'sad-trombone' effect (Hessels et al., 2019; CHIME/FRB Collaboration et al., 2019c), and show narrowband burst envelopes (Gourdji et al., 2019; Pearlman et al., 2020). On average, repeating FRBs exhibit longer-duration burst profiles (CHIME/FRB Collaboration et al., 2019c). Additionally, the repeaters FRB 20121102A, FRB 20180916B and FRB 20190711A show remarkably consistent and characteristic polarimetric properties (highly linearly polarised, no evidence of circular polarisation, and constant PPA during and between bursts). In contrast, when including apparent non-repeaters, the landscape of FRB polarimetric properties is diverse (Caleb et al., 2018; Day et al., 2020). As with pulsars, FRBs exhibit a range of polarisation fractions and PPA variations. Repeating FRBs appear to live in a diverse set of host galaxies and local environments (Chatterjee et al., 2017; Marcote et al., 2020; Heintz et al., 2020), implying that these characteristic properties are exclusive to the emission mechanism, rather than effects from the local medium. In this work, we have supported this characteristic observational picture of repeating FRBs with our polarisation measurements of FRB 20180916B at 1.7 GHz. We also suggest that the dynamic range of temporal structure of $2\,\mathrm{ms}/4\,\mu\mathrm{s} = 500$ could be another characteristic to add to this overall description of repeating FRBs.

The results presented here highlight the importance of high-time-resolution polarimetric studies of FRBs. With lower time resolution data, narrow temporal components and subtle variations in the PPA are averaged out. It is possible that previous flat PPA measurements from FRB 20121102A and FRB 20180916B are a result of this. We encourage future observations of FRBs with μs time resolution and full polarisation information. We also encourage searches for quasi-periodic oscillations in individual high-S/N FRBs, like the analysis conducted here. Studying FRBs in such fine detail is crucial for understanding their emission physics.

2.5 Methods

First we continue the discussion by comparing FRB 20180916B with other FRBs, and consider a characteristic observational description of repeating FRBs. We then describe the methods used in this work in more detail.

Is there a characteristic observational description of repeating FRBs?

Our high-time-resolution, polarimetric measurements of FRB 20180916B demonstrate remarkable phenomenological similarity to FRB 20121102A (Michilli et al., 2018b; Gajjar et al., 2018). Both of these repeating FRBs show 20-30 μs sub-bursts (in some high-S/N bursts, at least), approximately 100% linear polarisation, approximately 0% circular polarisation, and a constant PPA during the bursts. Moreover, between 16 bursts found in three observations spanning 25 days, Michilli et al. (2018b) report consistent PPAs throughout. Michilli et al. (2018b) fit for a variable RM per day, but a global PPA for all epochs. Gajjar et al. (2018) quote different average PPAs between bursts, but this is potentially because they allow the RM to vary between bursts detected within approximately 1 hour. The covariance between RM and PPA makes it difficult to distinguish small variations in the former compared to the latter. Here we find that the PPA of FRB 20180916B is also remarkably similar *between* bursts, as shown in Figure 2.5 and Table 2.2.

Comparing our 1.7-GHz measurements with the available 110 − 188 MHz (LOFAR; Pleunis et al., 2021b), 300–400 MHz (GBT; Chawla et al., 2020) and 400–800 MHz (CHIME/FRB; CHIME/FRB Collaboration et al., 2019c) bursts, we find that the polarimetric properties are also persistent over at least four octaves in radio frequency. However, the lack of absolute PPA calibration prevents us from investigating whether the average PPA is both persistent in time and between radio frequencies. In the case of FRB 20121102A, it appears that the linear polarisation fraction decreases towards lower frequencies (Plavin et al., 2022). It is, as yet, unclear whether that is due to an intrinsic change in the emission physics, or whether it reflects a propagation effect. The RM of FRB 20121102A is highly variable (Michilli et al., 2018b; Gajjar et al., 2018; Hilmarsson et al., 2021a), and 2−3 orders of magnitude larger than FRB 20180916B. The association of FRB 20121102A with a persistent, compact radio source (Chatterjee et al., 2017; Marcote et al., 2017) – whereas none is detected coincident with FRB 20180916B (Marcote et al., 2020) – further demonstrates that their local environments are different, despite both being near to a star-forming region (Tendulkar et al., 2017; Bassa et al., 2017; Marcote et al., 2020; Tendulkar et al., 2021).

Regardless of differences in host galaxy type and the local environment, however, the remarkable similarity of burst properties demonstrates that FRB 20121102A and FRB 20180916B have the same physical origin. This is further emphasised by the detection of periodicity in the burst activity rate of FRB 20180916B (Chime/Frb Collaboration et al., 2020) with $P_{\rm activity}$ ∼16 day, and the potential detection of a similar effect from FRB 20121102A(Rajwade et al., 2020; Cruces et al., 2021) with $P_{\rm activity}$ ∼157 day.

To date, the only other repeating FRB that has polarisation information from more than one burst, and is localised to a host galaxy, is FRB 20190711A (Day et al., 2020; Kumar et al., 2021). FRB 20190711A clearly shows the downward-drifting 'sad trombone' effect characteristic of repeating FRBs (Hessels et al., 2019; CHIME/FRB Collaboration et al., 2019a). Also, the polarimetric properties of FRB 20190711A show a striking observational similarity; it is also highly linearly polarised, approximately 0% circularly polarised and has a constant PPA across the burst profiles. FRB 20190711A has been localised to a star-forming galaxy (Macquart et al., 2020; Heintz et al., 2020), different from the hosts of FRB 20121102A (found in a faint starburst galaxy; Chatterjee et al. 2017) and FRB 20180916B (localised to a massive quiescent galaxy; Marcote et al. 2020).

Recently, Luo et al. (2020) report the polarisation properties of 7 bursts from the repeating FRB 180301. FRB 180301 shares a number of properties with other well-studied repeating FRBs, including downward-drifting sub-bursts, narrowbandedness, and no evidence of circular polarisation. However, the approximately 100 % linear polarisation and flat PPA across burst profiles is not always observed in the case of FRB 180301 (Luo et al., 2020).

The so-far non-repeating FRB 20181112A shows 4 sub-bursts spanning a total burst duration of 1.5 ms, with different apparent RMs and DMs between sub-bursts (Cho et al., 2020). Day et al. (2020) also found similar effects in their sample of five FRBs. The apparent RM variations of approximately 10–20 rad m^{-2} seen in the ASKAP FRB sample are too subtle to probe for FRB 20180916B given the data we present here and the uncertainty on the delay calibration. We note, however, that (apparent) RM variations at this level are likely excluded based on previously published FRB 20180916B polarimetric results taken at 110–188 MHz with LOFAR (Pleunis et al., 2021b), 300–400 MHz using GBT (Chawla et al., 2020) and 400 − 800 MHz using CHIME/FRB (CHIME/FRB Collaboration et al., 2019c) because they would lead to a lower polarisation fraction than observed.

Nonetheless, at the high-time-resolution afforded by these data, we detect subtle PPA variations of a few degrees between sub-bursts lasting $\lesssim$ 100 µs each. This is most visible for burst B1 (Figure 2.5). For the bright, 60 µs dominant component of B4 (B4-sb2), where we have maximum S/N per unit time, there is the suggestion of PPA variations of a few degrees, when studying this component at 1 µs time resolution (Figure 2.5). This could be interpreted as potential small PPA swings, or that this burst component is actually composed of many sub-µs components with PPAs that vary on the level of a few degrees, similar to what we see between the 100 µs burst components.

FRB 20180916B shows some of the shortest-timescale temporal features seen in any FRB to date. For comparison, FRB 20121102A, FRB 20170827A and FRB 20181112A have shown 30 µs substructures (Michilli et al., 2018b; Farah et al., 2018; Cho et al., 2020). In the case of FRB 20170827, the burst shows a single component of width 30 µs (Farah et al., 2018), and similarly, FRB 20121102A produced a single burst of width 30 µs (Michilli et al., 2018b). FRB 20181112A, also shows a single narrow component, but the results are limited by scattering at the 20 µs level (Cho et al., 2020). In this work, we have demonstrated that not only does FRB 20180916B also exhibit short-duration components similar to what has been seen in other FRBs (e.g. the 30 µs spike in the inset on Figure 2.5), but, in fact, we

observe temporal scales spanning three orders of magnitude, the shortest reaching only a few μs.

Marcote et al. (2020) estimated a Galactic scattering time of 2.7 μs at 1.7 GHz from the measurement of the scintillation bandwidth. Independently, Chawla et al. (2020) place a constraint on the scattering timescale of FRB 20180916B of $\tau < 1.7$ ms at 350 MHz, which, assuming a frequency scaling of $\tau \propto \nu^{-4}$, gives a scattering time at 1.7 GHz of < 3 μs, consistent with Marcote et al. (2020). The shortest timescale structure observed in this work is consistent with this scattering prediction. Our results rule out that burst B4 is composed of a few extremely bright sub-μs shots of emission well-spaced in time, similar to what is observed in Crab giant pulses (Hankins et al., 2003). If the 20 μs morphology that we observe in the profile of B4 are made up of sub-μs shots of emission, they must be closely packed in time and of approximately equal amplitude.

Refined DM

We refine the burst DM using the PSRCHIVE tool pdmp (van Straten & Bailes, 2011) to search for the DM that maxmises S/N of burst B4 (the brightest in our sample) in the 1 μs resolution data. The DM is found to be $348.772 \pm 0.006\,\mathrm{pc\ cm^{-3}}$, which is $0.012\,\mathrm{pc\ cm^{-3}}$ greater than the value the data is coherently dedispersed to. In case the burst is comprised of bright μs shots of emission, we additionally search for the DM that maximises the peak in the profile structure (using the metric of maximising (max-min) of the time series). This was found to be $348.775\,\mathrm{pc\ cm^{-3}}$, consistent with the pdmp-determined value. We thereafter incoherently dedispersed all the 1 μs data to the pdmp-determined value ($+0.012\,\mathrm{pc\ cm^{-3}}$). This slight shift in DM does not result in significant intra-channel temporal smearing.

Short timescale structure in B4-sb2

To test whether the single-time-bin spikes that appear in B4-sb2 (panel l, Figure 2.1) are physical or consistent with amplitude-modulated noise (Rickett, 1975; Cordes, 1976), we remove the envelope of the burst from the data. To do this we use a Blackman window function, with a smoothing window of 19 bins, to create a model of the envelope of the burst (shown in panel c of Figure 2.2). This model is then divided out of the data, leaving the residuals shown in panel d of Figure 2.2, with off-burst noise also shown for comparison. We find no statistical outliers in this burst, implying that the narrow features are consistent with amplitude-modulated noise.

Power spectra modelling and statistics

The power spectrum (in log space; see Figure 2.3) was fit with a power law of the form

$$f(\nu) = A\nu^{-\alpha} + C, \tag{2.2}$$

where A is the amplitude, α is the power law slope, and C is a white noise component, using the Bayesian analogue of a maximum likelihood estimation, as implemented in the

Stingray modelling interface (Huppenkothen et al., 2019). There are many astrophysical phenomena whose lightcurve is observed to have a power law component in the Fourier domain, often referred to as 'red noise' (e.g., gamma-ray bursts; Cenko et al. 2010, active galactic nuclei; McHardy et al. 2006 and magnetars; Huppenkothen et al. 2013). We perform a goodness-of-fit test by simulating 100 fake power spectra from the best fit, and performing the same Bayesian maximum likelihood fit. The measured p-value is then the fraction of the simulations with a maximum likelihood lower than the likelihood of our fit. The results of this analysis are shown in Table 2.1. There are apparent oscillations in the ACF, consistent with the fluctuations seen in the profile. The power spectrum shows a power law slope, consistent with red noise. To test the statistical significance of any features in the power spectrum on top of the red noise slope, we use two metrics (for a detailed explanation, see Huppenkothen et al. 2013). First, to search for any significant narrow features in the power spectrum, we compute the residuals as a function of frequency, ν,

$$R(\nu) = \frac{2P(\nu)}{M(\nu)}, \tag{2.3}$$

where $P(\nu)$ is the power spectrum, and $M(\nu)$ is the best fit noise component. Using the Markov chain Monte Carlo (MCMC) package emcee (Foreman-Mackey et al., 2013) to generate 100 simulated residuals, we generate the distribution of $\max(R_{\rm sim}(\nu))$, and determine the probability that the observed peak value, $\max(R(\nu))$, is consistent with noise. We find no statistically significant outliers using this statistic. The second method we use is more sensitive to lower amplitude, wider features in the power spectrum, which are often referred to as quasi-periodic oscillations (QPOs) and are observed in a number of astrophysical phenomena (e.g., accreting low-mass X-ray binaries; van der Klis 2006, black hole binaries; Remillard et al. 2006 and magnetar X-ray flares; Israel et al. 2005). This second method is a model comparison method. In addition to the red-noise fit described above, we fit a function with a Lorentzian describing the QPO summed with a red-noise power law (as defined above). We calculate the likelihood ratio, and calibrate this likelihood ratio using MCMC simulations of the simpler model (in our case, the power law model; see Protassov et al. 2002 for details). This analysis returns the posterior predictive p-value quoted in Table 2.1, i.e. for both B4-sb1 and B3 we cannot rule out the simpler model of a red noise power law slope. For all of the Bayesian fits described we give conservative prior distributions: flat distribution for the power law slope α, flat distribution for the amplitude A, normal distribution for the white noise component C, and a flat distribution for the Lorentzian parameters. Since we see fluctuations of approximately 60 μs in the ACF of B4-sb1, we use this as the inital guess for the centroid frequency of the Lorentzian.

The bright envelope of burst B4-sb2 dominates in both the ACF and power spectrum, and so any features associated with quasi-periodic oscillation are difficult to detect. One way to bypass this issue would be to remove the envelope (divide out a smooth model of the burst envelope), but this can introduce features in the power spectrum that are not physical (Huppenkothen et al., 2013). We therefore only perform this analysis on burst B3 and B4-sb1, which do not have a prominent envelope that would significantly affect the results. The results are shown in Figure 2.3 and Table 2.1.

Polarimetric calibration and RM measurement

We did not perform an independent polarisation calibrator scan to use for polarimetric calibration. Instead, we use the test pulsar observation of PSR B2111+46 to determine the calibration solutions to apply to our target data. A similar polarimetric calibration technique was used for radio bursts detected from SGR 1935+2154 using voltage data from the VLBI backend of the Westerbork single-dish telescope RT1 (Kirsten et al., 2021b).

We assume that any leakage between the two polarisation hands only affects Stokes V (defined as V = LL − RR using the PSR/IEEE convention; van Straten et al. 2010). We also assume that the delay between the two polarisation hands only significantly affects Stokes Q and U. The calibration we apply ignores second-order effects. We performed a brute force search for the RM that maximises the linear polarisation fraction using the PSRCHIVE tool rmfit (van Straten & Bailes, 2011). With rmfit we select a range of RMs to search, in a number of trial steps. The delay between the polarisation hands approximately manifests as an offset from the true RM of the source, assuming the delay is frequency-independent. For this reason, we select a larger range of RMs than what would be motivated by the known measured RM of FRB 20180916B ($-114.6\,\mathrm{rad\,m^{-2}}$; CHIME/FRB Collaboration et al. 2019c), and we search from $-5000\,\mathrm{rad\,m^{-2}}$ to $5000\,\mathrm{rad\,m^{-2}}$ in 500 equally spaced steps.

For PSR B2111+46, we measure an RM of $-657\,\mathrm{rad\,m^{-2}}$, which is 438 units from the true RM of PSR B2111+46 ($-218.7\,\mathrm{rad\,m^{-2}}$; Force et al. 2015). This approximately translates to a delay of 5.5 ns. We use the rmfit-RM to Faraday correct the pulsar data, and we reproduce the polarimetric properties and PPA of PSR B2111+46 within 8% of published properties (Gould & Lyne, 1998). Figure 2.4 illustrates the calibration we applied. We note that we had $< 1\,\mathrm{minute}$ on PSR B2111+46, which has a rotational period of approximately 1 s (Arzoumanian et al., 1994), so it is likely that our observed average profile did not completely stabilise to the published average profile, which is based on the sum of many more individual pulses. As such, the aforementioned 8% deviation should be treated as an upper limit on the inaccuracy of the polarimetric calibration.

We assume there are no significant changes to the calibration required between the test pulsar scan and the detected FRB 20180916B bursts ($< 1\,\mathrm{hr}$ between the PSR B2111+46 scan and burst B1). Bursts B1 and B4 have a sufficient S/N to determine an RM using rmfit (S/N values determined in Marcote et al. 2020 are quoted in Table 2.2). B1 and B4 are separated in time by $> 4\,\mathrm{hr}$ and we note their measured rmfit-RMs differ by approximately 8 units (1–2% of the measured value). Thus we conclude that the bursts have consistent RMs. The measured rmfit-RM for B4 is $-536 \pm 5\,\mathrm{rad\,m^{-2}}$, which when combined with the offset due to a delay between the polarisation hands (+438 units, measured using the PSR B2111+46 data) gives a true RM of $-98\,\mathrm{rad\,m^{-2}}$. We note that we have not removed the delay between polarisation hands from the data before running rmfit, and thus the error quoted is lower than the true error as it does not reflect uncertainties associated with the covariance between RM and delay. This is tackled in the following steps using a Q-U fit.

To better determine the burst RM and associated errors, we perform a joint least squares fit of Stokes Q and U spectra (as a function of frequency, ν), using the following equations:

$$Q/I = L\cos(2(c^2\mathrm{RM}/\nu^2 + \nu\pi D + \phi)), \tag{2.4}$$

$$U/I = L\sin(2(c^2\mathrm{RM}/\nu^2 + \nu\pi D + \phi)), \tag{2.5}$$

where c is the speed of light, and the free parameters L, the linear polarisation fraction, D, the delay between polarisation hands, and $\phi = \phi_\infty + \phi_{\mathrm{inst}}$, where ϕ_∞ is the absolute angle of the polarisation on the sky (referenced to infinite frequency), and ϕ_{inst} is the phase difference between the polarisation hands. We perform the joint fit on Q/I and U/I spectra for PSR B2111+46 and for burst B4, where the delay, D, is assumed to be the same for both the pulsar and target scans. We fix the known RM of PSR B2111+46 (Force et al., 2015), $-218.7\,\mathrm{rad\ m^{-2}}$. We measure $D = 5.4 \pm 0.2\,\mathrm{ns}$, consistent with our prediction from the offset in RM from the true RM of PSR B2111+46 using rmfit. Additionally, we measure the RM of burst B4 to be $-104 \pm 20\,\mathrm{rad\ m^{-2}}$, where the large fractional error arises due to covariances between the fit parameters (RM, D and ϕ) that could not be removed as we did not record independent information from a polarisation calibrator source. We find the RM to be consistent with the previously measured RM values for FRB 20180916B (CHIME/FRB Collaboration et al., 2019c; Chawla et al., 2020).

To correct for parallactic angle, we rotate the linear polarisation vector by

$$\theta = 2\tan^{-1}\left(\frac{\sin(\mathrm{HA})\cos(\phi)}{(\sin(\phi)\cos(\delta) - \cos(\phi)\sin(\delta)\cos(\mathrm{HA})}\right), \tag{2.6}$$

where HA is the hour angle of the burst, ϕ is the latitude of Effelsberg, and δ is the declination of FRB 20180916B. The parallactic angle corrected PPA is shown in the top panel of each sub-figure in Figure 2.5. We plot the probability distribution of PPA per time bin, following Everett & Weisberg (2001), and mask any bins where the unbiased linear S/N is below 3.

Acknowledgements

We thank Pawan Kumar, Brian Metzger, Lorenzo Sironi, Maxim Lyutikov, Michiel van der Klis and Phil Uttley for helpful discussions.

The European VLBI Network is a joint facility of independent European, African, Asian, and North American radio astronomy institutes. Scientific results from data presented in this publication are derived from the following EVN project code: EM135. This work was also based on simultaneous EVN and PSRIX data recording observations with the 100-m telescope of the MPIfR (Max-Planck-Institut für Radioastronomie) at Effelsberg, and we thank the local staff for this arrangement.

J.W.T.H. acknowledges funding from an NWO Vici grant (“AstroFlash”; VI.C.192.045). F.K. acknowledges support by the Swedish Research Council. B.M. acknowledges support from the Spanish Ministerio de Economía y Competitividad (MINECO) under grant AYA2016-76012-C3-1-P and from the Spanish Ministerio de Ciencia e Innovación under grants

PID2019-105510GB-C31 and CEX2019-000918-M of ICCUB (Unidad de Excelencia “María de Maeztu” 2020-2023).

Chapter 3

Burst timescales and luminosities as links between young pulsars and fast radio bursts

K. Nimmo, J. W. T. Hessels, F. Kirsten, A. Keimpema, J. M. Cordes, M. P. Snelders, D. M. Hewitt, R. Karuppusamy, A. M. Archibald, V. Bezrukovs, M. Bhardwaj, R. Blaauw, S. T. Buttaccio, T. Cassanelli, J. E. Conway, A. Corongiu, R. Feiler, E. Fonseca, O. Forssén, M. Gawroński, M. Giroletti, M. A. Kharinov, C. Leung, M. Lindqvist, G. Maccaferri, B. Marcote, K. W. Masui, R. Mckinven, A. Melnikov, D. Michilli, A. G. Mikhailov, C. Ng, A. Orbidans, O. S. Ould-Boukattine, Z. Paragi, A. B. Pearlman, E. Petroff, M. Rahman, P. Scholz, K. Shin, K. M. Smith, I. H. Stairs, G. Surcis, S. P. Tendulkar, W. Vlemmings, N. Wang, J. Yang, J. P. Yuan

Nature Astronomy, 2022, 6, 393

Abstract

Fast radio bursts (FRBs) are extragalactic radio flashes of unknown physical origin. Their high luminosities and short durations require extreme energy densities, like those found in the vicinity of neutron stars and black holes. Studying the burst intensities and polarimetric properties on a wide range of timescales, from milliseconds down to nanoseconds, is key to understanding the emission mechanism. However, high-time-resolution studies of FRBs are limited by their unpredictable activity levels, available instrumentation and temporal broadening in the intervening ionised medium. Here we show that the repeating FRB 20200120E can produce isolated shots of emission as short as about 60 nanoseconds in duration, with brightness temperatures as high as 3×10^{41} K (excluding relativistic effects), comparable to 'nano-shots' from the Crab pulsar. Comparing both the range of timescales and luminosities, we find that FRB 20200120E observationally bridges the gap between known Galactic young pulsars and magnetars, and the much more distant extragalactic FRBs. This suggests a common magnetically powered emission mechanism spanning many orders of magnitude in

timescale and luminosity. In this work, we probe a relatively unexplored region of the short-duration transient phase space; we highlight that there likely exists a population of ultra-fast radio transients at nanosecond to microsecond timescales, which current FRB searches are insensitive to.

3.1 Introduction

In the late 1960s, the discovery of radio pulsars was enabled by observations using an unprecedented time resolution of $50-100$ ms (Hewish et al., 1968). The subsequent discovery of the Crab pulsar(Staelin & Reifenstein, 1968) eventually led to the insight that its giant pulses (Heiles & Campbell, 1970; Staelin, 1970) show structure on timescales as short as 0.4 nanoseconds (Hankins et al., 2003). These 'nano-shots' have exceptionally high brightness temperatures of $\sim 10^{40}$ K (Hankins & Eilek, 2007). The more recent discovery of the fast radio burst (FRB) phenomenon (Lorimer et al., 2007; Thornton et al., 2013) has shown that nature produces millisecond duration radio flashes that are apparently 10^{9-12} times more luminous than those of average pulsars (Petroff et al., 2019; Cordes & Chatterjee, 2019; Petroff et al., 2022).

As with pulsars, the recording of raw voltage data can allow us to study FRB signals on timescales of microseconds (μs) down to nanoseconds (ns). Thus far, such observations have demonstrated that FRB signals can show temporal structure on timescales of tens of microseconds down to just a few microseconds (Farah et al., 2018; Michilli et al., 2018b; Cho et al., 2020; Nimmo et al., 2021). Nimmo et al. (2021) also discuss how individual FRBs can display a range of temporal structure, from a few microseconds up to milliseconds. The temporal behaviour of FRBs — along with their polarimetric properties (Michilli et al., 2018b; Day et al., 2020) and dynamic spectra (Hessels et al., 2019) — provide key inputs for distinguishing between the dozens of proposed source models and emission mechanisms (Platts et al., 2019). Furthermore, these burst properties can aid in observationally distinguishing the populations of repeating and apparently one-off FRBs, thereby strengthening the case that they have physically distinct origins (CHIME/FRB Collaboration et al., 2019c; Fonseca et al., 2020; Pleunis et al., 2021a).

Kirsten et al. (2022) recently associated the repeating FRB 20200120E (Bhardwaj et al., 2021a) with [PR95] 30244, a globular cluster that is part of the M81 galactic system. At a distance of 3.6 Mpc, FRB 20200120E is the closest-known extragalactic FRB, bridging the gap between the putative Galactic FRB source SGR 1935+2154 (a known magnetar at a distance of $\sim 3-10$ kpc; CHIME/FRB Collaboration et al. 2020; Bochenek et al. 2020; Zhong et al. 2020) and FRB 20180916B at a luminosity distance of 149 Mpc (Marcote et al., 2020). FRB 20200120E is also at high Galactic latitude ($\sim 41.2^{\circ}$), which reduces the effect of temporal scatter broadening arising from the Milky Way interstellar medium (ISM). This suggests that FRB 20200120E could be an excellent source to study at the highest-possible temporal resolutions.

Here we present a spectro-polarimetric study of 5 FRB 20200120E bursts detected with the Effelsberg 100-m telescope during a broader localisation campaign (Kirsten et al., 2021b) using *ad hoc* interferometric observations with dishes from the European Very-long-baseline interferometry (VLBI) Network (EVN). In this Article we present both extremely high time resolution, and lower time resolution analyses of the bursts, with full polarimetry, and thereafter discuss the observational connections between FRB 20200120E and well-studied repeating FRBs, the Crab pulsar and the Galactic magnetar SGR 1935+2154.

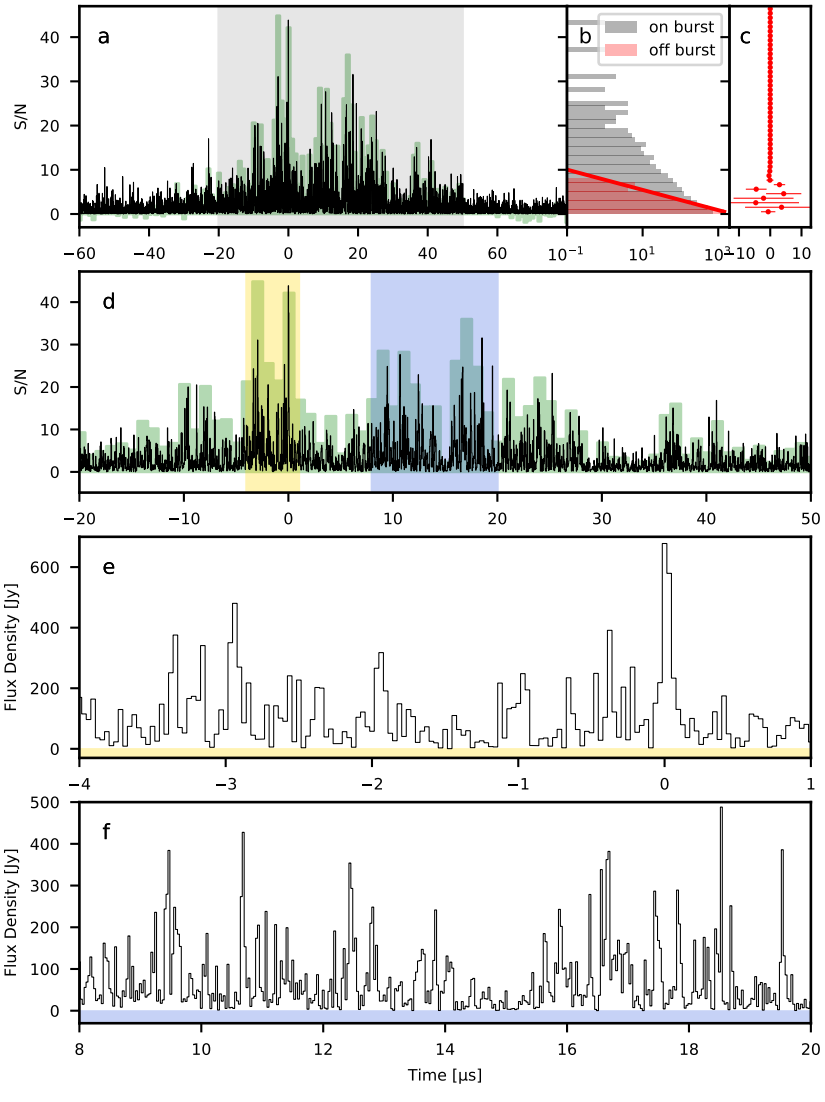

Figure 3.1: Burst B3 from FRB 20200120E exhibits sub-microsecond temporal structure. Panel **a** shows the temporal profile of burst B3 at 31.25 ns time resolution (black) and downsampled to 1 μs resolution (green). Panel **b** shows a histogram of the S/N values in the 31.25 ns data (black), also showing the χ^2-distributed (2 degrees of freedom) noise distribution (red) arising in the limiting case of $\delta t \delta \nu \sim 1$, where δt and $\delta \nu$ are the time and frequency resolutions of the data, respectively. The residuals of the off-burst histogram with the best-fit χ^2-distributed with 2 degrees of freedom is shown in panel **c**. This plot contains temporal profiles computed for the bright scintle only, i.e. the frequency range 1318 − 1334 MHz. The data were generated with SFXC and are coherently dedispersed to 87.7527 pc cm^{-3}. Panel **d** shows a zoom in of panel **a**, highlighting the temporal regions plotted in panels **e** (yellow) and **f** (blue) panels.

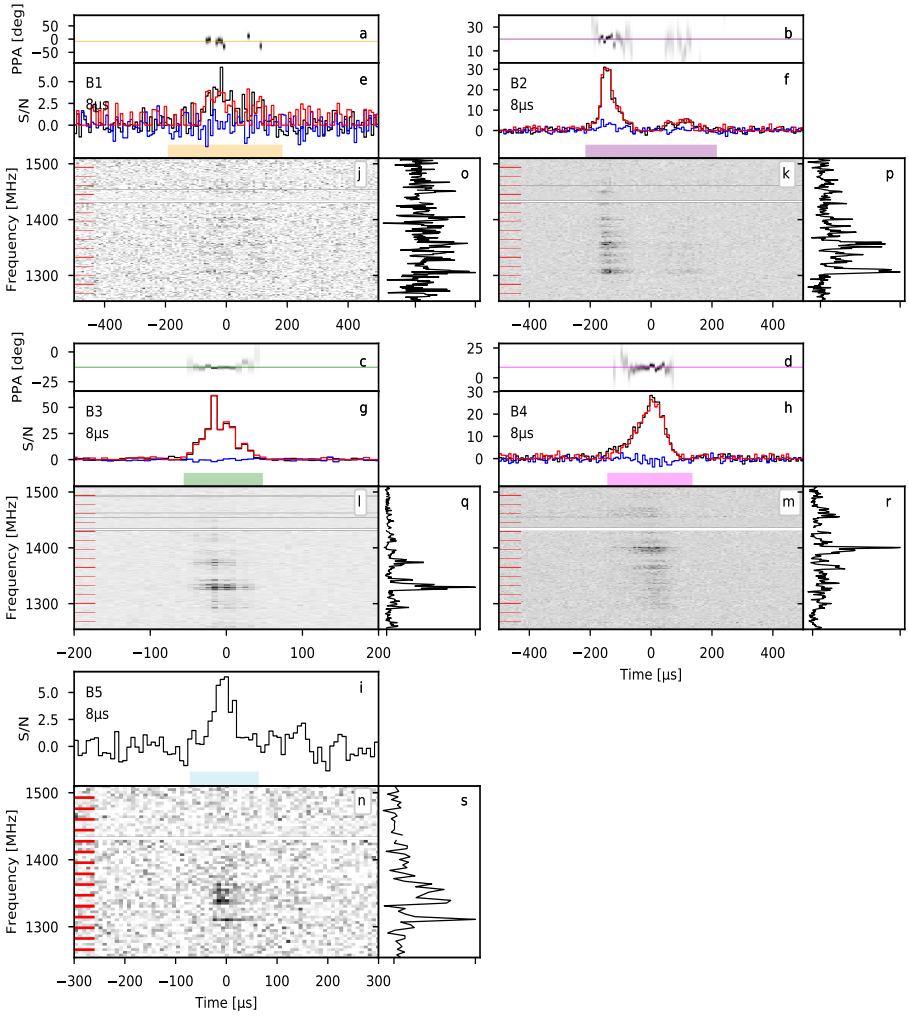

Figure 3.2: The polarimetric profiles, dynamic spectra, time-averaged spectra and polarization position angle (PPA) of the bursts detected from FRB 20200120E. For B5 only Stokes I is shown (see text). The data are plotted with 8 μs and 1 MHz time and frequency resolution, respectively (with the exception of B1 and B5 which are plotted with 4 MHz frequency resolution). The data were generated with SFXC and are coherently dedispersed within each 16 MHz subband to 87.75 pc cm^{-3} (and also incoherently shifted between subbands). Panels **a**–**d** are the PPA across the burst profile, where the color gradient represents the linear polarization S/N (black is high S/N and white is low S/N), and the colored horizontal line represents the weighted best-fit line to the PPA. Only the PPAs above a linear S/N threshold of 3 are plotted. Panels **e**–**h** show the total intensity (Stokes I; black), unbiased linear polarization (Everett & Weisberg 2001; red) and circular polarization (blue) burst profiles (panel **i** shows the Stokes I profile of burst B5). In the top-left of the panels are the burst name used throughout this work, and the time resolution used for plotting. The colored bar at the bottom of the panels represent the $\pm 2\sigma$ burst width used to measure the polarization fractions and burst fluence. Panels **j**–**n** are the dynamic spectra and panels **o**–**s** are the time-averaged frequency spectra. The red marks on the dynamic spectra outline the edges of the subbands. Data that have been removed due to radio frequency interference have not been plotted.

3.2 Observations & Data

We observed FRB 20200120E (Bhardwaj et al., 2021a) using an *ad hoc* EVN array at 1.4 GHz, on 2021 February 20 UT 1700 – 2200, 2021 March 7 UT 1545 – 2045, and 2021 April 28 UT 1100 – 2200. For details on the interferometric array configuration and localisation results, see Kirsten et al. (2022). With the 100-m Effelsberg telescope, we recorded dual circular polarization raw voltages (R and L) using 32 MS/s real sampling per 16-MHz subband and 2-bit samples written in VDIF format (Whitney et al., 2010), with a total bandwidth of 256 MHz.

Throughout this work we label the FRB 20200120E bursts as Bn, ordered according to their arrival time, and matching the nomenclature used in Kirsten et al. (2022).

3.3 Results

As described in Methods (§3.5), we create total-intensity filterbank data containing each burst at the native sampling of the voltage data (31.25 ns), using SFXC. The filterbank data were created with 32-bit digitization, in order to avoid saturation. The data are coherently dedispersed within the 16 MHz subbands, and each subband is also time shifted to correct for dispersive delay (incoherent dedispersion), both using our measured dispersion measure (DM) of 87.7527 ± 0.0003 pc cm^{-3} (Methods §3.5). We assume the same DM for all bursts. This DM is $> 9\sigma$ lower than the previously reported measurement of 87.782 ± 0.003 pc cm^{-3} (where the quoted value is based on the average of 3 bursts; Bhardwaj et al. 2021a). The observed difference in DM could be due to unresolved time-frequency structure in the Bhardwaj et al. (2021a) bursts, often seen in repeating FRBs (Hessels et al., 2019). Future measurements are needed to determine if the DM is frequency or time dependent.

In Figure 3.1a, we present the profile of burst B3 at 31.25 ns resolution (black), and downsampled to 1 µs resolution (green), in the frequency range 1318 – 1334 MHz. This range corresponds to the single subband containing the brightest spectral feature in the burst (visible in the burst dynamic spectrum shown in Figure 3.2l). By using a single subband, we avoid artefacts due to the inaccuracy of incoherent dedispersion. There are clear few-bin-wide temporal structures in the 31.25 ns profile of burst B3 (Figure 3.1). The question remains whether the sub-microsecond structures we observe are isolated shots of emission or noise fluctuations consistent with the χ^2-distribution of amplitude-modulated noise (AMN; Methods §3.5). We calculate the probability of drawing the bright ~ 60 ns duration feature at Time $= 0$ in Figure 3.1 from the *local* brightness distribution, where in this case "local" is defined as ± 1.5625 µs (± 50 bins) around the bright feature (Methods §3.5). We find that the probability of drawing this high signal-to-noise (S/N), two-bin-wide structure from the distribution is $\mathrm{p} = 4 \times 10^{-8} \times 100\,\mathrm{bins}/2 = 2 \times 10^{-6}$ (Figure 3.3). Therefore, we find this feature to be inconsistent with the local AMN distribution, and conclude that this structure is a real isolated shot. In addition to this bright 60 ns shot, we find at least another 2 significant sub-microsecond shots of emission in burst B3.

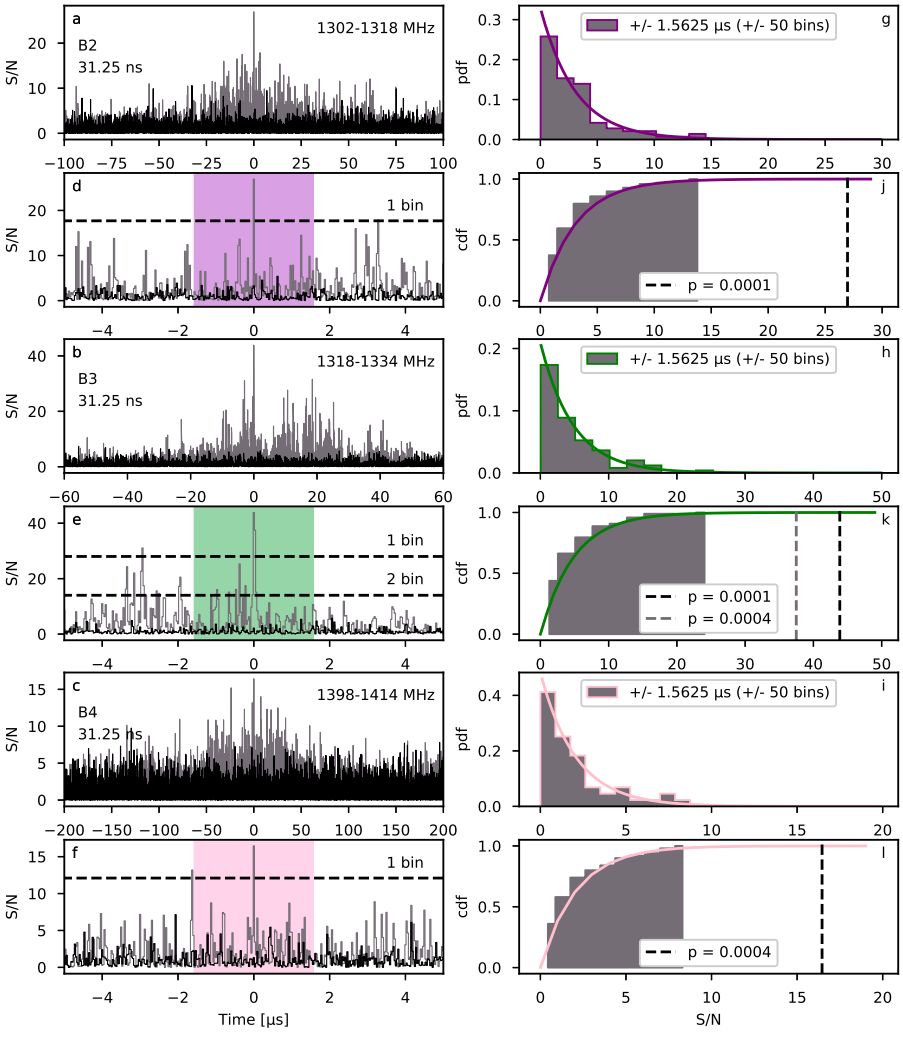

Figure 3.3: The probability that the brightest 1–2 bin features in the 31.25 ns burst profiles are consistent with the local amplitude modulated noise distribution. Panels **a–c** show the 31.25 ns resolution profiles (grey) with off burst noise (black) shown for comparison. The burst name and time resolution is shown in the top left corner and the frequency range averaged over to produce the burst profile in the top right corner of the panels. Panels **d–f** are zoomed-in profiles containing the highest S/N feature in the burst profile. The colored region represent the local region (time span ± 1.5625 μs) used to determine the probability density function (pdf; panels **g–i**) and cumulative density function (cdf; panels **j–l**). Note that the feature at the center of the colored region is not added to the distribution, since this is the feature which we want to determine the significance of relative to the local distribution. An exponential distribution fit is overplotted (colored lines) on the pdf and cdf. The highest S/N feature is represented by the vertical dashed line on the cdf (where in the case of B3, there are two dashed lines since the feature is 2 bins wide), and the legend shows the probability (or 1-cdf) of these features. The horizontal dashed lines on panels **d–f** represent the $3\,\sigma$ levels for single-bin features, using this local distribution (also for 2-bin features in the case of B3).

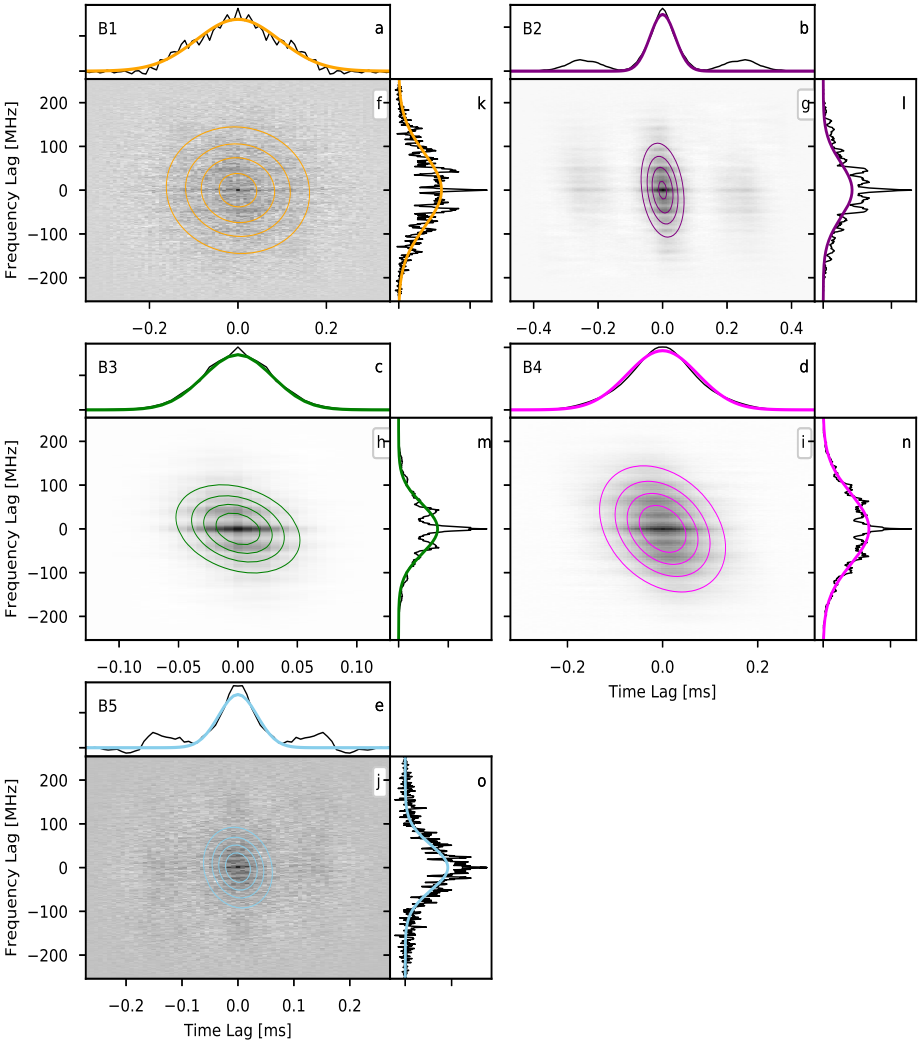

Figure 3.4: Low time resolution 2D autocorrelation functions (ACFs) of the bursts detected from FRB 20200120E. Panels **f–j** show the 2D ACF with colored contours overplotted representing the 2D Gaussian fit 1,2,3 and 4 σ. The zero lag spike is not plotted. The ACF is computed using filterbank data generated with SFXC (Keimpema et al., 2015), with time and frequency resolution of 8 µs and 125 kHz, respectively. The data were dedispersed using a DM of 87.75 pc cm^{-3}. Panels **a–e** show the frequency-averaged time ACF, with the frequency-averaged Gaussian fit overplotted, and similarly panels **k–o** show the time-averaged frequency ACF, with the time-averaged Gaussian fit overplotted. The time and frequency scales characterised in this plot, arise from the burst temporal width and frequency extent. The colored lines coordinate with other figures in this work (e.g. Figure 3.2 and Figure 3.5).

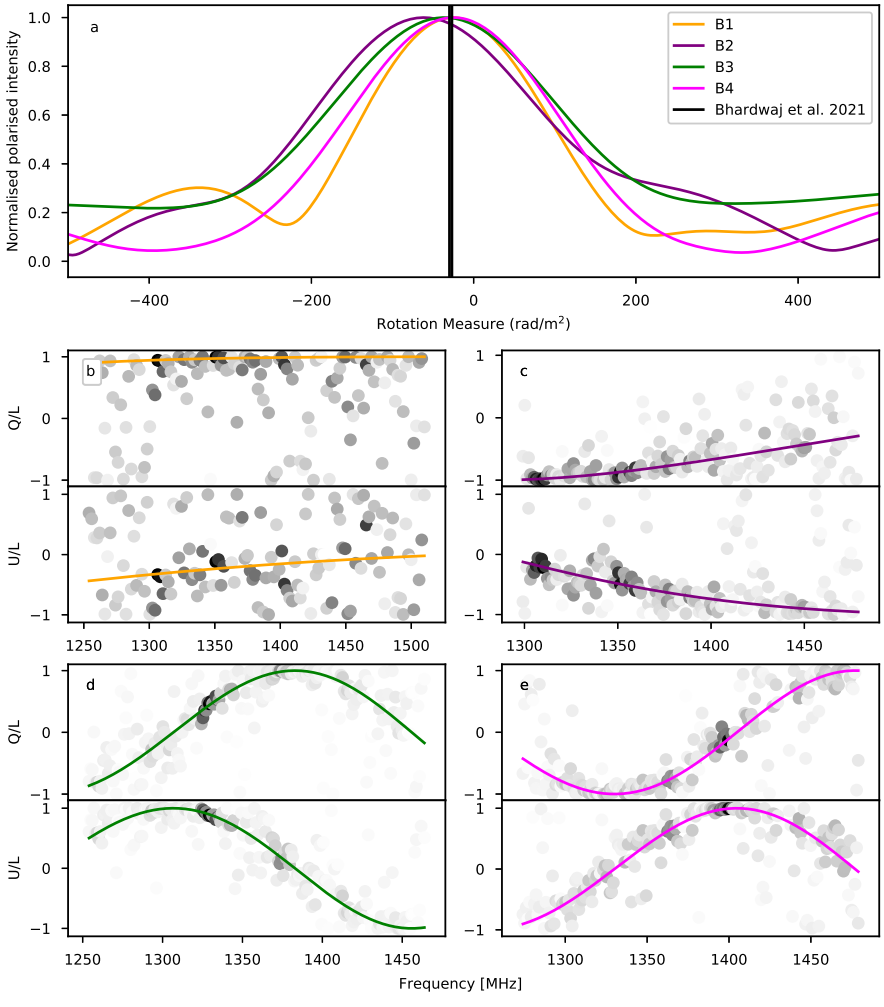

Figure 3.5: Rotation measure (RM) determination for B1 – B4 from FRB 20200120E. Panel **a** shows the Faraday spectrum per burst (labelled), determined using RM synthesis (Brentjens & de Bruyn, 2005), with the grey line showing the previous RM measurement of this source (Bhardwaj et al., 2021a). The grey-scale scatter points panels **b–e** show the Stokes Q (top) and Stokes U (bottom) spectra normalised by the linear polarization L= $\sqrt{Q^2 + U^2}$, where the darker color represents a higher S/N. The colored lines show the best-fit QU-fitting result, where we fit for both the RM and the delay between the polarization channels (Methods §3.5). The color of the line indicates which burst is being plotted, using the legend in the top figure.

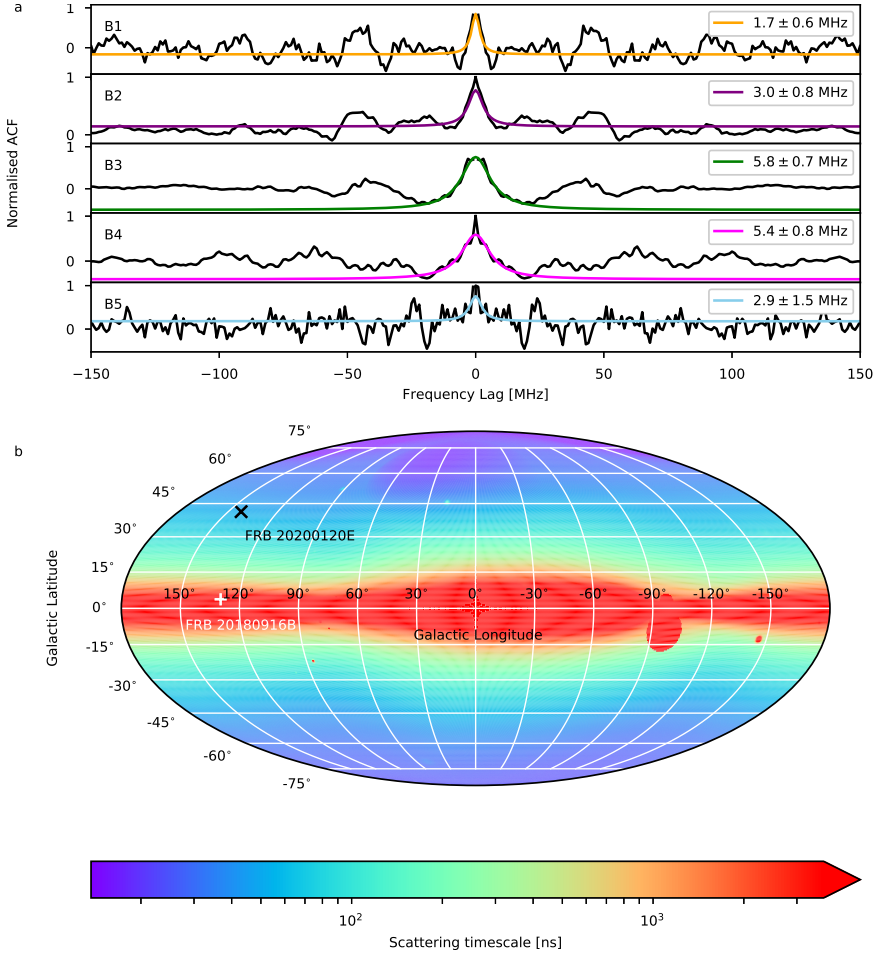

Figure 3.6: Measurement of the scintillation bandwidth in the autocorrelation function (ACF) of each of the five bursts from FRB 20200120E. Sub-figure **a** shows the time-averaged frequency ACF from Figure 3.4 after subtracting the Gaussian fit (black). The Lorentzian fit to the central component is shown by the colored line. The burst name is shown in the top left of each panel, and the measured scintillation bandwidth (defined as the half-width at half-maximum of the Lorentzian; Rickett 1990) is shown in the top right of each panel. Sub-figure **b** shows a colormap of the expected scattering timescale at 1.4 GHz as a function of Galactic longitude and latitude, from the NE2001 Galactic electron density model (Cordes & Lazio, 2002). The sky positions of both FRB 20200120E and FRB 20180916B are shown by the black cross and white plus, respectively.

Bursts B2 and B4 also have sufficient S/N to study at the highest-possible temporal resolution (Methods §3.5; Figure 3.3). Contrary to burst B3, which exhibits few-bin temporal structure, the highest S/N spikes in B2 and B4 are single-bin unresolved features. This poses a concern since the bright spectral feature dominating the subband used to create the burst profile, has a spectral extent less than the subband width (we attribute the spectral features to scintillation, see below). This results in an effective time resolution less than the native sampling of the data. Therefore, single-bin features are more likely to be consistent with a noise process. The probability of drawing the bright single-bin features from their local distributions are $p = 1 \times 10^{-4} \times 100\,\mathrm{bins} = 0.01$ and $p = 4 \times 10^{-4} \times 100\,\mathrm{bins} = 0.04$ for B2 and B4, respectively. These relatively high probabilities, combined with the effective resolution argument above, suggests that the high-resolution features in both B2 and B4 are consistent with the χ^2 AMN distribution.

The total burst duration and spectral structure were quantified by performing a 2-dimensional autocorrelation of the lower-time-resolution burst dynamic spectra, following Nimmo et al. (2021) (8 μs, 125 kHz; see Supplementary Information §3.6 for details). The burst temporal width and frequency extent are reported in Table 3.1. As is clear in the autocorrelation functions (ACFs; Figure 3.4), there is an additional narrower frequency scale, which we measure to be consistent with the expected scintillation from the Milky Way ISM (Supplementary Information §3.6; Figure 3.6a; Cordes & Lazio 2002). The scintillation bandwidth measurements are reported in Table 3.1. Additionally, we report the fluence, peak flux density and isotropic-equivalent spectral luminosity of the bursts, computed within the $\pm 2\sigma$ width region (Table 3.1; Supplementary Information §3.6).

Table 3.1: Burst properties.

Burst	Time of Arrival[a] [MJD]	Fluence[b] [Jy ms]	Peak S/N[c]	Peak Flux Density[b,c] [Jy]	Spectral Luminosity[b,d,e] [10^{28} erg s^{-1} Hz^{-1}]	Width[f] [μs]	Frequency Extent[f] [MHz]	Scintillation bandwidth[h] [MHz]
B1	59265.88304437179	0.13 ± 0.03	6.6	1.59 ± 0.32	0.56 ± 0.13	156 ± 1	140 ± 1	1.7 ± 0.6
B2	59265.88600912486	0.63 ± 0.13	36.1	8.71 ± 1.74	2.3 ± 0.6	$62 \pm 1, 93 \pm 0.5$[g]	$103 \pm 1, 89 \pm 1$[g]	3.0 ± 0.8
B3	59280.69618745651	0.53 ± 0.11	64.8	15.6 ± 3.12	8.0 ± 1.9	46.7 ± 0.1	94 ± 1	5.8 ± 0.7
B4	59280.80173397988	0.71 ± 0.14	29.3	7.07 ± 1.41	4.0 ± 1.0	117 ± 1	134 ± 1	5.4 ± 0.8
B5	59332.50446581106	0.09 ± 0.02	6.9	1.66 ± 0.33	1.0 ± 0.2	56.6 ± 0.1	86 ± 1	2.9 ± 1.5

[a] Corrected to the Solar System Barycenter to infinite frequency assuming a dispersion measure of 87.75 pc cm^{-3}, reference frequency 1502 MHz and dispersion constant of $1/(2.41 \times 10^{-4})$ MHz^2 pc^{-1} cm^3 s.
The times quoted are dynamical times (TDB).
[b] We estimate a conservative 20% error on these measurements, arising due to the uncertainty in the system equivalent flux density (SEFD) of Effelsberg.
[c] Determined for a time resolution of 8 μs.
[d] Using the distance to the globular cluster [PR95] 30244 of 3.63 ± 0.34 Mpc (Freedman et al., 1994).
[e] Isotropic-equivalent.
[f] Defined as $1/\sqrt{2}$ multiplied by the FWHM of the autocorrelation function (ACF).
[g] Width per burst component.
[h] The uncertainties are a combination of the 1-σ fit uncertainty, and $1/\sqrt{N}$, where $N \approx 5$ is the number of scintles.

There are three clear timescales measured in the average temporal ACF (averaged over the four brightest subbands; Methods §3.5) of burst B3 at 31.25 ns resolution (Figure 3.7f–h): a 40 μs timescale, consistent with the total burst extent in time, a clear 1 μs timescale, and even a shorter timescale (40 ns) consistent with temporal structure on the few-bin level. In contrast, bursts B2 and B4 both exhibit a timescale on the order of 10 μs, consistent with their total burst duration (Figures 3.8 & 3.9). There is evidence for structure on the few-bin level in the B4 ACF, although the height of this narrow ACF feature relative to the wider ACF

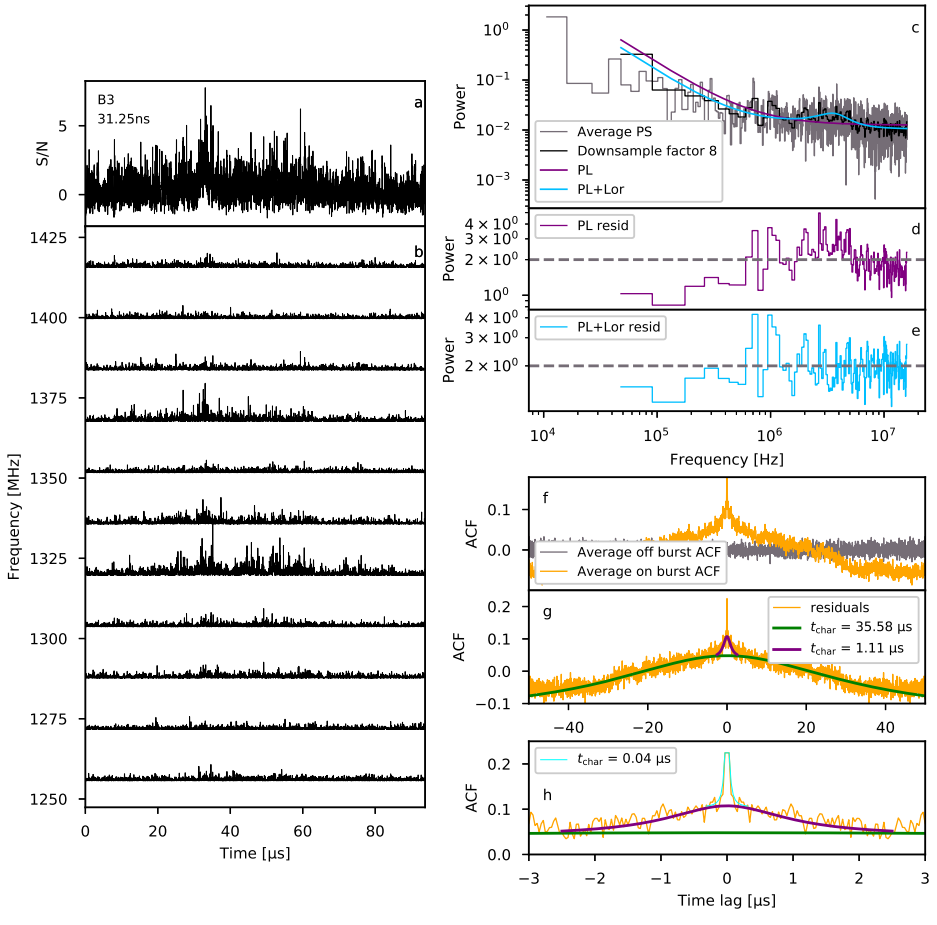

Figure 3.7: Dynamic spectrum of burst B3 from FRB 20200120E with time resolution 31.25 ns, temporal autocorrelation function (ACF) and power spectrum (PS). Panel **b** shows the dynamic spectrum in the form of temporal profiles per subband. This data was generated with SFXC, and each subband has been coherently dedispersed to 87.7527 pc cm^{-3}. Panel **a** shows the frequency-averaged burst profile. Panel **c** shows the average power spectrum (PS) of the four subbands containing significant burst structure in the top panel (grey), with a downsampled PS (factor 8) overplotted in black. The purple and blue lines represent fits to the PS of a red noise power law plus white noise model and a power law/white noise plus Lorentzian model, respectively. Panels **d** and **e** below show the residuals ($2 \times D/M$, for data D and model M) of both models, matching the colors above. The dashed lines represent the perfect case of $D = M$. Panel **f** shows the average temporal ACF of the same four subbands (top panel, orange). For comparison the off burst ACF is also shown (grey). The residual of the average ACF subtracted the noise ACF is shown in panel **g** below, with the green and purple Lorentzian fits to the ACF residuals highlighting two distinct temporal scales in the data. Panel **h** shows a zoom in on the ACF residuals highlighting a third temporal scale by the cyan Lorentzian fit.

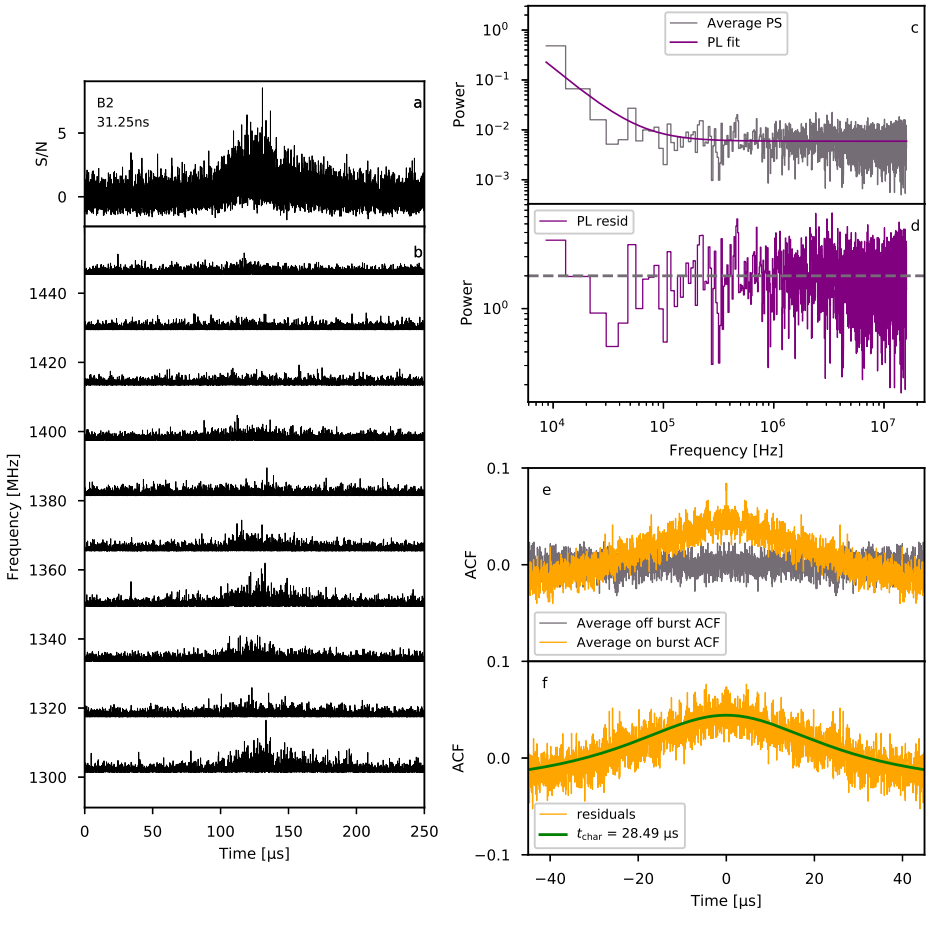

Figure 3.8: The same as Figure 3.7, for burst B2 from FRB 20200120E. Note the average ACF only shows one temporal scale (unlike the three seen for burst B3). Additionally, we only plot the red noise power law plus white noise model since any wide Lorentzian features are less apparent in this power spectrum, than the case of B3.

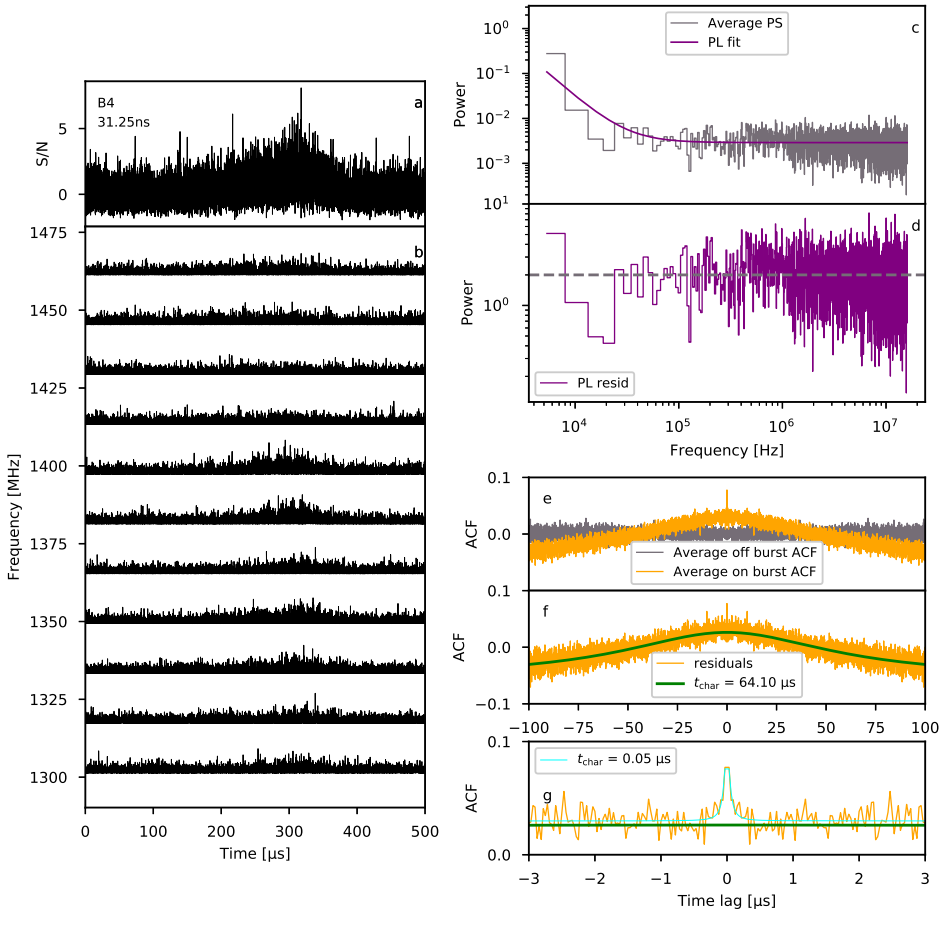

Figure 3.9: The same as Figures 3.7 and 3.8, for burst B4 from FRB 20200120E. Note the average ACF shows two temporal scales (unlike the 3 seen for burst B3). Additionally, we only plot the red noise power law plus white noise model since any wide Lorentzian features are less apparent in this power spectrum, than the case of B3.

feature is smaller for B4 than B3 (height of cyan Lorentzian relative to green Lorentzian in Figures 3.7h & 3.9g), implying either that the S/N of these temporal fluctuations are lower, or that there are fewer temporal features on this timescale. No additional short-timescale components were measured in burst B2 (Figure 3.8). This further supports the conclusions above that we have resolved microsecond and sub-microsecond structure in burst B3, with no evidence for similar structure in B2 and B4. Additionally, there is a range of timescales observed in the bursts, sometimes observed *within* bursts: from tens of nanoseconds to tens of microseconds. In Figure 3.10 we compare the isotropic-equivalent luminosity of the three highest-significance shots of emission in the B3 31.25 ns profile with other short-duration transients, including that of the bright $\sim$ 5 μs component of B3 seen in the 1 μs resolution data (Figure 3.11b), and the wider burst envelopes seen in B1, B2, B4 and B5 (Methods §3.5; Table 3.1).

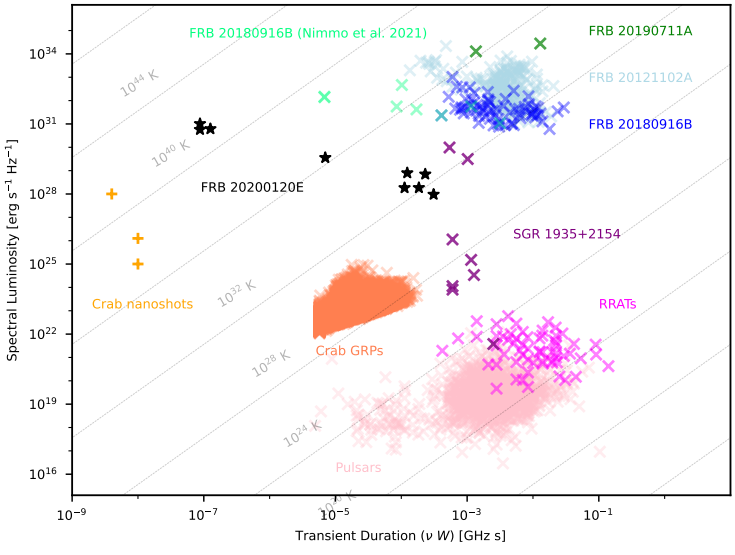

Figure 3.10: Nanosecond to second transient phase space. The FRB 20200120E burst temporal structures and their measured isotropic-equivalent spectral luminosity are shown by the black stars. We plot the three highest significance isolated shots from burst B3 (left-most black stars), the bright 5 μs structure evident in the 1 μs time resolution data of burst B3 (Figure 3.11), as well as the wider burst structure seen in B1, B2, B4 and B5 (right-most black stars). The other FRBs plotted are the published localized repeating FRBs, with known distances: FRB 20121102A (Spitler et al., 2016; Scholz et al., 2017; Law et al., 2017; Michilli et al., 2018b; Hessels et al., 2019; Gourdji et al., 2019; Gajjar et al., 2018; Hardy et al., 2017; Houben et al., 2019; Majid et al., 2020; Josephy et al., 2019; Rajwade et al., 2020; Caleb et al., 2020), FRB 20180916B (CHIME/FRB Collaboration et al., 2019c; Marcote et al., 2020; Chawla et al., 2020; Chime/Frb Collaboration et al., 2020; Pleunis et al., 2021b; Nimmo et al., 2021), and FRB 20190711A (Macquart et al., 2020; Kumar et al., 2021). In purple we plot the radio bursts from the Galactic magnetar SGR 1935+2154 (CHIME/FRB Collaboration et al., 2020; Bochenek et al., 2020; Zhang et al., 2020; Kirsten et al., 2021b; Good & Chime/Frb Collaboration, 2020). Giant pulses from the Crab pulsar (GRPs) are shown in orange (Karuppusamy et al., 2010), and the 'nano-shots' are represented by the yellow crosses (Hankins et al., 2003; Hankins & Eilek, 2007; Jessner et al., 2010). The pulsar and Rotating RAdio Transient (RRAT) population are shown in pink (Keane, 2018). Note that for pulsars, the points on the figure represent average pulses, where individual pulses can be brighter or weaker by approximately 1 or 2 orders of magnitude. The grey lines represent lines of constant brightness temperature.

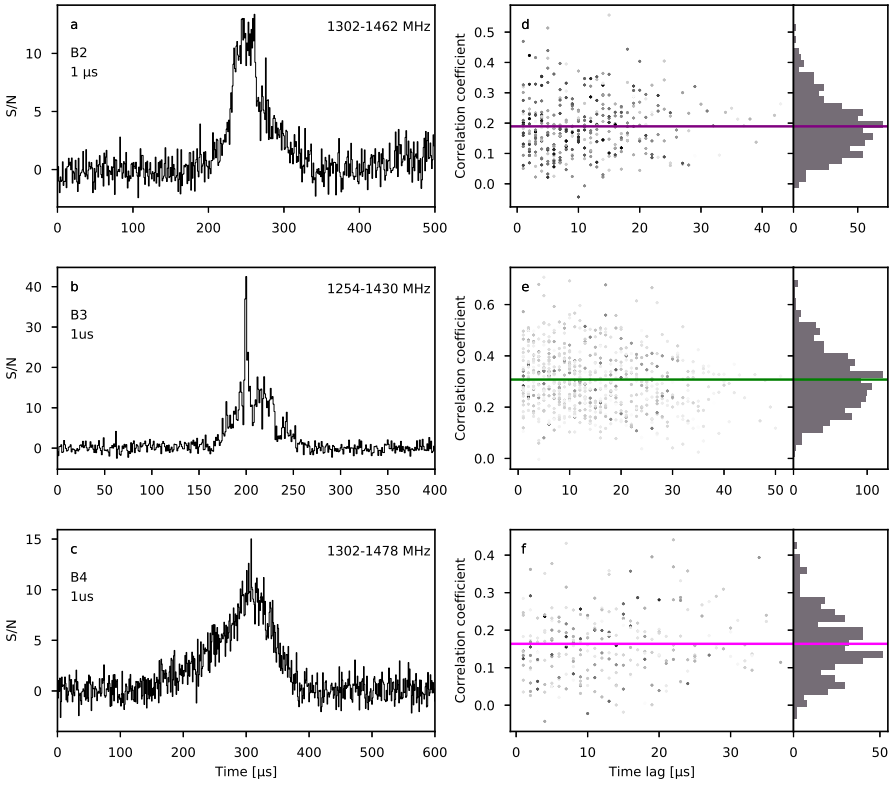

Figure 3.11: Correlation coefficient between single time bin (1 μs) spectra of bursts B2, B3 and B4 from FRB 20200120E, testing for consistency with the Scintillating Amplitude Modulated Polarized Shot Noise prediction (0.33 for 100 % polarized emission; Cordes et al. 2004). Panels **a–c** show the 1 μs burst profile with the burst name and time resolution shown in the top left corner and the frequency range averaged over to produce the burst profile in the top right corner of each panel. Panels **d–e** show the correlation coefficient between single time bin spectra above a S/N threshold of 9 as a function of the time separation between bins. The color gradient indicates the geometric mean of the two time bins used to determine the correlation coefficient (darker color implying a higher geometric mean). Also plotted is a histogram of the correlation coefficients. The colored line represents the geometric mean S/N weighted correlation coefficient.

The power spectra of bursts B2, B3 and B4 (panel **c**; Figures 3.7–3.9) are all consistent with red noise (Methods §3.5), with B2 and B4 exhibiting a steeper power law ($\alpha = 1.85 \pm 0.04$ and 2.04 ± 0.05, respectively) than B3 ($\alpha = 1.46 \pm 0.05$). This is consistent with the results we have presented above; the power spectrum of B3 shows more power at higher frequencies (shorter timescales), than bursts B2 and B4.

Table 3.2: Burst polarization properties and polarization position angle fit results.

Burst	RM[a] [rad m^{-2}]	PPA offset[b] [deg]	RM (global)[a,c] [rad m^{-2}]	PPA offset (global)[c] [deg]	$L_{unbiased}/I$[d] [%]	V/I[d] [%]	χ^2 [e]	Degrees of freedom[e]
B1	-21.9 ± 13.1	28.5	-54.2 ± 4.8	68.3	94 ± 9	4 ± 9	18.9	7
B2	-57.2 ± 5.1	0	-54.2 ± 4.8	0	103 ± 3	-13 ± 3	59.6	27
B3	-37.1 ± 4.2	−8.6	-36.9 ± 3.8	−9.3	102 ± 2	1 ± 1	15.5	11
B4	-36.4 ± 8.0	13.1	-36.9 ± 3.8	14.3	94 ± 2	6 ± 2	25.7	22

[a] The large fractional errors arise due to covariances between fit parameters in the QU-fitting, see text for more details.
[b] Offset from a weighted mean of the bursts from a single epoch.
[c] The global values are assuming all bursts detected on the same day have the same RM.
[d] The quoted uncertainties are 1σ uncertainties, and do not include uncertainties from the calibration. Note: we reproduce the published pulsar circular (linear) fractions within 3% (10%) and 1% (6%) for the Feb 20 and March 7 observations, respectively.
[e] Fit results of weighted least squares fitting of a straight line to the PPA.

Following Nimmo et al. (2021), the polarimetric data were calibrated using the known polarization properties of the pulsar PSR B0355+54 (Taylor et al. 1993; see Supplemetary Information §3.6 for details). The full polarimetric burst profiles and polarization position angles (PPA) are shown in Figure 3.2. Note that we could not recover the polarimetric properties of burst B5, likely due to the low S/N of the burst. Bursts B1 – B4 are highly linearly polarized ($> 90\%$), and exhibit little-to-no circular polarization (Table 3.2). As reported in Table 3.2, there is a tentative $3 - 4\,\sigma$ detection of 13 % and 6 % circular polarization in B2 and B4, respectively. In the 8 μs resolution profiles, there is evidence for small variations in the PPA across the bursts, with a ΔPPA between bursts from the same epoch within $\sim 30^\circ$. We determine the rotation measure (RM) of the bursts, and conclude that they are in agreement with previous measurements (-29.8 rad m^{-2}; Bhardwaj et al. 2021a).

As presented above, burst B3 exhibits variations on both microsecond as well as sub-microsecond timescales. The Stokes parameters are only physically meaningful with sufficient averaging (van Straten, 2009). Therefore, in Figure 3.12 we show the frequency-averaged polarization profile and PPA of burst B3 at 125 ns resolution. In these data we average over a total of 44 channels (over the frequency range 1254 – 1430 MHz), and therefore have 44 degrees of freedom. The ∼100 ns – 1 μs structures are highly linearly polarized, consistent with the polarization properties at lower time resolution. Additionally, the PPA varies between the sub-μs temporal features by up to a few 10s of degrees.

3.4 Discussion

The timescales and luminosities measured in the FRB 20200120E bursts presented in this work populate a previously vacant, relatively unexplored region of the short-duration transient phase space. They bridge the gap between extragalactic FRBs and Galactic neutron

stars (Figure 3.10). Here we elaborate on how FRB 20200120E compares observationally with other short-duration radio transients, and discuss the implications of our findings.

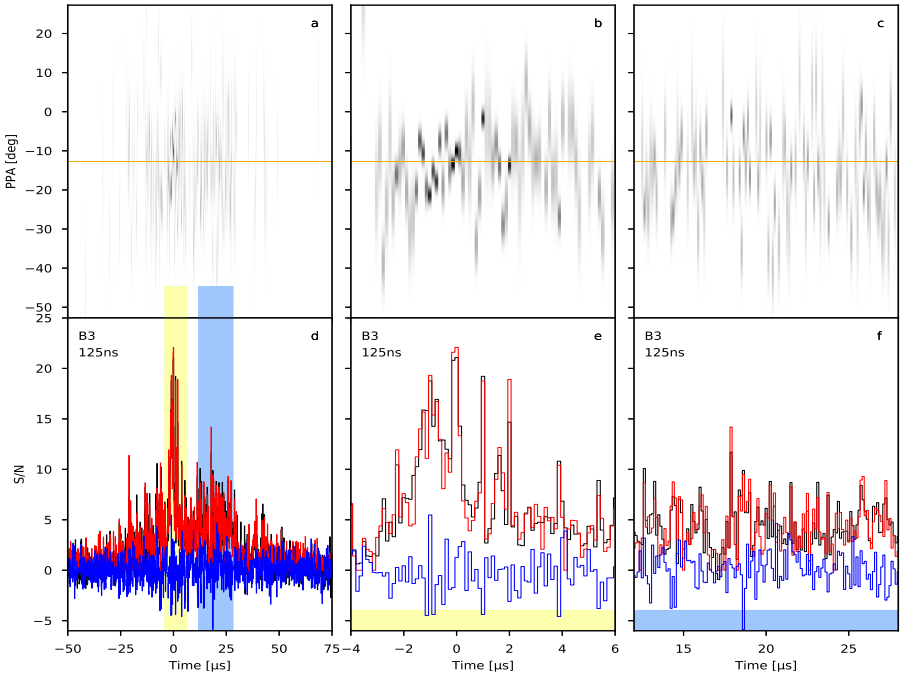

Figure 3.12: High time resolution polarimetric profile and polarization position angle (PPA) for burst B3 from FRB 20200120E. Panels **a**–**c** show the PPA as a function of time, with the orange line representing the weighted best-fit line to the PPA. Only the PPAs above a linear S/N threshold of 5 are plotted. Panels **d**–**f** show the polarimetric profile of the burst sampled at 125 ns, with Stokes I (black), unbiased linear polarization (Everett & Weisberg 2001; red) and circular polarization (blue). The yellow and blue regions plotted on panels **a** and **d** represent the time ranges used for plotting panels **b**,**e** and panels **c**,**f**, respectively. This data was generated with SFXC, with 4 MHz channels and coherently (within subbands) and incoherently (between subbands) dedispersed to 87.7527 pc cm^{-3}. The frequency information was averaged for the frequency range 1254 – 1430 MHz (visually, the extent of the burst in frequency), which, in this data product, corresponds to averaging by a factor of 44.

Repeating fast radio bursts

The polarimetric properties of FRB 20200120E are consistent with those of most well-studied repeaters (Michilli et al., 2018b; Nimmo et al., 2021; Day et al., 2020). As is often observed, we find a very high ($\sim$ 100%) linear and low ($\lesssim$ 10%) circular polarization fraction as well as a polarization position angle (PPA) that is roughly constant during bursts. As with FRB 20180916B (Nimmo et al., 2021), we find that FRB 20200120E shows small PPA variations (ΔPPA) on timescales $< 10\,\mu$s. Between bursts, we see variations in the PPA of a few tens of degrees, in contrast to the $< 10^{\circ}$ ΔPPA from bursts detected at the same observing epoch, seen in other repeaters (Michilli et al., 2018b; Nimmo et al., 2021). We note

that at least one repeater (FRB 20180301A) has shown lower linear polarization fractions ($40 - 80\%$) and significant PPA swings in some bursts (Luo et al., 2020).

The spectrum of FRB 20200120E shows at least two scales of variation. We find narrow-band brightness variations on the scale of ~ 5 MHz, which we ascribe to scintillation in the Milky Way ISM. The other ~ 100 MHz spectral variation may be intrinsic to the source emission mechanism or imparted by local propagation effects. This spectral envelope is similar to what is seen from other repeaters (Hessels et al., 2019; Gourdji et al., 2019; Pleunis et al., 2021a). Additionally, the downward-drifting burst sub-structure, often referred to as the 'sad-trombone effect', that is often seen in repeaters (Hessels et al., 2019), has previously been observed for FRB 20200120E (Bhardwaj et al., 2021a).

Though FRB 20200120E shares many characteristics of repeating FRBs, its $\sim 100\,\mu$s burst envelopes are atypically narrow. The range of timescales observed, however, roughly a factor of 1000, is comparable to what has been found in a similar analysis of FRB 20180916B (Nimmo et al., 2021). In the case of FRB 20180916B, Nimmo et al. (2021) were limited by a larger scatter-broadening of 2.7 μs (note that FRB 20180916B is at a Galactic latitude of only 3.7°; Marcote et al. 2020; see also Figure 3.6b), and could not rule out the possibility that the wider sub-bursts are composed of closely spaced microsecond structures. Burst B3 from FRB 20200120E has clear isolated shots of duration ~ 60 ns, and also evidence that the sub-microsecond shots are clustered on microsecond timescales (Figure 3.7f–h). For bursts B2 and B4, there is no clear evidence for isolated shots in the 31.25 ns burst profile, but it is possible that the S/N is too low to detect these individual shots, consistent with the lower <0.33 measured correlation coefficient (Methods §3.5; Figure 3.11d–f).

The strikingly similar observational properties of FRB 20200120E with other repeaters suggests that they have similar physical origins. FRB 20200120E is the closest known extragalactic FRB discovered to date (Kirsten et al., 2022). The remarkable proximity of FRB 20200120E has revealed radio bursts with an isotropic-equivalent spectral luminosity 2–3 orders of magnitude weaker than bursts from other repeating FRBs (Figure 3.10). Such low luminosity bursts would not be detectable at the distance of any other precisely localized repeating FRBs. Continued monitoring of FRB 20200120E will be important to compare the energy distribution and activity rate with other repeaters.

Crab pulsar

We have discovered resolved structure in bursts from FRB 20200120E with durations of $\sim 5\,\mu$s, down to ~ 60 ns, 2 orders of magnitude shorter timescales than have been probed for FRBs, to date. Crab pulsar giant pulses (GPs) show temporal structure in the range μs – ms, which sometimes resolve down to sub-nanosecond timescales, often referred to as 'nano-shots' (Hankins et al., 2003). Crab nano-shots are known to be extremely energetic, with brightness temperatures reported up to 10^{41} K (ignoring relativistic effects; Hankins & Eilek 2007). The sub-microsecond shots in B3 exhibit a comparable, extremely high brightness temperature (again, ignoring relativistic effects; Figure 3.10). This is at least four orders of magnitude higher than typically seen from the FRB population (10^{32}–10^{37} K; Petroff et al.

2019). In the line of sight to FRB 20200120E, the expected scatter broadening from the Milky Way ISM is $\sim$ 50 ns at 1.4 GHz (Cordes & Lazio, 2002), in rough agreement with our measured scintillation bandwidth ($1/(2\pi\Delta\nu_{\rm scint}$) $\sim$ 27 ns). This implies that the $\sim$ 60 ns structure observed in this work is likely the shortest resolvable temporal scale at our observing frequency.

Bursts B2, B3 and B4 are consistent with the Scintillating Amplitude Modulated Polarized Shot Noise model (Methods §3.5), which has been used to describe many aspects of pulsar emission, including GPs from the Crab pulsar (Cordes et al., 2004; Karuppusamy et al., 2010). However, only B3 is observed to resolve down to microsecond and sub-microsecond temporal scales. This is similar to observations of the Crab pulsar, where not all GPs resolve down to individual nano-shots (Hankins & Eilek, 2007; Jessner et al., 2010). Furthermore, most Crab GPs consist of at least one broadband 'micro-burst', with a characteristic timescale of a few microseconds (Hankins & Eilek, 2007; Hankins et al., 2016), similar to the structure that can be seen in burst B3 at 1 μs time resolution and consistent with the measured 1.11 μs timescale in the temporal ACF (Figures 3.7g & 3.11b). Sometimes, the Crab micro-bursts are seen to resolve down to individual narrowband nano-shots (see e.g. Figure 4 of Hankins & Eilek 2007), consistent with the features seen at 31.25 ns in burst B3.

Band-limited giant pulses from the Crab pulsar (Hankins & Eilek, 2007; Thulasiram & Lin, 2021; Bij et al., 2021), as well as from the 'Crab's twin' pulsar PSR J0540−6919 (Geyer et al., 2021), have been observed. These are reminiscent of the narrow-banded emission observed from repeating FRBs. This adds further weight to the phenomenological connection of giant pulse emission with FRBs.

Galactic magnetar SGR 1935+2154

The FRB 20200120E bursts also exhibit wider characteristic timescales of 10 − 100 μs. These wider components have isotropic-equivalent energies on the order of 10^{32-33} erg, which is 2–3 orders of magnitude weaker than the bright FRB-like radio burst from the Galactic magnetar SGR 1935+2154 (Bochenek et al., 2020; CHIME/FRB Collaboration et al., 2020). Thus, SGR 1935+2154 has produced more energetic radio bursts than some extragalactic FRBs, eliminating the gap in luminosity (Figure 3.10) and thereby strengthening the connection between magnetars and FRBs. The observed energies are much lower than the proposed low-energy cutoff at $\sim 10^{34}$ erg for the low-twist magnetar model (Wadiasingh et al., 2020), implying that the FRB luminosity function does not abruptly end at $\sim 10^{34}$ erg. The brightness temperatures of these wider components are $\sim 10^{32}$ K, comparable to SGR 1935+2154 (Bochenek et al., 2020; CHIME/FRB Collaboration et al., 2020), and also consistent with the lower end of the observed FRB brightness temperatures (Figure 3.10).

Implications

Previously, it has been shown that millisecond-duration radio bursts from the Galactic magnetar SGR 1935+2154 span 7–8 orders of magnitude in apparent luminosity (Kirsten et al.,

2021b), bridging from the brightest pulsars, to 1–2 orders of magnitude lower than the weakest known extragalactic FRBs. By probing FRB 20200120E at timescales of tens of nanoseconds, we highlight that this coherent radio source observationally links repeating FRBs with GP emission from young pulsars, and the bright FRB-like emission from magnetars. The timescales and luminosities measured in this work fill the gap in the luminosity-duration phase space (Figure 3.10), further emphasising that observationally the division between source populations (FRBs, pulsars, magnetars) is not clear.

Constraints on the shortest timescale variations in FRB lightcurves are key for understanding the physical mechanism producing the bursts, and can ultimately reveal clues about the progenitor. The observational connection to the Crab pulsar, SGR 1935+2154, and repeating FRBs, supports a common magnetically-powered emission mechanism spanning many orders of magnitude in timescale and luminosity. The $\sim$60 ns to 5 µs timescales observed in B3 correspond to a light-travel size of 20–1500 m, ignoring relativistic effects. The sub-microsecond timescales observed are too short to be naturally explainable via emission from a synchrotron maser in a relativistic shock (Metzger et al., 2019), since it would require a small region to be emitting at any given time. Nimmo et al. (2021) previously argued that the short timescales observed in FRB 20180916B are more naturally explainable in the context of a neutron star magnetospheric origin. The results presented here further support a magnetospheric origin of the FRB emission.

Magnetic reconnection is one possible way to harness the magnetic energy to power a coherent radiation mechanism that produces the radio emission. This has been proposed to explain Crab nano-shots (Philippov et al., 2019), the FRB-like radio burst from SGR 1935+2154 (Yuan et al., 2020), and FRBs (Lyubarsky, 2020; Lyutikov, 2021). A range of temporal scales and magnetic energy releases can be expected from this mechanism, which is consistent with the observed dynamic range of timescales, and large range of FRB luminosities: from the weaker possible FRBs emitted by the relatively old magnetar SGR 1935+2154, and the bursts from FRB 20200120E, to the more energetic FRBs potentially coming from extragalactic young, active magnetars.

The observed timescales and luminosities from FRB 20200120E can be explained by magnetic reconnection events in the close vicinity of a relatively young, isolated, highly magnetized neutron star. The association of FRB 20200120E with an old globular cluster strongly implies that, if the source is a magnetar, it was not formed through a core-collapse supernova (Kirsten et al., 2022). The globular cluster origin of FRB 20200120E also allows for the exploration of alternatives to a magnetar progenitor: for example, a highly energetic millisecond pulsar or an accreting system, in which case the observational similarities with the Crab pulsar and SGR 1935+2154 are more coincidental.

Future observations of FRB 20200120E at observing frequency $\geq$ 5 GHz (where the scatter broadening will be lower), with a bandwidth $>$ 200 MHz, are needed to explore shorter timescales. Continued monitoring of FRB 20200120E will provide statistics on the distribution of emission timescales and whether the burst activity is periodic, like FRB 20180916B (Chime/Frb Collaboration et al., 2020). Such data will also help determine whether, e.g., there are quasi-periodic fluctuations in the burst lightcurves, hinted at in the case of

FRB 20180916B (Nimmo et al., 2021), or a secular variation in the widths of burst envelopes.

Lastly, we highlight that the short timescales measured from FRB 20200120E in this work motivate searches for a population of *ultra*-fast radio bursts, despite the considerable technical challenges that such a search entails.

3.5 Methods

In this section, we describe the analysis in more detail. Since this was an interferometric campaign, we regularly observed a phase calibrator source (5.5 minutes on target, 2.0 minutes on the calibrator). The total time on FRB 20200120E was 2.93 hr per observation.

Burst search

We performed two independent analyses on the single-dish Effelsberg data to search for bursts from FRB 20200120E. The voltage data were converted to total-intensity filterbanks using digifil with time and frequency resolutions of 64 μs and 125 kHz, respectively. These data were searched using a Heimdall-based pipeline and burst candidates were classified using the machine learning classifier, FETCH (Agarwal et al., 2020). A more detailed description of this pipeline was presented in Kirsten et al. (2021b). In parallel, we also recorded total intensity filterbanks using the PSRIX pulsar backend (Lazarus et al., 2016), with time and frequency resolution of 102.4 μs and 0.49 MHz, respectively, and a total bandwidth of 250 MHz. The PSRIX pulsar backend data were analysed using a PRESTO-based pipeline (Ransom, 2001), and single pulse candidates were classified using an automated classifier based on Michilli et al. (2018a). We recorded a test pulsar scan of PSR B0355+54 to inspect the data quality.

Five bursts from FRB 20200120E were discovered in the search of the raw voltages using the Heimdall-based search (B1 and B2 on 2021 February 20; B3 and B4 on 2021 March 7; and B5 on 2021 April 28). Only four of the five bursts were found in the PSRIX data because burst B1 occurred during the ~ 40 s latency between the start of the VLBI recording and the pulsar backend recording. Initially, B2 was flagged as radio frequency interference in the PSRIX data by the automated classifier (Michilli et al., 2018a) due to strong scintillation structure.

Data products

For further analysis of the burst properties — using full polarimetric information at a range of time and frequency resolutions — we generated filterbank data from the raw voltages using both SFXC (Keimpema et al., 2015) and digifil (van Straten & Bailes, 2011).

SFXC

Using SFXC (phased array branch), we produced relatively low time resolution filterbank data (8 μs), in order to have sufficient spectral resolution (125 kHz) to study frequency structure due to scintillation, and to determine the rotation measure (RM). The data are coherently dedispersed within the 16-MHz subbands, and incoherently dedispersed between the subbands using a DM of 87.75 pc cm^{-3}, which is within $\sim$ 0.003 pc cm^{-3} of the value we measured using higher time resolution data (see below). This 0.003 pc cm^{-3} offset corresponds to a dispersive delay, across the burst extent in frequency, that is less than the time resolution. Using dspsr (van Straten & Bailes, 2011) we created archive files containing each burst at the resolution of the filterbank data, and remove frequency channels from the data that are contaminated by radio frequency interference using the psrchive tool pazi (Hotan et al., 2004).

The real-sampled VDIF data with 16-MHz subbands allow for up to 31.25 ns time resolution. Due to the Fast Fourier Transform-based (FFT-based) correlation and delay corrections implemented in SFXC (phased array), the practical time resolution limit is 125 ns. In this case, the data have 4 channels per subband. Since SFXC does not window the data before the FFT, potential spectral leakage artefacts are a concern, especially in the case of a low number of channels per subband. This data is used to study the polarimetry at high time resolution.

Additionally, we output coherently dedispersed total intensity (Stokes I) at the original data sampling rate (i.e. no channelization within subbands) using the SFXC bolometer branch. Here we have no concerns of spectral leakage or any other artefacts that may be introduced at the channelization stage of the processing. Note that the VLBI backed, DBBC2 (Tuccari et al., 2010), uses digital down conversion to create independent 16 MHz subbands, meaning that adjacent 31.25 ns samples are not correlated.

Digifil

We also used digifil to produce data at the highest-possible time resolution, in order to verify the results presented in this work. digifil utilises a convolving filterbank, which reduces spectral leakage effects (van Straten & Bailes, 2011). However, digifil converts to complex-sampled data internally, resulting in a factor of 2 decrease in the time resolution for a given number of channels (for the Nyquist limit). Thus, the best time resolution we can achieve with our 16-MHz subbands is 62.5 ns. digifil produces one filterbank file per subband, and the subbands are combined with incoherent dedispersion.

In both the digifil and SFXC data, the incoherent dedispersion between subbands is performed with integer sample shifts.

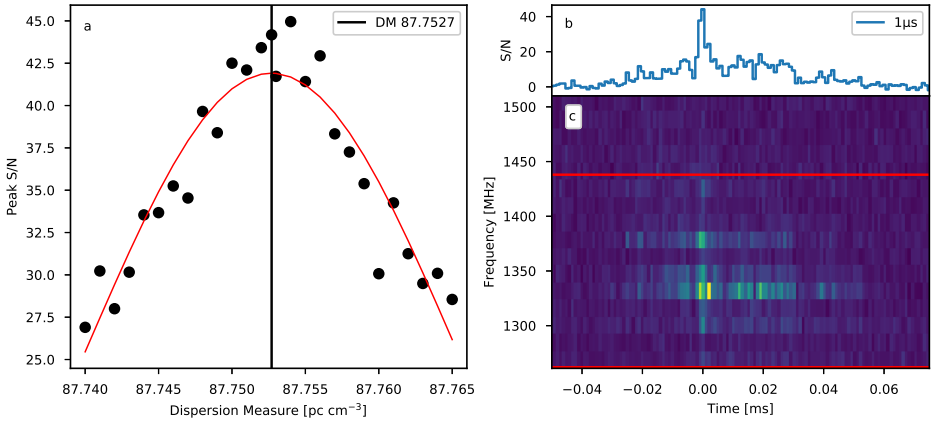

Figure 3.13: Constraining the dispersion measure (DM) using the short timescale structure in burst B3 from FRB 20200120E. Using data products generated using SFXC (Keimpema et al., 2015), with a time and frequency resolution of 500 ns and 1 MHz, respectively, we coherently (within subbands) and incoherently (between subbands) dedisperse to a range of DMs, downsample in time by a factor of 2, and compute the peak S/N of the frequency-averaged profile (panel **a**). Also plotted in panel **a** is a Gaussian fit to the peak S/N as a function of DM, with the best-fit DM (DM = 87.7527$\pm$0.0003 pc cm^{-3}) shown by the grey line. Panel **b** shows the burst profile and panel **c** the dynamic spectrum coherently and incoherently dedispersed to the best-fit DM. The time and frequency resolutions used for plotting are 1 μs and 16 MHz, respectively. The red lines on the dynamic spectrum indicate the frequency extent averaged over to determine the peak S/N per DM, and to produce the burst profile.

Refined dispersion measure determination

At the native time resolution of the voltage data (31.25 ns), the DM must be correct to < 0.0005 pc cm^{-3} to avoid DM smearing across the 256 MHz bandwidth larger than the time bin width.

To limit potential spectral leakage artefacts in the SFXC data, we produced 500 ns time resolution filterbank files, with 16 channels per subband (1 MHz channels), at a range of DM values around the expected DM (determined by eye in the dynamic spectrum of burst B3). The data are coherently dedispersed within the 16 MHz subbands, and each subband is then time shifted to correct for dispersive delay, to limit DM smearing within each channel, and across the band. These data were then downsampled in time to 1 μs (i.e. a downsampling factor of 2). The reason for producing the data products in this way, as opposed to creating 1 μs resolution data with higher frequency resolution, is to minimise smearing due to incoherent dedispersion between subbands (integer bin shift). We can accurately determine the DM of burst B3 by maximizing the S/N of the bright $\sim$ 5 μs component (Figure 3.13), despite any downward-drifting, 'sad-trombone' effect, that may be present in the burst dynamic spectrum. This is because by maximizing the S/N of the narrow temporal structure, we are essentially maximizing the structure in the burst (as opposed to maximizing the S/N of the entire burst, which has been shown to incorrectly represent the DM, e.g. Gajjar et al. 2018). In Figure 3.13, we plot the peak S/N of the burst profile as a function of DM, and fit a Gaussian function to determine the best DM. We search for a DM in the range $87.74 - 87.765$ pc cm^{-3}

in steps of 0.001 pc cm^{-3} and find that the best DM is DM$=$ 87.7527 $\pm$ 0.0003 pc cm^{-3}, where the uncertainty is determined by σ/A, where σ and A are the standard deviation and amplitude of the Gaussian fit, respectively. We note that the range of DMs searched does not include the previously measured DM (Bhardwaj et al., 2021a), since the dynamic spectrum of burst B3 is visibly over-corrected when dedispersed to this value. Both measurements of the DM use the same dispersion constant of $1/(2.41\times10^{-4})$ MHz^2 pc^{-1} cm^3 s, thus they can be directly compared.

In panels **c** and **d** of Figure 3.13 we plot the burst profile and dynamic spectrum coherently (within channels) and incoherently (between subbands) dedispersed to this best-fit DM, respectively. This analysis was repeated on digifil filterbank data products generated with 62.5 ns time and 16 MHz frequency resolution, coherently and incoherently dedispersed, and then downsampled to 1 µs time resolution. We find a consistent DM value from digifil and SFXC data (noting also that both softwares use the same dispersion constant of $1/(2.41\times10^{-4})$ MHz^2 pc^{-1} cm^3 s).

We assume the same DM for all bursts in our sample.

Scintillating Amplitude Modulated Polarized Shot Noise

In the uncertainty principle limit $\delta t\delta\nu \sim 1$, where δt and $\delta\nu$ are the time and frequency resolution (respectively) of individual samples, the off-burst noise is χ^2-distributed with 2 degrees of freedom (Figure 3.1b). For a modestly broadband noise-like signal, the statistics are χ^2-distributed where the degrees of freedom depend on the polarization fraction. We perform a least-squares fit of a χ^2-distribution to the on-burst distribution and find the best fit to have 2 degrees of freedom, consistent with 100 % polarized Scintillating Amplitude Modulated Polarized Shot Noise (SAMPSN; Cordes 1976). The superposition of the off-burst χ^2-distribution and the on-burst χ^2-distribution reasonably describes the total burst S/N distribution, where the residuals can likely be attributed to the fact that the shape of the burst envelope is not well-modelled.

Due to strong spectral dips near the subband edges, sufficient frequency resolution is required in order to robustly correct the bandpass and compare individual bin spectra with each other. We therefore created a 1 µs, 500 kHz filterbank using SFXC. Shown in Figure 3.11 is the correlation coefficient between individual 1 µs time bins above a S/N threshold of 9 in burst B3, as a function of their time separation. We find that the correlation coefficients have a geometric mean S/N weighted average of 0.31. The scintillation frequency structure is expected to be perfectly correlated within the duration of the burst (we observe that the B1 and B2 spectra, separated by 4.3 minutes, are correlated; Figure 3.14), while the Amplitude Modulated Polarized Shot Noise frequency structure will change depending on the degree of polarization (Cordes et al., 2004). SAMPSN predicts a correlation coefficient of

$$\rho = \frac{1}{2 + p_{\mathrm{frac}}^2}, \tag{3.1}$$

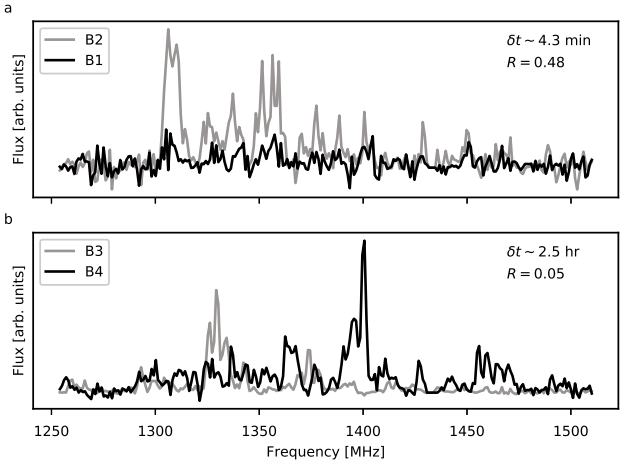

Figure 3.14: Comparing the time-averaged spectra between bursts detected close in time. Panel **a** shows the time-averaged spectra for B1 (black) and B2 (grey). Panel **b** shows the time-averaged spectra for B3 (grey) and B4 (black). In the top right of each panel, we quote the time between the two bursts in the plot, δt, and the correlation coefficient of the burst spectra, R.

where $p_{\rm frac}$ is the total polarization fraction. Our measured $\rho = 0.31$ implies that the signal is 100 % polarized, consistent with the high linear polarization fraction we measure in the frequency-averaged burst profiles (Figure 3.2), and the on-burst S/N distribution.

For B2 and B4, we find a weighted average correlation coefficient of the individual 1 µs time bin spectra (above a S/N of 9) of 0.19 ± 0.001 and 0.16 ± 0.001, respectively, significantly lower than the 0.33 expectation for SAMPSN (Cordes et al., 2004), and the 0.31 measured from B3, but also significantly greater than 0. This is consistent with highly polarized SAMPSN (similar to B3), where potentially the lower correlation coefficient can be attributed to low S/N and/or sparseness of shot pulses. This is consistent with the lack of evidence for resolved shots of emission in the high time resolution profiles of bursts B2 and B4 (Figure 3.3).

Resolved sub-microsecond emission?

To test whether the sub-microsecond temporal structures we observe are isolated shots of emission or, alternatively, consistent with AMN, we compare the high S/N features with the *local* brightness distribution. For burst B3, which exhibits envelope fluctuations on the µs level (Figure 3.11b), we define the local distribution as ± 1.5625 µs (± 50 bins) around the brightest feature (which we wish to measure the significance of). We take this range of bins to ensure that we are including enough samples to measure the local distribution, and to ensure we are not taking too many samples such that we lose the information about the burst envelope *locally*. Using an Anderson-Darling test (Stephens, 1974), we confirm that

this local distribution is exponentially distributed. Note that since we cannot distinguish (by eye) between temporal spikes that are due to AMN versus individual emission spikes, we include all time bins (within the range mentioned), excluding the central feature, in the distribution; therefore, the probabilities measured are lower-limits. We fit a χ^2-distribution with 2 degrees of freedom, using a least-squares fit, to the S/N values within the range defining the local distribution. This distribution is expected for 100 % polarized SAMPSN (Cordes, 1976). For the high S/N, 2-bin wide feature in burst B3 (Time= 0, Figure 3.1), the probability of drawing this from the local distribution is $p = 4 \times 10^{-8} \times 100\,\mathrm{bins}/2 = 2 \times 10^{-6}$ (Figure 3.3), i.e. inconsistent with AMN, supporting that this component is a resolved, isolated shot of emission.

We repeated the same analysis on bursts B2 and B4, since they have sufficient S/N to study at the highest time resolution. For B2 we created the temporal profile at 31.25 ns using the subband 1302–1318 MHz, and for B4 we use subband 1398–1414 MHz: in both cases this is the subband containing the brightest spectral feature (Figure 3.3). In the case of B3, at the highest time resolution there are temporal fluctuations that are multiple bins wide. In contrast, the only bright structure in both B2 and B4 at the highest time resolution are unresolved single-bin spikes. Given that the frequency extent of the bright spectral feature is less than the subband width of 16 MHz (we attribute the spectral features to scintillation; see below), this results in an effective time resolution lower than the sampling resolution. Single bin spikes in this case are therefore more likely to be consistent with the noise process. We tested the significance of the brightest unresolved structure using the same method as described for B3. Again, we confirm that the local distribution around the structure of interest is exponentially distributed using an Anderson-Darling test (Stephens, 1974). The probability of the highest unresolved spike in B2 and B4 is $p = 1 \times 10^{-4} \times 100\,\mathrm{bins} = 0.01$ and $p = 4 \times 10^{-4} \times 100\,\mathrm{bins} = 0.04$, respectively. Given the effective resolution argument above, combined with the high probabilities of occurring by chance, there is not strong evidence supporting that these structures are isolated, unresolved shots of emission. Instead, we conclude that these features are consistent with the χ^2 AMN distribution.

Temporal ACF and power spectrum

In Figures 3.7–3.9, we present each coherently dedispersed subband of burst B3, B2 and B4, respectively, (covering the frequency extent of the burst) at 31.25 ns resolution. This is essentially the burst dynamic spectrum at poor frequency resolution. We select the four brightest subbands that contain the most burst structure, and computed the ACF of the time profile. These ACFs were averaged together and shown in panel **e** of Figures 3.7–3.9. The reason for computing the ACF in this manner, as opposed to creating a frequency-averaged profile and computing the ACF, is to limit the smearing due to inaccuracies in the incoherent dedispersion (the subbands are shifted by an integer number of bins). For all three bursts, we measure a characteristic timescale on the order of 10 μs, determined by fitting a Lorentzian function to the ACF (out to a time lag that is chosen by eye, to help the fitting distinguish between multiple timescales). This timescale is consistent with the full burst extent in time. In burst B3, we measure an additional two timescales: a clear 1.11 μs timescale, and

even a shorter timescale (40 ns) consistent with temporal structure on the few-bin level (Figure 3.7f–h). For B4, we additionally measure a short-temporal scale suggesting that there is temporal structure of a few-bins in the B4 31.25 ns profile (Figure 3.9g). Although, it is worth noting that the height of this narrow ACF feature relative to the wider ACF feature (height of the cyan Lorentzian relative to the green Lorentzian in Figures 3.7h and 3.9g) is smaller for B4 than B3, implying either that the S/N of these temporal fluctuations are lower, or that there are fewer temporal features on this timescale. In B2, we see no evidence for power on shorter timescales in the ACF (Figure 3.8e–f).

The burst power spectra are presented in panel **c** of Figures 3.7–3.9. We perform a Bayesian maximum likelihood fit of a power law (red noise) plus constant (white noise) of the form

$$f(\nu) = A\nu^{-\alpha} + C, \tag{3.2}$$

where A is the amplitude, α is the slope of the power law, and C is a white noise component, to the power spectrum, using the Stingray modelling interface (Huppenkothen et al., 2019). Additionally, we fit a red noise plus white noise plus Lorentzian model to the data, to search for the presence of a quasi-periodic oscillation (QPO). This search was motivated by the hint of structure in the ACF of bursts from FRB 20180916B (Nimmo et al., 2021), and additionally, the low amplitude, wide frequency bump seen by eye in the downsampled power spectrum of burst B3 (Figure 3.7c). First, we compute the Bayesian Information Criterion for each model fit, defined as

$$\mathrm{BIC} = -2\ln(L) + k\ln(n), \tag{3.3}$$

where L is the maximum likelihood of the fit, k is the number of parameters in the model, and n is the number of data points. A lower BIC implies the data is better represented by that model, although it does not mean that the preferred model is a good fit to the data. Since the number of model parameters k is included in the BIC, models with more parameters are penalized to avoid overfitting the data. Here we computed the $\Delta\,\mathrm{BIC} = \mathrm{BIC}_{PL} - \mathrm{BIC}_{PL+lor}$, where BIC_{PL} is the BIC of the red noise model, and BIC_{PL+lor} is the BIC of the red noise plus QPO model. For B3, we measure a $\Delta\,\mathrm{BIC} = -12.1$, which is significantly in favor of the red noise model. We then measure the goodness-of-fit p-value of the red noise model, which is the fraction of 100 simulations (using the MCMC package `emcee`; Foreman-Mackey et al. 2013) with a maximum likelihood lower than the likelihood of our fit. This p-value is 0.53, implying the fit to the data is good. Finally, we test the significance of the highest outlier in the residuals of our best-fit model. The residuals are defined as

$$R(\nu) = \frac{2P(\nu)}{M(\nu)}, \tag{3.4}$$

for the power spectrum $P(\nu)$ and best-fit model $M(\nu)$. By simulating 100 power spectra from the posterior distribution (using `emcee`) and computing the highest outlier for each simulation, we can compute a p-value (the fraction of simulated outliers that are higher than our measured outlier). We find no significant outliers in the residuals, implying we have no evidence of a QPO in the data. The power spectra of B2 and B4 are also found to be consistent with red noise. A summary of the Δ BIC, red noise goodness-of-fit p-value with power law index, and p-value of outliers are presented in Table 3.3.

Table 3.3: High time resolution autocorrelation function and power spectra results.

Burst	Characteristic timescales [μs]	Red. χ^2 [a]	Power law index [b]	Δ Bayesian Information Criterion[c]	Goodness of fit p-value[d]	Outlier p-value[e]
B2	28.5 ± 0.2	2.0	1.85 ± 0.04	−20.5	0.50	0.98
B3	0.04 ± 0.3, 1.1 ± 0.4, 35.6 ± 0.5	2.4, 1.64, 1.3	1.46 ± 0.05	−12.1	0.53	0.99
B4	0.05 ± 0.02, 64.1 ± 1.5	2.7,1.9	2.04 ± 0.05	−15.4	0.66	0.97

[a] The reduced χ^2 of the Lorenzian fit to the high time resolution ACF in Figures 3.7–3.9.
[b] The power law index measured for the power spectra.
[c] Metric for model comparison (BIC for power law red noise model − BIC for power law plus Lorentzian).
[d] Goodness of fit of the best fit model.
[e] p-value of the highest outlier in the residuals of the power spectrum.

3.6 Supplementary Information

Fluence and luminosity

The burst profiles, in S/N units, are converted to physical units (flux density, Jy) using the radiometer equation (Cordes & McLaughlin, 2003), using typical values for Effelsberg's 1.4 GHz receiver temperature (20 K) and gain ($1.54\,\mathrm{Jy\,K^{-1}}$). We expect these system values to be accurate to within 20%, which dominates the errors on the peak flux density and fluence (note that the peak flux density depends strongly on the time resolution used, and the values reported in Table 3.1 are calculated using a time resolution of 8 μs). We additionally consider a sky background temperature of 0.8 K, by extrapolating from the 408 MHz map (Remazeilles et al., 2015), using a spectral index of −2.7 (Reich & Reich, 1988), and adding a 3 K contribution from the cosmic microwave background (Mather et al., 1994). For the 8 μs burst profiles, we report the peak S/N, peak flux density and fluence (measured in the $\pm 2\sigma$ width region) in Table 3.1. We also report the isotropic-equivalent spectral luminosity of the bursts, taking the distance to FRB 20200120E as 3.63 ± 0.34 Mpc (Kirsten et al., 2022).

Burst temporal extent and spectral structure

We performed a 2-dimensional Gaussian fit to the burst dynamic spectra (Figure 3.2), to determine the burst extents in time and frequency. The measured widths were clearly underestimated compared with what can be seen by eye in the dynamic spectra, likely since the bursts are not well-modelled by a 2-dimensional Gaussian function. In the case of B1, B3, B4, and B5 we use the Gaussian mean in time as the Time=0 reference in Figure 3.2, and use this to calculate the burst time of arrival corrected to the Solar System Barycenter at infinite frequency, reported in Table 3.1. For B2, since there are two clear burst components, we fit a 2-dimensional Gaussian to each and determined the Time=0 reference as the center of the means of those Gaussians. Note that we do not fit pulse broadening functions to estimate the scattering timescale since the estimated scattering timescale from the Milky Way ISM is ~ 50 ns ($<< 8$ μs) at 1.4 GHz (Cordes & Lazio, 2002), and is consistent with the frequency structure we attribute to scintillation (see below).

To more accurately determine the burst widths, we performed a 2-dimensional autocorrelation of the dynamic spectra, and fit these with 2-dimensional Gaussian functions (Figure 3.4).

Note the zero-lag noise spike is removed from this ACF. We convert the standard deviation of this Gaussian fit (in both time and frequency) to a full-width at half-maximum (FWHM) by multiplying the standard deviation by the factor $2\sqrt{2\ln(2)}$. We report the burst time width ($t_{wid} = 1/\sqrt{2} \times$ FWHM) and frequency extent ($\nu_{wid} =$ FWHM) in Table 3.1. In Figure 3.2, the colored bars below each burst profile indicate the $\pm 2\sigma$ width used for calculations of the fluence and polarization fractions.

In addition to the frequency extent measured with the 2-dimensional ACF, there is another, narrower frequency scale evident in the one-dimensional frequency ACF (or simply by eye in the dynamic spectra of the bright bursts). Shown in Figure 3.6a is the frequency ACF after subtracting the larger frequency scale Gaussian. We perform a least-squares fit of a Lorentzian function to the center of this ACF (defined by eye using the clearly visible central feature in the ACF; Figure 3.6a). A Lorentzian frequency ACF is expected for scintillation (Rickett, 1990). The fit function is of the form

$$\frac{a}{x^2 + \nu_{\rm scale}^2} + b, \tag{3.5}$$

where a is the amplitude, b is a vertical offset, and $\nu_{\rm scale}$ is the scintillation bandwidth (defined as the half-width at half-maximum of the ACF; Rickett 1990). The scintillation bandwidth measurements are reported in Table 3.1. The Galactic ISM is expected to introduce a broadening due to scattering of $\sim$ 50 ns (at 1.4 GHz) along this line-of-sight (Cordes & Lazio, 2002), in rough agreement with our measured scintillation bandwidth ($1/(2\pi\Delta\nu_{\rm scint}) \sim 27$ ns). We therefore attribute this narrower spectral structure to scintillation from the Milky Way ISM. This interpretation is supported by the stronger correlation in the spectrum of two bursts (B1 and B2) separated by 4.3 minutes, compared to the lack of correlation between bursts B3 and B4, which are separated by 2.5 hrs (Figure 3.14). The expected scintillation time is $\sim$ 10 minutes (at 1.4 GHz) at high Galactic latitudes, which is dependent on an effective velocity (the assumption for Galactic sources is 100 km s^{-1}; Cordes & Lazio 1991, 2002). This effective velocity is likely smaller for an extragalactic source than for a Galactic pulsar in the same line of sight, since the effective velocity is usually dominated by the velocity of the pulsar. Assuming an effective velocity of $\sim$ 30 km s^{-1}, the expected scintillation time will be $\sim$ 30 minutes (at 1.4 GHz), consistent with the decorrelation timescale constraints using FRB 20200120E.

Polarization calibration

To study the polarization properties of the bursts, we must first calibrate the data. In these observations, we did not record a noise diode scan to use for delay calibration; instead, we use the test pulsar data, also taken to inspect the general data quality, to calibrate the polarimetric data. This analysis strategy has been used successfully in previous work to determine the polarimetric properties of radio bursts from the Galactic magnetar SGR 1935+2154, detected using voltage data of the Westerbork RT1 VLBI backend (Kirsten et al., 2021b), and also in a study of the repeating FRB 20180916B, using data from the Effelsberg telescope as part of an EVN campaign (Nimmo et al., 2021). Since we detected bursts on separate epochs, we calibrate the data using the test pulsar scan closest in time to the bursts. B1 and

B2 are $<$ 1 hr from the PSR B0355+54 calibration scan, and B3 and B4 are $\sim$ 4 hr and $<$ 2 hr from the PSR B0355+54 scan, respectively. We note that we could not recover the polarimetric properties of burst B5 likely due to the low S/N of the burst, and so the April 28 epoch is omitted from the remainder of this section.

The data could exhibit leakage between the polarization channels, which we assume only significantly affects Stokes V (defined as V=LL−RR using the PSR/IEEE convention; van Straten et al. 2010). In the pulsar data, without calibrating the leakage, we reproduce the circular polarization fraction to within 3% and 1% of the published values (Gould & Lyne, 1998), for the Feb 20 and Mar 7 epochs, respectively. We, therefore, apply no leakage calibration.

A delay between the polarization hands is more crucial to correct for since it can significantly impact our interpretation of the linear polarization fraction and RM. Using the known RM of PSR B0355+54, 79 rad m^{-2} (Taylor et al., 1993), we performed a brute-force search for the delay between polarization hands, D, that maximises the linear polarization, by rotating the data using the factor

$$\mathrm{e}^{-2i\mathrm{RM}(c^2/\nu^2)}\mathrm{e}^{-2i\nu\pi D}, \tag{3.6}$$

where c is the speed of light and ν is the frequency in Hz. We searched for delays between -15 and 15 ns, in steps of 0.01 ns. Note that previous work with the VLBI recorder at Effelsberg showed an instrumental delay of 5.4 ns (Nimmo et al., 2021). The estimated delays are -0.18 ns and -4.11 ns for the Feb 20 and Mar 7 observations, respectively.

After removing the effect of the estimated delays, we performed RM synthesis (Brentjens & de Bruyn, 2005) on the burst data to estimate the RMs of the bursts. The Faraday spectra for each burst are shown in Figure 3.5a.

To refine the RM and delay measurements further, we performed a joint least squares fit of Stokes Q and U spectra normalised by the linear polarization L= $\sqrt{\mathrm{Q}^2+\mathrm{U}^2}$, using the following equations

$$Q/L = \cos(2(c^2\mathrm{RM}/\nu^2 + \nu\pi D + \phi)), \tag{3.7}$$

$$U/L = \sin(2(c^2\mathrm{RM}/\nu^2 + \nu\pi D + \phi)), \tag{3.8}$$

where ϕ is a linear combination of the absolute angle of polarisation on the sky (referenced to infinite frequency) and the phase difference between the R and L polarisation channels. The estimates of the delay and RM are given as initial guesses to the fit, and we simultaneously fit the pulsar and the two bursts from the same observational epoch. We force the delay to be the same between the pulsar and FRB data, fix to the known RM of the pulsar (79 rad m^{-2}), and initially we allow for a different RM per burst. The measured delays are -0.22 ± 0.02 ns and -4.16 ± 0.03 ns, for the Feb 20 and Mar 7 observations, respectively, and the measured RMs are presented in Table 3.2. The QU-fits are shown in Figure 3.5. The measured RMs have large uncertainties due to covariances between the fit parameters, which is difficult to alleviate due to the low number of rotations (due to either RM or delay) across the burst frequency extent. We conclude that the bursts in this work have consistent RM values (B2's

RM is slightly over 3σ from B3, but this apparent difference should be verified in future observations of this source using an independent delay calibrator), which is also in agreement with the previously reported RM ($-29.8\,\mathrm{rad\,m^{-2}}$; Bhardwaj et al. 2021a). We note that neither this work nor Bhardwaj et al. (2021a) correct for the ionospheric contribution to the RM, but this effect is likely to be $\lesssim 2\,\mathrm{rad\,m^{-2}}$.

The data for each burst were then corrected for the measured delay and RM. The polarization position angle (PPA) was calculated using the following equation:

$$\mathrm{PPA} = 0.5 \arctan\left(\frac{U}{Q}\right), \tag{3.9}$$

and, to correct for the parallactic angle, this is rotated by

$$\theta = 2\tan^{-1}\left(\frac{\sin(\mathrm{HA})\cos(\phi_{\mathrm{lat}})}{(\sin(\phi_{\mathrm{lat}})\cos(\delta) - \cos(\phi_{\mathrm{lat}})\sin(\delta)\cos(\mathrm{HA})}\right), \tag{3.10}$$

where HA is the hour angle of the burst, ϕ_{lat} is the latitude of the Effelsberg telescope, and δ is the declination of FRB 20200120E. Due to the fact that our observations did not feature an independent polarization calibrator scan, there remains an uncalibrated absolute phase offset in the data. Therefore, we cannot compare the PPAs between our two observational epochs, or with other PPA measurements of FRB 20200120E. By allowing for individual RM values per burst, we find that B1 and B2 exhibit a ΔPPA of 28.5°, and the ΔPPA between B3 and B4 is 21.7°. The unbiased linear polarization is computed following Everett & Weisberg (2001), where

$$L_{\mathrm{unbias}} = \begin{cases} \sigma_I \sqrt{\left(\frac{L_{\mathrm{meas}}}{\sigma_I}\right)^2 - 1}, & \text{if } \frac{L_{\mathrm{meas}}}{\sigma_I} \geq 1.57 \\ 0, & \text{otherwise} \end{cases} \tag{3.11}$$

where $L_{\mathrm{meas}} = \sqrt{Q^2 + U^2}$, and σ_I is the standard deviation in the off-burst Stokes I data.

Bursts B1 – B4 are highly linearly polarized ($> 90\%$), and exhibit little-to-no evidence for circular polarization. There is a tentative $3 - 4\,\sigma$ detection of 13 % and 6 % circular polarization in B2 and B4, respectively. The linear and circular fractions, as well as the PPA offset from a weighted mean PPA of bursts from a single epoch, are presented in Table 3.2, and the polarization profile and PPA for each burst is shown in Figure 3.2.

It has been seen in the literature that some repeating FRBs exhibit a constant PPA ($\Delta(\mathrm{PPA}) < 10^\circ$) and RM per observing epoch (Michilli et al., 2018b; Nimmo et al., 2021). Therefore, in addition to the individual burst RM measurements, we fit for a global RM per observing epoch. In this global fit, we find that the PPA of B1 and B2 differ by 68.3° (Table 3.2). This large ΔPPA may result from the low S/N of burst B1. The ΔPPA between B3 and B4 in this global fit is 23.6°, comparable to the difference we measured in the independent-RM fit above, unsurprising given the very similar RM values in the independent fits.

Acknowledgements

We thank W. van Straten for help with digifil. The European VLBI Network is a joint facility of independent European, African, Asian, and North American radio astronomy institutes. Scientific results from data presented in this publication are derived from the following EVN project code: EK048. This project has received funding from the European Union's Horizon 2020 research and innovation programme under grant agreements No 730562 (RadioNet) and 101004719 (OPTICON-RadioNet Pilot). A.B.P is a McGill Space Institute (MSI) Fellow and a Fonds de Recherche du Quebec - Nature et Technologies (FRQNT) postdoctoral fellow. B.M. acknowledges support from the Spanish Ministerio de Economía y Competitividad (MINECO) under grant AYA2016-76012-C3-1-P and from the Spanish Ministerio de Ciencia e Innovación under grants PID2019-105510GB-C31 and CEX2019-000918-M of ICCUB (Unidad de Excelencia "María de Maeztu" 2020-2023). C.L. was supported by the U.S. Department of Defense (DoD) through the National Defense Science & Engineering Graduate Fellowship (NDSEG) Program. D.M. is a Banting Fellow. E.P. acknowledges funding from an NWO Veni Fellowship. F.K. acknowledges support from the Swedish Research Council. FRB research at UBC is supported by an NSERC Discovery Grant and by the Canadian Institute for Advanced Research. J.P.Y. is supported by the National Program on Key Research and Development Project (2017YFA0402602). K.S. is supported by the NSF Graduate Research Fellowship Program. K.W.M. is supported by an NSF Grant (2008031). M.B. is supported by an FRQNT Doctoral Research Award. N.W. acknowledges support from the National Natural Science Foundation of China (Grant 12041304 and 11873080). P.S. is a Dunlap Fellow and an NSERC Postdoctoral Fellow. The Dunlap Institute is funded through an endowment established by the David Dunlap family and the University of Toronto. V.B. acknowledges support from the Engineering Research Institute Ventspils International Radio Astronomy Centre (VIRAC). Research by the AstroFlash group at University of Amsterdam, ASTRON and JIVE is supported in part by an NWO Vici grant (PI Hessels; VI.C.192.045).

Chapter 4

A burst storm from the repeating FRB 20200120E in an M81 globular cluster

K. Nimmo, J. W. T. Hessels, M. P. Snelders, R. Karuppusamy, D. M. Hewitt, F. Kirsten, B. Marcote, U. Bach, A. Bansod, E. D. Barr, J. Behrend, V. Bezrukovs, S. Buttaccio, R. Feiler, M. P. Gawroński, M. Lindqvist, A. Orbidans, W. Puchalska, N. Wang, T. Winchen, P. Wolak, J. Wu, and J. Yuan

Submitted to Monthly Notices of the Royal Astronomical Society

Abstract

The repeating fast radio burst (FRB) source FRB 20200120E is exceptional because of its proximity ($d = 3.6$ Mpc) and association with a globular cluster. Here we report 60 bursts detected with the 100-m Effelsberg telescope at 1.4 GHz. We observe large variations in the burst rate, and report the first FRB 20200120E 'burst storm', where the source suddenly became active and 53 bursts occurred within only 40 minutes. We find no strict periodicity in the burst arrival times during the storm, nor any evidence for periodicity in the source's activity between observations. The burst storm shows a steep burst energy distribution (power-law index $\alpha = 2.39 \pm 0.12$) and a bi-modal wait-time distribution, with log-normal means of $0.94^{+0.07}_{-0.06}$ s and $23.61^{+3.06}_{-2.71}$ s. We attribute these peaks in the wait-time distribution to a characteristic event timescale and pseudo-Poisson burst rate, respectively. The secondary wait-time peak at ~ 1 s is $\sim 50\times$ longer than the ~ 30 ms timescale seen for both FRB 20121102A and FRB 20201124A — potentially indicating a larger emission region, or slower burst propagation through this region. At the same time, FRB 20200120E shows, on average, order-of-magnitude lower burst durations and luminosities compared with FRB 20121102A and FRB 20201124A. Lastly, in contrast to FRB 20121102A, which has observed dispersion measure (DM) variations of $\Delta\mathrm{DM} > 1\,\mathrm{pc\,cm^{-3}}$ on month-to-year timescales, we determine that the DM of FRB 20200120E has remained stable ($\Delta\mathrm{DM} < 0.15\,\mathrm{pc\,cm^{-3}}$) between measurements separated by > 10 months. Overall, the observational characteristics of

FRB 20200120E deviate quantitatively from other active repeaters, but it is unclear whether it is qualitatively a different type of source.

4.1 Introduction

Fast radio bursts (FRBs) are highly luminous, millisecond-duration radio transients, originating at extragalactic distances (Lorimer et al., 2007; Thornton et al., 2013). Despite 15 years of research in the field (for recent reviews see, e.g., Petroff et al. 2019, 2022; Cordes & Chatterjee 2019), and more than 600 FRBs discovered to date (e.g., CHIME/FRB Collaboration et al. 2021), their nature is still debated. The diverse burst phenomenology (Pleunis et al., 2021a), including a relatively small fraction ($\sim$ 4%) of FRB sources exhibiting repeating bursts (Spitler et al., 2016), potentially indicates multiple FRB origins. Athough FRBs are highly luminous, their large extragalactic distances (typically hundreds of megaparsecs to gigaparsecs) mean that we are strongly sensitivity limited, and therefore only observe the bright end of the distribution of potentially observable fast radio transients.

FRBs in the local Universe (luminosity distance $d_L <$ a few hundred Mpc) provide us with the unique opportunity to connect our knowledge of fast radio transients in the Milky Way and its satellites — e.g., the Crab pulsar (Hankins & Eilek, 2007), the 'Crab twin' in the Large Magellanic Cloud PSR B0540−69 (Geyer et al., 2021) and the Galactic magnetar SGR 1935+2154 (CHIME/FRB Collaboration et al., 2020; Bochenek et al., 2020) — to the much more distant FRB population. We can do this through detailed characterisation of their local environments (e.g., Marcote et al. 2020; Tendulkar et al. 2021; Kirsten et al. 2022), by applying strong constraints on multi-wavelength counterparts to the radio emission (Scholz et al., 2020), and by conducting higher-sensitivity searches for low-luminosity FRBs (Kirsten et al., 2022; Nimmo et al., 2022a; Majid et al., 2021).

The closest known extragalactic FRB discovered to date, FRB 20200120E (Bhardwaj et al., 2021a), was discovered by the Canadian Hydrogen Intensity Mapping Experiment FRB project (CHIME/FRB; CHIME/FRB Collaboration et al. 2018) and subsequently precisely localised using the European Very long baseline interferometry (VLBI) Network (EVN) to a globular cluster in the M81 galactic system (Kirsten et al., 2022). Not only is the globular cluster origin of FRB 20200120E in stark contrast to the star-forming environments of other well-studied repeating FRBs (Chatterjee et al., 2017; Marcote et al., 2017; Bassa et al., 2017; Marcote et al., 2020; Tendulkar et al., 2021; Nimmo et al., 2022b; Fong et al., 2021; Ravi et al., 2022), but the luminosities of the bursts are 1–2 orders of magnitude weaker than those observed from other repeaters, and even less luminous than the bright FRB-like transient from SGR 1935+2154 (CHIME/FRB Collaboration et al., 2020; Bochenek et al., 2020). Furthermore, the FRB 20200120E burst widths are atypically narrow (a factor of $\sim$ 30 shorter than typical FRB 20121102A bursts at a comparable frequency; Nimmo et al. 2022a; Majid et al. 2021; Li et al. 2021).

Nimmo et al. (2022a) discuss the observational connections between FRB 20200120E, the Crab pulsar, the Galactic magnetar SGR 1935+2154, and the more distant FRBs using the measured luminosities, range of burst timescales, burst morphologies, and polarimetry. In doing so, they highlight the spectrum of short-duration radio emission spanning many orders of magnitude in luminosity and timescales, and emphasise that the exact division between transient types (e.g., pulsar and FRB emission) is presently unclear.

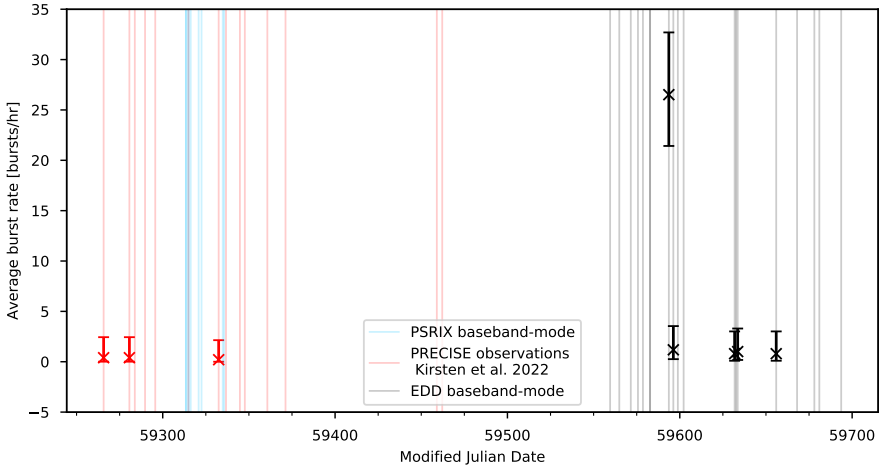

Figure 4.1: Summary of the observations of FRB 20200120E presented in this work, in addition to those reported in Kirsten et al. (2022) and Nimmo et al. (2022a). The coloured lines show the observation epochs (where colour signifies the observation type, as described in Section 4.2). The cross markers show the average burst rate per observing epoch, unless there were no detections. For a tabular version of this information, see Table 4.1.

To date, only 14 bursts from FRB 20200120E have been reported in the literature (Bhardwaj et al., 2021a; Nimmo et al., 2022a; Majid et al., 2021)[1]. A larger sample of bursts from FRB 20200120E provides the ability to probe its time-variable activity, search for any underlying periodicity and study the energy and wait-time distributions to compare with similar studies of Galactic neutron stars, and other repeating FRBs.

Here we report the detection of 60 new bursts from FRB 20200120E, detected via monitoring with the 100-m Effelsberg telescope at 1.4 GHz from 2021 April to 2022 April. During this monitoring, we report the first observed 'burst storm' from FRB 20200120E where 53 of the 60 bursts occurred within a $\sim$ 40 minute time window. In Section 4.2 we describe the Effelsberg monitoring observations, and the data products. In Section 4.3 we describe the search for bursts, followed by a description of the burst analysis and results in Section 4.4. In Section 4.5, we discuss our results in the context of previous FRB observations, and compare with observations of Galactic neutron stars, before presenting the conclusions of this work in Section 4.6.

4.2 Observations

Between December 11 2021 and April 24 2022, we monitored FRB 20200120E (using the EVN-PRECISE[2] position; Kirsten et al. 2022) with the 100-m Effelsberg telescope using the recently developed Effelsberg Direct Digitization (EDD) backend operating in baseband-

[1] Additional CHIME/FRB bursts are reported on in the CHIME/FRB public database.
[2] Pinpointing Repeating Chime Sources with the EVN

mode. This allowed us to simultaneously record total intensity pulsar backend psrfits (Hotan et al., 2004) data with time and frequency resolution of 40.96 μs and 0.1953 MHz, respectively (exceptions to this are noted in Table 4.1), alongside the raw voltages ('baseband' data, dual circular polarisation) in Data Acquisition and Distributed Analysis (DADA) format (van Straten et al., 2021) sampled at 1/400 MHz. We used the central pixel of the 7-beam 21-cm receiver, with an observing bandwidth from 1.2–1.6 GHz. In total, we have observed for 28.4 hr using this observing setup, which is summarised in Table 4.1. We recorded psrfits data of the test pulsar B0355+54. Due to an incorrect observing set-up, the raw voltages of 2022 February 21 and 22 (MJDs 59631, 59632) were not recorded.

We add the EVN-PRECISE observations originally reported in Kirsten et al. (2022) and Nimmo et al. (2022a) to Table 4.1, with an additional three PRECISE observations using the VLBI backend that occurred on 2021 June 6, September 2 and September 5. Using the VLBI Digital Base Band Converter (DBBC2; Tuccari et al. 2010) backend at Effelsberg, these observations recorded baseband data with dual circular polarisation (2-bit sampling) in VDIF (Whitney et al., 2010) format. Additionally, we recorded total intensity filterbank data with the PSRIX pulsar backend (Lazarus et al., 2016) with a time and frequency resolution of 102.4 μs and 0.49 MHz, respectively. The observing bandwidth is 1255–1505 MHz and the total observing time using this observing setup is 63.6 hr (all but 12.1 hr originally reported in Kirsten et al. 2022 and Nimmo et al. 2022a). Note that these are VLBI observations, and therefore had frequent scans of calibrator sources. In such cases, the time on source is therefore approximately 65 % of the reported times.

Furthermore, we also report on observations obtained through Director's Discretionary Time at Effelsberg between 2021 April 9 and 2021 May 1. These observations were using the PSRIX pulsar backend in baseband-mode: recording total intensity filterbank data products with time and frequency resolution of 65.5 μs and 0.24 MHz, respectively, simultaneously with the raw voltages (dual circular). The observing bandwidth is 1233–1483 MHz, and total observing time with this setup is 13.7 hr.

All of the observations are summarised in Table 4.1 and Figure 4.1.

4.3 Burst search and discovery

4.3.1 EDD baseband-mode

The total intensity EDD psrfits data were first converted to filterbank format using digifil (van Straten & Bailes, 2011), at the native resolution of the data, to be compatible with Heimdall[3]. Frequency channels in our observing band that frequently contain radio frequency interference (RFI) were masked before searching for single pulses with Heimdall, using a S/N threshold of 7. Candidates found in the Heimdall search were then classified using FETCH (models A and H, probability threshold 0.5; Agarwal et al. 2020). We inspected the FETCH candidate plots by eye, and also the plots of any Heimdall candidate within $\pm 3\,\mathrm{pc\,cm^{-3}}$ of the known FRB dispersion measure (DM) and above a S/N threshold of 10.

[3] https://sourceforge.net/projects/heimdall-astro/

Table 4.1: FRB 20200120E Effelsberg monitoring observation details.

Start MJD[a]	Duration [hr]	Observation type	Number of bursts	Average burst rate [/hr]
59265.708[b]	4.99	PRECISE, VLBI backend	2	$0.4^{+2.0}_{-0.4}$
59280.656[b]	4.99	PRECISE, VLBI backend	2	$0.4^{+2.0}_{-0.4}$
59283.792[b]	4.99	PRECISE, VLBI backend	0	$0.0^{+1.8}_{-0.0}$
59289.750[b]	4.99	PRECISE, VLBI backend	0	$0.0^{+1.8}_{-0.0}$
59295.667[b]	4.99	PRECISE, VLBI backend	0	$0.0^{+1.8}_{-0.0}$
59313.437	0.07	PSRIX baseband-mode	0	$0.0^{+1.8}_{-0.0}$
59313.458	1.00	PSRIX baseband-mode	0	$0.0^{+1.8}_{-0.0}$
59314.508	2.21	PSRIX baseband-mode	0	$0.0^{+1.8}_{-0.0}$
59314.887[b]	2.04	PRECISE, VLBI backend	0	$0.0^{+1.8}_{-0.0}$
59315.191	0.89	PSRIX baseband-mode	0	$0.0^{+1.8}_{-0.0}$
59316.235	1.17	PSRIX baseband-mode	0	$0.0^{+1.8}_{-0.0}$
59320.828	2.22	PSRIX baseband-mode	0	$0.0^{+1.8}_{-0.0}$
59322.514	2.00	PSRIX baseband-mode	0	$0.0^{+1.8}_{-0.0}$
59332.458[b]	4.99	PRECISE, VLBI backend	1	$0.2^{+1.9}_{-0.2}$
59334.807	2.08	PSRIX baseband-mode	0	$0.0^{+1.8}_{-0.0}$
59335.634	2.01	PSRIX baseband-mode	0	$0.0^{+1.8}_{-0.0}$
59336.708[b]	7.01	PRECISE, VLBI backend	0	$0.0^{+1.8}_{-0.0}$
59344.771[b]	2.50	PRECISE, VLBI backend	0	$0.0^{+1.8}_{-0.0}$
59347.625[b]	4.99	PRECISE, VLBI backend	0	$0.0^{+1.8}_{-0.0}$
59360.708[b]	4.99	PRECISE, VLBI backend	0	$0.0^{+1.8}_{-0.0}$
59371.234	2.48	PRECISE, VLBI backend	0	$0.0^{+1.8}_{-0.0}$
59459.027	4.50	PRECISE, VLBI backend	0	$0.0^{+1.8}_{-0.0}$
59462.168	5.11	PRECISE, VLBI backend	0	$0.0^{+1.8}_{-0.0}$
59559.584[c]	2.00	EDD baseband-mode	0	$0.0^{+1.8}_{-0.0}$
59564.902	2.00	EDD baseband-mode	0	$0.0^{+1.8}_{-0.0}$
59571.573	2.00	EDD baseband-mode	0	$0.0^{+1.8}_{-0.0}$
59575.735	1.38	EDD baseband-mode	0	$0.0^{+1.8}_{-0.0}$
59578.622	2.00	EDD baseband-mode	0	$0.0^{+1.8}_{-0.0}$
59582.677	0.20	EDD baseband-mode	0	$0.0^{+1.8}_{-0.0}$
59582.785	0.50	EDD baseband-mode	0	$0.0^{+1.8}_{-0.0}$
59593.650	2.00	EDD baseband-mode	53	$26.5^{+6.2}_{-5.1}$
59596.262	0.85	EDD baseband-mode	1	$1.2^{+2.4}_{-0.9}$
59598.871	2.50	EDD baseband-mode	0	$0.0^{+1.8}_{-0.0}$
59602.235	0.03	EDD baseband-mode	0	$0.0^{+1.8}_{-0.0}$
59631.818[d]	2.50	EDD baseband-mode	2	$0.8^{+2.2}_{-0.7}$
59632.673[d]	2.15	EDD baseband-mode	0	$0.0^{+1.8}_{-0.0}$
59633.599	1.99	EDD baseband-mode	2	$1.0^{+2.3}_{-0.8}$
59655.950	2.50	EDD baseband-mode	2	$0.8^{+2.2}_{-0.7}$
59668.052	0.78	EDD baseband-mode	0	$0.0^{+1.8}_{-0.0}$
59678.079	1.36	EDD baseband-mode	0	$0.0^{+1.8}_{-0.0}$
59680.974	1.65	EDD baseband-mode	0	$0.0^{+1.8}_{-0.0}$
59693.655	0.85	EDD baseband-mode	0	$0.0^{+1.8}_{-0.0}$

[a] Topocentric.
[b] Originally reported in Kirsten et al. (2022) and Nimmo et al. (2022a).
[c] Frequency resolution of these data is 0.4 MHz.
[d] No raw voltages due to incorrect observing set-up.

In this search, we found 37 bursts on 2022 January 14 (MJD 59593), 1 burst on 2022 January 17 (MJD 59596), and 2 bursts on each of 2022 February 21, 23 and March 17 (MJDs 59631, 59633, and 59655, respectively). On closer inspection of the Heimdall candidates on 2022 January 14 (pre-FETCH), with DMs $\pm 1\,\mathrm{pc\,cm^{-3}}$ around the best-known value of $87.7527\,\mathrm{pc\,cm^{-3}}$ (Nimmo et al., 2022a), an additional 7 bursts were discovered. These bursts were all reported with relatively low Heimdall S/N values of < 10. Therefore the low S/N, combined with the narrow temporal burst widths, are likely the cause of the misclassification by FETCH. A similar exercise was repeated on the other observations, and no additional bursts were discovered. Note that post 2022 January 14, we altered the analysis pipeline to keep candidate plots for inspection for any Heimdall candidate within $\pm 3\,\mathrm{pc\,cm^{-3}}$ of the known FRB DM and above a S/N threshold of 7.

Due to the high density of bursts discovered on 2022 January 14, we saved the raw voltages for the entire 2 hr observation for further inspection. This was not possible for all observations due to the high data volume of the raw voltages (1 hr is approximately 5.5 TB of raw voltage data). Therefore, for the bursts discovered at other epochs, we saved only the 2.048 s baseband recording containing the burst (and sometimes also the neighbouring recording if the dispersion sweep crossed between recordings).

Table 4.2: The success of burst searches on 2022 January 14 EDD data. ✓ indicates that a burst was classified as astrophysical by FETCH (models A and H, probability threshold 0.5).

	40.96 µs pulsar		40.96 µs baseband		1.28 µs baseband
Burst	Heimdall S/N	FETCH	Heimdall S/N	PRESTO S/N	PRESTO S/N
B1	13.6	✓	12.4	13.4	9.3
B2	36.6	✓	Lost baseband data		
B3	12.8	✓	10.8	10.8	–
B4	7.9	–	7.5	8.6	–
B5	21.6	✓	17.8	21.6	9.6
B6	–	–	7.3	–	–
B7	8.7	✓	8.7	9.6	–
B8	9.3	✓	8.4	10.3	–
B9	8.4	✓	7.6	8.7	–
B10	20.2	✓	19.0	20.6	12.9
B11	7.8	✓	–	8.7	–
B12	16.7	✓	16.5	17.9	14.7
B13	20.8	✓	16.7	18.6	14.5
B14	–	–	9.7	10.9	8.7
B15	–	–	–	–	7.7
B16	7.2	–	7.7	8.0	7.0
B17	24.7	✓	22.3	25.0	17.2
B18	–	–	11.9	13.1	10.6
B19	–	–	7.0	7.8	9.6
B20	19.8	✓	18.8	21.7	16.3
B21	17.2	✓	14.2	17.2	15.4

Continued: Burst search results

B22	7.6	✓	–	7.2	–
B23	11.0	✓	9.0	10.5	9.8
B24	10.2	✓	9.1	10.3	7.4
B25	7.6	✓	–	–	–
B26	17.0	✓	15.1	16.2	14.6
B27	7.1	✓	–	7.4	–
B28	8.9	–	–	–	7.1
B29	8.1	✓	7.7	8.5	–
B30	–	–	–	8.0	–
B31	22.5	✓	21.1	24.3	18.3
B32	–	–	–	7.8	9.0
B33	25.2	✓	19.4	26.4	15.3
B34	16.2	✓	14.4	17.3	17.3
B35	21.8	✓	19.8	22.2	15.2
B36	8.9	–	7.4	7.9	7.2
B37	20.7	✓	19.8	23.0	25.4
B38	9.5	✓	7.1	11.0	9.5
B39	7.7	✓	–	–	–
B40	12.9	✓	10.4	11.4	10.0
B41	9.2	–	7.4	9.0	8.0
B42	8.6	–	7.0	8.0	9.2
B43	21.6	✓	19.5	23.3	15.0
B44	15.1	✓	12.4	14.2	12.8
B45	7.1	✓	–	–	–
B46	–	–	–	7.2	7.1
B47	20.6	✓	16.8	21.0	18.7
B48	10.8	✓	9.0	11.5	9.4
B49	14.5	✓	12.1	17.1	16.9
B50	14.0	✓	14.5	17.6	18.1
B51	8.2	✓	–	9.0	8.7
B52	7.7	–	–	9.2	–
B53	–	–	–	9.7	–

4.3.1.1 January 14 baseband data re-search

Using digifil, we created 8-bit total intensity filterbank data from the baseband DADA data at a resolution of 40.96 μs and 0.1953 MHz in time and frequency, respectively. This resolution matches that of the pulsar data. The goal of searching these data products was to ensure that we understood the filterbank data created and could recover the same bursts discovered in the search of the pulsar data. These data products were searched for single pulses using both Heimdall and PRESTO (Ransom, 2001). For the Heimdall-based search, we mask frequency

channels that frequently exhibit RFI before searching for single pulses, and inspect the candidates with a DM within $\pm 1\,\mathrm{pc\,cm^{-3}}$ of the known DM of FRB 20200120E. For PRESTO-based searches, we use the PRESTO tool rfifind to mask time and frequency blocks that contain RFI before searching for single pulses using single_pulse_search.py. The PRESTO single-pulse candidates were then grouped into events using a modified version of SpS (Michilli et al., 2018a), and events with a DM within $\pm 1\,\mathrm{pc\,cm^{-3}}$ of the known DM were inpected by eye.

The Heimdall search of the baseband data returned 34 of the 44 bursts found in the pulsar data: 9 of those missing all have S/N < 9, and 1 (B2) falls within a ~ 4 minute gap in the baseband data where we have missing data. The loss of some low-S/N bursts in the baseband search is likely because of different scalings applied in the creation of the filterbank data. We did, however, find 4 previously undiscovered bursts in the Heimdall search of the baseband data. These bursts also have relatively low S/N, and likely were missed in the search of the pulsar data for the same reasons as above.

The PRESTO search of the baseband data returned 39 of the original 44 bursts, where, again, B2 falls within the data loss region. The other missing 4 bursts are a subset of the missing bursts in the Heimdall search. Of the 4 *new* Heimdall-discovered bursts, PRESTO found 3. Furthermore, PRESTO discovered an additional 4 low-S/N bursts, bringing the number of bursts discovered in the 2022 January 14 observation to 52. In general, the PRESTO S/N values appear higher than Heimdall, which is likely how PRESTO found additional bursts that Heimdall missed above our detection threshold of 7. Additionally, the RFI flagging method and boxcar width trialling is different between the Heimdall and PRESTO searches, which could impact the discovery of bursts, especially in the low-S/N regime. Note there is a timestamp mislabelling in the pulsar backend data, creating a fictitious 125 ms delay between the baseband recording and pulsar backend recording. This was identified, measured and calibrated for using bursts detected in both the pulsar and baseband data.

4.3.1.2 January 14 1.28 μs search

Motivated by the clear microsecond timescales seen in a burst from FRB 20200120E (Nimmo et al., 2022a), we re-searched the 2022 January 14 observation at 1.28 μs time resolution. We used digifil to create coherently dedispersed (using a DM of $87.7527\,\mathrm{pc\,cm^{-3}}$; Nimmo et al. 2022a) 8-bit total intensity filterbank data with time and frequency resolution 1.28 μs and 0.78 MHz, respectively. The true DM value must be within $\sim 0.3\,\mathrm{pc\,cm^{-3}}$ of the DM used for coherent dedispersion to ensure that the dispersion smearing within a channel is smaller than the time resolution. Fortunately, $0.3\,\mathrm{pc\,cm^{-3}}$ is much greater than the uncertainty on the known DM (Nimmo et al., 2022a), and we confirm in Section 4.4 that the DM has not significantly changed from the previous measurement.

The Heimdall search of the 1.28 μs data returned none of the 52 bursts, and no additional bursts. For the PRESTO-based search, we incoherently dedispersed using trial DMs from 87.6 to $87.9\,\mathrm{pc\,cm^{-3}}$ in steps of $0.01\,\mathrm{pc\,cm^{-3}}$. This results in maximal DM step-size smearing of ~ 6 μs across the entire 400 MHz band, or ~ 3 μs for the centre 200 MHz, where the bursts in our sample reside. We, therefore, downsample to 2.56 μs for the search. The PRESTO search

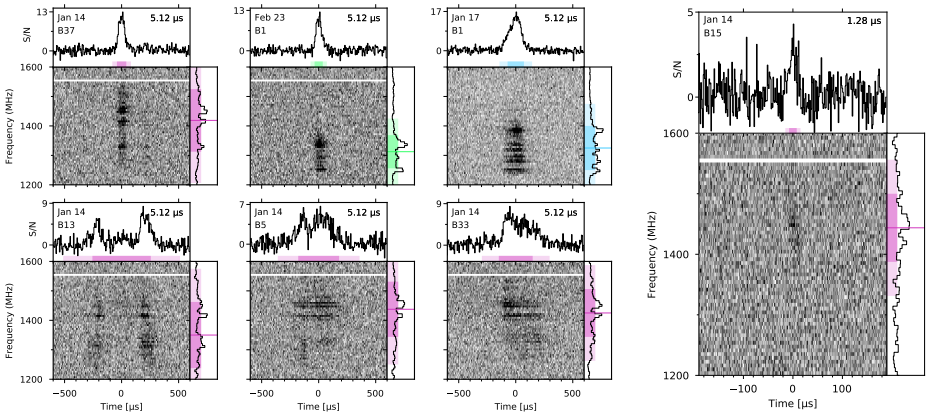

Figure 4.2: Burst profiles, dynamic spectra and time-averaged spectra for a subset of the FRB 20200120E bursts presented in this work. The filterbank data plotted is created by channelising the raw voltages to a resolution of 5.12 µs and 0.1953 MHz in time and frequency, respectively, for sub-figure (a), and 1.28 µs and 0.7813 MHz for sub-figure (b). Sub-figure (b) shows the burst discovered in the microsecond search of the data (see Section 4.3.1.2); this is the narrowest burst in this sample. The frequency resolution has been downsampled by a factor of 32 (sub-figure (a)) and 8 (sub-figure (b)) for visualisation purposes. The data are coherently (within frequency channels) and incoherently (between channels) corrected for dispersion using a DM of 87.7527 pc cm^{-3} (Nimmo et al., 2022a). The coloured bars highlight the 1-σ (dark) and 2-σ (light) error regions on the burst extent in both frequency and time, where the different colours represent different observing epochs: 2022 January 14 (purple), 2022 January 17 (blue) and 2022 February 23 (green). Time = 0 represents the burst centroid in time, and the horizontal coloured line in the burst spectrum represents the frequency centroid. Frequency channels that have been masked due to RFI have been omitted from the dynamic spectra (white horizontal lines). The burst profile is created by averaging the dynamic spectrum within the 2-σ burst extent in frequency, and similarly the burst spectrum is created by averaging the dynamic spectrum within the 2-σ burst extent in time.

returned 35 of the 52, and discovered an additional burst, bringing the **total burst count** to 53 on 2022 January 14. The additional burst found in our high-time-resolution search is the narrowest burst in our sample, with a temporal scale of $\sim$ 14 µs, which combined with its low S/N is the reason it was not caught in either of the 40.96 µs searches. The behaviour of Heimdall is not well-studied at extremely high time resolutions (e.g. µs) and the fact that we recover a significant fraction of the bursts using PRESTO, implies that Heimdall has significantly lost sensitivity at this resolution.

Table 4.2 summarises the results of the searches on the 2022 January 14 observation. The burst profiles, dynamic spectra and time-averaged spectra for selected FRB 20200120E bursts can be found in Figure 4.2, highlighting the diverse burst morphology observed including the exceptionally narrow $\sim$ 14 µs burst. In Figures 4.3 and 4.4 we show the complete time-ordered burst plot for the entire 60 burst sample presented in this work.

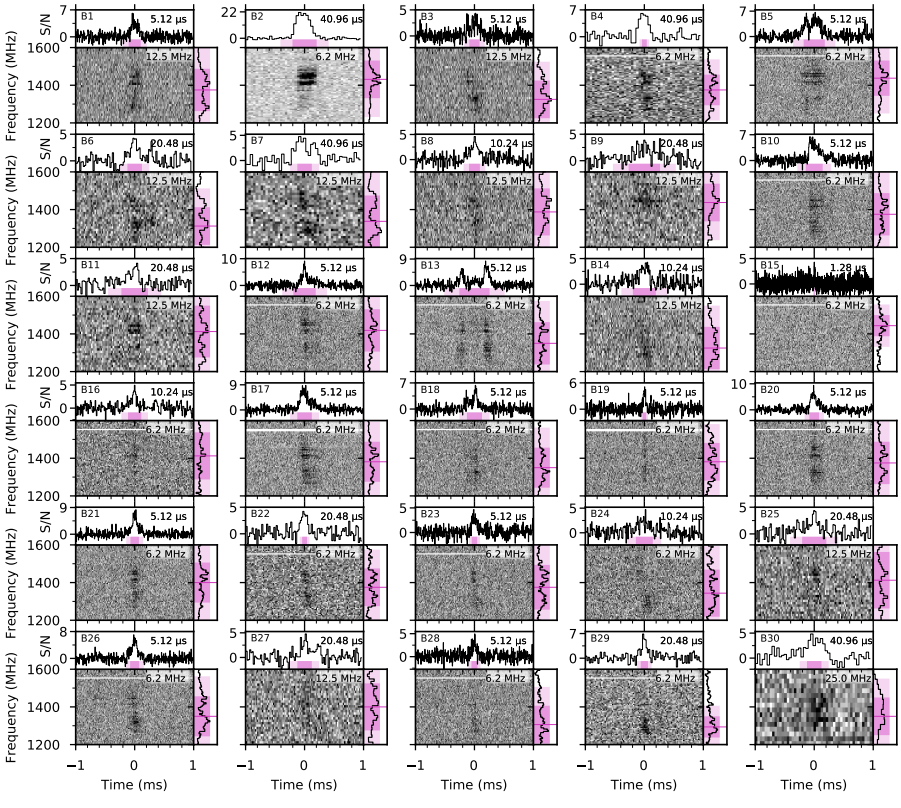

Figure 4.3: Frequency-averaged burst profiles, dynamic spectra and time-averaged spectra for all of the FRB 20200120E bursts presented in this work, ordered according to their arrival time. The filterbank data plotted is created by channelising the raw voltages to a resolution of 5.12 µs and 0.1953 MHz in time and frequency, respectively. The exception to this is B15, which was discovered in the microsecond search and the filterbank data is created with a resolution of 1.28 µs and 0.7813 MHz (see Figure 4.2 for a zoom-in panel of burst B15). Both the time and frequency have been downsampled by various factors for plotting, with the resolutions being shown on the burst profile and dynamic spectra, respectively. The data are coherently (within frequency channels) and incoherently (between channels) corrected for dispersion using a DM of 87.7527 pc cm^{-3} (Nimmo et al., 2022a). The coloured bars highlight the 1-σ (dark) and 2-σ (light) error regions on the burst extent in both frequency and time, where the different colours represent different observing epochs: 2022 January 14 (purple), 2022 January 17 (blue), 2022 February 21 (grey), 2022 February 23 (green) and 2022 March 17 (yellow). Time = 0 represents the burst centroid in time, and the horizontal coloured line in the burst spectrum represents the frequency centroid. Frequency channels that have been masked due to RFI have been omitted from the dynamic spectra (horizontal white lines). The burst profile is created by averaging the dynamic spectrum within the 2-σ burst extent in frequency, and similarly the burst spectrum is created by averaging the dynamic spectrum within the 2-σ burst extent in time.

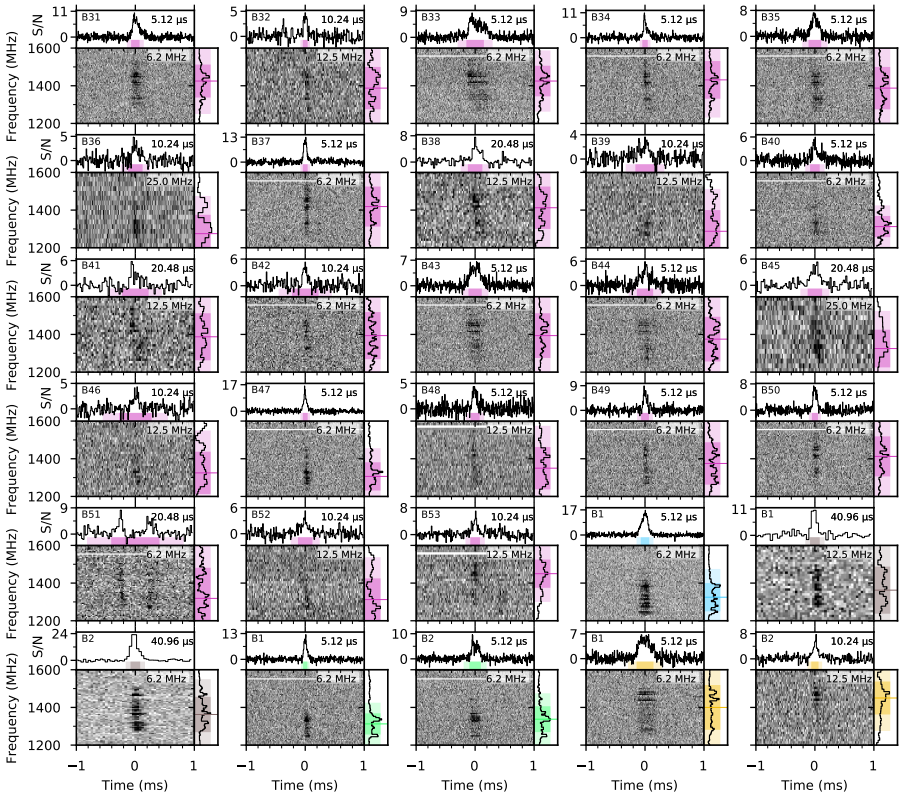

Figure 4.4: Continuation of Figure 4.3.

4.3.2 PRECISE observations

The VDIF data from the VLBI backend were searched using a Heimdall and FETCH pipeline, while the PSRIX pulsar data were searched with a PRESTO pipeline. Details of this analysis can be found in Kirsten et al. (2021b, 2022). No additional bursts were found in these data beyond the 5 reported in Kirsten et al. (2022) and Nimmo et al. (2022a), down to a fluence limit of 0.05 Jy ms (for a $7\,\sigma$, 100 μs duration burst).

4.3.3 PSRIX baseband-mode

The PSRIX filterbank data were searched for single pulses using tools in the PRESTO software suite, matching the analysis of the PRECISE PSRIX data in Section 4.3.2. No bursts were found down to a fluence limit of 0.05 Jy ms (for a $7\,\sigma$, 100 μs duration burst).

4.4 Burst analysis

4.4.1 Dispersion measure

Radio waves interact with free electrons on their journey to Earth, causing the lower frequencies to be delayed with respect to the higher frequencies (this relationship is quadratic in frequency; see Lorimer & Kramer 2004). Due to the complex morphology of FRB signals in time and frequency, constraining the quadratic sweep of dispersion can be challenging (Hessels et al., 2019). Conversely, without accurately correcting for dispersion, structure in the burst profiles could be unresolved. Using the sharp, relatively broadband, temporal features in one burst from FRB 20200120E (on timescales of microseconds), Nimmo et al. (2022a) constrained the DM to $87.7527 \pm 0.0003\,\mathrm{pc\,cm^{-3}}$, which was sufficient to resolve sub-microsecond timescales. This measurement is $> 9\sigma$ lower than the previous measurement from Bhardwaj et al. (2021a), which could be due to temporal evolution, spectral evolution, or unresolved burst structure in the Bhardwaj et al. (2021a) results. We note that the DM measurements have not accounted for Doppler shifting from Earth's orbital motion and rotation, although this should likely only contribute a $\sim 0.009\,\mathrm{pc\,cm^{-3}}$ difference in DM measurements between our observations and the previous DM measurement.

We selected bursts in our sample that have both a high S/N, and sharp structure in the 5.12 μs profile (Figures 4.3 and 4.4): namely B18, B19, B21, B34, B37, B47, B49 and B50 from 2022 January 14, as well as the narrowest burst in our sample (B15 from 2022 January 14, despite it having a relatively low S/N). Using digifil, we created 32-bit, coherently dedispersed (DM=$87.7527\,\mathrm{pc\,cm^{-3}}$) total intensity filterbank data containing the selected bursts, with 1.28 μs time resolution and 0.7813 MHz frequency resolution. To measure the DM, we incoherently shifted the frequency channels using DMs in the range 87.65–87.85 $\mathrm{pc\,cm^{-3}}$ in steps of $0.01\,\mathrm{pc\,cm^{-3}}$. In Figure 4.5 we plot the peak S/N of the 1.28 μs profile as a function of DM. In contrast to the results of Nimmo et al. (2022a), there is no clear micro-structure observed in these bursts, meaning the S/N does not rise and fall with DM as sharply. Note that the peak S/N versus DM mean of burst B36 is $< 87.65\,\mathrm{pc\,cm^{-3}}$ (the lower limit of the

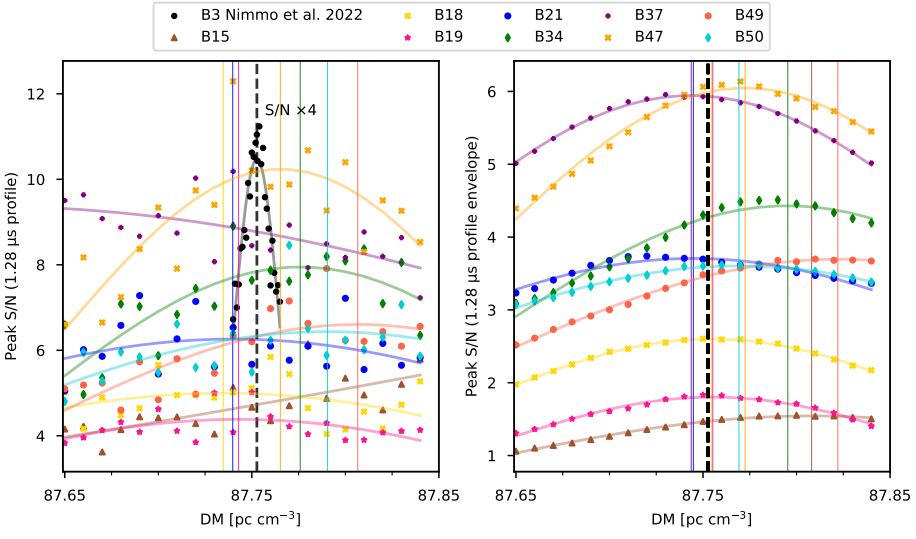

Figure 4.5: Peak S/N of 1.28 μs burst profile (left) and peak S/N of the smoothed burst envelope (right) as a function of DM. The bursts were selected based on their S/N values and fine structure observed in the 5.12 μs profiles. Gaussian fits are overplotted for each burst, matching the colour of the burst markers, and the mean of each Gaussian fit are shown by the coloured vertical lines. For comparison, a similar analysis of burst B3 from Nimmo et al. (2022a) is overplotted in black (left panel). The best DM measurement from Nimmo et al. (2022a), is shown by the black dashed line in both panels (DM= 87.7527 pc cm^{-3}).

x-axis scale in Figure 4.5), and we confirm the burst is visibly undercorrected at that 'best-fit' DM. We also plot the peak of the burst envelope as a function of DM, created by smoothing the 1.28 μs profile using a low-pass filter. The envelopes more clearly rise and fall with DM. In the absence of burst structure on microsecond (or shorter) timescales, we used the burst envelopes to measure a S/N weighted average DM of 87.77 ± 0.05 pc cm^{-3}, which is in agreement with the results of Nimmo et al. (2022a). We therefore conclude that the DM of FRB 20200120E has not changed by more than 0.15 pc cm^{-3} (3-σ) over the ∼1 year period of observation, and proceed using a DM of 87.7527 pc cm^{-3} (Nimmo et al., 2022a) for the analysis of the burst sample presented in this work. As mentioned in Section 4.3.1.2, this uncertainty in the DM results in a maximum smearing within frequency channels less than the time resolution for both 512 channel (1.28 μs) and 2048 channel (5.12 μs) data products created in this work.

4.4.2 Burst characterisation

For each burst, we coherently dedispersed and channelised the DADA baseband data to 2048 channels (0.1953 MHz and 5.12 μs frequency and time resolution, respectively) using digifil. This 32-bit Stokes I data is used to determine the burst properties for all bursts, with the exception of burst B2 on 2022 January 14, and both B1 and B2 on 2022 February 21, where only the 40.96 μs/0.1953 MHz pulsar data were retained. Frequency channels

contaminated by RFI were masked manually for each burst. The data were downsampled before measuring their properties: a summary of the resolutions used for the analysis can be found in Table 4.3. The frequency channels are shifted to correct for dispersion, and normalised such that the mean and standard deviation of the noise in each channel is 0 and 1, respectively.

Table 4.3: Burst properties.

Burst	Time of Arrival[a]	Fluence[b]	S/N[c]	Spectral Luminosity	Width[d]	Frequency[d] Extent	Time/Frequency Resolution
	[MJD]	[Jy ms]		[10^{28} erg s^{-1} Hz^{-1}]	[μs]	[MHz]	[μs / MHz]
2022 January 14							
B1	59593.70900072	0.13 ± 0.03	11.7	0.50 ± 0.10	171 ± 2	188.1 ± 1.6	5.12 / 12.5
B2	59593.71119049	0.54 ± 0.11	33.1	1.04 ± 0.21	346 ± 2	176.0 ± 0.8	40.96 / 6.2
B3	59593.72152561	0.14 ± 0.03	12.6	0.64 ± 0.13	152 ± 2	166.8 ± 2.1	5.12 / 12.5
B4	59593.72163241	0.08 ± 0.02	10.8	0.81 ± 0.16	133 ± 4	138.9 ± 1.9	40.96 / 6.2
B5	59593.72285434	0.36 ± 0.07	23.2	0.80 ± 0.16	302 ± 1	166.5 ± 0.5	5.12 / 6.2
B6	59593.72347595	0.09 ± 0.02	6.4	0.28 ± 0.06	207 ± 7	168.2 ± 5.0	20.48 / 12.5
B7	59593.72366265	0.11 ± 0.02	9.2	0.36 ± 0.07	240 ± 8	245.5 ± 7.4	40.96 / 12.5
B8	59593.72377264	0.10 ± 0.02	9.7	0.44 ± 0.09	161 ± 4	213.1 ± 4.5	10.24 / 12.5
B9	59593.72393352	0.15 ± 0.03	7.8	0.22 ± 0.04	445 ± 7	169.6 ± 2.3	20.48 / 12.5
B10	59593.72402411	0.26 ± 0.05	19.7	0.71 ± 0.14	245 ± 1	192.5 ± 0.7	5.12 / 6.2
B11	59593.72406203	0.10 ± 0.02	6.2	0.18 ± 0.04	384 ± 10	241.7 ± 5.9	20.48 / 12.5
B12	59593.72564746	0.22 ± 0.04	14.7	0.46 ± 0.09	322 ± 2	192.7 ± 0.8	5.12 / 6.2
B13	59593.72597616	0.32 ± 0.06	17.8	0.49 ± 0.10	431 ± 3	195.0 ± 1.1	5.12 / 6.2
B14	59593.72658502	0.17 ± 0.03	10.5	0.35 ± 0.07	328 ± 5	195.9 ± 2.5	10.24 / 12.5
B15	59593.72694393	0.05 ± 0.01	12.2	2.29 ± 0.46	14 ± 1	99.8 ± 6.7	1.28 / 6.2
B16	59593.72696785	0.08 ± 0.02	7.0	0.28 ± 0.06	192 ± 6	212.9 ± 6.5	10.24 / 6.2
B17	59593.72767015	0.32 ± 0.06	26.2	1.03 ± 0.21	211 ± 1	177.0 ± 0.5	5.12 / 6.2
B18	59593.72777136	0.16 ± 0.03	12.6	0.50 ± 0.10	217 ± 2	185.8 ± 1.5	5.12 / 6.2
B19	59593.72778012	0.06 ± 0.01	8.9	0.71 ± 0.14	55 ± 2	171.5 ± 5.6	5.12 / 6.2
B20	59593.72835081	0.21 ± 0.04	20.9	0.99 ± 0.20	140 ± 1	187.9 ± 0.8	5.12 / 6.2
B21	59593.72836174	0.18 ± 0.04	19.9	1.01 ± 0.20	124 ± 1	180.3 ± 1.0	5.12 / 6.2
B22	59593.72876785	0.06 ± 0.01	8.5	0.59 ± 0.12	99 ± 4	167.1 ± 5.6	20.48 / 6.2
B23	59593.72956599	0.08 ± 0.02	10.7	0.68 ± 0.14	84 ± 2	205.6 ± 3.8	5.12 / 6.2
B24	59593.72966465	0.11 ± 0.02	8.3	0.30 ± 0.06	251 ± 4	218.5 ± 3.0	10.24 / 6.2
B25	59593.72978254	0.11 ± 0.02	7.2	0.22 ± 0.04	366 ± 12	270.3 ± 9.0	20.48 / 12.5
B26	59593.73021930	0.17 ± 0.03	16.8	0.87 ± 0.17	133 ± 1	177.7 ± 1.0	5.12 / 6.2
B27	59593.73065954	0.09 ± 0.02	7.4	0.29 ± 0.06	215 ± 9	224.1 ± 8.7	20.48 / 12.5
B28	59593.73098736	0.08 ± 0.02	9.5	0.65 ± 0.13	89 ± 3	171.5 ± 3.0	5.12 / 6.2
B29	59593.73118289	0.12 ± 0.02	9.7	0.74 ± 0.15	111 ± 3	96.2 ± 2.5	20.48 / 6.2
B30[e]	59593.73118737	0.12 ± 0.02	9.4	0.39 ± 0.08	–	–	40.96 / 25.0
B31	59593.73127253	0.27 ± 0.05	27.4	1.49 ± 0.30	126 ± 1	146.5 ± 0.5	5.12 / 6.2
B32	59593.73139847	0.07 ± 0.01	9.8	0.64 ± 0.13	76 ± 4	193.5 ± 8.0	10.24 / 12.5
B33	59593.73162219	0.45 ± 0.09	30.4	1.19 ± 0.24	249 ± 1	137.3 ± 0.4	5.12 / 6.2
B34	59593.73176535	0.16 ± 0.03	20.9	1.38 ± 0.28	80 ± 1	168.0 ± 1.1	5.12 / 6.2
B35	59593.73215265	0.24 ± 0.05	20.8	0.86 ± 0.17	187 ± 1	187.4 ± 0.7	5.12 / 6.2
B36[e]	59593.73228158	0.09 ± 0.02	5.9	0.27 ± 0.05	–	–	10.24 / 25.0
B37	59593.73230289	0.19 ± 0.04	27.4	1.86 ± 0.37	71 ± 1	185.4 ± 0.8	5.12 / 6.2
B38[e]	59593.73244190	0.11 ± 0.02	9.4	0.37 ± 0.07	–	–	20.48 / 12.5
B39	59593.73245115	0.11 ± 0.02	6.7	0.26 ± 0.05	280 ± 8	192.1 ± 5.5	10.24 / 12.5
B40	59593.73278832	0.17 ± 0.03	13.2	0.84 ± 0.17	139 ± 2	101.0 ± 0.0	5.12 / 6.2
B41	59593.73324614	0.04 ± 0.01	2.5	0.07 ± 0.01	405 ± 1	214.8 ± 3.9	20.48 / 12.5
B42	59593.73325516	0.08 ± 0.02	4.7	0.13 ± 0.03	380 ± 9	215.7 ± 4.7	10.24 / 6.2
B43	59593.73364935	0.27 ± 0.05	23.3	0.95 ± 0.19	192 ± 1	199.9 ± 0.6	5.12 / 6.2
B44	59593.73369348	0.19 ± 0.04	14.6	0.54 ± 0.11	231 ± 2	200.6 ± 1.1	5.12 / 6.2
B45[e]	59593.73403931	0.11 ± 0.02	8.0	0.35 ± 0.07	–	–	20.48 / 25.0
B46	59593.73420280	0.07 ± 0.01	3.9	0.11 ± 0.02	468 ± 14	203.5 ± 6.0	10.24 / 12.5
B47	59593.73421902	0.24 ± 0.05	27.7	2.33 ± 0.47	69 ± 1	126.7 ± 0.6	5.12 / 6.2
B48	59593.73505336	0.10 ± 0.02	9.8	0.50 ± 0.10	135 ± 3	206.4 ± 3.5	5.12 / 12.5
B49	59593.73520064	0.13 ± 0.03	15.1	0.80 ± 0.16	111 ± 1	193.6 ± 1.4	5.12 / 6.2
B50	59593.73588107	0.13 ± 0.03	17.1	1.03 ± 0.21	92 ± 1	178.6 ± 1.2	5.12 / 6.2
B51	59593.73632506	0.17 ± 0.03	7.5	0.16 ± 0.03	704 ± 20	274.7 ± 7.3	20.48 / 6.2
B52[e]	59593.73726150	0.09 ± 0.02	6.9	0.29 ± 0.06	–	–	10.24 / 12.5

Continued: Burst properties.

B53	59593.73726998	0.11 ± 0.02	9.3	0.51 ± 0.10	150 ± 2	131.8 ± 2.5	10.24 / 12.5
2022 January 17							
B1	59596.29769138	0.56 ± 0.11	49.9	3.06 ± 0.61	127 ± 1	134.6 ± 0.3	5.12 / 6.2
2022 February 21							
B1	59631.91114554	0.10 ± 0.02	10.2	0.49 ± 0.10	196 ± 6	216.2 ± 5.0	40.96 / 12.5
B2	59631.91878154	0.32 ± 0.06	30.3	1.54 ± 0.31	150 ± 0	160.7 ± 1.0	40.96 / 6.2
2022 February 23							
B1	59633.63710622	0.21 ± 0.04	24.6	2.36 ± 0.47	63 ± 0	102.7 ± 0.6	5.12 / 6.2
B2	59633.64288987	0.27 ± 0.05	20.9	1.10 ± 0.22	163 ± 0	119.0 ± 0.5	5.12 / 6.2
2022 March 17							
B1	59655.95339151	0.35 ± 0.07	26.4	0.95 ± 0.19	245 ± 0	199.6 ± 0.6	5.12 / 6.2
B2	59655.95391696	0.10 ± 0.02	11.0	0.67 ± 0.13	115 ± 0	148.8 ± 6.3	10.24 / 12.5

[a] Corrected to the Solar System Barycentre at infinite frequency using a DM of 87.7527 pc cm^{-3} (Nimmo et al., 2022a), a dispersion constant of $1/(2.41 \times 10^{-4})$ MHz^2 pc^{-1} cm^3 s, and the VLBI FRB 20200120E position (Kirsten et al., 2022). The times quoted are dynamical times (TDB).

[b] Computed within the $\pm 2\sigma$ region of the burst temporal width assuming Effelsberg's system temperature and gain is 20 K and 1.54 Jy K^{-1}, respectively, and also considering a cosmic microwave background temperature of 3 K and additional sky background temperature of 0.8 K (see Section 4.4.2).

[c] Boxcar S/N: defined as the sum of the burst profile in S/N units within $\pm 2\sigma$ of the burst temporal width normalised by the $\pm 2\sigma$ width in time bins.

[d] Defined as the full-width at half maximum of the Gaussian fit to the ACF divided by $\sqrt{2}$.

[e] Burst extents in time and frequency could not be measured accurately due to low S/N and temporal/spectral structure. We assume the mean values from the remaining January 14 burst sample (132 μs and 113 MHz) to compute the fluence.

To measure the burst extent in time and frequency we computed the 2-dimensional autocorrelation function (ACF) of the dynamic spectra. We fitted a 2-dimensional Gaussian to the ACF, from which we derived the burst width and frequency extent reported in Table 4.3. In a few cases (marked in Table 4.3), the low S/N and strong scintillation structure resulted in visibly under-estimated burst extents from the ACF analysis. For these bursts, we do not report burst widths and frequency extents, and instead assume the average values from the other bursts at that observing epoch, to use for fluence calculations. For all bursts, we fitted a 2-dimensional Gaussian to the dynamic spectrum to determine the centroid of the burst in time and frequency. The coloured bars in Figures 4.2 and 4.3 highlight the 1-σ (dark) and 2-σ (light) burst extents, Time $= 0$ represents the burst centroid in time, which we define as the time of arrival (ToA) of the burst, and the horizontal coloured line on the burst spectrum represents the frequency centroid. Note for B13 and B51 on 2022 January 14, we observe 2 clear burst components. The ToA and frequency centroid are, therefore, the centre of the means of a Gaussian fit to each component. In Figure 4.6 we show histograms of the central frequencies, temporal widths and frequency extents of the bursts, with mean values of 1.38 GHz, 129 μs and 111 MHz, respectively.

The central frequencies are potentially influenced by scintillation from the Milky Way's interstellar medium (ISM) since FRB 20200120E bursts exhibit strong scintillation spectral structure (visible in their dynamic spectra; see Figure 4.2). The strong scintles can skew the 2-dimensional Gaussian fit, used to determine the burst centroid. In addition, the central frequencies of the 2 bursts detected on each of February 21, 23 and March 17, fall to the same side of the mean value in the distribution during a single epoch. The influence of scintillation on the central frequency must be minimal, however, since the bursts on January 17, February 21, 23 and March 17 agree well with the January 14 distribution (Figure 4.6).

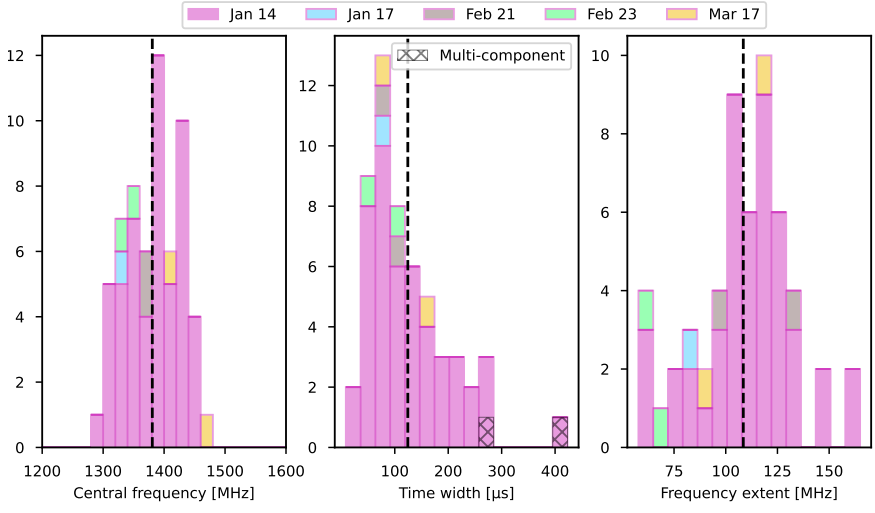

Figure 4.6: Histograms of the burst central frequencies (left panel), temporal widths (middle panel) and frequency extents (right panel). The colours represent the different observing epochs and match the colours used throughout this work (see, e.g., Figures 4.3 and 4.4). In the middle panel, the hatched bins represent the two bursts where we have clearly identified multiple distinct components (B13 and B51 on 2022 January 14). The longer temporal widths are therefore a reflection of the sub-burst separation, while the individual burst components are in fact more narrow. The black dashed line represents the mean value.

The expected frequency scale arising due to ISM scintillation is ~ 3 MHz (Cordes & Lazio, 2002), consistent with the single-bin spectral structure observed in the 6.25 MHz-resolution spectra (Figure 4.7), that persists through individual observations. Since the measured burst spectral extents are ~ 100 MHz, a factor of ~ 30 higher than the scintillation scale, the burst frequency extents are likely not heavily influenced by scintillation from the Milky Way interstellar medium.

The burst ToAs (Table 4.3) are corrected to the Solar System Barycentre at infinite frequency (using a dispersion constant of $1/(2.41 \times 10^{-4})$ MHz^2 pc^{-1} cm^3 s, and the VLBI position of FRB 20200120E; Kirsten et al. 2022). The burst profiles are converted to S/N units by subtracting the mean of local noise data (containing no signal), and then dividing by the standard deviation of the noise. The burst profiles are then converted to physical units (Jy) using the radiometer equation (Cordes & McLaughlin, 2003), and typical values for Effelsberg's system temperature (20 K) and gain (1.54 Jy K^{-1}). These values are uncertain at the 20% level, which dominates the errors on the flux density. We also add a 3 K contribution from the cosmic microwave background (Mather et al., 1994), and a sky background temperature of 0.8 K, which is derived by extrapolating from the 408 MHz sky map (Remazeilles et al., 2015), using a spectral index of -2.7 (Reich & Reich, 1988). The fluence is then calculated by summing over the $\pm 2\sigma$ burst extent in time *and* frequency. Using the known distance to FRB 20200120E (3.63 Mpc; Kirsten et al. 2022), we computed the isotropic-equivalent

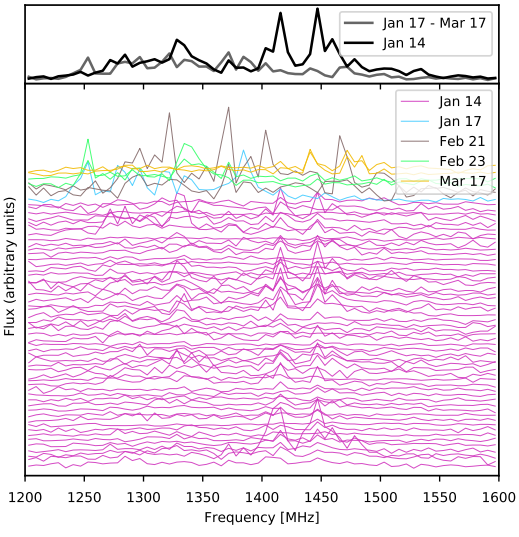

Figure 4.7: Burst spectra at 6.25 MHz resolution. As shown in the legend, the colours represent bursts detected on different days. Strong single-bin spectral features due to scintillation are apparent and persistent through individual observing epochs. The average burst spectra (weighted by burst S/N) for 2022 January 14 bursts (black) and for bursts detected on the other days (grey) are shown in the top panel. In addition to the narrow-band spectral structure due to scintillation, there is also spectral structure on the scale of $\sim$ 100 MHz, consistent with the measured burst frequency extents (Figure 4.6). On 2022 January 14, two $\sim$ 100 MHz bumps are visible in the stacked spectrum at $\sim$ 1300 and $\sim$ 1450 MHz, reminiscent of the spectral structure seen in the single burst presented in Majid et al. (2021). Note the flattening of the burst spectra at $\sim$ 1550 MHz arises from frequent flagging of data in that spectral range due to persistent RFI.

spectral luminosity of each burst and report these values alongside the burst fluences in Table 4.3.

There are no clear trends of the burst properties with time through the 2022 January 14 observation (Figure 4.9). Perhaps the burst widths and fluences are slightly decreasing through the observation, but the scatter on the data points is too large to confirm a downward trend. The bursts on other observing days tend to have lower burst widths and frequency extents than the mean values of the January 14 observation, while in general they show higher fluences than average (Figure 4.9). More observations are required to test whether the burst properties are drawn from different distributions as the burst rate changes.

Motivated by the high S/N microstructure and sub-microsecond structure seen in bursts from FRB 20200120E (Nimmo et al., 2022a; Majid et al., 2021), we created higher-time-resolution filterbank data for bursts which have sufficient S/N at 5.12 µs to explore the structure on microsecond timescales. Using digifil, we created 32-bit coherently dedispersed total intensity filterbank data containing the bursts with a resolution of 1.28 µs and 0.7813 MHz in time and frequency, respectively. The burst profiles are created by averaging over the $\pm 2\sigma$ burst extent in frequency. In Figure 4.10, the 1.28 µs burst profiles are shown and compared with the 1 µs profile of burst B3 from Nimmo et al. (2022a), which shows very clear

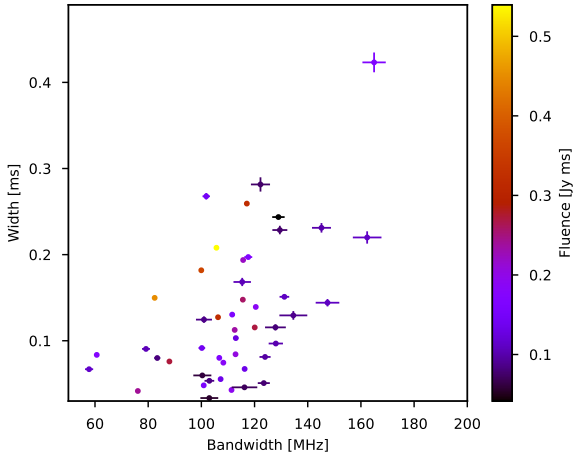

Figure 4.8: Burst time duration versus frequency extent for bursts during the 2022 January 14 observation. The error bars are the 1σ fit errors from the 2-dimensional autocorrelation analysis described in the text, and reported in Table 4.3. The colour scale represents the burst fluence.

microstructure. We caution that if the DM has changed by $\sim 0.1\,\mathrm{pc\,cm^{-3}}$ ($< 3\sigma$ from the DM uncertainty measured in Section 4.4.1), this will result in $\sim 60\mu$s of smearing from 1.5 GHz to 1.3 GHz, therefore washing out microsecond structure. It is clear, however, from Figure 4.5 that the 1.28 μs peak S/N does not rapidly increase in S/N close to $\pm 0.1\,\mathrm{pc\,cm^{-3}}$ around the DM used (B36 is increasing towards $87.65\,\mathrm{pc\,cm^{-3}}$, but as noted in Section 4.4.1 is visibly undercorrected at its best-fit value). If the bursts presented in this work had similarly high S/N microstructure as seen in B3 from Nimmo et al. (2022a), this would be evident in the 5.12 μs burst dynamic spectra (Figures 4.3 and 4.4). We cannot rule out the presence of low S/N microstructure; however, it is evident that the sample of bursts presented in this work do not exhibit the same high-S/N microstructure that has been observed previously from this source.

Since this burst sample does not allow us to explore a range of timescales, as in Nimmo et al. (2022a), we instead compute the rise and decay timescales of the high S/N bursts. We use a fluence threshold of 0.16 Jy ms, which we measure to be the completeness limit for the fluence distribution (see Section 4.4.5). Using this conservative fluence threshold limits the effect of noise on the measurements, while also giving a sufficient sample to study the distribution of rise and decay times (Figure 4.11). We define the rise time as the time it takes the burst to increase from 10% to 90% of the burst energy computed between the peak and peak$-2\sigma_{\mathrm{wid}}$, where σ_{wid} is the 1 σ burst width. Likewise, the decay time is the time between 90% to 10% of the burst energy computed between the peak and peak$+2\sigma_{\mathrm{wid}}$. We performed this analysis with time resolution of 20.48 μs (with the exception of B2 on January 14 and both bursts on February 21, where only the 40.96 μs pulsar data is available). We find that the rise times are preferentially lower than the decay times (Figure 4.11). As the fluence decreases, the rise and decay times approach equality, and occasionally the rise time

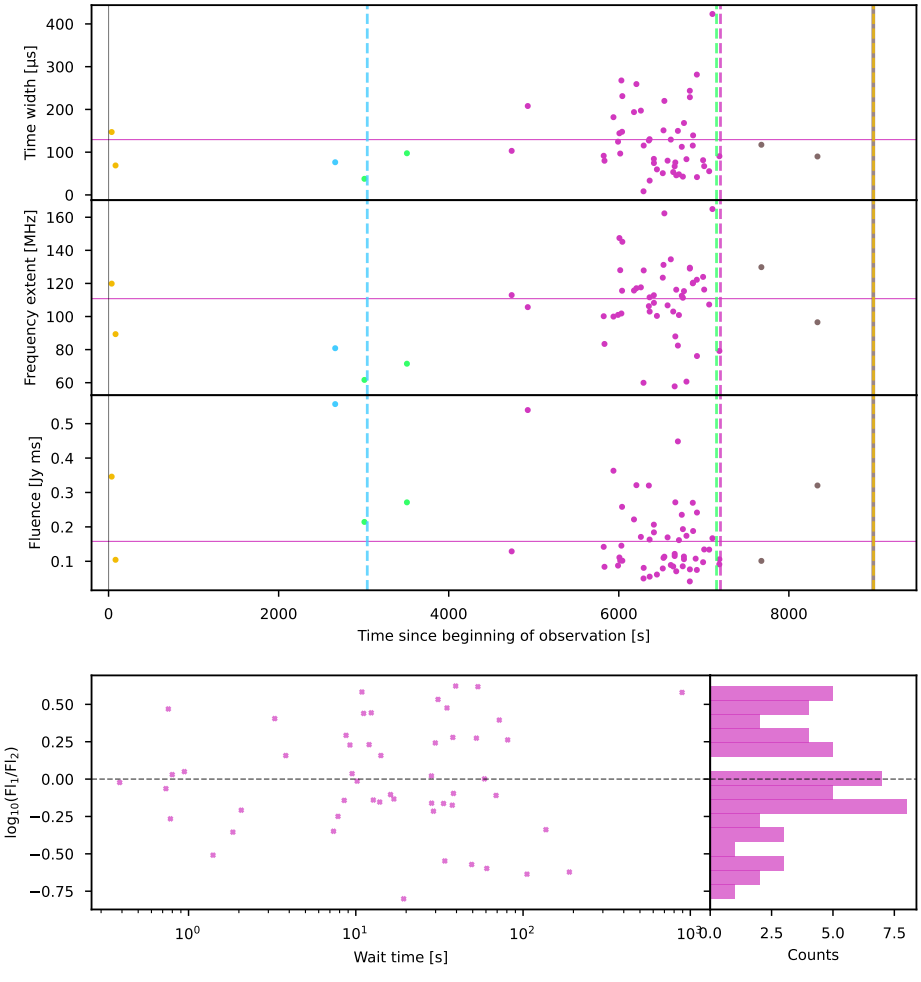

Figure 4.9: Top sub-figure: Burst widths in time (top panel), bandwidths (middle panel) and fluences (bottom panel), as a function of time relative to the beginning of the observing epoch. As shown in the legend, the colours represent the different observing epochs. The vertical black line represents the start of the observations, and the coloured vertical dashed lines indicate the end of each observation. The horizontal purple line represents the mean value for the 2022 January 14 observation (burst storm). Bottom sub-figure: The ratio of burst fluences of consecutive bursts on 2022 January 14 as a function of their time separation, with a histogram shown on the right. The black dashed line represents the divide between the fluence of the first burst (Fl_1) being lower than the fluence of the second burst (Fl_2), and vice versa.

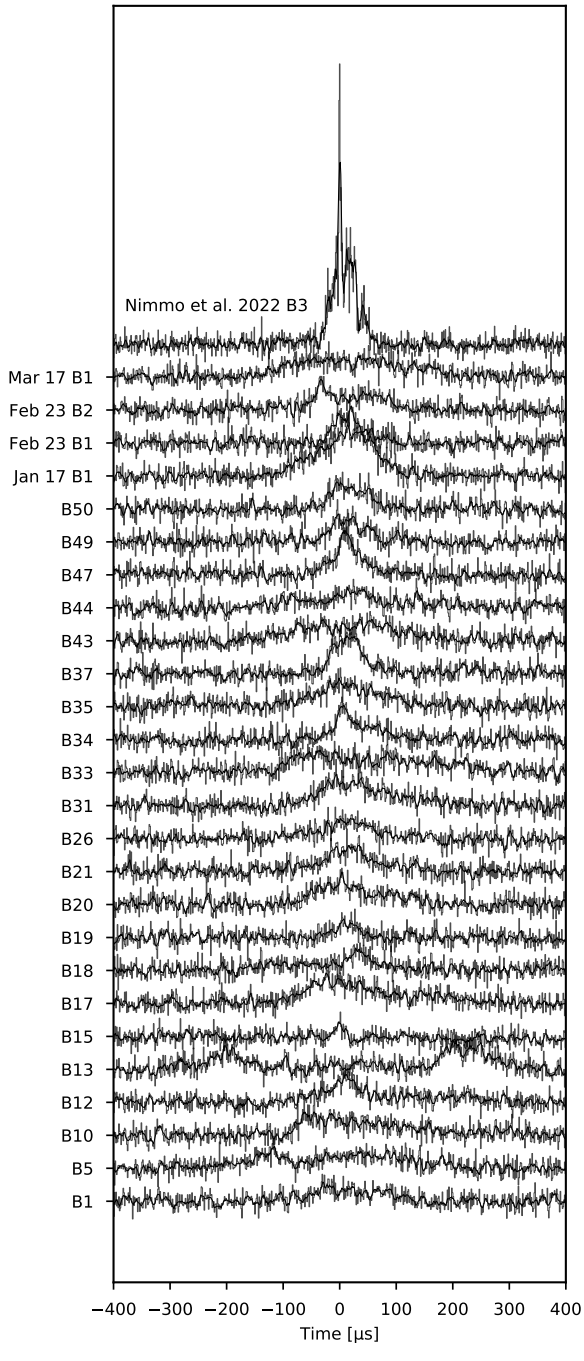

Figure 4.10: 1.28 μs burst profiles of a sample of high S/N bursts presented in this work (burst names are shown on the y-axis). The burst profiles are created by averaging over the $\pm 2\sigma$ burst extent in frequency. The burst profiles are normalised such that they have the same off-burst noise statistics. Overplotted on the 1.28 μs profiles are the smoothed burst profiles, using a Savitzky-Golay filter (Savitzky & Golay 1964; 11 bins, and polynomial order 2). The top burst profile is B3 from Nimmo et al. (2022a) at 1 μs time resolution, which has clear high-S/N microstructure visible.

exceeds the decay time. This evolution with fluence is likely a reflection of the increased influence of noise in the data as the fluence decreases. The range of rise times measured is from 47 to 356 μs, and decay times from 37 to 266 μs.

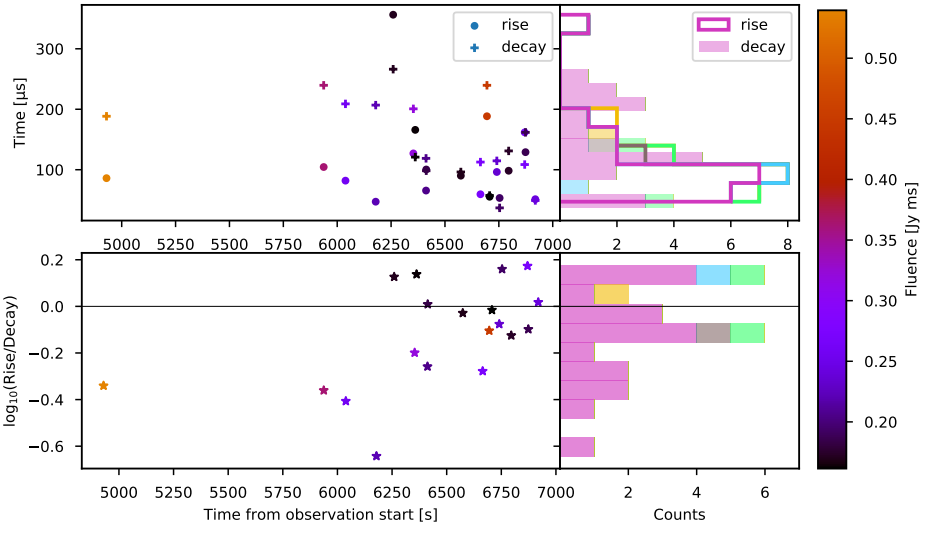

Figure 4.11: Rise and decay times of bursts above a fluence threshold of 0.16 Jy ms. Left panels are as a function of time from the beginning of the 2022 January 14 observation, and the colour of the scatter points represent the burst fluence. The right panels are histograms of the rise and decay times (top), and the ratio of rise/decay (bottom), where the colours represent the multiple observing epochs (matching the colour scheme of other plots in this work). The horizontal black line in the bottom plots show the divide between bursts that rise faster than they decay, and vice versa.

4.4.3 Burst rates, wait times and clustering

Reported in Table 4.1 are the average burst rates per observation during our FRB 20200120E monitoring campaign. For burst rates throughout this paper we report Poisson errors. Even during the observation on 2022 January 14, the burst rate is changing: all of the 53 bursts were discovered in the final $\sim$ 40 minutes of a 2-hr observation. We computed the burst rate in 200-s time chunks (Figure 4.12) to monitor the evolution of burst rate through the observation. We find that the burst rate ramps up to a maximum of 252^{+17}_{-16} bursts/hr, before falling back down towards the end of the observation. Excluding the first two bursts, which occur significantly earlier than the remaining 50, the burst storm has an approximate duration of 20 min. We do caution that the storm extends to the end of our observation, beyond which we do not know the activity behaviour of FRB 20200120E.

The distribution of the time difference between consecutive bursts, the so-called 'wait times', of the 2022 January 14 burst storm is bi-modal (Figure 4.13). We fitted two log-normal functions to the wait-time distribution using least-squares fitting. The best fit log-normal

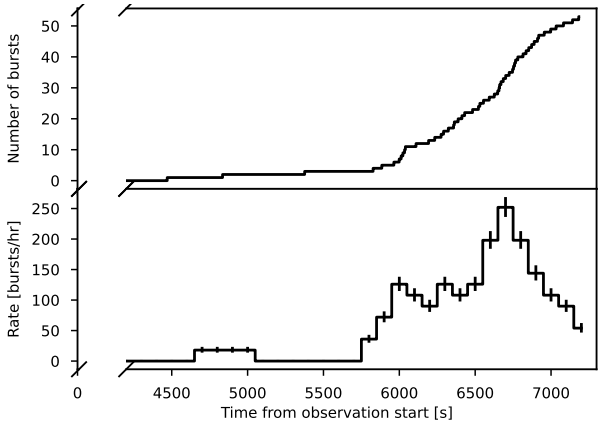

Figure 4.12: Cumulative burst distribution (top) and evolution of burst rate per 200 s time interval (bottom) during the 2022 January 14 FRB 20200120E burst storm. The error bars on the rate are Poissonian. The x-axis is broken to show that there were no bursts detected in the first ∼4700 s of the observation.

means are $0.94^{+0.07}_{-0.06}$ s and $23.61^{+3.06}_{-2.71}$ s. We also included bins in the wait time distribution for the time separation of bursts from other observing epochs (Figure 4.13), which are all longer than the $23.61^{+3.06}_{-2.71}$ s log-normal mean. This is likely a reflection of the highly varying burst rates between observing epochs (Table 4.1). The median duration of the 5 observations with burst detections from our monitoring campaign is $\sim$ 2 hr, meaning we are unable to measure wait times longer than this. The fact that the wait time distribution appears to tail off at $\sim$ 1000 s is a reflection of being naturally less sensitive to longer wait times due to the limited observation durations.

Also shown in Figure 4.13 is the cumulative wait time distribution for the burst storm on 2022 January 14. We test for burst clustering during the burst storm by comparing the cumulative density function (CDF) for a Poisson distribution

$$P_{\rm Poisson} = 1 - e^{-t_{\rm wait} R}, \tag{4.1}$$

with the CDF for a Weibull distribution

$$P_{\rm Weibull} = 1 - e^{-(t_{\rm wait} R_W \Gamma(1+1/k))^k}, \tag{4.2}$$

where $t_{\rm wait}$ are the wait times between consecutive bursts, R and R_W are the rates for a Poisson and Weibull distribution, respectively, k is the Weibull shape parameter and Γ is the gamma function (Oppermann et al., 2018). The Weibull distribution is equivalent to a Poisson distribution when $k = 1$, while $k < 1$ implies that the bursts are clustered, with more clustering implied for lower k. We performed a least-squares fit of both the Poisson and Weibull distributions to the wait time cumulative distribution. The best-fit Poissonian rate is 131 ± 1 bursts/hr, and the best-fit Weibull rate is 111 ± 3 bursts/hr, with shape parameter 0.79 ± 0.44. The reduced χ^2 for the fits are 1.1 (50 degrees of freedom) and 0.2 (49 degrees of freedom) for Poisson and Weibull, respectively, indicating that the burst rate is Poissonian

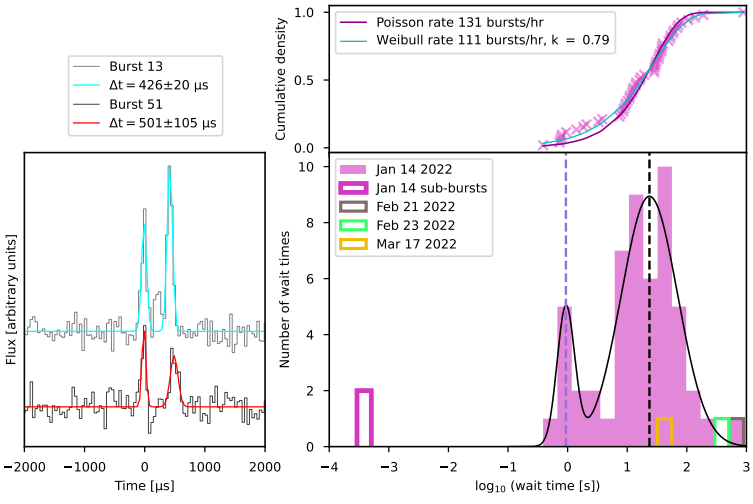

Figure 4.13: Wait time distribution (right sub-figure, bottom panel) and cumulative distribution of wait times (right sub-figure, top panel). The purple wait time histogram is that of the bursts on 2022 January 14. We fit the sum of two log-normal distributions to the 2022 January 14 histogram (excluding the sub-burst separations), shown by the black line, and the means of the two log-normals are shown by the purple dashed ($0.94^{+0.07}_{-0.06}$ s) and black dashed ($23.61^{+3.06}_{-2.71}$ s) lines. The open grey, green and yellow bins represent the time separation of bursts on 2022 February 21, 23 and March 17, respectively (as highlighted in the figure legend). The burst profiles of the two identified multi-component bursts in our sample, bursts B13 and B51 on 2022 January 14, are shown in the left sub-figure at 40.96 μs time resolution. Overplotted on the profiles are double Gaussian fits to the profiles, and shown in the legend are the measured separations of the Gaussian means. The open purple histogram at short wait times plotted on the wait time distribution represents the measured sub-burst separations. Overplotted on the cumulative wait time distribution (right sub-figure, top panel) are the best-fit Poisson cumulative density function (CDF) in purple, and the best-fit Weibull CDF in blue.

during the burst storm. Furthermore, the large uncertainties on the Weibull shape parameter are also consistent with a Poissonian distribution (the special case of $k = 1$). This supports the use of Poissonian error bars on the rate in Figure 4.12.

The fits to the cumulative wait time distribution reflect only the statistics *during* the burst storm, and do not account for the $\sim$ 4700 s leading up to the burst storm where no bursts were detected (Figure 4.12). Following Oppermann et al. (2018), and the analysis presented in Kirsten et al. (2021b)[4], we calculated the posterior distribution of the 2022 January 14 observation (Figure 4.14, left) and the combined posterior distribution of the observations on January 17, February 21, February 23 and March 17 (Figure 4.14, right). The likelihood function is computed using the burst ToAs reported in Table 4.3 relative to the beginning of the observation, and incorporates any gaps between the beginning of the observation and the first burst, and the final burst to the end of the scan. We do not include the non-detection observations, since we are specifically interested in exploring whether the difference between

[4] https://github.com/MJastro95/weibull_analysis

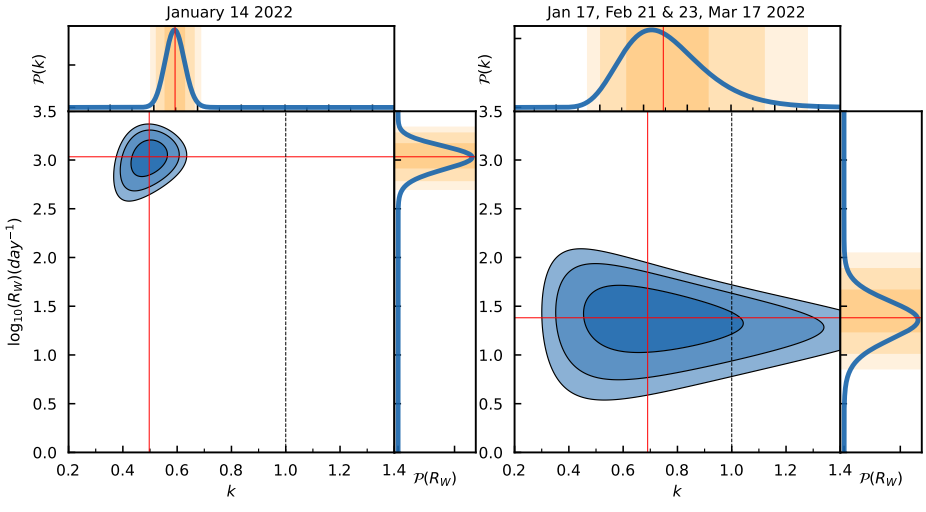

Figure 4.14: Posterior distributions of the Weibull shape parameter k and rate R_W for the 2022 January 14 observation (left) and the combination of 2022 January 17, February 21, 23 and March 17 observations (right). In each sub-figure the contour plot represents the 2-dimensional distribution, where the contours are 68%, 95% and 99% confidence intervals. The red lines highlight the maximum probability density of the distribution (i.e., the most likely values). The black dashed line highlights $k = 1$, which is where the Weibull distribution is equivalent to a Poisson distribution. The top and right panels show the marginal distribution for k and R_W, respectively. The orange shaded regions represent the 68%, 95% and 99% confidence intervals.

2022 January 14 and other detection days is solely the burst rate. To combine observations we are assuming that the scans are independent and calculate the likelihood of the data as the product of the likelihoods of the individual observations. The prior ($f(k, R_W)$) is defined as uniform, and the posterior distribution is calculated as

$$\text{Post}(k, R_W|d) \propto \mathcal{L}(d|k, R_W) f(k, R_W), \tag{4.3}$$

for the likelihood of the data d, $\mathcal{L}(d|k, R_W)$.

We find that for the 2022 January 14 observation, the most likely values of k and R_W are $0.50^{+0.04}_{-0.05}$ and $1079^{+377}_{-242}\,\text{day}^{-1}$, respectively, where the uncertainties reflect the 68% confidence interval. This indicates that the bursts are highly clustered (since $k < 1$), which is evident already from Figure 4.12. In contrast, the combined observations of January 17, February 21, 23 and March 17 result in most likely values of $k = 0.69^{+0.20}_{-0.17}$ and $R_W = 24^{+22}_{-7}\,\text{day}^{-1}$, showing no strong evidence for clustering, and consistent with $k = 1$ within the 95% confidence interval (Figure 4.14).

4.4.4 Periodicity searches

In this work we have a relatively large burst sample, mostly concentrated in a short time interval on 2022 January 14. We, therefore, used various methods to search for a periodic

arrival time of the bursts during the 2022 January 14 observation, as well as a periodicity in the activity of bursts over the > 1 yr span of observations. Note that we only include the bursts presented in this work and in Kirsten et al. (2022) for the periodicity analysis since they were all detected with Effelsberg (observations with comparable sensitivity) at the same observing frequency (frequency-dependent activity is seen in FRB 20180916B; Pleunis et al. 2021b; Pastor-Marazuela et al. 2021).

4.4.4.1 Burst arrival times

Using PRESTO (Ransom, 2001), we created dedispersed time series (DM$= 87.7527\,\mathrm{pc\,cm^{-3}}$; Nimmo et al. 2022a) of the entire 2-hr observation, the last $\sim$ 40 minutes, and the $\sim$ 15 minutes around the peak burst rate of 2022 January 14, after masking the RFI using rfifind. The reason for segmenting the data in this manner is to increase sensitivity to the scenario where the periodic emission has 'turned on' (e.g., nulling pulsars; Backer 1970). The time series were created from the 40.96 µs pulsar backend data since there are roughly a few minutes of missing data from the raw voltages (see Section 4.3.1.1). These time series were Fourier transformed (using a Fast Fourier Transform, FFT) and then searched for periodic signals using PRESTO's accelsearch. We first use a maximum Fourier frequency derivative of 8 bins and 8 maximum number of harmonics, and second a maximum Fourier frequency derivative of 200 bins and 16 maximum number of harmonics. The only periodic candidates above a S/N threshold of 7 and coherent power of 100 are confined to a small spectral range, and therefore are attributed to RFI.

We then performed a brute force search of an integer divisor of the burst ToAs commonly used for period searches of rotating radio transients (RRATs; McLaughlin et al. 2006)[5]. We performed this test twice: once on all bursts excluding the first two which are separated in time from the main outburst of FRBs, and second a subset of those bursts which have a wait time from the previous burst > 2.5 s. For the latter, we are using only bursts in the long wait time log-normal (Figure 4.13), which we attribute to the burst rate, and exclude bursts in the shorter wait time log-normal which we attribute to a typical 'event duration' (see Section 4.5.5). Folding at the best-fit period from each search returns bursts across all burst phases (Figure 4.15, bottom sub-figure). Therefore, we conclude that there is no strict period in the arrival times of the bursts during the FRB 20200120E burst storm. We note that this method is insensitive to the arrival of bursts at various rotational phases of the progenitor.

To increase our sensitivity to the situation where the bursts arrive at a wider range of phases, or at multiple distinct rotational phases, we folded the observation using a range of trial periods from 1 ms to 25 s. We made step sizes of $(1/n_{\mathrm{bins}})/(2442.5\,\mathrm{s})$ in frequency space, where 2442.5 s is the time separation between the first and last burst on 2022 January 14, and n_{bins} are the number of bins the period is divided into: we choose 25 bins which corresponds to a minimum duty cycle of 4%. In the folded observation, we count the number of burst ToAs that fall into each phase bin, and use the χ^2 statistic to compare with a uniform distribu-

[5] Using rrat_period in the PRESTO psr_utils package.

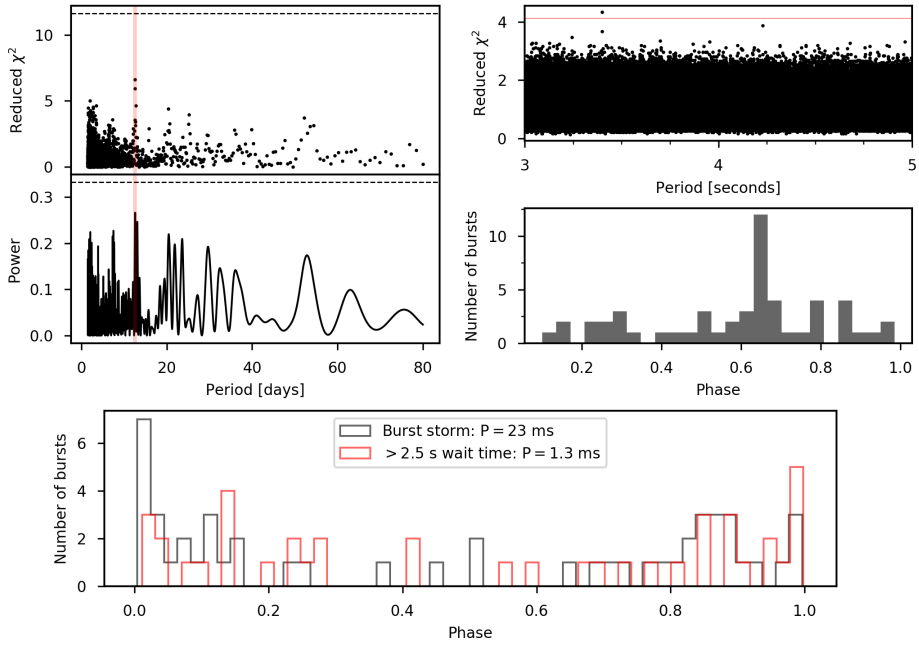

Figure 4.15: Periodicity search results. Top-left sub-figure: The reduced χ^2 for a uniform distribution of burst times as a function of trial activity period (top panel, using 3 bins) and the Lomb-Scargle periodogram (bottom panel) for the entire > 1 yr span of FRB 20200120E observations. The $1-\sigma$ significance level is indicated by the dashed horizontal black line, calculated by bootstrapping 100 and 1000 trials for the reduced χ^2 and Lomb-Scargle, respectively. The red vertical line highlights a candidate at 12.5 days (although continuous monitoring of FRB 20200120E is required to test the significance of this period). Top-right sub-figure: The reduced χ^2 for a uniform distribution of burst times around the highest significance candidate for bursts detected during the 2022 January 14 observation (top panel, using 25 bins). The horizontal red line shows the $3-\sigma$ significance, calculated from the χ^2 survival function. The highest significance candidate (period 3.40 ms) is barely 3σ. Folding the burst ToAs using this period results in bursts arriving across all phases (bottom panel). Bottom sub-figure: The distribution of burst phases assuming the period measured from the brute-force search of an integer divisor of the burst ToAs. See Section 4.4.4 for details of the analysis resulting in this figure.

tion. During the 2022 January 14 observation we have even exposure to all phase bins, but when considering a longer period in the activity of FRB 20200120E (see Section 4.4.4.2), the uneven exposure must be accounted for. This analysis is described in detail in Chime/Frb Collaboration et al. (2020). The reduced χ^2 as a function of period for $n_{\rm bins} = 25$ is shown in Figure 4.15. We computed a significance from the χ^2 survival function, and find 4 periods with significance $\sim 3\sigma$. For those 4 period candidates, we fold the burst ToAs using those periods and find that in all cases the burst ToAs appear across $> 90\%$ of the phase. In Figure 4.15 we plot reduced χ^2 for a small range of periods around the highest significance candidate (period $P = 3.40$ ms), and also plot the histogram of phases after folding the burst ToAs using this period. Since there are no periods that confine the burst ToAs in phase

in a statistically significant way, we conclude that we find no evidence for periodicity in the arrival times.

4.4.4.2 Burst activity

The repeating FRB 20180916B has a confirmed 16.33 ± 0.12 day periodicity in its bursting activity (Chime/Frb Collaboration et al., 2020; Pleunis et al., 2021b). Additionally, FRB 20121102A has a tentative $\sim$ 160 day period in its activity (Rajwade et al., 2020; Cruces et al., 2021). With the $>$ 1 yr span of Effelsberg observations, as well as multi-epoch detections, we aim to search for a similar periodic activity from FRB 20200120E. It may be that the PRECISE detections of 2021 February–April (Kirsten et al., 2022), are one activity cycle, and the 2022 January–March detections presented in this work are a second cycle, giving a period of $\sim$ 11 months, and an activity window of $\sim$ 3 months (Figure 4.1). In this case, however, having only 2 cycles, and a deficit of observations from June 2021 to December 2021, means this is impossible to confirm. Perhaps, however, there is a shorter period in the activity ($<$ 11 months). We used two methods to search for periods between 1.5 days and 80 days: we constrain the lower search limit to 1.5 days to minimise the effect of the sidereal day and above 80 days there are too few cycles to constrain any period meaningfully with the current data.

Since our observations of FRB 20200120E are not evenly sampled in time, we created a Lomb-Scargle periodogram (Lomb, 1976; Scargle, 1982), from 1.5 days to 80 days in 50000 linear steps. We created a list of observation epochs (using the time stamp of the observations beginning), paired with a list of 1s and 0s: 1 when the observation contained at least 1 burst, and 0 when the observation resulted in a non-detection. Following VanderPlas (2018), we then subtracted the mean of this time series, since the Lomb-Scargle model assumes the time series is centred around the mean. The periodogram is shown in Figure 4.15 (top left sub-figure, bottom panel), with a $\sim$12.5-day candidate highlighted. Note that Lomb-Scargle periodograms have a complicated window function due to the uneven sampling of the data. We produced this window function by making a Lomb-Scargle periodogram of a time series reflecting our observing cadence: the time series is 1 for days where we had observations, and 0 for every other day. We confirm that this $\sim$12.5-day candidate is not present in the window function, and is therefore present in the data itself. To determine the 1 σ significance level, we randomly selected 8 days out of our list of observing epochs as 'detection days' and compute the maximum value of the Lomb-Scargle periodogram. We repeated this exercise 1000 times and from the distribution of maximum values compute the 1 σ significance level. The 12.5-day candidate is $< 1\sigma$ in significance when following this approach.

Additionally, we fold the $>$ 1 yr span of observations using periods between 1.5 days to 80 days. We step in frequency by 0.1/(390 days) – or (1/(10 bins))/(separation of first detection and last detection) – and bin the data into 3, 5, and 10 bins. We compare detections per bin with a uniform distribution, similar to the analysis we conducted on the single 2022 January 14 observation described above, calibrating for the uneven exposure per bin (Chime/Frb Collaboration et al., 2020). In Figure 4.15 (top left sub-figure, top panel)

we show the reduced χ^2 as a function of period using a binning of 3 bins per period. The 12.5-day candidate is also evident in this analysis, but with similarly low significance. We bootstrap the significance by randomly selecting 8 detection days from our observing epochs and computing the largest reduced χ^2 value, repeating this exercise 100 times, and from the distribution of maximum reduced χ^2 we compute the $1\,\sigma$ significance level.

Although there is again a candidate at a period of 12.5 days, it is not statistically significant. Continued monitoring of FRB 20200120E at 1.4 GHz is required to confirm whether FRB 20200120E's activity is periodic similar to the behaviour of FRB 20180916B (Chime/Frb Collaboration et al., 2020) and the tentative activity period detected for FRB 20121102A (Rajwade et al., 2020; Cruces et al., 2021).

4.4.5 Energetics

The cumulative distribution of burst fluences appears to turn-over towards low fluences (Figure 4.16). This is likely the result of our inability to detect all bursts close to the sensitivity limit of our observations. We must determine a completeness threshold, above which the fluence distribution accurately reflects the source's behaviour. Selecting the completeness threshold, though, is somewhat ambiguous, and can heavily influence the inferred fluence distribution properties. We used the method of maximum-likelihood to measure the optimal fluence threshold resulting in the best power law fit (Clauset et al., 2007), under the assumption that the bursts follow a power-law energy distribution above some threshold. This method returns a limit of 0.16 Jy ms, which is chosen as the completeness limit since it lines up with where the distribution begins to turn-over by eye, and agrees with the limit derived using the radiometer equation (Cordes & McLaughlin, 2003) and assuming a minimum S/N of 10, a burst width of 300 µs and a burst bandwidth of 150 MHz. This threshold is also consistent with where the power law index, α ($R \propto Fl^{-\alpha}$, for burst rate R above some fluence Fl), flattens out as a function of fluence threshold (Figure 4.16, right), estimated using a Maximum-likelihood method, described in Crawford et al. (1970) and James et al. (2019).

We fitted the cumulative distribution of burst fluences on 2022 January 14 above a completeness threshold of 0.16 Jy ms, using a power-law and a least-squares fit method (Figure 4.16). The fluences are considered to have 20% uncertainty, arising due to the uncertainty in the system values for Effelsberg. The best-fit power law has index $\alpha = 2.39 \pm 0.12$. The uncertainties are the quadratic sum of the statistical fit uncertainties, combined with systematic uncertainties derived by sampling 15 fluences above the completeness threshold, performing the same least-squares fit to the distribution and repeating this process 500 times to measure the standard deviation of the power law indices measured.

In Figure 4.16, in addition to the fluence distribution of the bursts on 2022 January 14, we also plot the fluences of bursts detected at our other observing epochs. Due to the different burst rates between observations, and having only 1 or 2 bursts per observation outside of the burst storm on 2022 January 14, it is difficult to constrain how the energy distribution changes from epoch-to-epoch, as is seen in other FRBs (e.g., Jahns et al., 2022). To test whether the fluences measured on days other than 2022 January 14 are drawn

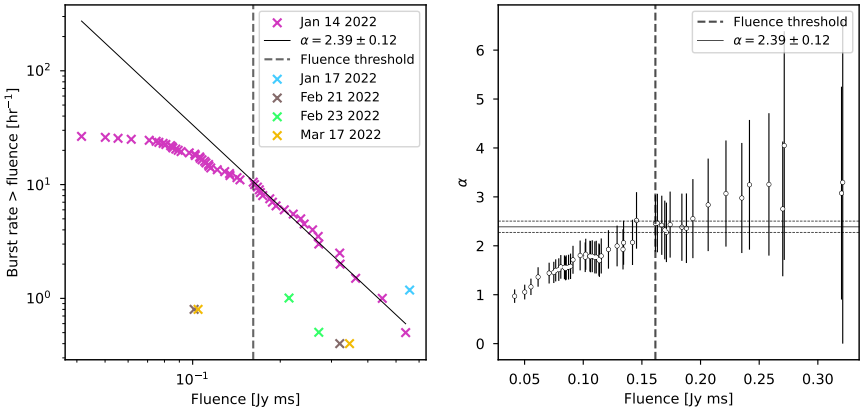

Figure 4.16: Left: Distribution of burst fluences. Different coloured markers, as shown in the legend, represent bursts detected on different observing days. The black solid line represents the best fit power-law to the 2022 January 14 bursts above the fluence threshold. Right: The slope of the power-law α, determined by Maximum-likelihood estimation (Crawford et al., 1970; James et al., 2019) as a function of fluence. The best fit α from the least-squares fit to the distribution is shown by the horizontal line. In both panels, the dashed vertical line represents the completeness limit of 0.16 Jy ms.

4

from a different energy distribution, we performed a Kolmogorov-Smirnov (KS) test using the Python scipy.stats package tool ks_2samp[6]. The critical value for the KS-test is $D = c(p)\sqrt{\left(\frac{N_1+N_2}{N_1 N_2}\right)} = 0.66$, where $c(p) = 1.63$ corresponding to a significance level of 0.01, and N_1, N_2 are the sizes of the two distributions we are comparing. We find a KS statistic of $0.51 < 0.66$, and therefore we *cannot* reject the null hypothesis that the 2022 January 14 fluences and the fluences of the other epochs are drawn from the same distribution. We repeated this exercise adding the first 2 bursts from 2022 January 14 to the fluences at other epochs, motivated by the fact that these bursts occur $\sim$ 15 minutes before the burst storm, seemingly less related to the high activity (see, e.g., Figure 4.12). In this case the critical value is $D = 0.59$ and the measured test statistic is $0.34 < 0.59$, which still cannot rule out all fluences being drawn from the same distribution.

4.5 Discussion

FRB 20200120E is a singular source: it provides a valuable bridge between the populations of known pulsars and bursting magnetars in the Milky Way and Magellanic clouds, and the much more distant FRBs in extragalactic space (Nimmo et al., 2022a). Here we discuss FRB 20200120E in the context of other fast radio transient sources. We show that FRB 20200120E presents many similarities to the phenomena seen from radio-emitting magnetars and repeating FRBs, but its range of luminosities, burst durations, and wait times also distinguish it from these other known sources. It may be possible to reconcile these quanti-

[6] https://docs.scipy.org/doc/scipy/reference/generated/scipy.stats.ks_2samp.html

tative differences by invoking an evolutionary sequence, or spectrum of neutron stars, with a range of rotational rates and magnetic field strengths. Alternatively, FRB 20200120E may originate from a qualitatively different source class.

4.5.1 Lack of DM variations

Comparing our most recent bursts with those detected $>$ 10 months earlier (Nimmo et al., 2022a; Kirsten et al., 2022), we constrain DM variations towards FRB 20200120E to $< 0.15\,\mathrm{pc\,cm^{-3}}$. This is a strong constraint compared to, e.g., the $> 1\,\mathrm{pc\,cm^{-3}}$ variations seen from FRB 20121102A on timescales of months to years (Hessels et al., 2019; Li et al., 2021). The strong constraint on DM variation is consistent with the conclusion that FRB 20200120E is in a relatively 'clean' local environment compared to the extreme magneto-ionic environments of FRB 20121102A (Michilli et al., 2018b) and FRB 20190520B (e.g., Niu et al., 2021). Furthermore, this motivates continued searches for FRB 20200120E bursts at low radio frequencies (< 400 MHz) since such detections can measure more subtle variations in the local medium (Pleunis et al., 2021b). Likewise, the lack of DM variation is also consistent with the hypothesis that FRB 20200120E was formed via accretion-induced collapse, or compact binary merger, in its dense globular cluster environment (Kirsten et al., 2022; Lu et al., 2022; Kremer et al., 2021). Note, however, that the Crab pulsar, which is likely the product of a core-collapse supernova, also shows only small DM variations ($\lesssim 0.02\,\mathrm{pc\,cm^{-3}}$; Driessen et al. 2019). Whereas some repeating FRBs are noisy probes of the intervening magneto-ionised medium, because of their extreme local plasma environments (e.g. Niu et al. 2021), FRB 20200120E demonstrates that some repeaters will serve as accurate probes of the intervening magneto-ionised medium.

4.5.2 Burst storm & time dependent burst rate

The burst rate of FRB 20200120E varies significantly between observing epochs (Table 4.1), with a peak rate of $26.5^{+6.2}_{-5.1}$ bursts/hr averaged over the 2022 January 14 observation. The burst rate is also observed to be highly time variable during the 2022 January 14 observation, with no bursts detected until 1.3 hr into the 2 hr observation, and the rate (computed in 200 s time intervals) ramping up to a maximum 252^{+17}_{-16} bursts/hr, before falling back down towards the end of the observation (Figure 4.12). Due to this rapid rise and decay in burst rate, we refer to this as the first observed 'burst storm' from FRB 20200120E.

The first-discovered repeating FRB, FRB 20121102A (Spitler et al., 2016), is one of the few repeating FRBs whose long-term activity has been studied in detail. The burst rate varies significantly between observing epochs (Li et al., 2021; Hewitt et al., 2021; Jahns et al., 2022) similar to the behaviour we observe here: the peak rate in $\sim$1-hr observations has been observed to be as high as 218 ± 16 bursts/hr, which is less than a factor of 2 higher than the 131 ± 1 bursts/hr Poisson rate for FRB 20200120E (Figure 4.13). Evidence of burst clustering has been observed for FRB 20121102A (Oppermann et al., 2018; Oostrum et al., 2020). At least some of this burst clustering is related to the apparently periodic activity cycle that FRB 20121102A follows ($\sim$160 days; Rajwade et al. 2020; Caleb et al. 2020). During these

active windows, however, the burst wait times are Poisson distributed, but the rate changes from day-to-day (Cruces et al., 2021; Jahns et al., 2022). Although there is only a hint of an activity period for FRB 20200120E, given our observations, we find a similar behaviour: during the burst storm the bursts are consistent with being Poisson distributed (Figure 4.13), and the observations on other days with detections (excluding the storm) are consistent with being Poisson distributed as well (Figure 4.14). The observation of 2022 January 14, however, shows clustering on < 1 hr timescales (Figures 4.12,4.14). This rapid rise in burst rate, before quickly decreasing in rate has been seen before for FRB 20121102A, although at much higher observing frequencies (Gajjar et al., 2018; Zhang, 2018a). For comparison, we plot the burst rate as a function of time in 200 s intervals for both the FRB 20200120E burst storm, and that of FRB 20121102A (Figure 4.17). We, unfortunately, do not see the rate drop completely to zero before the end of our observation, and the FRB 20121102A storm had presumably begun before the beginning of the Gajjar et al. (2018) observation. We do, however, find the durations of the two storms, with rate above 80 bursts/hr, to be comparable ($\sim$ 20 minutes).

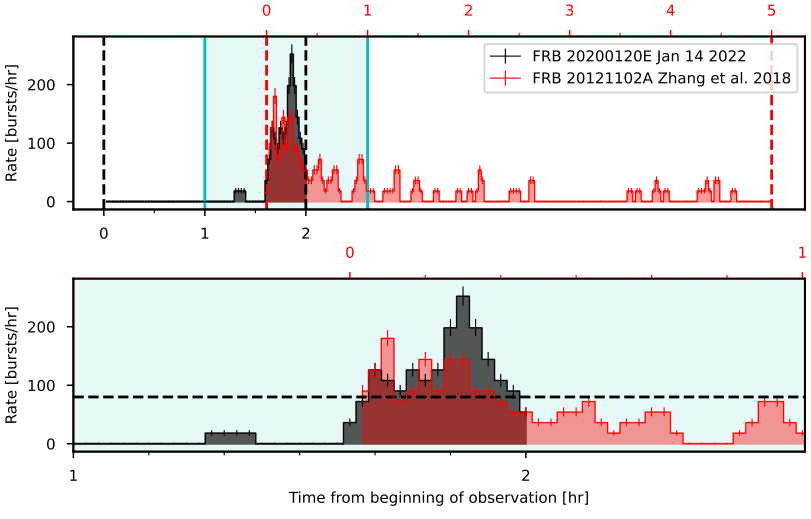

Figure 4.17: Comparison between the burst rate as a function of time for the FRB 20200120E burst storm presented in this work, and that of an observation of FRB 20121102A (Gajjar et al., 2018; Zhang, 2018a). The rates are computed in 200 s time intervals. For the FRB 20200120E observations the time axis is the lower x-axis (in black) from the beginning of the 2022 January 14 observation, while the upper x-axis (in red) is the time axis for FRB 20121102A from the beginning of the Gajjar et al. (2018) observation. The plots have been arbitrarily aligned in time by eye to highlight the comparable temporal extents. The shaded blue region highlights the extent plotted in the zoom-in panel below. The horizontal dashed line represents a burst rate of 80 bursts/hr, above which the duration of the storm for both FRB 20200120E and FRB 20121102A are comparable ($\sim$20 min).

Significant change of burst rate over month-to-year timescales has been observed for the highly active repeating FRB 20201124A (Lanman et al., 2022). Since CHIME is a transit telescope, it has almost daily exposure to FRB 20201124A. This provides strong constraints on the burst rate of FRB 20201124A in the years prior to discovery in 2020, and how the

burst rate slowly evolved into an outburst in 2021 (Lanman et al., 2022). The burst rate through the outburst varies on day-to-day timescales, rising sharply to the peak reaching a plateau and rapidly turning off (Xu et al., 2021). Perhaps this is a similar phenomenon to what has been observed from FRB 20200120E in this work (Figure 4.1). Xu et al. (2021) also observe day-to-day changes in the Weibull k parameter, varying from Poissonian ($k = 1$) to clustered ($k < 1$) between observations. The peak burst rate per observation at 1.5 GHz (similar central frequency as the observations presented in this work) is $45.8^{+7.8}_{-8.3}\,\mathrm{hr}^{-1}$ (Xu et al., 2021), consistent with our measured burst rate from the 2022 January 14 observation (Table 4.1).

Magnetars are observed to go into outburst, producing tens to hundreds of X-ray bursts per hour (Gavriil et al., 2004; Israel et al., 2008; van der Horst et al., 2012). The Galactic magnetar SGR 1935+2154, is currently the only known Galactic object that has produced a millisecond-duration radio transient with luminosity comparable to that of the extragalactic FRBs (albeit still 1–2 orders of magnitude weaker than the least luminous FRBs; CHIME/FRB Collaboration et al. 2020; Bochenek et al. 2020). SGR 1935+2154 went into outburst in 2020, hours before the FRB-like transient was discovered, with a burst rate of $\sim$ 720 bursts/hr (Fletcher & Fermi GBM Team, 2020; Palmer, 2020; Younes et al., 2020). This outburst was observed to have a consistently high rate for at least 20 minutes, before rapidly dropping in rate to $\sim$ 29 bursts/hr in only 3 hours.

In the case of giant pulse emitters, variations in giant pulse rate have been observed between observing epochs: e.g., the Crab pulsar (PSR B0531+21), where the rate of high fluence ($>$ 130 Jy ms) giant pulses vary by up to a factor of 5 between observing days (Bera & Chengalur, 2019), and the 'Crab twin' PSR B0540−69 in the Large Magellanic Cloud, which has giant pulse rate variations of 65 /hr to 221 /hr between epochs separated by $\sim$ months (Geyer et al., 2021).

4.5.3 Energetics

The spectral luminosities of FRB 20200120E bursts are at least two orders of magnitude lower compared to other known repeating FRBs (Nimmo et al., 2022a), and even $\sim 10\times$ lower than the exceptionally bright event seen from SGR 1935+2154 on April 28 2020 (Bochenek et al., 2020; CHIME/FRB Collaboration et al., 2020). In our unprecedentedly large sample of FRB 20200120E bursts we also see a relatively narrow range of burst fluences, spanning only about an order-of-magnitude from 0.04 Jy ms to 0.6 Jy ms. This limited range is partly due to being strongly sensitivity limited, despite the large aperture of the Effelsberg telescope. Furthermore, many of the bursts we detect are below our nominal completeness threshold of 0.16 Jy ms and only detectable because of their bright, narrow-band scintles. Larger on-sky time ($>$ 100 hr) may still reveal FRB 20200120E bursts that are more comparable in their energetics to other repeaters, but nonetheless FRB 20200120E appears to be, at least on average, an anomalously weak source that is only detectable because of its exceptional proximity to Earth (Bhardwaj et al., 2021a; Kirsten et al., 2022).

Furthermore, we measure a steep power-law ($\alpha = 2.39 \pm 0.12$, see Section 4.4.5) burst energy distribution above our fluence threshold of 0.16 Jy ms. Unless FRB 20200120E is found to have a bi-modal and/or time-variable energy distribution, with a flatter tail at high fluences, then it is unlikely that ongoing observing campaigns will detect bursts that are much above a fluence of 2 Jy ms at 1.4 GHz (corresponding to an isotropic-equivalent spectral luminosity of $\sim 2.4 \times 10^{29}$ erg s^{-1} Hz^{-1}). For comparison, Bhardwaj et al. (2021a) find fluences of $\sim$ 2 Jy ms in the 400 − 800 MHz range. Given that the bursts we detect at 1.4 GHz are typically $\sim$ 0.2 Jy ms, this suggests an average spectral index, $S \propto \nu^{-\beta}$ of $\beta \sim 2 - 3$. If this were to continue to low radio frequencies, then the expected average fluence at 150 MHz is $\sim 30 - 130$ Jy ms, easily detectable by LOFAR or uGMRT.

The burst energy distribution of FRB 20200120E is comparable to that of the Crab pulsar (Karuppusamy et al., 2010). It is significantly steeper than the energy distribution seen from FRB 20121102A (Li et al., 2021; Hewitt et al., 2021), but conversely much flatter compared to what has been observed from FRB 20201124A (Lanman et al., 2022). We caution, however, that FRB 20121102A has shown a bi-modal and time-variable burst energy distribution (Li et al., 2021; Hewitt et al., 2021). This bi-modality could indicate that the source produces multiple types of bursts, or that some bursts are apparently boosted in energy due to local propagation effects like plasma lensing (Cordes et al., 2017). Our burst energy distribution for FRB 20200120E is based on a single burst storm and may not be representative of its average behaviour. Future detections of burst storms from FRB 20200120E can test this. The pulse energy distributions of the Crab and other pulsars appear to be stable with time (Bera & Chengalur, 2019). If the burst energy distributions of repeating FRBs are found to be time variable then models of the emission process need to explain this behaviour.

4.5.4 Burst durations and morphology

The $\sim$ 100 µs bursts from FRB 20200120E are on average $> 10\times$ shorter-duration compared to other known repeaters (Nimmo et al., 2022a; Pleunis et al., 2021a; Li et al., 2021; Xu et al., 2021). Previous studies have also detected (sub-)microsecond burst structure from FRB 20200120E (Nimmo et al., 2022a; Majid et al., 2021). Coupled with the much lower burst luminosities from FRB 20200120E compared to other repeaters, this suggests that future studies using large burst samples should investigate whether there is a correlation between burst duration and luminosity. Multi-frequency observations of FRB 20121102A have demonstrated that its bursts are on average narrower and less luminous at high radio frequencies (Michilli et al., 2018b; Gajjar et al., 2018; Josephy et al., 2019). Future observations should aim to establish such a trend for FRB 20200120E as well.

The voltage data we have collected here has also allowed us to constrain how often FRB 20200120E produces ultra-short bursts, on timescales of microseconds or less. The lack of interstellar or intergalactic scattering towards FRB 20200120E, along with its stable DM, also make it a prime target to explore ultra-short timescales. We find no evidence for microstructure in our sample of FRB 20200120E bursts, nor do we identify any additional bursts in a separate search of the 2022 January 14 data at a time resolution of 1 µs. While

some FRB 20200120E bursts do present structure on (sub-)microsecond timescales (Nimmo et al., 2022a; Majid et al., 2021), we conclude that such timescales are relatively rare[7] and that most bursts have minimum timescales of variation on the order of $> 10\,\mu s$.

Nonetheless, we find that the rise times of FRB 20200120E bursts are typically very short: $50 - 200\,\mu s$. This constrains the size of the emission region to tens of kilometres or less, though relativistic effects may also be relevant. The decay times we measure are typically twice as long, and this asymmetry should be explained in emission models. We note that magnetar X-ray bursts are often also well modelled by a faster rise and slower decay (Huppenkothen et al., 2015).

In any case, the intrinsic asymmetry of the bursts, along with the potential for time-frequency drifts (Hessels et al., 2019), demonstrates that caution is needed when inferring scattering times from FRBs. Burst B33 from 2022 January 14 is the best example of a 'sad trombone' drift in our new burst sample (see Figure 4.2). This effect is also clearly visible in the baseband data from the discovery of FRB 20200120E (Bhardwaj et al., 2021a, see their Figure 1), and provides an important phenomenological link with the rest of the known repeater population. In addition, we find that the FRB 20200120E bursts are sometimes narrow band ($\Delta\nu \sim 200\,MHz$), as has been seen in other repeaters (Hessels et al., 2019; Gourdji et al., 2019; Kumar et al., 2021). The average burst spectrum from the burst storm shows two $\sim 100\,MHz$ features (Figure 4.7), reminiscent of the spectral structure in the Majid et al. (2021) FRB 20200120E burst, and unlike typical repeater spectra. However, it has been shown that narrow-band FRB 20121102A bursts exhibit preferred frequencies, consistent on timescales of days (Gourdji et al., 2019; Hewitt et al., 2021).

4.5.5 Burst wait times

We find 3 peaks in the wait time distribution of bursts from FRB 20200120E (Figure 4.13). The main peak at $\sim 25\,s$ simply reflects the overall burst rate, where on relatively short timescales of $< 1\,hr$ we find the wait times to be reasonably well modelled by a Poissonian process.

We also find a secondary peak in the burst wait times of FRB 20200120E at $\sim 1\,s$. This is reminiscent of the secondary, shorter-timescale wait time peaks seen for FRB 20121102A (Gourdji et al., 2019; Li et al., 2021; Hewitt et al., 2021; Jahns et al., 2022) and FRB 20201124A (Xu et al., 2021), though those sources both show such a peak at $\sim 30\,ms$, roughly a $50\times$ shorter timescale. These secondary wait-time peaks demonstrate that once a burst has occurred, it is more likely to detect a second or third burst in short succession. This deviates from the general Poisson wait-time distribution. We suggest that these secondary wait-time peaks represent a timescale on which repeated burst emission can occur, and that this could be related to the overall physical size in which burst emission can be generated around the central engine as well as the timescale on which perturbations traverse this region. If so, then the much longer $\sim 1\,s$ timescale of FRB 20200120E could indicate a much larger

[7] It is, of course, possible that micro-bursts are common but that they typically overlap in time, therefore our results indicate that **isolated** micro-bursts are rare.

overall emission region, or slower propagation of disturbances, compared to the $\sim$ 30 ms timescales that are observed for FRB 20121102A and FRB 20201124A. While the secondary wait-time peak of FRB 20200120E is $\sim 50\times$ longer in duration compared to FRB 20121102A and FRB 20201124A, its bursts are typically $\sim 30\times$ shorter. It is worth considering whether these timescales are related.

Lastly, two of the bursts we detect from FRB 20200120E show sub-millisecond separations between sub-bursts, and this suggests that there may also be a tertiary wait-time peak on this timescale. Other repeaters have also shown a characteristic spacing of wait-times between sub-bursts on timescales of roughly milliseconds (e.g., Hessels et al. 2019). This timescale may reflect the microphysics related to the coherent emission process: e.g., the interplay between charge bunching and radiative feedback (Lyutikov, 2021). Some authors have also interpreted the quasi-periodic spacing of FRB sub-bursts in the context of outward propagating plasma oscillations (Sobacchi et al., 2021).

4.5.6 Periodicity constraints

We searched for a strict periodicity in the arrival times of the bursts, focusing on the relatively large sample of 53 bursts from the 2022 January 14 storm. Given the short burst durations of typically $\sim$ 100 μs, our analysis should be sensitive to rotational periods of $\sim$ 1 ms or longer, if the bursts are clustered in rotational phase. Note that the methods we used are sensitive to bursts occurring in multiple rotational phase windows, as is sometimes seen from pulsars and radio-emitting magnetars (Camilo et al., 2006). The sample of 53 bursts from the 2022 January 14 observation shows no statistically significant evidence for a short-duration period in the burst arrival times, and hence we conclude that — if FRB 20200120E is a rotating object with a period between 1 ms and 25 s — the bursts are roughly evenly distributed in rotational phase. This is consistent with the lack of detectable periodicity in other repeaters (Gourdji et al., 2019; Li et al., 2021; Hewitt et al., 2021).

Nonetheless, we caution that a larger burst sample may reveal a more subtle clustering of bursts in rotational phase, and that clustering could potentially be time-variable: e.g., radio-emitting magnetars show evolving pulse profiles that can be stable on timescales of days to weeks or longer (Camilo et al., 2006). The lack of observable periodicity distinguishes FRB 20200120E from known giant pulse emitters and suggests that the emission region changes chaotically between the bursts.

We also searched the collection of known bursts from all our observations to see if there is evidence for periodicity in FRB 20200120E's activity rate. Such searches are motivated by the well-established 16.3-day periodicity of FRB 20180916B (Chime/Frb Collaboration et al., 2020) and the candidate 160-day periodicity of FRB 20121102A (Rajwade et al., 2020; Cruces et al., 2021). Though we find a hint for a 12.5-day period, a factor of a few more cycles are needed to ascertain if this will become statistically significant, or not.

4.6 Conclusions & future work

We have presented the first-known 'burst storm' from FRB 20200120E, in which 53 bursts were detected in < 1 hr of observation with the 100-m Effelsberg telescope on 2022 January 14. We characterise this event as a burst storm because of the high and rapidly varying burst rate, which is reminiscent of the X-ray burst storms seen from magnetars. The energy distribution of the burst storm is a steep power law ($\alpha = 2.39 \pm 0.12$ above a fluence threshold of 0.16 Jy ms). We used these closely spaced bursts to search for a strict periodicity in the arrival times, but find no such signal, consistent with other known repeating FRBs. The burst wait times do, however, show a secondary peak at ~ 1 s. This is reminiscent of the secondary wait-time peaks seen for two other repeating FRBs on significantly shorter timescales of ~ 30 ms. The secondary wait time peak may represent a characteristic timescale related to the overall size of the system.

We also present an additional 7 bursts, which were detected in 4 other observing sessions in 2022 January through March. During these observations, the lower and more stable burst rate suggests that the source was in a different state compared to the 2022 January 14 storm. We used these and other observations, including those with non-detections, to search for periodic activity but find only tentative evidence for a 12.5-day period.

The observational record to date demonstrates that the DM of FRB 20200120E is highly stable, unlike some other repeaters, and that its bursts are characteristically $\sim 30\times$ shorter in duration and $\sim 100\times$ less luminous compared to other known repeaters. Nonetheless, the narrow-band emission and time-frequency drift ('sad trombone' effect) seen from FRB 20200120E provide important observational links to other repeaters. By comparing our $1.2 - 1.6$-GHz burst sample to that detected from $400 - 800$ MHz by CHIME/FRB (Bhardwaj et al., 2021a), we find that the average spectral index is quite steep: $\beta = 2 - 3$, indicating that there are good prospects for detecting FRB 20200120E at very low frequencies (< 400 MHz).

We show that FRB 20200120E bursts typically have fast rise (~ 100 μs) and slower decay (~ 200 μs), but that this asymmetry is not due to scattering. Whereas previous observations have demonstrated (sub-)microsecond structure in the bursts from FRB 20200120E, we find that such short timescales occur rarely (or that the microstructure is typically bunched in time, as opposed to being resolvable). Additionally, searches of our voltage data using coherent dedispersion and a time resolution of 1.28 μs led to the discovery of only one additional, low-S/N burst compared to our initial searches at 40.96 μs time resolution. This burst is the narrowest in the sample presented here, with a temporal scale of ~ 14 μs. We find no bursts with durations < 10 μs.

Given the observations to date, we suggest that the most urgent avenues for future observational investigation are:

- Detect the source both below 400 MHz and above 3 GHz to establish whether the burst widths are frequency-dependent.

- Continue the observational timeline in order to establish or rule out periodic variations in the source's activity.
- Use future detections to further constrain subtle DM and RM variations.

From the point-of-view of understanding the nature of FRB 20200120E, we encourage theorists to focus on a self-consistent picture that explains the: i. low burst luminosities, ii. short burst durations, iii. $\sim$ 1-s secondary wait-time peak and iv. steep average burst spectrum. Each of these quantities deviates quite significantly from other known repeaters, and it may be possible to link these burst properties to those of the central engine (e.g., its rotation rate, magnetic field strength, age, etc.).

Acknowledgements

K. N. would like to thank P. Chawla and K. Rajwade for helpful discussions about the analysis presented in this work.

This paper is based on observations with the 100-m telescope of the MPIfR (Max-Planck-Institut für Radioastronomie) at Effelsberg.

Research by the AstroFlash group at University of Amsterdam, ASTRON and JIVE is supported in part by an NWO Vici grant (PI Hessels; VI.C.192.045).

This project has received funding from the European Union's Horizon 2020 research and innovation programme under grant agreements No 730562 (RadioNet) and 101004719 (OPTICON-RadioNet Pilot).

B. M. acknowledges support from the Spanish Ministerio de Economía y Competitividad (MINECO) under grants AYA2016-76012-C3-1-P, FPA2017-82729-C6-2-R, and MDM-2014-0369 of ICCUB (Unidad de Excelencia "María de Maeztu")

ZOOMING-IN IN SPACE

Chapter 5

Milliarcsecond localization of the repeating FRB 20201124A

K. Nimmo, D. M. Hewitt, J. W. T. Hessels, F. Kirsten, B. Marcote, U. Bach, R. Blaauw, M. Burgay, A. Corongiu, R. Feiler, M. P. Gawroński, M. Giroletti, R. Karuppusamy, A. Keimpema, M. A. Kharinov, M. Lindqvist, G. Maccaferri, A. Melnikov, A. Mikhailov, O. S. Ould-Boukattine, Z. Paragi, M. Pilia, A. Possenti, M. P. Snelders, G. Surcis, M. Trudu, T. Venturi, W. Vlemmings, N. Wang, J. Yang, J. Yuan

The Astrophysical Journal Letters, 2022, 927, L3

Abstract

Very long baseline interferometric (VLBI) localisations of repeating fast radio bursts (FRBs) have demonstrated a diversity of local environments: from nearby star-forming regions to globular clusters. Here we report the VLBI localisation of FRB 20201124A using an *ad-hoc* array of dishes that also participate in the European VLBI Network (EVN). In our campaign, we detected 18 bursts from FRB 20201124A at two separate epochs. By combining the visibilities from both epochs, we were able to localise FRB 20201124A with a 1-σ uncertainty of 2.7 milliarcseconds (mas). We use the relatively large burst sample to investigate astrometric accuracy, and find that for $\gtrsim 20$ baselines ($\gtrsim 7$ dishes) that we can robustly reach milliarcsecond precision even using single-burst data sets. Sub-arcsecond precision is still possible for single bursts, even when only $\sim$ six baselines (four dishes) are available. In such cases, the limited *uv*-coverage for individual bursts results in very high side-lobe levels. Thus, in addition to the peak position from the dirty map, we also explore smoothing the structure in the dirty map by fitting Gaussian functions to the fringe pattern in order to constrain individual burst positions, which we find to be more reliable. Our VLBI work places FRB 20201124A 710 ± 30 mas (1-σ uncertainty) from the optical centre of the host galaxy, and consistent with originating from within the recently-discovered extended radio structure associated with star-formation in the host galaxy. Future high-resolution optical obser-

vations, e.g. with *Hubble Space Telescope*, can determine the proximity of FRB 20201124A's position to nearby knots of star formation.

5.1 Introduction

Fast radio bursts (FRBs) are highly luminous, short-duration coherent radio transients (for recent reviews see Petroff et al., 2019, 2022; Cordes & Chatterjee, 2019). The vast majority of the observed FRB population are apparently one-off events, but a few percent of the known FRBs have been seen to repeat. Whether all FRBs are capable of repeating, or if the observed FRB population comes from multiple origins, remains debated. Nonetheless, the large sample provided by CHIME/FRB (CHIME/FRB Collaboration et al., 2018) shows statistical differences between the properties of apparent one-offs and repeaters (Pleunis et al., 2021a). The repeating sources are particularly valuable in our efforts to understand the nature of FRBs, since they allow for follow-up observations to, e.g., explore their burst energy distribution (Gourdji et al., 2019; Li et al., 2021; Hewitt et al., 2021), characterise the evolution of the burst properties with time and frequency (Gajjar et al., 2018; Michilli et al., 2018b; Hilmarsson et al., 2021a; Pleunis et al., 2021b), and probe the immediate surroundings of the FRB source through precise localisation with very long baseline interferometry (VLBI) and high-resolution optical imaging (Bassa et al., 2017; Tendulkar et al., 2021; Mannings et al., 2021).

To date, 19 FRBs have been localised with sufficient precision ($<$ a few arcseconds) to identify their host galaxy (e.g., Chatterjee et al., 2017; Ravi et al., 2019; Bannister et al., 2019; Heintz et al., 2020; Bhandari et al., 2022)[1]. Thus far, only three of these are localised to 1–10 milliarcsecond precision using VLBI (Marcote et al., 2017, 2020; Kirsten et al., 2022). With VLBI precision, the exact location of the FRB progenitor within the host galaxy can be determined and matched with any prominent features, like spiral arms, the galactic nucleus, or star-forming regions. This is particularly useful if the host can be resolved with *Hubble Space Telescope* observations (Bassa et al., 2017; Tendulkar et al., 2021; Mannings et al., 2021).

VLBI localisations of repeating FRBs have uncovered a diversity of local environments: FRB 20121102A, the first-known repeater, is spatially coincident with a compact persistent radio source and inside a star-forming region in a dwarf host galaxy (Chatterjee et al., 2017; Marcote et al., 2017; Tendulkar et al., 2017; Bassa et al., 2017); FRB 20180916B is located in the spiral arm of a Milky Way-like host, approximately 250 pc from the peak of a prominent star-forming knot (Marcote et al., 2020; Tendulkar et al., 2021); and FRB 20200120E was discovered to be in a globular cluster that is associated with the grand design spiral galaxy M81 (Bhardwaj et al., 2021a; Kirsten et al., 2022). This diversity highlights that the progenitors of repeating FRBs are able to live in different types of environments or, alternatively, that there is more than one progenitor type for repeating FRBs. Additional VLBI FRB localisations, combined with comparably high resolution optical and radio imaging, allow us to study the immediate environments of FRBs (e.g. a surrounding nebula) and to compare with other astronomical source classes. This will help uncover the full diversity of FRB local environments, giving insight into the FRB progenitor(s).

[1] https://frbhosts.org/

In this Letter, we present the European VLBI Network (EVN) localisation of the repeating FRB 20201124A. FRB 20201124A was in a period of heightened activity in April 2021 (Chime/Frb Collabortion, 2021), during which we detected a total of 18 bursts at two epochs. A preliminary EVN position was originally reported in Marcote et al. (2021), who used data only from the first epoch. Here, we describe in detail the interferometric observations (§ 5.2), followed by the analysis and results (§ 5.3). Because we detected a relatively large sample of bursts at two separate epochs, a first for FRB observations using the VLBI technique, we use this to test the astrometric accuracy of the method (§ 5.4). We investigate the astrometric accuracy for individual bursts and low number of available antennas. Finally, we discuss our results in the context of recent studies of FRB 20201124A and other FRBs.

5.2 Observations

We observed FRB 20201124A on April 10 2021 15:00 – 21:00 UT (project ID pr153a) and April 19 2021 13:30 – 19:30 UT (project ID pr156a) as part of our ongoing FRB VLBI localisation project, PRECISE (Pinpointing REpeating ChIme Sources with Evn dishes)[2]. We used an *ad-hoc* array of 6 and 9 radio telescopes (that are also part of the EVN) on April 10 and 19, respectively. We pointed at the position derived from earlier Very Large Array (VLA) observations: RA (J2000) = $5^{\rm h}08^{\rm m}03.5^{\rm s}$, Dec (J2000) = $+26^\circ03'37.8''$ (Law et al., 2021). The telescopes that participated in our campaign were Onsala (On-85), Toruń, Irbene, Westerbork single-dish RT1, Noto and Effelsberg at Epoch 1, and Onsala (On-85), Toruń, Irbene, Westerbork single-dish RT1, Medicina, Svetloe, Badary, Sardinia and Effelsberg at Epoch 2. The central observing frequency of our observations was 1.4 GHz, and the bandwidth and number of subbands was dependent on the capabilities at each station (see Table 5.1). Phase referencing was done with a cycle time of 6–8.5 min: 1.5–2.5 min on the phase calibrator source (J0502+2516, at a separation of 1.4° from FRB 20201124A), followed by 4.5–6.5 min on target. We use the position of J0502+2516 reported in the rfc2018a catalogue[3] during correlation: RA (J2000) = $5^{\rm h}02^{\rm m}58.474768^{\rm s}$, Dec (J2000) = $+25^\circ16'25.27549''$ (offset by 0.09 mas in RA and Dec from the rfc2021c catalogue[4], i.e. within the listed uncertainty of 0.12 mas). Scans of J1048+7143 and J0555+3948 were taken to use as fringe finders and bandpass calibrators in the first and second epoch, respectively. Additionally, we observed the pulsar PSR J2257+5909 for 5 min per epoch to test the data quality of the single-dish data, and frequent, phase-referenced scans of J0501+2530 to use as an interferometric check source. In total, we observed the target FRB 20201124A for 7.1 hours.

We recorded raw voltage data with dual circular polarisation and 2-bit sampling from each telescope that participated, in either VDIF (Whitney et al., 2010) or MARK5B (in the case of Svetloe and Badary; Whitney 2004) format. In parallel, we simultaneously recorded pulsar backend data at Effelsberg during both epochs and at Sardinia during Epoch 2. At Effelsberg, total intensity filterbank data were recorded using the PSRIX pulsar backend (Lazarus et al., 2016). Unfortunately, the PSRIX data recorded on April 10 suffered from an incorrect

[2] https://www.ira.inaf.it/precise/Home.html
[3] http://astrogeo.org/vlbi/solutions/rfc_2018a/
[4] http://astrogeo.org/sol/rfc/rfc_2021c/

Table 5.1: Individual telescope configurations used during our interferometric observations.

Telescope	Frequency coverage (MHz)	No. of subbands	Epoch[a]
Effelsberg (Ef)	1254 – 1510	16 × 16 MHz	1,2
Onsala (O8)	1254 – 1510	16 × 16 MHz	1,2
Toruń (Tr)	1254 – 1510	16 × 16 MHz	1,2
Irbene (Ir)	1382 – 1510	8 × 16 MHz	1,2
Westerbork (Wb)	1382 – 1510	8 × 16 MHz	1,2
Noto (Nt)	1318 – 1574	16 × 16 MHz	1
Medicina (Mc)	1350 – 1478	8 × 16 MHz	2
Svetloe (Sv)	1382 – 1510	8 × 16 MHz	2
Badary (Bd)	1382 – 1510	8 × 16 MHz	2
Sardinia (Sr)	1350 – 1606	8 × 32 MHz	2

[a] Epochs during which the telescope participated, where Epoch 1 corresponds to EVN project code EK048D, and Epoch 2 is EK048E.

observing set-up and were not usable. The PSRIX data on April 19 was recorded with time and frequency resolutions of 102.4 µs and 0.49 MHz, respectively, and a usable frequency range of 1255–1505 MHz. At Sardinia, the pulsar data were recorded using the Digital Filterbank Mark III backend (DFB; Prandoni et al., 2017), in psrfits format (Hotan et al., 2004). These data have time and frequency resolutions of 128 µs and 1 MHz, respectively and a frequency range of 1140.5–2163.5 MHz, of which 1210.5–1739.5 MHz is usable (given the receiver response and radio frequency interference).

5.3 Analysis and Results

5.3.1 Burst discovery

For both Effelsberg and Sardinia, the raw voltage data and pulsar backend data were independently searched for bursts using distinct analysis pipelines. We converted the raw voltage data to filterbank format with a time and frequency resolution of 128 µs and 125 kHz, respectively, using digifil (van Straten & Bailes, 2011). We used a Heimdall-based search to identify candidate FRBs, which were then classified using the machine learning classifier FETCH (specifically, models A and H with a 50% probability threshold; Agarwal et al., 2020). In total, 27 candidates were identified by FETCH, of which 18 were deemed astrophysical in nature by human inspection: 13 bursts on April 10 (Epoch 1) and a further 5 on April 19 (Epoch 2).

A single-pulse search of the PSRIX and DFB data was conducted using PRESTO tools (Ransom, 2001), including masking of radio frequency interference (RFI) using the rfifind tool. The candidate FRBs were then classified using an automated clustering classifier based on Michilli et al. (2018a). The data quality and analysis strategy was tested using a scan of the test pulsar PSR J2257+5909. We independently found all 5 bursts from Epoch 2 in the PSRIX data while only B14 was found in this way in the DFB data from Sardinia. The DFB data were additionally searched using a Spandak-based pipeline[5] (Gajjar et al., 2021, 2018)

[5] https://github.com/gajjarv/PulsarSearch

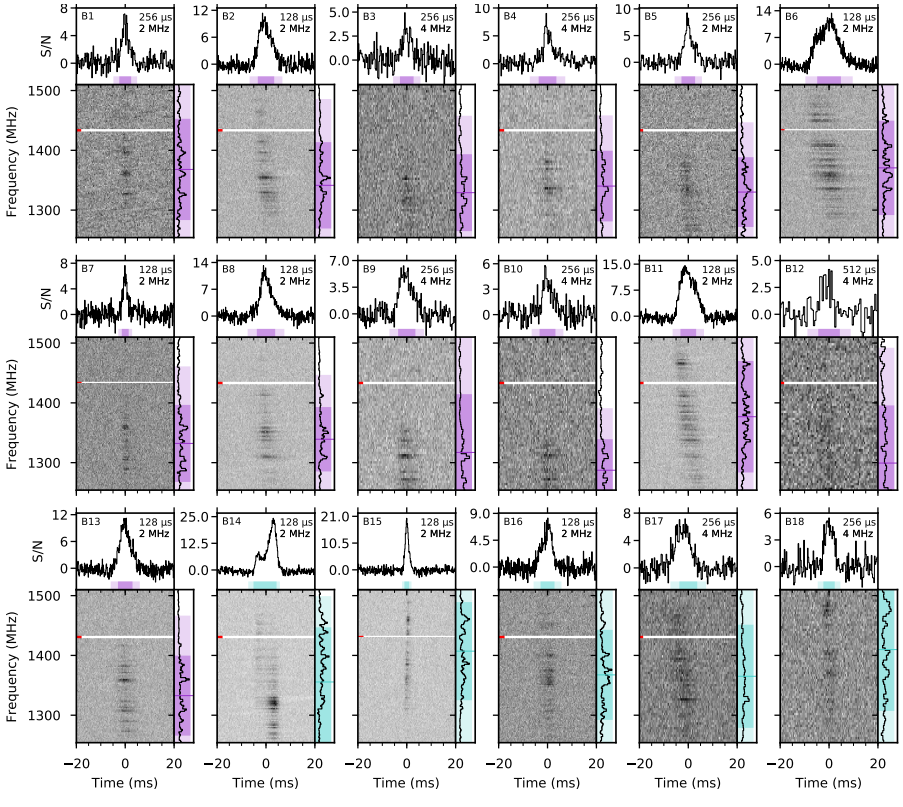

Figure 5.1: Dynamic spectra, temporal profiles, and time-averaged spectra for all 18 bursts presented in this work. For each sub-figure, the burst name and time/frequency resolution is shown in the top left and top right, respectively. The coloured bars represent the 1-σ (dark) and 2-σ (light) regions of the temporal width and spectral extent of each burst. The purple colour is used for bursts detected during Epoch 1, and cyan for those detected during Epoch 2. Data which has been masked due to radio frequency interference is not plotted, and indicated with the red ticks. Each burst has been de-dispersed using a dispersion measure of 412 pc cm^{-3}.

which discovered B15 and B16. Post-search analysis revealed that the other bursts were either below the S/N threshold of 7 used in the search, or coincident with severe RFI and consequently ruled non-astrophysical by the classifier.

For the remainder of this Letter, the bursts are named Bn, where n is an integer from 1 to 18, ordered according to the burst arrival time.

5.3.2 Localisation

The interferometric data were correlated using the software correlator SFXC (Keimpema et al., 2015) at the Joint Institute for VLBI ERIC (JIVE; in the Netherlands), with an integration time of 2 s and 64 channels per 16 MHz subband (under the EVN correlation-only proposal EK048, PI: Kirsten). Using the arrival times of the 18 FRB 20201124A bursts detected during our PRECISE campaign, a second correlation was performed for only the data containing bursts, where the gate width used for correlation was determined by eye to maximise the signal-to-noise ratio (S/N). These values are recorded in Table 5.2. The phase centre used for correlation was the VLA FRB 20201124A localisation position (Law et al., 2021), which has an uncertainty of approximately 1 arcsecond. This meant that we were not required to correlate the data for a third time to move the phase centre closer to the FRB position, as has been required in previous VLBI FRB projects (Marcote et al., 2020; Kirsten et al., 2022).

Table 5.2: Interferometric burst properties.

Burst	Peak position[a] [RA, Dec (J2000)]	Gaussian position[b] [RA, Dec (J2000)]	$\sigma^{c}_{\rm maj}$ [mas]	$\sigma^{d}_{\rm min}$ [mas]	θ^{e} [deg]	Peak flux density[f] [Jy/beam]	S/N[g]	Gate width [ms]	Effective no. of baselines[h]
Epoch 1									
B1	$05^{\rm h}08^{\rm m}03.5070^{\rm s}$, $+26^\circ03'38.503''$	$05^{\rm h}08^{\rm m}03.5099^{\rm s}$, $+26^\circ03'38.5068''$	496.1	196.5	46.4	0.34 ± 0.06	11.3	4.12	10
B2	$05^{\rm h}08^{\rm m}03.5073^{\rm s}$, $+26^\circ03'38.504''$	$05^{\rm h}08^{\rm m}03.5133^{\rm s}$, $+26^\circ03'38.4931''$	731.9	331.5	52.5	0.65 ± 0.05	13.8	8.49	10
B3	$05^{\rm h}08^{\rm m}03.4865^{\rm s}$, $+26^\circ03'38.601''$	$05^{\rm h}08^{\rm m}03.4997^{\rm s}$, $+26^\circ03'38.5736''$	1029.9	498.5	55.8	0.19 ± 0.04	5.2	4.02	6
B4	$05^{\rm h}08^{\rm m}03.5170^{\rm s}$, $+26^\circ03'38.441''$	$05^{\rm h}08^{\rm m}03.5112^{\rm s}$, $+26^\circ03'38.5055''$	773.1	353.3	55.8	0.32 ± 0.05	7.4	5.15	6
B5	$05^{\rm h}08^{\rm m}03.5140^{\rm s}$, $+26^\circ03'38.529''$	$05^{\rm h}08^{\rm m}03.5097^{\rm s}$, $+26^\circ03'38.5686''$	624.6	270.7	89.9	0.24 ± 0.03	10.7	7.50	6
B6	$05^{\rm h}08^{\rm m}03.5068^{\rm s}$, $+26^\circ03'38.504''$	$05^{\rm h}08^{\rm m}03.5079^{\rm s}$, $+26^\circ03'38.496''$	762.3	324.8	105.6	0.95 ± 0.06	13.5	14.54	15
B7	$05^{\rm h}08^{\rm m}03.4822^{\rm s}$, $+26^\circ03'38.482''$	$05^{\rm h}08^{\rm m}03.5155^{\rm s}$, $+26^\circ03'38.5333''$	1203.2	487.3	110.8	0.33 ± 0.05	7.3	3.78	6
B8	$05^{\rm h}08^{\rm m}03.5063^{\rm s}$, $+26^\circ03'38.496''$	$05^{\rm h}08^{\rm m}03.5076^{\rm s}$, $+26^\circ03'38.4971''$	1267.3	382.9	114.4	0.54 ± 0.06	13.4	10.75	6
B9	$05^{\rm h}08^{\rm m}03.5102^{\rm s}$, $+26^\circ03'38.229''$	$05^{\rm h}08^{\rm m}03.5046^{\rm s}$, $+26^\circ03'38.4606''$	1535.8	611.9	109.0	0.23 ± 0.04	9.2	8.47	6
B10	$05^{\rm h}08^{\rm m}03.5290^{\rm s}$, $+26^\circ03'38.985''$	$05^{\rm h}08^{\rm m}03.5148^{\rm s}$, $+26^\circ03'38.8008''$	1088.9	334.2	118.2	0.21 ± 0.03	7.7	6.01	6
B11	$05^{\rm h}08^{\rm m}03.5097^{\rm s}$, $+26^\circ03'38.519''$	$05^{\rm h}08^{\rm m}03.5062^{\rm s}$, $+26^\circ03'38.4736''$	1327.6	274.1	128.2	1.29 ± 0.20	16.6	10.56	15
B12	$05^{\rm h}08^{\rm m}03.4839^{\rm s}$, $+26^\circ03'38.661''$	–	–	–	–	0.17 ± 0.03	4.3	5.12	15
B13	$05^{\rm h}08^{\rm m}03.5509^{\rm s}$, $+26^\circ03'39.034''$	–	–	–	–	0.67 ± 0.06	13.3	8.18	6
Epoch 2									
B14	$05^{\rm h}08^{\rm m}03.5076^{\rm s}$, $+26^\circ03'38.507''$	$05^{\rm h}08^{\rm m}03.5071^{\rm s}$, $+26^\circ03'38.4802''$	530.1	249.9	105.6	0.79 ± 0.05	21.8	9.44	21
B15	$05^{\rm h}08^{\rm m}03.5076^{\rm s}$, $+26^\circ03'38.509''$	$05^{\rm h}08^{\rm m}03.5059^{\rm s}$, $+26^\circ03'38.4744''$	450.9	235.8	108.0	1.27 ± 0.10	12.6	3.14	21
B16	$05^{\rm h}08^{\rm m}03.5072^{\rm s}$, $+26^\circ03'38.509''$	$05^{\rm h}08^{\rm m}03.5072^{\rm s}$, $+26^\circ03'38.4593''$	503.0	198.4	119.8	0.61 ± 0.06	9.9	6.54	21
B17	$05^{\rm h}08^{\rm m}03.5072^{\rm s}$, $+26^\circ03'38.508''$	$05^{\rm h}08^{\rm m}03.5106^{\rm s}$, $+26^\circ03'38.4852''$	665.5	238.6	125.1	0.42 ± 0.03	16.4	7.07	21
B18	$05^{\rm h}08^{\rm m}03.5075^{\rm s}$, $+26^\circ03'38.511''$	–	–	–	–	0.37 ± 0.04	8.7	5.52	21

[a] Position of the intensity peak on the dirty map.
[b] Centroid of the 2-dimensional Gaussian fit to the intersection of the cross fringe pattern in the dirty map.
[c] The 1-σ major axis of the Gaussian
[d] The 1-σ minor axis of the Gaussian
[e] The rotational angle of the Gaussian. Measured anti-clockwise.
[f] Determined using the peak of the individual burst dirty maps.
[g] S/N of the clean maps per individual burst, where the clean maps are generated by fitting a circular Gaussian to the visibilities and inverse Fourier transforming using DIFMAP's modelfit tool.
[h] As is clear in Figure 5.1, some bursts are narrowband with emission mainly below 1380 MHz. Some of the participating telescopes did not observe the lower frequencies (Table 5.1) and therefore have reduced sensitivity to these bursts. The "effective" number of baselines is including only the telescopes where the burst emission falls significantly within the observing band.

The analysis steps for interferometric calibration and imaging were performed using standard tasks in the Astronomical Image Processing System, AIPS (Greisen, 2003) and DIFMAP

(Shepherd et al., 1994). Initially, using the products from the automated EVN Pipeline[6], we performed *a-priori* amplitude calibration using the gain curves and system temperature measurements from each station. We also applied a bandpass calibration, in addition to some basic flagging when telescopes were off-source. Burst B5 occurred while Effelsberg was still slewing, and so these data were flagged by this initial flagging step. Therefore, we removed these flags from the burst interferometric data to recover the data for burst B5. We note that B5 occurred at most a few seconds before Effelsberg was pointing at the exact VLA position of FRB 20201124A, and therefore was only at most 10% of Effelsberg's half-power radius (270 arcseconds at 1.4 GHz) from the beam centre. We conclude that the offset is too small to require an additional primary beam correction for this burst. At Epoch 1 (EVN correlation project code: EK048D, PRECISE observing code: pr153a), no fringes were detected from Irbene until 17:35 UT, and therefore there is no data from Irbene for bursts B1–B4. The station Badary had reduced time during Epoch 2 (EK048E, pr156a) and therefore did not observe after 15:45 UT, resulting in no data for this station during any of the bursts detected at Epoch 2. Delays due to dispersion in the ionosphere are corrected for using the Jet Propulsion Laboratory total electron content maps provided by CDDIS (Noll, 2010). We first remove the instrumental delay, i.e. phase jumps between the subbands, using the bright calibrator sources J1048+7143 and J0555+3948 for Epoch 1 and 2, respectively. Then we correct the phases for the entire observation, as a function of time and frequency, by performing a fringe-fit using all calibrator sources. Throughout, we use the most sensitive dish, the 100-m Effelsberg telescope, as our reference antenna for calibration. During Epoch 2, the phase solutions for Irbene were rapidly varying, thus we conclude that the solutions applied to the target are unreliable and we therefore flag these data. In Table 5.2, we report the "effective" number of baselines. This accounts for: the stations that did not record data at the time of the burst; stations that were flagged during calibration; and, additionally, the loss of sensitivity due to the spectra of some bursts peaking in the lower part of the observing band of Effelsberg, where some telescopes did not observe (see Table 5.1 for frequency coverage per participating telescope, and Figure 5.1 for the burst dynamic spectra).

The phase calibrator, J0502+2516, was then imaged using DIFMAP, independently for both epochs. During Epoch 1, the recovered flux from the phase calibrator was 0.179 Jy, while during Epoch 2, the flux had dropped to 0.102 Jy, and the clean image exhibited strong side-lobes, which we attribute to persistent amplitude errors after calibration. Additionally, radio maps of J0502+2154 from December 2018 at 5 GHz and 8.6 GHz exhibit an unresolved flux of ~ 0.18 Jy[7], allowing us to assume our higher measured flux is the true value. We therefore use a model of J0502+2516 determined using the data from Epoch 1 to self-calibrate the data from both epochs. This is an appropriate step, since the active galactic nucleus (AGN) J0502+2516 is not expected to vary in brightness significantly on $\sim$week timescales. The self-calibrated peak brightness of the phase calibrator is 0.178 Jy beam^{-1} and 0.179 Jy beam^{-1} for Epoch 1 and 2, respectively. The self-calibration solutions were then transferred to the target, before imaging. Throughout this work we make images of size 8192×8192, with 1-mas pixels.

[6] https://evlbi.org/evn-data-access

[7] http://astrogeo.org/cgi-bin/imdb_get_source.csh?source_name=J0502%2B2516

Table 5.3: Burst properties from Effelsberg single-dish data.

Burst	Time of Arrival[a] [MJD]	Fluence[b] [Jy ms]	S/N[c]	Peak Flux Density[b] [Jy]	Spectral Luminosity[d] [10^{31} erg s^{-1} Hz^{-1}]	Width[e] [ms]	Frequency Extent[e] [MHz]	Scintillation bandwidth[f] [MHz]
Epoch 1								
B1	59314.63581536	0.94 ± 0.19	13.9	0.31 ± 0.06	2.38 ± 0.48	4.0 ± 0.3	141.1 ± 0.5	3.0 ± 0.7
B2	59314.67002510	3.68 ± 0.74	44.1	0.73 ± 0.15	6.78 ± 1.36	5.6 ± 0.1	120.2 ± 0.1	2.2 ± 0.3
B3	59314.69180857	0.61 ± 0.12	7.5	0.24 ± 0.05	1.34 ± 0.27	4.7 ± 0.1	107.1 ± 0.7	2.8 ± 1.1
B4	59314.71490874	1.49 ± 0.30	16.3	0.43 ± 0.09	2.56 ± 0.51	6.0 ± 0.1	98.4 ± 0.2	2.5 ± 0.6
B5	59314.75153586	1.53 ± 0.31	18.2	0.46 ± 0.09	0.33 ± 0.67	4.7 ± 0.2	97.2 ± 0.3	2.3 ± 0.6
B6	59314.79580654	6.50 ± 1.30	67.9	0.91 ± 0.16	8.20 ± 1.64	8.1 ± 0.1	131.4 ± 0.1	1.9 ± 0.3
B7	59314.80440853	0.94 ± 0.19	16.4	0.52 ± 0.10	4.11 ± 0.82	2.4 ± 0.1	107.3 ± 0.2	2.8 ± 0.5
B8	59314.82591958	4.48 ± 0.90	46.1	0.92 ± 0.18	7.29 ± 1.26	6.3 ± 0.1	89.6 ± 0.1	2.3 ± 0.5
B9	59314.83037838	1.40 ± 0.28	17.0	0.27 ± 0.05	2.40 ± 0.48	5.9 ± 0.1	81.2 ± 0.1	2.0 ± 0.5
B10	59314.84159434	1.31 ± 0.26	12.4	0.34 ± 0.07	2.51 ± 0.50	5.4 ± 0.3	86.4 ± 0.5	3.4 ± 0.9
B11	59314.85888953	5.92 ± 1.18	76.0	0.89 ± 0.18	11.4 ± 2.3	5.3 ± 0.1	155.3 ± 0.1	1.3 ± 0.3
B12	59314.86388348	0.63 ± 0.13	6.7	0.13 ± 0.03	0.88 ± 0.18	7.4 ± 1.1	160.6 ± 0.7	-
B13	59314.87198956	3.39 ± 0.68	41.2	0.75 ± 0.15	6.98 ± 1.40	5.0 ± 0.1	111.4 ± 0.1	2.1 ± 0.4
Epoch 2								
B14[g]	59323.65617164	6.56 ± 1.31	82.1	1.51 ± 0.15	12.5 ± 2.5	2.3 ± 0.1	129.8 ± 0.2	1.1 ± 0.3
						3.6 ± 0.1	86.9 ± 0.1	
B15	59323.66919992	1.98 ± 0.40	46.3	1.23 ± 0.25	12.6 ± 2.5	1.6 ± 0.1	136.7 ± 0.1	1.7 ± 0.3
B16	59323.71603797	1.95 ± 0.39	26.3	0.5 ± 0.1	4.15 ± 0.83	4.8 ± 0.1	125.5 ± 0.1	3.3 ± 0.6
B17	59323.74152501	1.78 ± 0.36	21.2	0.31 ± 0.06	2.94 ± 0.59	6.1 ± 0.1	143.6 ± 0.2	1.1 ± 0.4
B18	59323.79497897	0.91 ± 0.18	13.8	0.24 ± 0.05	2.43 ± 0.49	3.9 ± 0.1	170.8 ± 0.6	1.3 ± 0.6

[a] Corrected to the Solar System Barycenter to infinite frequency assuming a dispersion measure of 412 pc cm^{-3}, reference frequency 1502 MHz and dispersion constant of $1/(2.41 \times 10^{-4})$ MHz^2 pc^{-1} cm^3 s. The times quoted are dynamical times (TDB).

[b] We estimate a conservative 20% uncertainty on these measurements, arising due to the uncertainty in the system equivalent flux density (SEFD) of Effelsberg.

[c] Boxcar S/N. Defined as the sum of the burst in S/N units within the 2σ uncertainty region of the width and spectral extent, normalised by the 2σ width in time bins.

[d] Taking the luminosity distance of FRB 20201124A as 453 Mpc (Day et al., 2021; Kilpatrick et al., 2021; Hilmarsson et al., 2021b)

[e] Full-width at half-maximum of the Gaussian fit to the autocorrelation function of the dynamic spectrum.

[f] The uncertainty on the scintillation bandwidth is the quadrature sum of the fit uncertainties and $1/\sqrt{N_{\rm scint}}$, where $N_{\rm scint}$ is the approximate number of scintles.

[g] B14 has two visible components.

In Figure 5.2 (left), we plot the clean 1.4-GHz map of all 18 bursts presented in this work. The combined *uv*-coverage of all 18 bursts results in a synthesised beam with major axis 37.3 mas, minor axis 17.98 mas, and position angle of 55.85°. The clean map is produced by fitting a Gaussian component to the visibilities in the *uv*-plane, and inverse Fourier transforming using DIFMAP's modelfit tool. The combined visibilities from all bursts provides us with the best available *uv*-coverage, and so from this we derive the J2000 position of FRB 20201124Ain the International Celestial Reference Frame (ICRF): $\mathrm{RA} = 05^{\mathrm{h}}08^{\mathrm{m}}03.5074^{\mathrm{s}} \pm 2.7$ mas, $\mathrm{Dec} = +26^{\circ}03'38.5052'' \pm 2.6$ mas. The peak emission is 24σ compared to the image noise, with the next-highest side-lobes measured at approximately 30% of the peak value. We note that the interferometric image S/N per individual burst (Table 5.2) is in general lower than the Effelsberg single-dish S/N (Table 5.3) per burst. The time-domain S/N is computed using off-burst data (data with only instrumental noise, and no signal), whereas the noise properties of the interferometric data are influenced by the signal itself, and contain strong residuals that become more prominent with brighter signals and lower *uv*-coverage. The combined image S/N (24σ) is lower than the expected combination of the individual burst S/N values (Table 5.2; quadrature sum is 51.2). This likely arises due to this dynamic range issue described above, and possibly also coherence loss when combining the individual bursts.

Additionally, we applied the same outlined calibration steps to the check source J0501+2530, and recovered the source with positional offset $\Delta\mathrm{RA} = 1.5$ mas, $\Delta\mathrm{Dec} =$

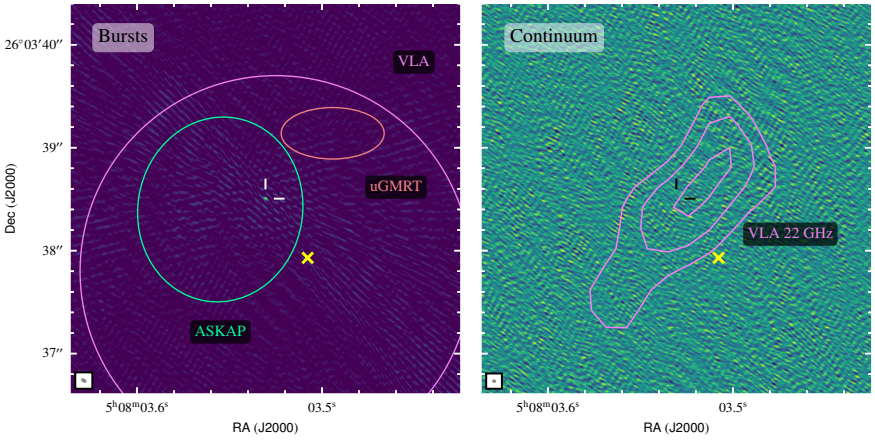

Figure 5.2: Left panel: Clean EVN 1.4-GHz map of the combined visibilities of all 18 bursts detected during both epochs (i.e. the inverse Fourier transform of the visibilities after deconvolving the telescope response). The white ticks indicate the position of FRB 20201124A. The localisation regions of FRB 20201124A as reported by VLA (Ravi et al., 2022), ASKAP (Fong et al., 2021) and uGMRT (Wharton et al., 2021c) are overplotted using pink, green and orange lines, respectively. Right panel: Dirty EVN map (before deconvolution of the interferometer response) of all continuum target data from both epochs to search for persistent radio emission. The position of FRB 20201124A is indicated by the black ticks. Overplotted are the 3, 4 and 5-σ contours of the resolved radio emission detected by the VLA at 22 GHz (Piro et al., 2021). In both panels, the optical centre of the host galaxy is indicated by the yellow cross (Fong et al., 2021). The synthesised beam is shown at the bottom left of each panel. Both maps are made using a natural weighting scheme.

0.6 mas from the expected position (as quoted in the rfc2021c catalogue[8]). The localisation of FRB 20201124A is therefore robust. The uncertainties on the final position of FRB 20201124A are the quadrature sum of the statistical uncertainties derived from the shape and size of the synthesised beam, normalised by the S/N (ΔRA$=$ 0.7 mas, ΔDec$=$ 0.4 mas), the statistical uncertainty on the phase calibrator position ($\pm$0.13 mas), an estimate of the systematic uncertainty due to the separation of the phase calibrator and target (conservatively $\pm$2.5 mas; Kirsten et al. 2015), and an estimate of the frequency dependent shift in the phase calibrator position from the ICRF (conservatively $\pm$1 mas; Plavin et al. 2019). The position of FRB 20201124A reported here is in agreement (within 2-σ) of the original EVN localisation reported in Marcote et al. (2021), which was determined using only the burst data from Epoch 1. Our position for FRB 20201124A is also in agreement with the independent measurements of the VLA (Ravi et al., 2022), the Australian Square Kilometre Array Pathfinder (ASKAP) (Fong et al., 2021), and the upgraded Giant Meterwave Radio Telescope (uGMRT; if one includes the estimated systematic uncertainties they discuss; Wharton et al. 2021c). These studies are approximately 2–3 orders of magnitude less precise than the localisation presented here, however (a comparison is shown in Figure 5.2).

[8] http://astrogeo.org/sol/rfc/rfc_2021c/

Additionally, we produced the dirty map of the entire $\sim$ 7 hours of target data from both epochs, to search for any compact persistent radio emission at the site of the FRB, or nearby (Figure 5.2; right). The rms noise in the continuum map, using a natural weighting scheme (using uvweight in DIFMAP) is 14 μJy beam^{-1}, and using a uniform weighting scheme is 25 μJy beam^{-1}. In addition, we tried applying different Gaussian tapers, 1 Mλ, 2 Mλ and 5 Mλ (using uvtaper in DIFMAP), to downweight the longer baselines and hence boosting any possible extended emission. We find no significant persistent radio source above 6 σ, in an area of 8$\times$8 arcseconds around the FRB. This is in agreement with the original report in Marcote et al. (2021), and follow-up efforts with the Very Long Baseline Array (VLBA; Ravi et al. 2022). The shortest baseline in our array is $\sim$ 270 km, between Effelsberg and Westerbork, and thus emission above an angular scale of $\sim$ 160 mas is resolved out.

5.3.3 Burst characterisation

The data were coherently dedispersed to a dispersion measure (DM) of 413 pc cm^{-3} (Chime/Frb Collabortion, 2021). We created 32-bit total intensity filterbank data for each burst by autocorrelating the single-dish Effelsberg raw voltage data using SFXC. These data have time and frequency resolutions of 8 μs and 125 kHz, respectively. We then created archive files using PSRCHIVE (Hotan et al., 2004), which have the same resolution as the filterbank data. The dynamic spectra, time profiles, and time-averaged spectra for all bursts are shown in Figure 5.1. We further refined the DM by optimising the frequency-averaged structure (using DM_phase[9]) of burst B14, which exhibits clear burst structure, to measure a DM of 412.2 $\pm$ 0.6 pc cm^{-3}. Additionally, using B15, which does not exhibit clear structure but is the narrowest burst in our sample, we measure a DM of 411.6 $\pm$ 0.4 pc cm^{-3}. Note that for B15, using DM_phase essentially maximises the S/N since it does not exhibit clear burst structure. The final DM, which we used to incoherently shift the frequency channels for all bursts in our sample, assuming the DM does not vary significantly on $<$ 10 day timescales, was determined by averaging the two measurements: DM = 412.0 $\pm$ 0.7 pc cm^{-3}.

To measure the temporal and spectral extent of the bursts, we performed a two-dimensional autocorrelation of each dynamic spectrum. The time of arrival and central frequency of the bursts were determined using a two-dimensional Gaussian fit to the dynamic spectrum. This method of peak and width determination is explained in more detail in Nimmo et al. (2022a), and the values for the bursts in this work are reported in Table 5.3.

Within the 2 σ burst width and spectral extent, indicated by the light purple and light cyan bars in Figure 5.1, we compute the burst fluence using the radiometer equation (Cordes & McLaughlin, 2003). For this, we use the typical Effelsberg system temperature, 20 K, combined with a cosmic microwave background contribution of 3 K, and a sky background temperature of 1 K, which we obtain by extrapolating from the 408 MHz sky map (Remazeilles et al., 2015) using a spectral index of $-$2.7 (Reich & Reich, 1988). We also use the typical Effelsberg gain of 1.54 Jy/K. The typical system values for Effelsberg are uncertain on the

[9] https://github.com/danielemichilli/DM_phase.git

20% level, dominating the uncertainty on the fluence and peak flux density measurements reported in Table 5.3.

We computed the one-dimensional auto-correlation function (ACF) of the burst spectra in order to measure the scintillation bandwidth. The scintillation bandwidth is defined as the half-width at half-maximum (HWHM) of a Lorentzian fit to the ACF of the spectrum. We note that the zero-lag noise spike is removed from each ACF. Additionally, we subtract the off-burst ACF to reduce the power at low lags due to noise. The narrow-bandedness of many of the bursts in our sample results in an additional frequency structure in the ACF with a characteristic bandwidth related to that of the frequency extent of the burst. For all bursts, other than B1, B15, B17 and B18, this broadband feature is visible in the ACF. We fit a one-dimensional Gaussian function to this wider component and subtract it from the ACF in order to disentangle the two frequency scales. Finally, we fit a Lorentzian function to the remaining structure in the ACF, and measure the scintillation bandwidth per burst (reported in Table 5.3), which we find to be consistent with the results presented in Main et al. (2022).

5.4 Discussion

5.4.1 Astrometry

The final position of FRB 20201124A is determined from a combined image of all 18 bursts presented in this work. The combination of many bursts, at two epochs, maximises the

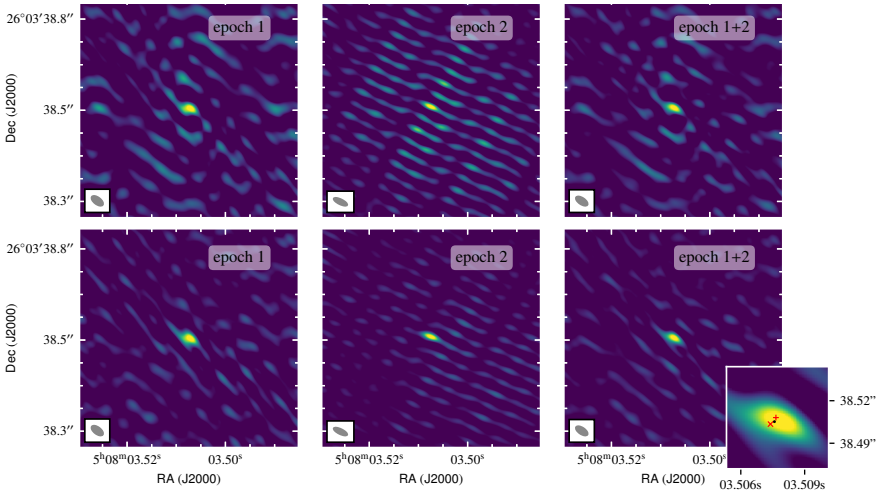

Figure 5.3: Top row: dirty maps (i.e. the inverse Fourier transform of the visibilities) of the combined visibilities of the 13 bursts discovered during Epoch 1 (left), the 5 burst during Epoch 2 (middle) and all bursts from both epochs (right). Bottom row: same as the top row except showing clean maps (i.e. the Fourier transform of the visibilities after deconvolving the telescope response). The zoom-in panel on the bottom right sub-plot shows the best-fit two-epoch position in black, with the positions from Epoch 1 and 2 independently represented by the red cross and plus, respectively. All images are made using a natural weighting scheme, and the scaling of each radio map goes from 5% to 85% of the peak value. The synthesised beam is shown at the bottom left of each panel.

uv-coverage. We also investigate the position of FRB 20201124A per observing epoch, in order to explore how consistent the FRB position is with an independent calibration, and observed on separate days. The position of FRB 20201124A using the combined visibilities of 13 bursts at Epoch 1 is $\mathrm{RA} = 05^{\mathrm{h}}08^{\mathrm{m}}03.5076^{\mathrm{s}} \pm 2.8$ mas, $\mathrm{Dec} = +26^{\circ}03'38.5035'' \pm 2.8$ mas (following the error determination described in Section 3.2, with a resulting S/N of 16.8, and using the Epoch 1 beam shape). Similarly, the position of FRB 20201124A using the combined visibilities of 5 bursts at Epoch 2 is $\mathrm{RA} = 05^{\mathrm{h}}08^{\mathrm{m}}03.5073^{\mathrm{s}} \pm 2.9$ mas, $\mathrm{Dec} = +26^{\circ}03'38.5081'' \pm 2.7$ mas (Epoch 2, S/N 18.5). Both per-epoch positions agree with the combined-epoch final position, and with each other, within 2-σ. In Figure 5.3, we plot the dirty maps (i.e. the inverse Fourier transform of the visibilities) of the combined visibilities from all 13 bursts in Epoch 1, the combined visibilities from all five bursts in Epoch 2, and the combined visibilities of all bursts from both epochs. Also shown in Figure 5.3 are the corresponding clean maps, with a visual comparison of the astrometry per epoch.

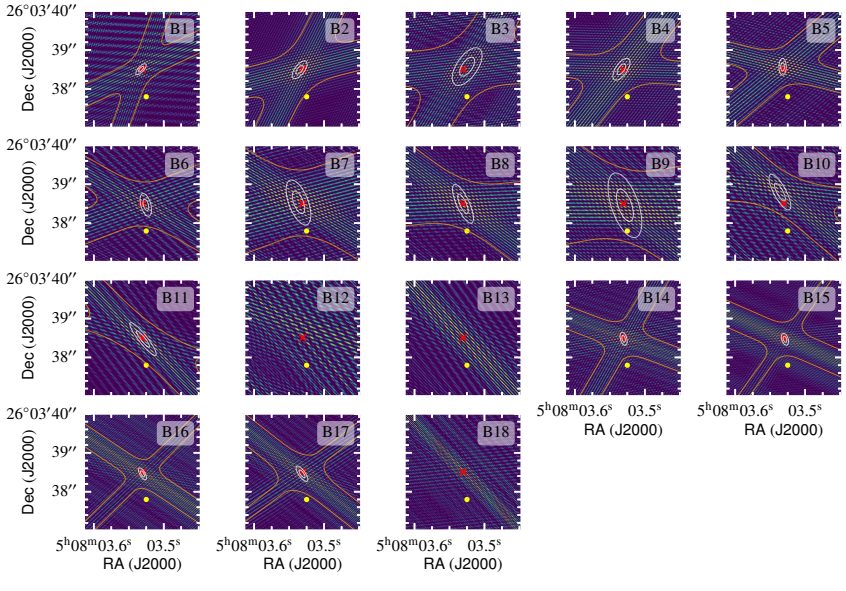

Figure 5.4: Dirty maps of the individual bursts, with the burst name shown at the top right corner of each panel. The orange contours represent the two 2-dimensional Gaussian fit (1-σ region) to the cross fringe pattern. The white contours represent the 1-σ and 2-σ Gaussian fit to the intersection of the double Gaussian, normalised by the S/N of the double Gaussian peak. Note: B12, B13 and B18 do not have a constraining Gaussian fit due to the lack of cross pattern in the dirty map. The best-fit FRB 20201124A position using all 18 bursts is shown by the red cross on each panel, and the phase centre used for correlation is indicated by the yellow point.

To explore the astrometry further, we determine the positions of each burst individually, using both the peak positions on the dirty map (dominated by the long baselines in the array), and Gaussian fits to the envelope of the fringe pattern (shown in Figure 5.4; dominated by the short baselines). We note that due to the lack of *uv*-coverage per individual burst (Figure 5.5), the peak sidelobe level in the dirty map is on average 97% of the main lobe,

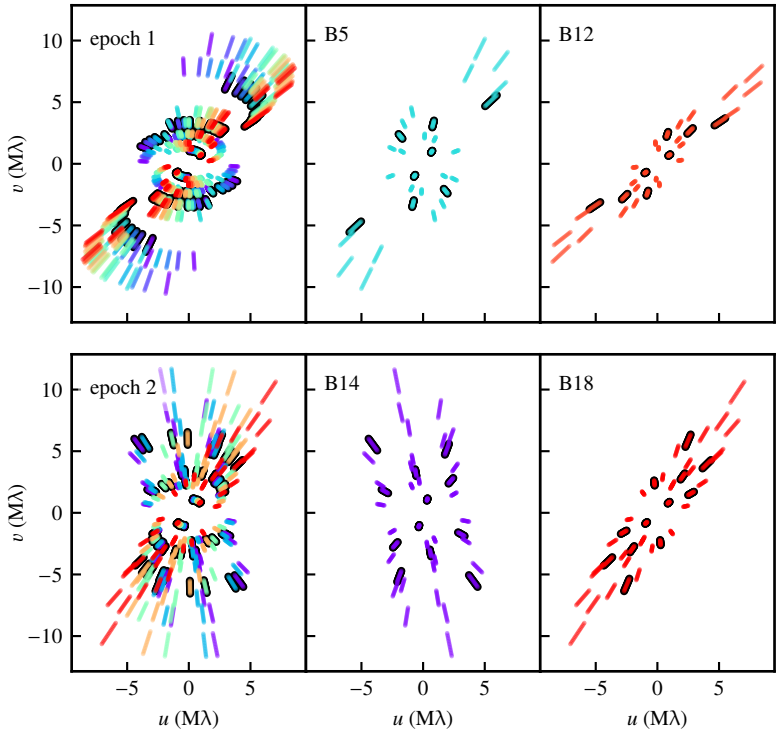

Figure 5.5: *uv*-coverage per observing epoch (left panels) and *uv*-coverage for representative individual bursts with (middle panels) and without (right panels) the cross-fringe pattern in the dirty map. The different colours represent individual bursts. There are multiple points plotted per baseline, representing the different frequency subbands. The points highlighted with the black outline represent baselines involving the Effelsberg telescope (the telescope with the highest sensitivity in our array) which dominates the structure seen in the dirty maps (Figure 5.4). For the representative individual bursts, the burst name is shown in the top left of the panel.

and in the worst case is $> 99\%$. This creates ambiguity in the individual burst positions, at a level comparable to the spacing between sidelobes. This was also evident and discussed in the case of the VLBI localisation of FRB 20121102A (Marcote et al., 2017), and highlights the need for an alternative approach. As an alternative approach, we fit smooth Gaussian functions to the dirty map pattern fringe pattern: we first fit 2-dimensional Gaussians to both arms of the cross pattern in the fringes, and then fit a single 2-dimensional Gaussian to their intersection. Note that we include the Gaussian fits only for bursts that exhibit a clear cross fringe pattern in their dirty map (Figure 5.4), which arises since the dirty map is dominated by baselines involving the Effelsberg telescope which span two primary axes in the *uv*-space (Figure 5.5). A Gaussian is not necessarily the optimal function to fit to the dirty map (the true function is dependent on the *uv*-coverage). However, it is clear from the two two-dimensional Gaussian fits in Figure 5.4, and the fact that $> 68\%$ of the 1-σ Gaussians in Figure 5.6 intersect with the position of FRB 20201124A, that this is a conservative approach

to measure the intersection of the cross fringe pattern and to account for the ambiguity of the burst position at the level of the sidelobe spacing.

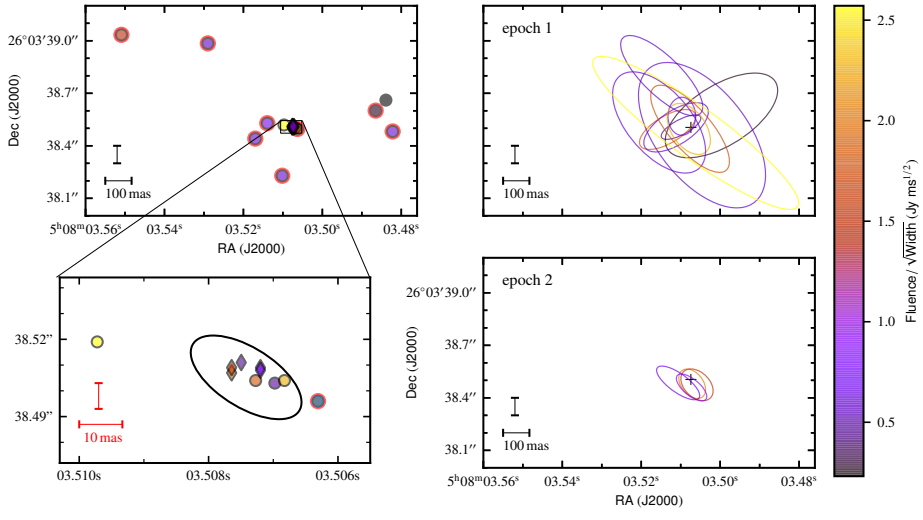

Figure 5.6: Individual burst positions determined using the intensity peak on the dirty maps (left) and a Gaussian fit to the dirty maps which exhibit a clear cross fringe pattern (right; see also Figure 5.4). Circles indicate bursts from Epoch 1 and diamonds bursts from Epoch 2. The colourbar represents the burst fluence divided by the square-root of the burst width, and is used as a measure of the burst detectability (a proxy for S/N; Marcote et al. 2017). The black bars represent a 100 mas angular scale, while the red bars in the zoom-in panel represent 10 mas angular scale. The black ellipse on the left bottom plot represents the synthesised beam centred on the best-fit FRB 20201124A position, while the cross on the right plots represent the best-fit FRB 20201124A position (in both cases, using all 18 bursts). The points on the left plot outlined in red indicate the bursts that were detected with only six baselines, highlighting the impact of low number of baselines on the scatter of individual burst positions.

The positions using both the peak and Gaussian fit methods are reported in Table 5.2, and illustrated in Figure 5.6. In Figure 5.7, we show the separation of the peak and Gaussian positions per burst, from the best-fit position of FRB 20201124A. As a result of the larger number of baselines ($= N(N-1)/2 = 21$, for number of telescopes N) during the second epoch, compared with the first, the peak positions of the Epoch 2 bursts agree within 10 mas of the true position. For the bursts from Epoch 1 (for which we have a lower number of baselines), the scatter in the peak positions increases and deviates farther from the true position, as expected. Accurately determining the astrometric uncertainty on the individual peak positions in the regime of low number of baselines, would likely require an empirical statistical study similar to Martí-Vidal et al. (2010b). However, based on Figure 5.7, an arcsecond localisation is feasible given one burst above a detectability threshold of Fluence/$\sqrt{\mathrm{Width}} \approx 0.3$ Jy ms$^{1/2}$ (Marcote et al., 2017), detected with only six baselines (four telescopes).

By looking at the phases of the visibilities of the individual bursts, there is clear scatter between approximately 50° and 100°. This scatter arises due to a combination of phase noise, and errors in phase-referencing. The phase uncertainty from phase noise, $\Delta\phi_{\mathrm{noise}}$, is related to the S/N as $\Delta\phi_{\mathrm{noise}} = \frac{1}{\mathrm{S/N}}$, for sufficient S/N (note that for small S/N this

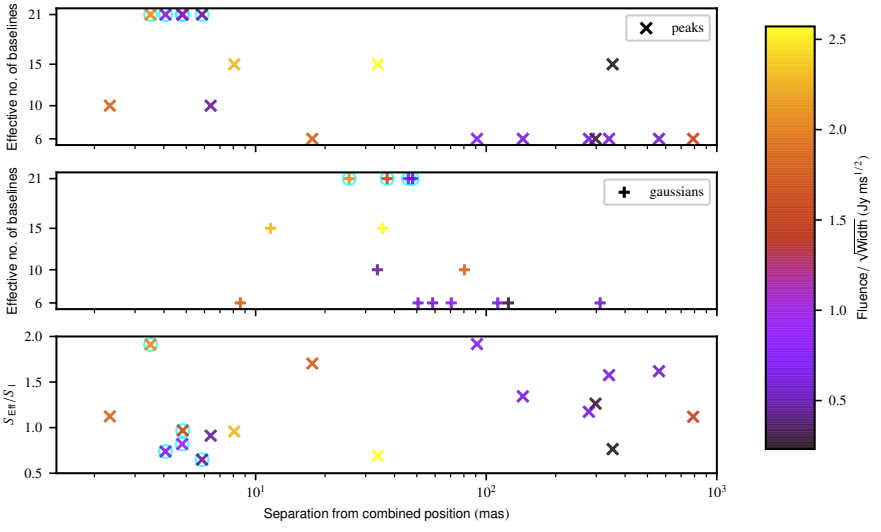

Figure 5.7: Separation of the peak (top) and Gaussian fit (middle) positions of the individual bursts as presented in Figure 5.6, from the best-fit FRB 20201124A position (using all 18 bursts) — as a function of effective number of baselines (defined in the text), and the detectability parameter, $\mathrm{Fluence}/\sqrt{\mathrm{Width}}$. The bottom panel shows the separation of the peak individual burst positions from the best-fit FRB 20201124A position, as a function of the burst peak flux density measured in the Effelsberg single-dish data ($S_{\rm Eff}$) divided by that measured in the interferometric data ($S_{\rm I}$). On all panels, the markers with the cyan circles indicate the bursts from Epoch 2.

approximation does not hold; Crane & Napier 1989). The uncertainty on the phase referencing accuracy arises due to a combination of separation of phase calibrator and target, atmospheric conditions, and accuracy of the correlation model. Martí-Vidal et al. (2010a,b) derive expressions to estimate VLBI astrometric uncertainties depending on the separation of phase calibrator and target, observing frequency, integration time, and the telescope's diffraction limit. Although this approach allows for the negligible integration time for individual bursts, the small number of baselines will have a significant effect on the astrometric accuracy in this limiting case. Therefore, the expressions for astrometric accuracy derived in Martí-Vidal et al. (2010a,b) will underestimate the uncertainties on the astrometry of individual bursts in this work, due to the lack of *uv*-coverage. Assuming we have a realistic phase uncertainty, in our sparse *uv*-coverage example, of 80°, arising from a combination of phase noise and calibration uncertainty, the expected positional shift of the fringe pattern is $\sim 1.22\lambda/b \times 100/180 \approx 89$ mas, where λ is our central observing wavelength, and b in this case is the shortest baseline of 270 km between Effelsberg and Westerbork (shortest baseline is relevant here since the cross fringe pattern is dominated by the short baselines). This is consistent with the scatter evident in the Gaussian fit positions on Figure 5.7 (mean = 70 mas, with standard deviation = 72 mas). It is reasonable to expect an even larger scatter on the peak positions since this combines the uncertainties on the short baselines, as well as on the long baselines. Additionally, the peak positions will be highly influenced by the phase noise on long baselines, which in general is larger than on shorter baselines. We indeed observe a

larger mean and scatter on the peak positions than on the Gaussian fit positions (Figure 5.7; peaks mean = 164 mas, with standard deviation = 223 mas). Note that we excluded three bursts (B12, B13 and B18) from the Gaussian fits due to the lack of a cross-pattern on the dirty maps, that we did not exclude from the peak positions in computing these statistics. By removing the peak positions of those same bursts, we still find a larger mean and scatter compared with the Gaussian fits (peaks mean = 120 mas, with standard deviation = 166 mas).

Therefore, due to the lower scatter in the Gaussian-fit positions in Figure 5.7 compared with the peak positions, we conclude that the safer approach to determine individual burst positions, with an array of < 20 baselines, is by using the Gaussian fit method. In this work, we are assuming that ionospheric turbulence is not varying drastically between observing epochs, or at least that our calibration is correcting for this sufficiently accurately: a fair assumption due to our relatively high observing frequency (> 1 GHz). Here we have provided an empirical investigation of astrometric uncertainties using one source at two epochs. This does not allow us to consider a wide range of observing conditions, so future such studies on other sources will be useful in our understanding of the limitations of VLBI FRB localisations.

5.4.2 The local environment of FRB 20201124A

The host galaxy of FRB 20201124A, SDSS J050803.48+260338.0 or hereafter J0508+2603 (Day et al., 2021) is a massive, star-forming galaxy (Ravi et al., 2022; Fong et al., 2021) at a redshift of $z = 0.098$ (Kilpatrick et al., 2021). The VLA (D-configuration; Ricci et al. 2021) detected unresolved compact persistent emission at 3 GHz and 9 GHz, in addition to the uGMRT (Wharton et al., 2021b) detection of unresolved persistent emission at 600 MHz. Follow-up with 22-GHz VLA observations in C-configuration, allowed for the emission to be resolved (Piro et al., 2021). The lack of compact emission in our EVN 1.4-GHz observations (Figure 5.2), supports the conclusion that the radio emission seen with lower resolution instruments is from star-formation (Ravi et al., 2022; Fong et al., 2021; Piro et al., 2021).

The milliarcsecond precision of our EVN localisation allows us to explore where the FRB location is relative to the radio star-formation emission (Piro et al., 2021), and the centre of the host galaxy (Fong et al., 2021). We find that FRB 20201124A is 710 $\pm$30 mas (projected distance: $\sim$1.3 kpc, assuming an angular size distance of 375.9 Mpc; Kilpatrick et al. 2021), from the optical centre of the host galaxy, statistically inconsistent with originating from the galaxy centre, similar to the discussion in Fong et al. (2021). The uncertainties on this offset arise as the quadrature sum of the radio position uncertainty (4.5 mas), the optical position uncertainty in Pan-STARRS (13 mas; Fong et al. 2021), and the astrometric tie uncertainty between Pan-STARRS and *Gaia* (22 mas; Magnier et al. 2020). We note that the *Gaia* reference frame and the ICRF agree on the few-milliarcsecond level (Mignard et al., 2016), therefore the uncertainties on the optical position and frame tying Pan-STARRS to *Gaia* dominate the error budget. FRB 20201124A is 175 $\pm$ 180 mas from the peak of the radio star-formation emission, where the uncertainty is dominated by the positional accuracy of the peak of the extended 22-GHz emission (Piro et al., 2021).

Future observations in optical and infrared, using high resolution instruments such as the *Hubble Space Telescope*, will allow for a measurement of the proximity of FRB 20201124A with star-forming knots in the host galaxy. This can be compared with the measured 250 pc and 260 pc offset from the peak of a nearby star-forming region in the case of FRB 20180916B (Tendulkar et al., 2021), and FRB 20121102A (Bassa et al., 2017; Kokubo et al., 2017), respectively. Additionally, these observations will allow for exploration of the role of star-formation on the period of high activity (Lanman et al., 2022), the production of extremely bright bursts (Kirsten et al., 2021a; Herrmann, 2021), as well as the presence of significant circular polarisation and polarisation angle swings in some bursts from FRB 20201124A (Hilmarsson et al., 2021b; Kumar et al., 2022).

Acknowledgements

We would like to thank the directors and staff at the various participating stations for allowing us to use their facilities and running the observations. The European VLBI Network is a joint facility of independent European, African, Asian, and North American radio astronomy institutes. Scientific results from data presented in this publication are derived from the following EVN project code: EK048. We used the 100-m telescope of the MPIfR (Max-Planck-Institut für Radioastronomie) at Effelsberg. This work was also based on simultaneous EVN and PSRIX data recording observations with the 100-m Effelsberg telescope, and simultaneous EVN and DFB recording with the Sardinia 64-m telescope. We thank the local staff for this arrangement. The Sardinia Radio Telescope is funded by the Department of Universities and Research (MIUR), the Italian Space Agency (ASI), and the Autonomous Region of Sardinia (RAS), and is operated as a National Facility by the National Institute for Astrophysics (INAF). This work is based in part on observations carried out using the 32-m Badary, Svetloe, and Zelenchukskaya radio telescopes operated by the Scientific Equipment Sharing Center of the Quasar VLBI Network (Russia). This work is based in part on observations carried out using the 32-m radio telescope operated by the Institute of Astronomy of the Nicolaus Copernicus University in Toruń (Poland) and supported by a Polish Ministry of Science and Higher Education SpUBgrant.

This project has received funding from the European Union's Horizon 2020 research and innovation programme under grant agreements nos. 730562 (RadioNet) and 101004719 (OPTICON-RadioNet Pilot). Research by the AstroFlash group at University of Amsterdam, ASTRON and JIVE is supported in part by an NWO Vici grant (PI Hessels; VI.C.192.045). B.M. acknowledges support from the Spanish Ministerio de Economía y Competitividad (MINECO) under grant AYA2016-76012-C3-1-P and from the Spanish Ministerio de Ciencia e Innovación under grants PID2019-105510GB-C31 and CEX2019-000918-M of ICCUB (Unidad de Excelencia "María de Maeztu" 2020-2023). JPY is supported by the National Program on Key Research and Development Project (2017YFA0402602). NW acknowledges support from the National Natural Science Foundation of China (Grant 12041304 and 11873080).

Chapter 6

A repeating fast radio burst source localized to a nearby spiral galaxy

B. Marcote, K. Nimmo, J. W. T. Hessels, S. P. Tendulkar, C. G. Bassa, Z. Paragi, A. Keimpema, M. Bhardwaj, R. Karuppusamy, V. M. Kaspi, C. J. Law, D. Michilli, K. Aggarwal, B. Andersen, A. M. Archibald, K. Bandura, G. C. Bower, P. J. Boyle, C. Brar, S. Burke-Spolaor, B. J. Butler, T. Cassanelli, P. Chawla, P. Demorest, M. Dobbs, E. Fonseca, U. Giri, D. C. Good, K. Gourdji, A. Josephy, A. Yu. Kirichenko, F. Kirsten, T. L. Landecker, D. Lang, T. J. W. Lazio, D. Z. Li, H. -H. Lin, J. D. Linford, K. Masui, J. Mena-Parra, A. Naidu, C. Ng, C. Patel, U. L. Pen, Z. Pleunis, M. Rafiei-Ravandi, M. Rahman, A. Renard, P. Scholz, S. R. Siegel, K. M. Smith, I. H. Stairs, K. Vanderlinde, A. V. Zwaniga

Nature, 2020, 577, 190

Abstract

Fast radio bursts (FRBs) are brief, bright, extragalactic radio flashes (Lorimer et al., 2007; Petroff et al., 2019). Their physical origin remains unknown, but dozens of possible models have been postulated (Platts et al., 2019). Some FRB sources exhibit repeat bursts (Spitler et al., 2016; CHIME/FRB Collaboration et al., 2019a,c; Kumar et al., 2019). Though over a hundred FRB sources have been discovered to date (Petroff et al., 2016), only four have been localised and associated with a host galaxy (Chatterjee et al., 2017; Ravi et al., 2019; Bannister et al., 2019; Prochaska & Zheng, 2019), with just one of the four known to repeat (Chatterjee et al., 2017). The properties of the host galaxies, and the local environments of FRBs, provide important clues about their physical origins. However, the first known repeating FRB has been localised to a low-metallicity, irregular dwarf galaxy, and the apparently non-repeating sources to higher-metallicity, massive elliptical or star-forming galaxies, suggesting that perhaps the repeating and apparently non-repeating sources could have distinct physical origins. Here we report the precise localisation of a second repeating FRB source (CHIME/FRB Collaboration et al., 2019c), FRB 20180916B, to a star-forming region in a

nearby (redshift $z = 0.0337 \pm 0.0002$) massive spiral galaxy, whose properties and proximity distinguish it from all known hosts. The lack of both a comparably luminous persistent radio counterpart and a high Faraday rotation measure (CHIME/FRB Collaboration et al., 2019c) further distinguish the local environment of FRB 20180916B from that of the one previously localised repeating FRB source, FRB 121102. This demonstrates that repeating FRBs have a wide range of luminosities, and originate from diverse host galaxies and local environments.

6.1 Results

The CHIME/FRB Collaboration is beginning to discover many repeating FRB sources (CHIME/FRB Collaboration et al., 2019a,c), which allows subsequent targeted observations using distributed radio telescope arrays to obtain precise interferometric localisations. CHIME/FRB discovered (CHIME/FRB Collaboration et al., 2019c) the repeating source FRB 20180916B, which we observed at a central frequency of 1.7 GHz and bandwidth of 128 MHz using eight radio telescopes of the European Very-long-baseline-interferometry Network (EVN) for 5.5 hours on June 19th, 2019. As described in the Methods §6.2, we simultaneously recorded both EVN single-dish raw voltage data as well as high-time-resolution intensity data using the PSRIX data recorder (Lazarus et al., 2016) in filterbank mode at the 100-m Effelsberg telescope.

In a search of the PSRIX data, we detected four bursts from FRB 20180916B with signal-to-noise ratios between 9.5 and 46. The observed dispersion measures (DM) of the bursts are consistent with those previously reported (CHIME/FRB Collaboration et al., 2019c) for this source. The burst properties, as derived from the PSRIX data, are listed in Table 6.1. No other dispersed single pulses of plausible astrophysical origin were found in this search, for DMs in the range 0–700 pc cm^{-3}. Using the EVN raw voltage data, we generated high-time-resolution (16-μs samples) Effelsberg auto-correlation data containing each burst. We used coherent dedispersion to mitigate the intra-channel smearing that dominated over the temporal resolution in the PSRIX data. By minimising dispersion broadening, we properly resolve the burst structure, and find a best-fit DM $= 348.76 \pm 0.10$ pc cm^{-3} using the brightest burst (Methods §6.2). We also detect brightness modulation with a characteristic frequency scale of 59 ± 13 kHz, which we interpret as scintillation imparted by the ionised interstellar medium of the Milky Way (Methods §6.2). The properties of the four bursts, as seen in the Effelsberg auto-correlations, are also shown in Table 6.1. The frequency-averaged burst profiles and dedispersed dynamic spectra are shown in Figures 6.1 and 6.2 for the Effelsberg auto-correlation and PSRIX data, respectively.

Table 6.1: FRB 20180916B burst properties as detected in both the Effelsberg PSRIX data and the Effelsberg auto-correlation data. S/N and Width are determined using `single_pulse_search.py`, and are the exact values returned by this program for the best-fit boxcar function. The DM quoted for the PSRIX data is the DM corresponding to the optimal S/N detection. The DM for the Effelsberg auto-correlation data is 348.76 pc cm^{-3}, which is the S/N optimising DM found for the brightest burst, B4, using the PSRCHIVE tool `pdmp`.
[a] Time of arrival of the centre of the burst envelope at the Solar System Barycentre after correcting to infinite frequency (i.e. after removing the time delay from dispersion) using a DM of 348.76 pc cm^3.

		PSRIX data			Auto-correlations		
Burst	Peak time[a] (MJD)	S/N	DM (pc cm^{-3})	Width (ms)	S/N	DM (pc cm^{-3})	Width (ms)
B1	58653.0961366466	14.65	345	1.64	9.87	348.76	2.40
B2	58653.1112573504	9.48	349	0.33	9.61	348.76	0.32
B3	58653.1465969404	11.08	356	0.74	9.78	348.76	1.12
B4	58653.2785078914	46.30	350	0.49	65.42	348.76	0.06

We then used the EVN raw voltage data to create coherently dedispersed cross-correlations, also known as visibilities, at the times of the four bursts. Radio interferometric images with

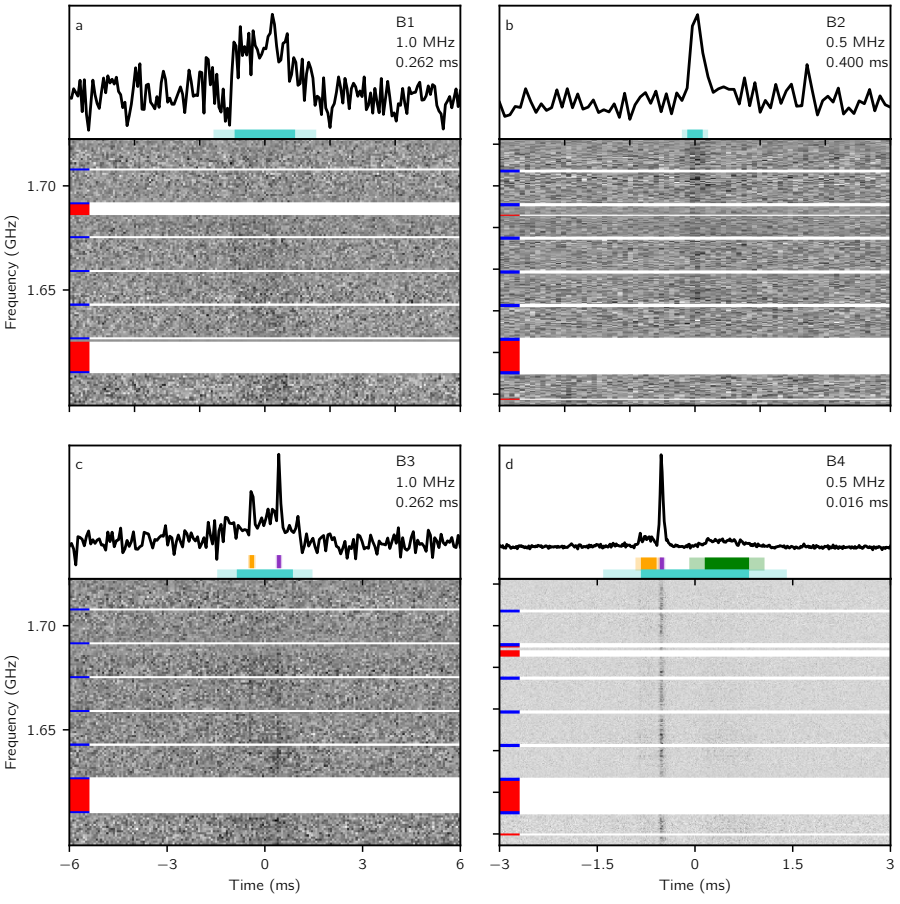

Figure 6.1: Burst detections in Effelsberg auto-correlation data. Band-averaged profiles and dynamic spectra of the four bursts, as detected using the coherently dedispersed Effelsberg auto-correlation data (**a**, **b**, **c** and **d**). Each burst was fitted with a Gaussian distribution to determine the full-width at half-maximum (FWHM) durations, which are represented by the dark cyan bars. The lighter cyan encloses the 2-σ region. Bursts B3 and B4 (**c** and **d**) show sub-bursts; the orange, purple and green bars correspond to the FWHM of these sub-bursts, and the lighter bar (of each colour) encloses the 2-σ region. Note the different time windows plotted: B1 and B3 (**a** and **c**) show 12 ms, whereas B2 and B4 (**b** and **d**) show 6 ms surrounding the burst peak. The solid white lines represent frequency channels that have been removed from the data due to either RFI or subband edges, indicated by the red and blue markers, respectively. The burst data have been downsampled by various factors in time and frequency to optimise the visual representation. The RFI excision was done prior to downsampling. The time and frequency resolution used for plotting is shown in the top right of each panel.

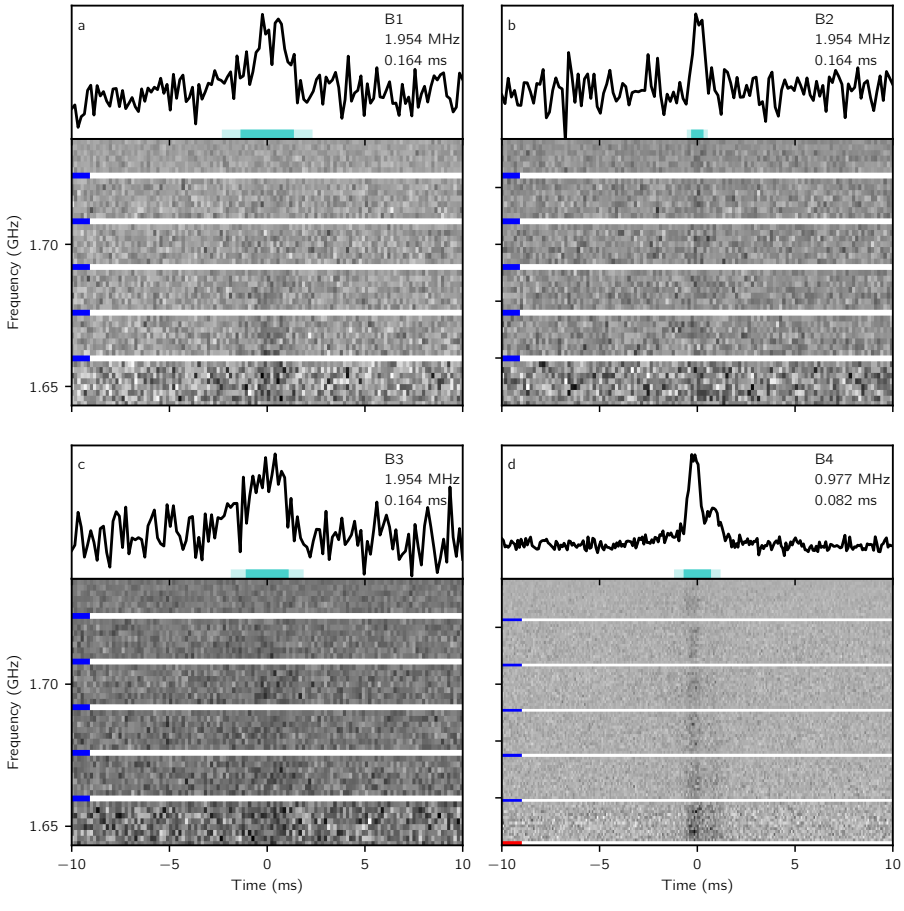

Figure 6.2: Burst detections in Effelsberg PSRIX data. Band-averaged profiles and dynamic spectra of the four bursts, as detected in the PSRIX data (**a**, **b**, **c** and **d**). A 20-ms time window is shown surrounding the burst centre. Each burst was fitted with a Gaussian distribution to determine the FWHM duration, which is represented by the cyan bars. The lighter cyan encloses the 2-σ region. The solid white lines are frequency channels that have been removed from the data due to either RFI or subband edges, indicated by the red and blue markers, respectively. For visual clarity, bursts B1, B2 and B3 (**a**, **b** and **c**) are downsampled in both time and frequency by a factor of two. The RFI excision was done prior to downsampling. The time and frequency resolution used for plotting is shown in the top right of each panel.

milli-arcsecond resolution were produced for each individual burst, using a single 0.7–2.7-ms integration, depending on the burst duration. Each image shows emission above at least seven times the r.m.s. noise level (Figure 6.3; see Methods §6.2 for a detailed explanation of the calibration and imaging process). The four burst images provide an average J2000 position for FRB 20180916B of $\alpha = 01^{\rm h}58^{\rm m}00.7502^{\rm s} \pm 2.3$ mas, $\delta = 65^\circ 43' 00.3152'' \pm 2.3$ mas. Visibilities with 2-second time resolution were also generated for the entire observation span. We used these to produce an image of the field around FRB 20180916B in order to search for a persistent radio counterpart, like that seen in the case of FRB 121102 (Chatterjee et al., 2017; Marcote et al., 2017). No such emission is detected above a 3-σ r.m.s. noise level of 30 μJy beam^{-1}. Independent observations using the Karl G. Jansky Very Large Array (VLA) at 1.6 GHz detect no coincident emission above a 3-σ r.m.s. noise level of 18 μJy beam^{-1} (see Methods §6.2 and Figure 6.4).

The precise EVN position shows that FRB 20180916B is spatially coincident with a galaxy catalogued in the Sloan Digital Sky Survey (Alam et al., 2015) as SDSS J015800.28+654253.0. Given the maximum expected redshift of approximately 0.11, as inferred by the measured DM (Methods §6.2), we find that the probability for chance coincidence is less than 1% for any type of galaxy with mass greater than $\sim 40\%$ that of the FRB 121102 host (Methods §6.2). Moreover, we thus conclude that the association of FRB 20180916B to this particular galaxy is significant. FRB 20180916B is close to the plane of the Milky Way, with Galactic longitude $l = 129.7^\circ$ and latitude $b = 3.7^\circ$. Its low DM excess compared to the Milky Way contribution (Methods §6.2) brought into question whether it could possibly be a Galactic disk or halo object (CHIME/FRB Collaboration et al., 2019c), but the host galaxy association shows that it is clearly extragalactic.

We used the 8-m Gemini-North telescope to characterise the morphology of the host galaxy and to measure a spectroscopic redshift (Methods §6.2). Deep optical imaging reveals that the host is a nearly face-on spiral galaxy (Figure 6.5) with a total stellar mass of approximately 10^{10} times that of the Sun (Methods §6.2), which is comparable to the total stellar mass of the Milky Way. No other comparably large and bright galaxy is visible in the broader field covered by Gemini-North (Figure 6.6). The milli-arcsecond precision of the EVN localisation shows that the FRB source is close to a bright feature in r'-band approximately 7 arcsec (projected separation of roughly 4.7 kpc) from the core of the host galaxy.

With Gemini-North long-slit spectroscopy, we simultaneously targeted the host galaxy centre and the offset position of FRB 20180916B (Figure 6.5). This revealed strong Hαemission, and several other spectral lines commonly associated with star formation (Figure 6.5). By measuring optical line ratios, we confirm that the host is indeed a star-forming galaxy (Figure 6.7).

Comparing with the rest frequencies of the lines, we find a redshift $z = 0.0337 \pm 0.0002$, which corresponds to a luminosity distance of 149.0 ± 0.9 Mpc (or an angular size distance of 139.4 ± 0.8 Mpc) using standard cosmological parameters (Wright, 2006). FRB 20180916B is thus the closest-known FRB source with a robust host galaxy identification and measured redshift. It is a factor of six closer than the repeater FRB 121102 (Tendulkar et al., 2017), and more than an order-of-magnitude closer than the (thus far) non-repeating

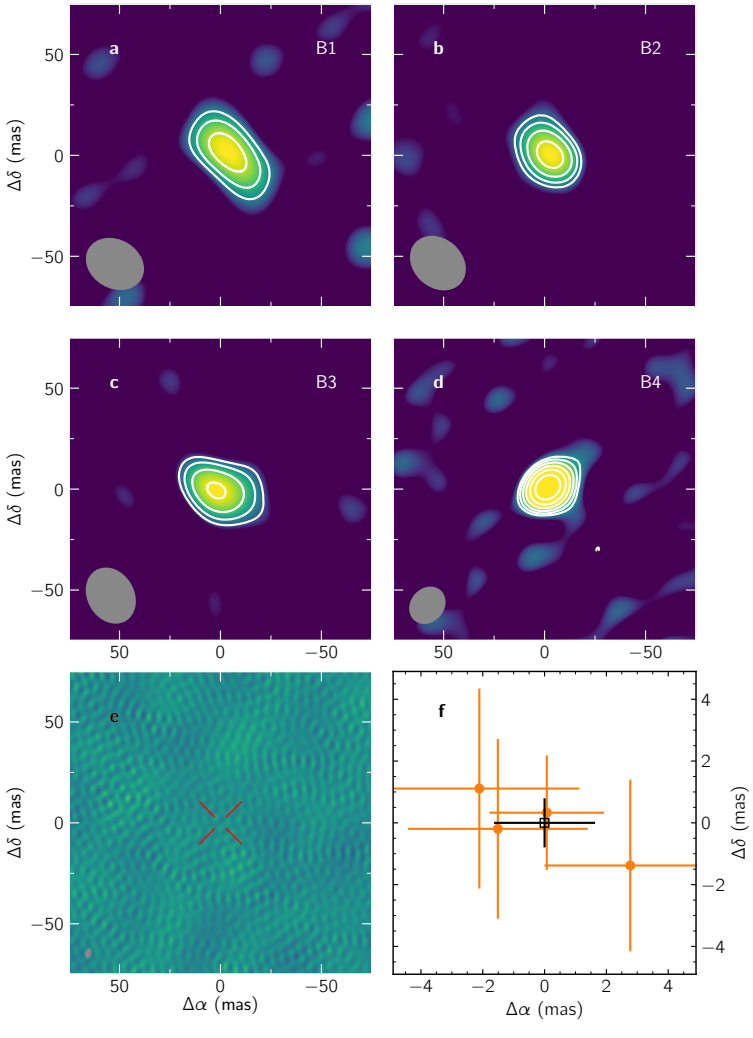

Figure 6.3: EVN images and burst positions. Each individual burst is imaged by using the EVN gated visibility data (**a**, **b**, **c** and **d**). Contours start at three times the r.m.s. noise level of each image (75, 65, 43, 100 mJy beam^{-1}, and 9.7 μJy beam^{-1}, respectively) and increase by factors of $\sqrt{2}$. **e:** image using the full span of the EVN observation and 2-s integration time; no significant ($> 3\sigma$) persistent radio emission is detected at the positions of the bursts (denoted by the red cross) and no signal above the 4-σ level is detected anywhere within the full field. For all images, the synthesised beam is represented by the grey ellipse in the bottom-left corner. The Tianma station was only included in the derivation of the continuum image (**e**). **f:** the positions derived from each individual burst and their associated 1-σ uncertainties (orange), with respect to the weighted-average burst position (black). All positions are referred to $\alpha = 01^{\rm h}58^{\rm m}00.7502^{\rm s}$, $\delta = 65^\circ 43' 00.3152''$.

sources FRB 180924 (Bannister et al., 2019), FRB 181112 (Prochaska & Zheng, 2019) and FRB 190523 (Ravi et al., 2019).

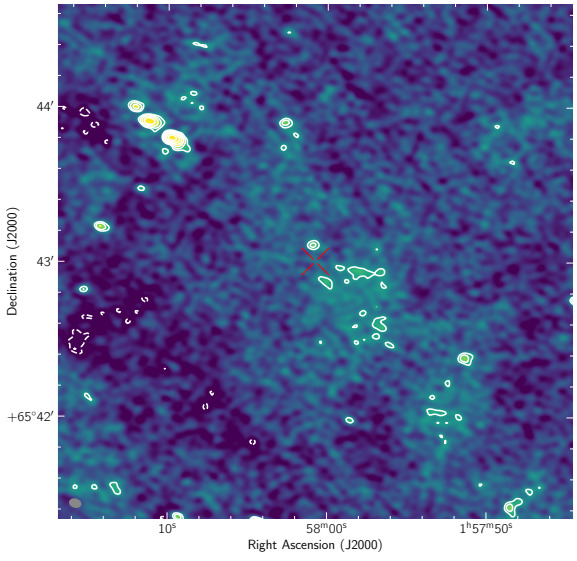

Figure 6.4: VLA field image. Field of the continuum radio emission around FRB 20180916B as seen by the VLA at 1.6 GHz with a bandwidth of 0.6 GHz. The position of FRB 20180916B is marked by the red cross at the centre of the image. Contours start at the 3-σ r.m.s. noise level of 18 μJy beam^{-1} and increase by factors of $\sqrt{2}$. The synthesized beam is represented by the grey ellipse in the bottom-left corner. Note that a faint source is detected at around 6 arcsec north of FRB 20180916B, but its separation is significant (>3-σ confidence level) and we thus conclude that it is not associated with FRB 20180916B.

The optical spectrum at the location of FRB 20180916B shows that both the associated star-forming clump and the host galaxy core are at the same redshift (Figure 6.5). However, the spectrum at the location of FRB 20180916B is dominated by emission from the clump, which is offset from the centre of the slit. Hence we have no independent direct estimate of the emission or dispersion measure at the position of FRB 20180916B from the Gemini-North data. By considering the various modelled foreground contributions to DM, we estimate that the host contribution is less than approximately 70 pc cm^{-3}, and could be substantially smaller (Methods §6.2).

FRB 20180916B is located at the apex of the 'v-shaped' star-forming clump (Figure 6.8) with a relatively large (Gusev, 2014) projected size of roughly 1.5 kpc and a star-formation rate of $\gtrsim 0.016$ M$_\odot$ yr^{-1} (and a star-formation surface density of $\approx 10^{-2}$ M$_\odot$ yr^{-1} kpc^{-2}). The v-shaped star-forming clump is a remarkable feature of the galaxy, suggesting the possibility that the region has undergone an interaction that triggered the star formation, either between multiple star-forming regions or conceivably involving a putative dwarf satellite companion.

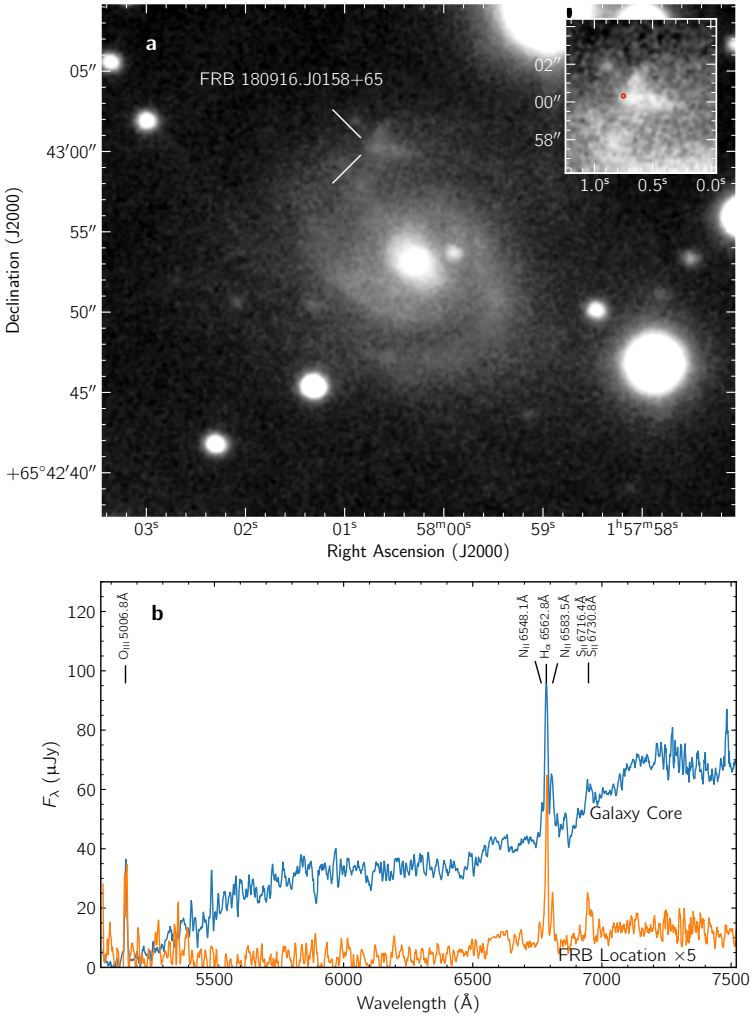

Figure 6.5: Gemini-North host galaxy image and optical spectrum. a: image of the host galaxy using the r' filter. The position of FRB 20180916B is marked. The inset shows a higher contrast zoom-in of the star-forming region containing FRB 20180916B (marked by the red circle). The uncertainty in the position of FRB 20180916B is smaller than the resolution of the image. **b:** sky-subtracted spectrum extracted from a 5 arcsec aperture around the host galaxy core (blue) and a 2 arcsec aperture around the location of FRB 20180916B (orange, scaled by a factor of five for clarity). Emission lines are identified along with their rest-frame wavelengths in air. Due to the complicated shape of the galaxy, the fluxes have not been corrected for slit losses.

The spiral host galaxy of FRB 20180916B contains over 100 times more stellar mass and has five times higher metallicity (see Figure 6.7 and Methods §6.2) than the dwarf host galaxy of FRB 121102. The discovery of this host demonstrates that some FRB sources exist in galaxies more similar to our own Milky Way. Previously, it has been noted (Tendulkar et al., 2017; Marcote et al., 2017; Metzger et al., 2017) that the host of FRB 121102 is similar to the type of low-metallicity galaxies with high specific star-formation rate that are associated with hydrogen-poor superluminous supernovae and long-duration gamma-ray bursts. In contrast, the FRB 20180916B host is unlike such galaxies; this weakens the case for a general link between all repeating FRB sources and these extreme astrophysical explosions. In a search of the Open Supernova Catalog (Guillochon et al., 2017), we find no previous supernovae or gamma-ray bursts at the location of FRB 20180916B.

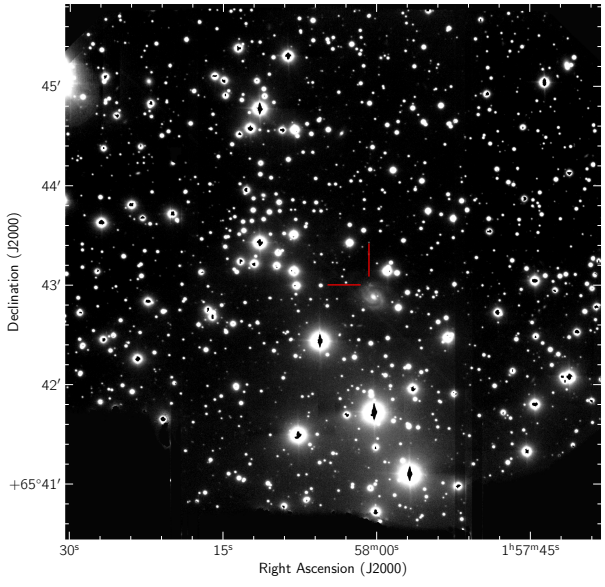

Figure 6.6: Full field of view of the Gemini r' filter. The position of FRB 20180916B is highlighted by the red cross. Note that the spiral galaxy associated with FRB 20180916B is the only clearly visible galaxy in the field.

The proximity of FRB 20180916B constrains the presence of any persistent radio counterpart to a luminosity (at a 3-σ confidence level) of $\nu L_\nu < 1.3 \times 10^{36}$ erg s^{-1} from the continuum EVN data (sensitive to milliarcsecond scales) and to $\nu L_\nu < 7.6 \times 10^{35}$ erg s^{-1} from the VLA data (sensitive to emission on arcsecond scales; see Methods §6.2). Compared to the persistent source associated with the repeating FRB 121102, this upper limit implies that any such source associated with FRB 20180916B must be at least 400 times fainter than the one associated with FRB 121102 (Marcote et al., 2017). The previously determined (CHIME/FRB Collaboration et al., 2019c) Faraday rotation measure of FRB 20180916B, RM $= -114.6 \pm 0.6$ rad m^{-2}, is three orders of magnitude lower than that of FRB 121102 (Michilli et al., 2018b), where RM $\sim 10^5$ rad m^{-2}. As previously suggested (CHIME/FRB

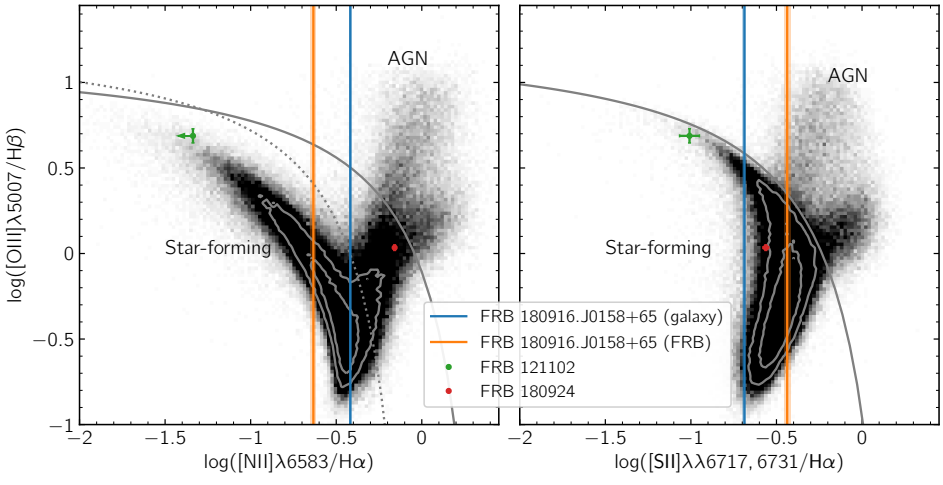

Figure 6.7: Host galaxy source of ionisation. Emission line flux ratios of **a**: [N II]/H$\alpha$and **b**: [S II]/Hαagainst [O III]/Hβ. The grey-scale distribution represents the SDSS DR12 sample (Alam et al., 2015) of 240,000 galaxies that display significant emission lines ($> 5\sigma$), where the solid and dotted grey lines denote the demarcations between star-forming and AGN-dominated galaxies (Kewley et al., 2001; Kewley & Dopita, 2002; Kauffmann et al., 2003). The host galaxies of FRB 121102 and FRB 180924 are consistent with star-forming and AGN-dominated galaxies, respectively (Tendulkar et al., 2017; Bannister et al., 2019). Though the Gemini-North spectrum of FRB 20180916B does not cover the [O III] and Hβ lines, its [N II]/H$\alpha$and [S II]/Hαline ratios are broadly consistent with a star-formation dominated galaxy (represented by the vertical lines and the 1-σ region as line width).

Collaboration et al., 2019c), we conclude that FRB 20180916B is located in a much less extreme local environment compared with FRB 121102, and that the physical mechanism for FRB repetition does not depend on such conditions. Nonetheless, models originally proposed for FRB 121102 (Margalit & Metzger, 2018; Metzger et al., 2019) — in which the bursts originate from a young and rapidly rotating magnetar — could potentially still explain the observed properties of FRB 20180916B by invoking an age of ∼300 yr, which is ten times older than that proposed for FRB 121102 (see Methods §6.2 for a brief comparison to existing models).

While the host galaxies of FRB 20180916B and FRB 121102 are markedly different, both sources are located near or within a star-forming region in the host galaxy. This contrasts with the elliptical host galaxies of FRB 180924 (Bannister et al., 2019) and FRB 190523 (Ravi et al., 2019), where there is comparatively little active star formation, but may be consistent with the star-forming galaxy of FRB 181112 (Prochaska & Zheng, 2019). This diversity in hosts and local environments allows for the possibility that repeating and apparently non-repeating FRB sources have physically distinct origins. However, comparison of FRB event rates with those of proposed progenitors disfavours models that invoke cataclysmic explosions and suggests that a large fraction of sources must be capable of repeating (Ravi, 2019). The recent finding that FRB 171019 produces repeat bursts that are almost 600 times fainter compared to the originally discovered signal (Kumar et al., 2019) underscores the fact that the detectability of repetition depends on instrumental sensitivity and

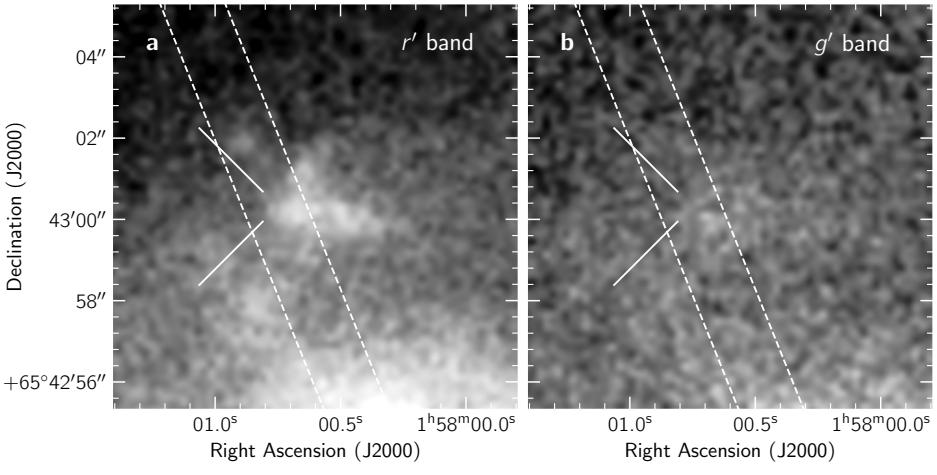

Figure 6.8: Zoomed-in images at the position of FRB 20180916B. Gemini data at r' (**a**) and g' bands (**b**). The position of FRB 20180916B is highlighted by the white cross. the uncertainty on its position is smaller than the resolution of these images. The dashed lines represent the orientation and placement of the 1.5 arcsec spectroscopic slit used to obtain the optical spectra. Note that the slit does not cover the full star-forming region but the region centred on FRB 20180916B and that the whole region is strongly affected by extinction ($E(g-r) = 1.73(9)$).

source proximity. If FRB 20180916B were at the distance of the other well-localised FRBs, only a small fraction of its (brightest) bursts would be visible.

Furthermore, it has been proposed that a young magnetar origin for the bursts of as-yet non-repeating FRBs in non-star-forming regions is still viable as long as it is possible to form such sources through a variety of channels, including direct stellar collapse, accretion-induced collapse, and through the merger of compact objects (Margalit et al., 2019). Ultimately, a larger number of precision localisations is needed before we can establish that multiple physical origins are required to explain the observed FRB phenomenon. There are now 11 repeating FRBs known (Spitler et al., 2016; CHIME/FRB Collaboration et al., 2019a; Kumar et al., 2019; CHIME/FRB Collaboration et al., 2019c), and with precision localisations it will be possible to establish whether repeating and apparently non-repeating FRB sources have demonstrably different environments.

FRBs have now been localised with luminosity distances that span approximately 150 Mpc to 4 Gpc. Estimating distance purely based on DM, it appears likely that there are FRBs that are even closer (Mahony et al., 2018) or more distant (Bhandari et al., 2018; CHIME/FRB Collaboration et al., 2019c) compared with this range. The four bursts presented here have isotropic-equivalent spectral energy densities as low as approximately 5×10^{27} erg Hz^{-1} (Table 6.2). Assuming similar beaming fractions, this makes them close to an order of magnitude less energetic compared to the weakest bursts seen from FRB 121102 to date (Gourdji et al., 2019), and between four to six orders-of-magnitude less energetic compared to

Table 6.2: Burst properties. Widths, fluences and spectral energy densities are determined using the Effelsberg auto-correlation data of the bursts from FRB 20180916B, with a centre frequency of 1.7 GHz and dedispersed for a DM $= 348.76$ pc cm^{-3}. W_{tot} is the FWHM of the total burst envelope, and $W_{sub\,n}$ represents the FWHM of any sub-bursts, ordered according to their arrival time (earliest sub-burst is labelled "sub1"). The coloured boxes correspond to the bars in Figure 6.1 highlighting which structure is associated with the quoted widths. The fluence is determined by integrating the burst profile over W_{tot} and is converted to physical units using the radiometer equation (see Methods §6.2; Cordes & McLaughlin 2003). The spectral energy density is estimated using the measured fluence and luminosity distance. The position offsets ($\Delta\alpha$, $\Delta\delta$) are referred to the average J2000 burst position of $\alpha = 01^{h}58^{m}00.7502^{s}$, $\delta = +65^{\circ}43'00.3152''$. The flux densities, S_ν, are measured by fitting a circular Gaussian to the EVN visibility data and are averages over the gate width.
[a] At 1.7 GHz reference frequency, and corresponding to the sum of all sub-bursts. A conservative fractional error of 30% is adopted for the derived fluences and energy densities. These are assumed to be isotropic.
[b] At 1.7 GHz reference frequency. The absolute flux scale may exhibit an additional ∼15% uncertainty due to possible systematic gain calibration offsets.
[c] See Methods for how the total burst width of B4 was determined.

Burst	W_{tot} (ms)	W_{sub1} (ms)	W_{sub2} (ms)	W_{sub3} (ms)	Fluence (Jy ms)[a]	Spectral energy density (10^{28} erg Hz^{-1})[a]	$\Delta\alpha$ (mas)	$\Delta\delta$ (mas)	S_ν (Jy)[b]
B1	1.86 ± 0.13	–	–	–	0.72	1.90	-2.1 ± 3.2	1.1 ± 3.2	0.74 ± 0.08
B2	0.24 ± 0.02	–	–	–	0.20	0.53	-1.5 ± 2.9	-0.2 ± 2.9	0.66 ± 0.05
B3	1.72 ± 0.14	0.14 ± 0.02	0.12 ± 0.01	–	0.62	1.64	2.8 ± 2.8	-1.4 ± 2.8	0.50 ± 0.04
B4	1.66 ± 0.05[c]	0.24 ± 0.01	0.06 ± 0.0006	0.68 ± 0.03	2.53	6.68	0.1 ± 1.9	0.3 ± 1.9	2.3 ± 0.3

FRB 180924 (Bannister et al., 2019) and FRB 190523 (Ravi et al., 2019). Unless multiple models are invoked, a viable model for FRBs must address this large range of (apparent) energy outputs.

Comparing instead with pulsar emission, we note that the bursts from FRB 20180916B are still at least a million times more energetic compared to the brightest giant pulses seen from the Crab pulsar — suggesting that they are not simply an exceptionally bright version of the known pulsar giant pulse phenomenon (Lyutikov, 2017).

As previously suggested (CHIME/FRB Collaboration et al., 2019c), the proximity of FRB 20180916B is an advantage for multi-wavelength follow-up of the host galaxy and local environment. Whereas targeted observations of FRB 121102 have failed to detect either prompt or persistent optical, X-ray or gamma-ray counterparts (Scholz et al., 2016, 2017; Hardy et al., 2017; MAGIC Collaboration et al., 2018), similar observations towards FRB 20180916B may strongly constrain magnetar-based models, even in the event of non-detections. FRB 20180916B is thus one of the most promising known sources for understanding the nature of FRBs.

6.2 Methods

6.2.1 A priori localisation.

The CHIME/FRB Collaboration discovered (CHIME/FRB Collaboration et al., 2019c) the repeating source FRB 20180916B and refined its position using the CHIME/FRB baseband mode. The automatic baseband triggering system of CHIME/FRB (CHIME/FRB Collaboration et al., 2018) captured (CHIME/FRB Collaboration et al., 2019c) raw voltages for a burst from FRB 20180916B. The intensity of the signal in the region surrounding the original de-

tection was then calculated by producing a grid of tightly-packed tied-array beams. A refined position was obtained by fitting this intensity map with a simple model of the telescope beam (Michilli et al., 2021). Since the analysis strategy was still in a preliminary stage at the time, we estimate a systematic uncertainty on this position of roughly three arcminutes, based on a small sample of four known pulsars. CHIME/FRB baseband localisations are expected to have higher precision in the future.

6.2.2 European VLBI Network and Effelsberg observations.

The EVN observed the field of FRB 20180916B on June 19th, 2019 for 5.5 h at a central frequency of 1.7 GHz and with a bandwidth of 128 MHz. The phase centre was placed at the position provided by the initial CHIME/FRB baseband localisation: $\alpha = 01^{\rm h}57^{\rm m}43.2^{\rm s}$, $\delta = 65^\circ42'01.02''$ (J2000 coordinates).

A total of eight dishes participated in the EVN observations: the 100-m Effelsberg, the 65-m Tianma, the 32-m Medicina, the 32-m Toruń, the 32-m Irbene, the 25-m $\times$ 38-m Jodrell Bank Mark II, the 25-m Onsala, and a single 25-m dish from the Westerbork array. The data were streamed in real time (e-EVN setup) to the EVN Software Correlator (SFXC; Keimpema et al. 2015) at the Joint Institute for VLBI ERIC (JIVE) in Dwingeloo, The Netherlands. The real-time visibility data are comprised of eight 16-MHz subbands of 32 channels each, with full circular polarisation products, and 2-s time averaging.

In parallel, we buffered the individual station raw voltage data in order to allow high-time-resolution correlations afterwards, at the times of any detected bursts. This method allows one to recover the signal from any position within the primary beam of the antennas (which have a full-width at half-maximum, FWHM, of roughly 7 arcmin in the case of the 100-m Effelsberg dish, and roughly 30 arcmin for the 25-m antennas), which would otherwise be smeared due to time and frequency averaging if it is more than tens of arcseconds away from the phase centre used in cross-correlation. We observed 3C454.3 and J0745+1011 as fringe-finders and bandpass calibrators. J0207+6246 was observed as phase calibrator (located 3.1° away from FRB 20180916B) in a phase-referencing cycle of 2 min on the calibrator and 5 min on the target, FRB 20180916B. We also observed J0140+6346 as a check source (3.1° away from the same phase calibrator) following the same phase-referencing cycle.

Simultaneously, we recorded high-time-resolution filterbank data at 1.7 GHz using the 100-m Effelsberg telescope and the PSRIX data recorder (Lazarus et al., 2016), which is designed for pulsar observations. We observed FRB 20180916B for a total on-source time of 3.47 h in the frequency range 1597–1737 MHz. This total bandwidth was divided into 144 spectral channels of 0.98 MHz each. Of these, the bottom 48 channels were corrupted by radio frequency interference (RFI), likely from Iridium satellites. Consequently, these channels were removed from the data prior to beginning the analysis, giving a usable bandwidth of 93.75 MHz. The data were recorded with full Stokes information and a time resolution of 81.92 μs. Before the beginning of the observation, we performed a short test scan on the known pulsar PSR B2111+46, in order to verify the data integrity.

6.2.3 Interferometric data reduction.

The EVN data were analysed using standard procedures within the Astronomical Image Processing System (AIPS; Greisen 2003) and Difmap (Shepherd et al., 1994) software packages. *A priori* amplitude calibration was performed using the known gain curves and system temperature measurements recorded at each station during the observations. Poor data, primarily due to RFI, were flagged manually ($\lesssim$ 10% of the total data). The remaining data were then fringe-fitted and bandpass calibrated using the fringe-finders and phase calibrator, which were imaged and self-calibrated to improve the final calibration of the data. The obtained solutions were transferred to FRB 20180916B and J0140+6346 before creating the final images.

The check source J0140+6346 was used to estimate both the absolute astrometric uncertainty and the potential amplitude losses that could have been introduced due to the phase-referencing technique. Although the latter accounted for less than approximately 10% of the total flux density scale, we found a significant offset ($\sim$ 4 mas) of the centroid of the check source position with respect to its known coordinates from the International Celestial Reference Frame (ICRF). The origin of this offset is explained by both the uncertainties associated with the phase-referencing technique (Chatterjee et al., 2004; Pradel et al., 2006; Kirsten et al., 2015) and the extended structure of J0207+6246, the phase calibrator. The core of this source shows multiple components that make the determination of the true position of the source ambiguous at the milli-arcsecond level. We corrected for this observed offset in all burst positions presented in this study, but an uncertainty on the final absolute positions of $\pm$1.7 mas and $\pm$2.1 mas in right ascension and declination, respectively, still remains due to the ambiguity in the exact position of this reference source and its extension (the source is resolved on milliarcsecond scales).

6.2.4 Search for FRB 20180916B bursts.

The PSRIX data were analysed in order to search for dispersed, millisecond-duration bursts, using the PRESTO (Ransom, 2001) software package. The tool rfifind was used to identify frequency channels and time samples contaminated by RFI. We estimate that $\sim$ 4% of the data were masked using rfifind. Incorporating the RFI mask, the data were then incoherently dedispersed to DMs in the range 0–700 pc cm^{-3} in steps of 1 pc cm^{-3} using prepsubband, generating dedispersed time series at each trial DM. To search for short-duration bursts, each dedispersed time series was convolved with boxcar functions of various widths, using single_pulse_search.py. Given the frequency resolution of the PSRIX data, the residual dispersive delay within each channel results in a temporal smearing of $\sim$ 0.6 ms at the expected (CHIME/FRB Collaboration et al., 2019c) DM of FRB 20180916B (349 pc cm^{-3}). This intra-channel smearing dominates over the sampling time, causing a loss of sensitivity to extremely narrow bursts. We were sensitive to bursts with widths exceeding the intra-channel smearing time, and up to 98.3 ms. A DM-time plot (known as a single-pulse plot, generated by single_pulse_search.py) was created for each scan and inspected by eye for candidates. For each candidate identified, the dynamic spectrum was

generated and inspected by eye to distinguish between astrophysical signals and terrestrial sources of RFI. During our 3.47-h on-source time, we found four bursts from FRB 20180916B at its known DM. As a final check, each dedispersed time series was filtered for RFI in the search for candidates with peak signal-to-noise ratio S/N > 7, using an automated classifier (Michilli et al., 2018a; Michilli & Hessels, 2018) that returned only the same four bursts found in the initial manual search.

Using the time of arrival of each individual burst, one-second duration Effelsberg auto-correlations were created for each burst, using the recorded EVN raw-voltage data. The auto-correlation data were generated with a higher temporal resolution (16-μs time bins) and frequency resolution (62.5-kHz channels) compared with the PSRIX data, and were coherently dedispersed to 350 pc cm^{-3}. Coherent dedispersion mitigates the effects of intra-channel smearing to less than 3 μs for DMs that are within a few units of 350 pc cm^{-3}. This provided us with the opportunity to better study the burst structure (limited only by our temporal resolution and the signal-to-noise), which is unresolved in the PSRIX data.

We identified the four bursts from FRB 20180916B in the auto-correlations (Figure 6.1 shows their band-averaged burst profiles and dynamic spectra). For comparison, we also show the profiles and dynamic spectra for the bursts in the PSRIX data (Figure 6.2).

6.2.5 Burst properties.

Using the brightest burst, labelled B4, we determined a precise DM for FRB 20180916B. We used the PSRCHIVE (Hotan et al., 2004) tool pdmp to determine the DM that corresponds to a peak in the signal-to-noise. Because B4 has a bright and narrow sub-burst, optimising the signal-to-noise is likely also equivalent to optimising the structure of the burst (Hessels et al., 2019), in this case. We searched DMs of 350 ± 3 pc cm^{-3} in steps of 0.01 pc cm^{-3} using pdmp, and found the optimal DM to be 348.76 ± 0.10 pc cm^{-3} (consistent with the DM of 349.2 ± 0.3 pc cm^{-3} determined for this source by CHIME/FRB (CHIME/FRB Collaboration et al., 2019c)). The bursts shown in both Figure 6.1 and Figure 6.2 are dedispersed to this DM value.

Table 6.2 lists the physical properties of the bursts using the Effelsberg auto-correlations, dedispersed to 348.76 pc cm^{-3}. We measured the burst FWHM duration and peak time using a Gaussian fit (Hessels et al., 2019). The brightest burst, B4, shows a complicated structure (as can be seen in Figure 6.1). The width of each individual sub-burst in B4 was determined using the same Gaussian fit as above. The total width of B4, however, was measured by defining the beginning of the burst as the peak time of the first sub-burst minus W_{sub1}, and the end of the burst as the peak time of the last sub-burst plus W_{sub3}.

To determine the fluence, we define a larger time window, determined by eye, than the quoted FWHM durations, which encompasses all of the burst flux. First, we produce a time series containing each burst by summing over all frequency channels. We define an off-pulse region, and use this to normalise the time series. We then convert the signal in each time bin to physical units by using the radiometer equation (Cordes & McLaughlin, 2003), and sum over the burst duration to estimate the fluence. It should be noted that B1 and B3

were downsampled by a factor of four for this analysis, resulting in a lower time resolution than the other bursts. For the radiometer equation, we take typical values for the system temperature $T_{\rm sys} \approx 20$ K and telescope gain $G \approx 1.54$ K Jy^{-1} for Effelsberg. For the fluence values quoted in Table 6.2, we provide a conservative fractional error of 30%. Also shown in Table 6.2 are the burst spectral energy densities (Law et al., 2017), using the derived burst fluences and luminosity distance to FRB 20180916B. All four bursts are significantly dimmer compared to those previously detected (CHIME/FRB Collaboration et al., 2019c) with CHIME/FRB, which is unsurprising given the higher sensitivity of the 100-m Effelsberg telescope.

Table 6.1 shows the detection properties of the bursts, as seen in both the PSRIX data and the Effelsberg auto-correlations. For the PSRIX data, we quote the maximum S/N detected using PRESTO's single_pulse_search.py with an associated DM. The burst S/N for the auto-correlations is that measured at DM $= 348.76$ pc cm^{-3}, again using single_pulse_search.py. The burst width in Table 6.1 is the boxcar width used in single_pulse_search.py resulting in the peak S/N value. The S/N of the four bursts, as discovered in the PSRIX data, are shown in Figure 6.9 as a function of time during our observation. The first three bursts appear clustered in time, occurring within 1.5 h from the beginning of our observation.

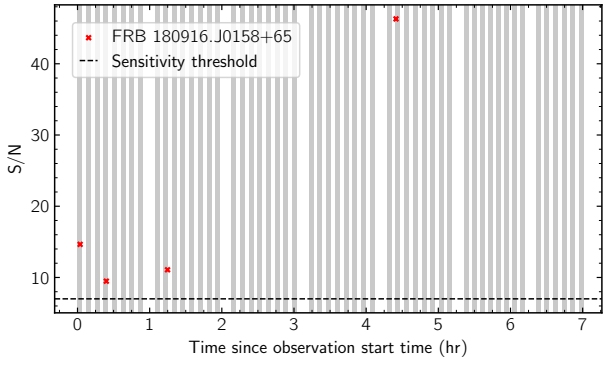

Figure 6.9: Burst brightness and arrival times. Burst S/N as a function of time during our 2019 June 19 observation of FRB 20180916B. The grey bars represent scans of the FRB 20180916B field. The red stars represent the four bursts (from left to right: B1, B2, B3, B4). The black dashed line indicates the detection threshold of our search in the pulsar-backend data (S/N = 7).

To study frequency-dependent brightness variations in the dominant sub-burst of B4 — which are expected if there is scintillation — we conducted a standard auto-correlation analysis (Cordes et al., 1985). We generated the spectrum of the burst within the FWHM duration ($W_{\rm sub2} = 0.06$ ms) using Effelsberg auto-correlations with a frequency resolution of 15.6 kHz. Spectral channels containing significant RFI, along with those at the edges of the 16-MHz subbands, were set to zero in the spectrum before generating the auto-correlation function (ACF).

We calculated the ACF using the following expression:

$$\mathrm{ACF}(\Delta\nu) = \frac{\sum_i (S(\nu_i) - \bar{S})(S(\nu_i + \Delta\nu) - \bar{S})}{\sqrt{\sum_i (S(\nu_i) - \bar{S})^2}\sqrt{\sum_i (S(\nu_i + \Delta\nu) - \bar{S})^2}}, \tag{6.1}$$

where ν is the frequency, $\Delta\nu$ is the frequency lag, and $\bar{S}$ is the mean of the spectrum. In this expression each summation is over the indices i which give non-zero values for both $S(\nu_i)$ and $S(\nu_i + \Delta\nu)$ (i.e. we only include the "good" data in the auto-correlation analysis). The ACF calculated using Equation 6.1 is shown in Figure 6.10.

The central part of the ACF (for lags in the range -1.016 to $+1.016$ MHz) after removing the zero lag was then fitted with a Lorentzian function (Rickett, 1990) of the form:

$$\frac{a}{x^2 + {\Delta\nu_d}^2} + b, \tag{6.2}$$

using a least squares fit, for free parameters a, the amplitude; $\Delta\nu_d$, the decorrelation bandwidth (also known as the scintillation bandwidth: defined (Cordes et al., 1985) as the half-width at half maximum of the ACF); and offset b. Figure 6.10 shows the fit to the ACF. The Lorentzian fit, with 127 degrees of freedom, returned a χ^2 of 105.2. We assume that the ACF between 3 and 20 MHz lags contain no structure and represents the noise in the central profile of the ACF. We measure the standard deviation in this region and use this as our uncertainty for the calculation of χ^2. The p-value of the fit is 0.92.

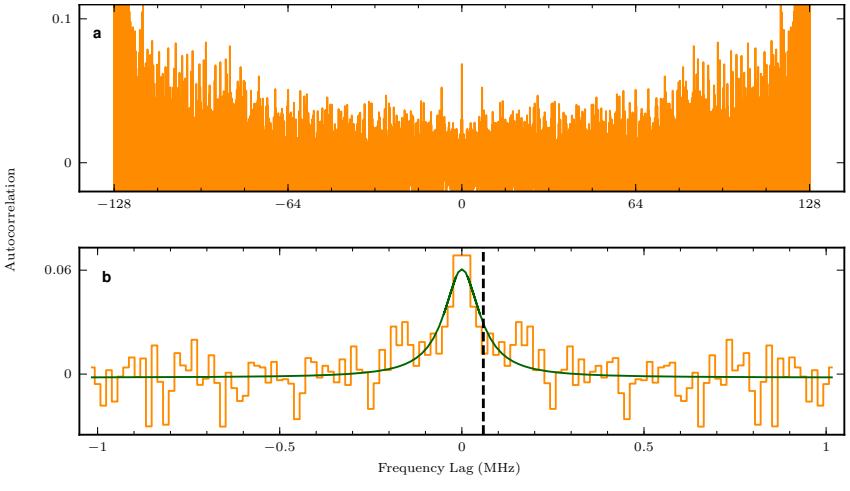

Figure 6.10: Auto-correlation function and scintillation bandwidth of brightest burst, B4. a: The auto-correlation function (ACF) of the spectrum of the bright, narrow burst component of burst B4. **b**: The ACF for lags between -1.016 and 1.016 MHz. The zero-lag noise spike has been removed from the ACF. A Lorentzian fit is shown in green in panel (**b**). The black vertical dashed line represents the scintillation bandwidth, defined as the half-width at half-maximum of the Lorentzian fit.

We measure the scintillation bandwidth to be 59 $\pm$ 13 kHz. This estimate is consistent with the NE2001 model (Cordes & Lazio, 2002) prediction of $\sim$ 60 kHz along the line-of-sight at our observing frequency of 1.7 GHz. Using the simple relationship

$$2\pi\tau\Delta\nu_d \sim 1, \tag{6.3}$$

we estimate a scattering timescale, τ, of $\sim$ 2.7 µs, which we find is also similar to the NE2001 model prediction of $\sim$ 2 µs along the line-of-sight (Cordes & Lazio, 2002). This constraint on the scattering time is much tighter compared to CHIME/FRB measurements (CHIME/FRB Collaboration et al., 2019c) of FRB 20180916B bursts, even after accounting for the different observing frequencies and the typical ν^{-4} scaling of scattering time. CHIME/FRB nominally measured scattering times of approximately 2 ms for two FRB 20180916B bursts, but these measurements are likely a reflection of burst morphology as opposed to genuine scattering effects (as was previously considered; CHIME/FRB Collaboration et al. 2019c).

6.2.6 High-time-resolution correlation and burst imaging.

Coherently dedispersed visibilities for each burst were created by re-correlating the EVN data for only the time ranges corresponding to the burst durations. The exact time ranges were initially determined from the Effelsberg PSRIX data and then refined using coherently dedispersed Effelsberg auto-correlations. From the resulting auto-correlations we created pulse profiles and used these to set the optimal correlator gates applied to the interferometric data.

The *a priori* position of FRB 20180916B provided at the time of the EVN observation had an uncertainty of $\sim$ 3 arcmin (see above), making it infeasible to localise the bursts by directly imaging this region at milli-arcsecond resolution (which would require an image with $\sim 10^{11}$ pixels). However, for strong signals, it is possible to estimate the position of the source from the geometric delays across the different telescope baselines. The differential geometric phase delay, $\Delta\phi_g$, of the source with respect to the phase centre (*a priori* pointing position) for a given baseline is given by (Fomalont & Perley, 1999; Thompson, 1999):

$$\Delta\phi_g = 2\pi\nu(u\,\Delta\alpha\,\cos\delta + v\Delta\delta) \tag{6.4}$$

where ν is the observed frequency, $(\Delta\alpha, \Delta\delta)$ is the positional offset of the source with respect to the phase centre in right ascension (α) and declination (δ), respectively, and (u, v) are the coordinate offsets for the given baseline.

We used the strongest burst, B4, to estimate the offset of the source with respect to the phase centre. We then re-correlated the data at this refined J2000 position of $\alpha = 01^{\rm h}58^{\rm m}00.5^{\rm s}$, $\delta = 65^\circ43'01.0''$ (with an estimated uncertainty of a few arcseconds), which was $\sim$ 2 arcmin from the *a priori* position — and thus consistent within the estimated uncertainties. We applied the previously described EVN calibration to these burst data and imaged the individual bursts. All bursts were detected above a 7-σ confidence level. Different imaging schemes were used during the imaging process in order to emphasise resolution (i.e. contribution from the longest baselines) or sensitivity (i.e. contribution from the core of

the array). The final images were produced by using a natural weighting and excluding data from the Tianma station which, despite providing the highest resolution, exhibited potential calibration issues that could affect the absolute burst positions by a few milli-arcseconds — especially for such short integration times, where the uv coverage is poor. Table 6.2 lists the burst properties obtained from the EVN images, which are shown in Figure 6.3. An image of the combined burst data was also produced. This final image is dominated by the emission of the strongest burst, B4, and thus we only consider the results from the four bursts individually.

The flux densities and positions were measured using Difmap and the Common Astronomy Software Applications (CASA) software packages by fitting a circular Gaussian distribution component to the detected emission in the uv plane, which is expected to be a robust method against station gain calibration uncertainties (Natarajan et al., 2017). The position of each burst was measured independently and then we determined a weighted average J2000 position for the source of $\alpha = 01^{\rm h}58^{\rm m}00.7502^{\rm s} \pm 2.3$ mas, $\delta = 65^{\circ}43'00.3152'' \pm 2.3$ mas, where we used the fluence of each burst as weights. This is within 1.7 arcsec of the position determined via mapping the geometric delays. The final positional uncertainty reflects the statistical uncertainties from the individual position measurements (~ 1 mas), the uncertainties in the absolute ICRF position of the phase calibrator (J0207+6246; 0.15 mas) and check source (J0140+6346; 0.1 mas), and the systematic uncertainty associated with the phase-referencing technique and the extended structure of the check source and phase calibrator ($\sim$2 mas), as explained previously. Uncertainties were added in quadrature.

Finally, we searched for continuum radio counterparts of FRB 20180916B by imaging the full interferometric data set with a field-of-view of 2×2 arcsec^2 centred at the position of the bursts (and thus also covering the full extent of the nearby star-forming region). We detected no emission at the position of FRB 20180916B as well as no significant ($< 4.5\sigma$) compact emission anywhere in the field above the r.m.s. noise level of 10 μJy beam^{-1} (19 μJy beam^{-1} when excluding the data from the Tianma station). We also searched for possible emission from the core of the galaxy, but found no signal above the 6-σ r.m.s. noise level in a 4×4 arcsec^2 area.

6.2.7 VLA observations.

In June 2019, we used the Karl G. Jansky Very Large Array (VLA) to perform a quasi-simultaneous search for millisecond transients and faint persistent emission associated with FRB 20180916B. The VLA observed from 1–2 GHz with baseline lengths up to 11 km, giving a synthesised beam size of roughly 4 arcsec. VLA visibilities were sampled at 5-ms time resolution and searched in real time by the Realfast system (Law et al., 2018a); the same data were integrated at 3-s time resolution and calibrated with the standard CASA calibration pipeline. In a total of 14 h of observing (with on-target efficiency of 80%), we found no millisecond transients to an 8-σ limit of approximately 50 mJy beam^{-1} in 5 ms or, equivalently, a fluence limit of 0.25 Jy ms. No VLA observing was coincident with known burst times detected by the EVN. We concatenated all 14 h of data, applied an iteration of phase self-

calibration using relatively bright background sources in the field of view of the antennas, and imaged 600 MHz of the bandwidth centred near 1.6 GHz to search for persistent radio emission on arcsecond scales. We confirmed that the astrometric accuracy of the deep image is good to better than 1 arcsec by associating seven bright field radio sources to the catalogued location in the NRAO VLA Sky Survey (NVSS; Condon et al. 1998). No persistent emission is detected at the position of FRB 20180916B brighter than a 3-σ limit of 18 μJy beam^{-1}. A 25-μJy source is located at a nearby J2000 position of $\alpha = 01^{\rm h}58^{\rm m}00.9^{\rm s},\ \delta = 65^{\circ}43'07''$ (see Figure 6.4), but this position is offset by approximately 7 arcsec from the location of FRB 20180916B, which is much more than the astrometric precision, estimated to be 0.4 arcsec (the VLA observed in its B configuration at the time). It is thus very unlikely to be associated with FRB 20180916B or the host galaxy.

6.2.8 Optical observations and host galaxy.

The EVN localisation of FRB 20180916B places it at the outskirts of SDSS J015800.28+654253.0, an apparent Sb spiral galaxy (possibly with a faint bar) with an estimated (Alam et al., 2015) photometric redshift $z_{\rm phot} = 0.07 \pm 0.05$.

We obtained imaging and spectroscopic observations of the host galaxy using the GMOS spectrograph on the Gemini-North telescope between July and September 2019 (Program ID GN-2019A-DD-110). We acquired 2×900-s exposures with each of the g' and r' filters. The images were processed with the gemini IRAF/pyraf package, and sources were extracted using Source Extractor (Bertin & Arnouts, 1996). The images were de-warped and astrometrically corrected by matching the point source positions to those from the *Gaia* Data Release 2 (DR2) Catalogue (Gaia Collaboration et al., 2016, 2018). The matching precision was 17–20 mas r.m.s. for each image. The seeing was measured to be 0.99 and 0.78 arcsec in the g' and r' images, respectively.

Figure 6.5 shows the r' image of the galaxy, along with the position of FRB 20180916B. The galaxy is nearly face-on, with spiral arm structures visible. FRB 20180916B appears co-located with one of the outer arms of the galaxy, near a bright clump in the r' image (see Figure 6.8 for a more detailed zoom on this region). We attribute this emission to that of Hα, which is bright in emission in the GMOS spectra and, at the redshift of the host galaxy, falls within the r' image. The total stellar mass of the galaxy has been estimated to be $\sim 10^{10}$ times the mass of the Sun by using the WISE W1 and W2 colours (Jarrett et al., 2017), which provide a more robust estimation given that they are less affected by extinction.

We performed long-slit optical spectroscopy, simultaneously targeting the galaxy core and the FRB location, in order to measure the redshift and spectral properties of the galaxy and the location of FRB 20180916B. We acquired 4×900-s spectroscopic observations with a 1.5 arcsec slit and the R400 grating — along with corresponding flat fields, copper-argon arcs, and observations of BD +28 4211 to correct for sensitivity and extinction. As shown in Figure 6.8, the slit was rotated to align with the host galaxy centre and FRB position.

The spectroscopic data were processed with the Gemini IRAF/pyraf package. The FWHM of the emission lines from the sky was measured to be 7–8 Å, matching the theoretical

Table 6.3: Properties of the spectral emission lines. Properties of the most relevant spectral lines observed at the location of the core of the galaxy and at the position of FRB 20180916B. Note that the fluxes are not corrected for extinction. Numbers in parentheses indicate 1-σ uncertainties in the least significant digits.

Line ID	Galaxy Core			FRB Location		
	Centroid (Å)	Width (Å)	Flux (10^{-16} erg cm^{-2} s^{-1})	Centroid (Å)	Width (Å)	Flux (10^{-16} erg cm^{-2} s^{-1})
O_{III} 4958.93 Å	5122.7	5.5	0.38(4)	–	–	–
O_{III} 5006.86 Å†	5155.6	5.6	4.76(4)	–	–	–
N_{II} 6548.05 Å	6767.9	5.5	0.31(4)	–	–	–
Hα 6562.8 Å	6784.8	10.9	6.57(4)	6787.5	6.5	1.002(8)
N_{II} 6583.45 Å	6806.9	10.3	2.51(4)	6809.0	5.1	0.233(8)
S_{II} 6716.44 Å	6943.7	7.4*	0.77(4)	6946.2	6.4††	0.243(5)
S_{II} 6730.81 Å	6953.8	7.4*	0.58(4)	6961.8	6.4††	0.123(5)

Notes: †: The O_{III} 5006.86 Å line is detected at the FRB location but is corrupted by a cosmic-ray hit. *,††: A single value of line width was fit for both lines.

resolving power of $R \approx 640$. The wavelength calibration with copper-argon emission lines had a precision of 0.7–0.8 Å. However, the lack of arc lines towards the bluer edge reduces the accuracy of the wavelength solution towards 5200 Å.

We extracted the spectrum within 5 arcsec of the galaxy centre as well as 2 arcsec around the location of FRB 20180916B itself. We used the trace of the galaxy centre, offset by 7.7 arcsec to trace the location of FRB 20180916B. Figure 6.5 shows the calibrated spectra at each location separately. We identify redshifted Hα, N_{II}, S_{II} and O_{III} lines with an average redshift of $z = 0.033 \pm 0.001$ if all lines are included and $z = 0.0337 \pm 0.0002$ when excluding the O_{III} lines that are at the blue edge of the CCD (and hence may have reduced wavelength calibration accuracy). Table 6.3 shows the line centroids, widths and fluxes. The spectrum at the location of FRB 20180916B is dominated by emission lines with little continuum emission. The O_{III} 5007Å line is detected at the FRB location but was corrupted by a cosmic-ray hit. As the slit was positioned at the edge of the nearby star-forming clump, we observe a non-uniform slit illumination pattern and the line centroids, especially for Hα, are shifted towards the redder wavelengths by ~ 1 Å. Nevertheless, we can confirm that both the clump and the galaxy are at the same distance.

The obtained flux for the Hαemission at the position of FRB 20180916B (which is dominated by the star-forming clump) implies a luminosity of $L_{H\alpha} \sim (2.0 \pm 0.1) \times 10^{39}$ erg s^{-1}, which corresponds to a star formation rate (Kennicutt et al., 1994) of ≈ 0.016 $M_{\odot}$ yr^{-1}. These values were extracted from a region of 1.5×2 arcsec^2 around the FRB, corresponding to 1.5 kpc^2, implying a star-formation surface density of $\approx 10^{-2}$ $M_{\odot}$ yr^{-1} kpc^{-2}. Note that these values can be significantly affected by extinction, which is estimated to be $E(B-V) \approx 1.01$.

From the Hα, N_{II}, and S_{II} line fluxes, we estimate the metallicity of the galaxy (Dopita et al., 2016) as $12 + \log(O/H) = 8.82$, close to solar neighborhood metallicity, and five times higher when compared to the host of FRB 121102 (< 8.1 on the same metallicity scale; Tendulkar et al. 2017).

6.2.9 Chance alignment probability with host galaxy.

The projected position of FRB 20180916B is coincident with a star-forming clump in the spiral galaxy SDSS J015800.28+654253.0. To confirm an association with the galaxy we have estimated the probability of chance coincidence between the two sources.

We have considered a uniform density of galaxies across the sky. Assuming a Poisson distribution of galaxies in the relevant co-moving volume, we estimate the number density of typical galaxies brighter than $M_B = -16$ (i.e., galaxies with masses greater than $\sim$ 40% of the dwarf galaxy host (Tendulkar et al., 2017) of FRB 121102) based on the all-galaxy luminosity function (Faber et al., 2007; Blanton et al., 2003), and their typical size distribution based on the galaxies reported in SDSS DR7 (Zhang & Yang, 2019). Then, we calculate the chance coincidence probability for a source to be co-located within twice the median half-light radius of any galaxy as a function of redshift.

At the measured redshift of $z \sim 0.0337$, the chance coincidence probability $P << 0.1\%$. However, we may consider the probability up to a redshift of $\sim$ 0.11, the maximum redshift considered for FRB 20180916B based on the observed DM (CHIME/FRB Collaboration et al., 2019c). Even in this case $P \lesssim 1\%$ (see Figure 6.11). The association between FRB 20180916B and the galaxy is thus statistically robust.

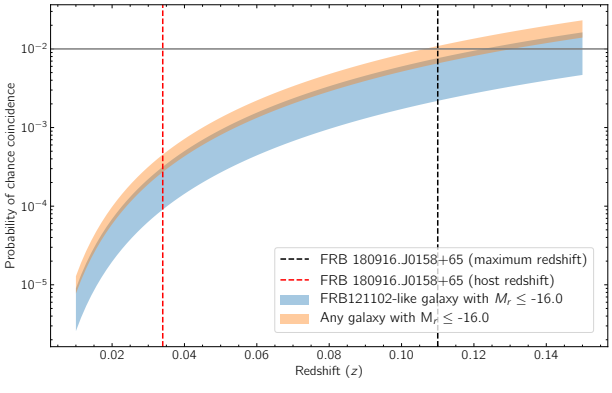

Figure 6.11: Redshift-cumulated probability of chance alignment coincidence. Probability of a chance alignment between FRB 20180916B and twice the median half-light radius of any galaxy with magnitude $M_B \leq -16$ (orange region) or with a dwarf galaxy like the host of FRB 121102 (blue region) as a function of redshift. The horizontal grey line represents the 1% probability threshold. At the redshift of the host galaxy, $z = 0.0337$ (vertical dashed red line), the chance coincidence probability is $P << 0.1\%$, and at the maximum possible redshift of $\sim$ 0.11 derived from the observed DM the probability is $\lesssim 1\%$ (vertical dashed black line).

6.2.10 Dispersion measure budget

FRB 20180916B is close to the Galactic plane, with longitude $l = 129.7^\circ$ and latitude $b = 3.7^\circ$. The total measured DM of FRB 20180916B is $\mathrm{DM_{Tot}} = 348.76$ pc cm^{-3}, and is expected to be the sum of contributions from the Milky Way disk ($\mathrm{DM_{MW}}$) and halo ($\mathrm{DM_{Halo}}$), the intergalactic medium ($\mathrm{DM_{IGM}}$), and host galaxy ($\mathrm{DM_{Host}}$; including both

the ISM and halo of the host). For the line-of-sight to FRB 20180916B, $\mathrm{DM_{MW}}$ is predicted to be 199 pc cm^{-3} and 325 pc cm^{-3} by the NE2001 and YMW16 Galactic electron density models, respectively (Cordes & Lazio, 2002; Yao et al., 2017). $\mathrm{DM_{Halo}}$ is estimated to be 50–80 pc cm^{-3} or approximately 45 pc cm^{-3} according to two available models (Prochaska & Zheng, 2019; Yamasaki & Totani, 2020). Given the range of model predictions, one can ascribe up to roughly 100 pc cm^{-3} to $\mathrm{DM_{IGM}}$ and $\mathrm{DM_{Host}}$. For redshift $z = 0.0337$, $\mathrm{DM_{IGM}}$ is expected to be (Inoue, 2004) approximately 34 pc cm^{-3} — though this estimate is highly line-of-sight dependent for low redshift (Li et al., 2019). Overall, after subtracting these various contributions, $\mathrm{DM_{Host}}$ is likely less than 70 pc cm^{-3}, and could be much smaller. The YMW16 model over-predicts $\mathrm{DM_{MW}}$ in this direction (unless the $\mathrm{DM_{Halo}}$, $\mathrm{DM_{IGM}}$ and $\mathrm{DM_{Host}}$ contributions are all much smaller than expected), and this illustrates that FRB DMs will help constrain Galactic electron density models. Conversely, because the line-of-sight to FRB 20180916B passes through the Galactic plane, with a large but uncertain Galactic DM contribution, it is unlikely to be a good probe for refining the DM-z relationship in the IGM (Inoue, 2004).

6.2.11 FRB 20180916B compared with the other localised repeating fast radio burst source, FRB 121102.

The physical origin of the FRB phenomenon remains unclear, and many of the proposed models (Platts et al., 2019) remain consistent with the observational facts we present here for FRB 20180916B. We now briefly consider the nature of FRB 20180916B by comparing to two of the families of models proposed for FRB 121102, which is the FRB source studied in most detail to date, and the only other well-localised repeater.

One of the models to explain the associated persistent radio counterpart to FRB 121102 proposes the existence of a 20–50 year-old supernova remnant and nebula powered by a young flaring magnetar (Lyubarsky, 2014; Beloborodov, 2017; Margalit & Metzger, 2018; Metzger et al., 2019). The absence of a similarly bright radio nebula associated with FRB 20180916B could be explained, in this model, as an older system whose emission has already faded. Assuming a similar model (Margalit & Metzger, 2018), the upper limits on persistent radio emission associated with FRB 20180916B are consistent with a system that is at least about five times older than FRB 121102, and thus $\gtrsim 200-500$ yr old. Additionally, the same model also predicts a characteristic decay of the RM with time. An RM as large as the one observed towards FRB 121102 (Michilli et al., 2018b) would drop to the RM observed (CHIME/FRB Collaboration et al., 2019c) towards FRB 20180916B at a source age of $\sim$ 300 yr. However, while the results we present here are conceivably consistent with the young magnetar scenario for repeating FRBs, we find no new support for this scenario.

Other models, inspired originally by FRB 121102, invoke interaction between a nearby strong plasma stream and a neutron's magnetosphere (Zhang, 2017). In the case of FRB 121102, the large (Michilli et al., 2018b) RM and the observational similarity (Marcote et al., 2017) of its compact, persistent radio source to low-luminosity active galactic nuclei (LLAGN) suggest that the bursts could originate from a massive black hole, or a neutron star

in the near vicinity. An accreting massive black hole can provide a plasma stream that could interact with a neutron star magnetosphere (Zhang, 2018b). The absence of a persistent radio counterpart to FRB 20180916B, and its location in the spiral arm of a morphologically well-defined galaxy, make such a model arguably less likely in the case of FRB 20180916B. For a black hole with a similar mass to that of the one considered for FRB 121102 (10^{5-6} $M_{\odot}$), our upper limits would imply a very low accretion rate of $\sim 10^{-7}$ $L_{\rm Edd}$. Nonetheless, this accretion rate is still compatible with the low end observed in LLAGN (Loewenstein et al., 2001). The presence of a massive black hole at the apex of the star-forming clump is thus not excluded, although rather unlikely. Nonetheless, in an interacting model (Zhang, 2017), the plasma stream can also have a different origin, and it is conceivable that FRB 20180916B is a neutron star interacting with, e.g., the jet of a stellar-mass black hole.

The proximity of FRB 20180916B will aid in performing deep multi-wavelength observations, which may help to discriminate between the various scenarios outlined above, while potentially also suggesting new ones.

Acknowledgements

We thank W. J. G. de Blok, L. Connor, N. Maddox, E. Petroff, H. Vedantham and J. Weisberg for valuable discussions. The European VLBI Network is a joint facility of independent European, African, Asian, and North American radio astronomy institutes. Scientific results from data presented in this publication are derived from the following EVN project code: EM135. This work was also based on simultaneous EVN and PSRIX data recording observations with the 100-m telescope of the MPIfR (Max-Planck-Institut für Radioastronomie) at Effelsberg, and we thank the local staff for this arrangement. Our work is also based on observations obtained at the Gemini Observatory (program DT-2019A-135), which is operated by the Association of Universities for Research in Astronomy, Inc., under a cooperative agreement with the NSF on behalf of the Gemini partnership: the National Science Foundation (United States), the National Research Council (Canada), CONICYT (Chile), Ministerio de Ciencia, Tecnología e Innovación Productiva (Argentina), and Ministério da Ciência, Tecnologia e Inovação (Brazil). B.M. acknowledges support from the Spanish Ministerio de Economía y Competitividad (MINECO) under grants AYA2016-76012-C3-1-P and MDM-2014-0369 of ICCUB (Unidad de Excelencia “María de Maeztu”). J.W.T.H. acknowledges funding from an NWO Vidi fellowship and from the European Research Council under the European Union’s Seventh Framework Programme (FP/2007-2013) / ERC Starting Grant agreement nr. 337062 (“DRAGNET”). M.B. is supported by an FRQNT Doctoral Research Award, Physics Department Excellence Award and a Mitacs Globalink Graduate Fellowship. R.K. is supported by ERC synergy grant nr. 610058 (“BlackHoleCam”). C.J.L. acknowledges support from NSF grant 1611606. D.M. is a Banting Fellow. K.A. acknowledges support from NSF grant AAG-1714897. B.A. is supported by a Chalk-Rowles Fellowship. A.M.A. acknowledges funding from an NWO Veni fellowship. S.B.S. acknowledges support from NSF grant AAG-1714897. F.K. thanks the Swedish Research Council. U.-L.P. receives support from the Ontario Research Fund Research Excellence Program (ORF-RE), NSERC, Simons Foundation, Thoth Technology Inc., and Alexander von Humboldt Foundation. Z.Pl. is supported

by a Schulich Graduate Fellowship. P.S. is a Dunlap Fellow and an NSERC Postdoctoral Fellow. The Dunlap Institute is funded through an endowment established by the David Dunlap family and the University of Toronto. K.M.S. is supported by an NSERC Discovery Grant, an Ontario Early Researcher Award, and a CIFAR fellowship. Part of this research was carried out at the Jet Propulsion Laboratory, California Institute of Technology, under a contract with the National Aeronautics and Space Administration. The NANOGrav project receives support from National Science Foundation (NSF) Physics Frontiers Center award number 1430284. FRB research at UBC is supported by an NSERC Discovery Grant and by the Canadian Institute for Advanced Research. The CHIME/FRB baseband system is funded in part by a Canada Foundation for Innovation John R. Evans Leaders Fund award to I.H.S. The National Radio Astronomy Observatory (NRAO) is a facility of the National Science Foundation operated under cooperative agreement by Associated Universities, Inc. The Astronomical Image Processing System (AIPS) is a software package produced and maintained by NRAO. The Common Astronomy Software Applications (CASA) package is software produced and maintained by NRAO. This research made use of APLpy, an open-source plotting package for Python hosted at http://aplpy.github.com, Astropy, a community-developed core Python package for Astronomy (Astropy Collaboration et al., 2013), and Matplotlib (Hunter, 2007).

Chapter 7

Resolving the decades-long transient FIRST J141918.9+394036: an orphan long gamma-ray burst or a young magnetar nebula?

B. Marcote, K. Nimmo, O. S. Salafia, Z. Paragi, J. W. T. Hessels, E. Petroff, R. Karuppusamy

The Astrophysical Journal Letters, 2019, 876, L14

Abstract

Ofek (2017) identified FIRST J141918.9+394036 (hereafter FIRST J1419+3940) as a radio source sharing similar properties and host galaxy type to the compact, persistent radio source associated with the first known repeating fast radio burst, FRB 121102. Law et al. (2018b) showed that FIRST J1419+3940 is a transient source decaying in brightness over the last few decades. One possible interpretation is that FIRST J1419+3940 is a nearby analogue to FRB 121102 and that the radio emission represents a young magnetar nebula (as several scenarios assume for FRB 121102). Another interpretation is that FIRST J1419+3940 is the afterglow of an 'orphan' long gamma-ray burst (GRB). The environment is similar to where most such events are produced. To distinguish between these hypotheses, we conducted radio observations using the European VLBI Network at 1.6 GHz to spatially resolve the emission and to search for millisecond-duration radio bursts. We detect FIRST J1419+3940 as a compact radio source with a flux density of $620 \pm 20\,\mu\mathrm{Jy}$ (on 2018 September 18) and a source size of $3.9 \pm 0.7\,\mathrm{mas}$ (i.e. $1.6 \pm 0.3\,\mathrm{pc}$ given the angular diameter distance of $83\,\mathrm{Mpc}$). These results confirm that the radio emission is non-thermal and imply an average expansion velocity of $(0.10 \pm 0.02)c$. Contemporaneous high-time-resolution observations using the 100-m Effelsberg telescope detected no millisecond-duration bursts of astrophysical origin. The source properties and lack of short-duration bursts are consistent with a GRB jet expansion, whereas they disfavor a magnetar birth nebula.

7.1 Introduction

Very-long-baseline radio interferometric (VLBI) observations are a powerful way to study astrophysical transients because they provide milliarcsecond angular resolution imaging and astrometry. Such transient events are produced by blast waves and slowly-evolving synchrotron afterglows, whose temporal evolution and interaction with the surrounding medium are well characterized by VLBI observations that can measure the projected size and proper motion of such emission.

For example, this technique was successfully used to spatially resolve the emission and measure the expansion speed of the afterglow associated with the long gamma-ray burst (GRB) 030329 (Pihlström et al., 2007). VLBI observations have also been used to study the first detected binary neutron star merger, GRB 170817A (Abbott et al., 2017). The obtained measurement of the proper motion and physical size constrained the nature of the source to be a relativistic jet (Mooley et al., 2018; Ghirlanda et al., 2019). Furthermore, VLBI observations contributed to the first precise localization of a fast radio burst (FRB), the repeating source FRB 121102 (Spitler et al., 2014, 2016; Scholz et al., 2016). The burst source was associated with a compact ($< 0.7\,\mathrm{pc}$; Marcote et al. 2017), persistent radio source with a luminosity of $\nu L_\nu \approx 3 \times 10^{38}\,\mathrm{erg\,s^{-1}}$ at 1.7 GHz (Chatterjee et al., 2017), located inside a low-metallicity star-forming region in a dwarf galaxy at a redshift of $0.19273(8)$ (Tendulkar et al., 2017; Bassa et al., 2017). The environment of FRB 121102 is remarkably similar to the ones where long GRBs (as well as superluminous supernovae) typically occur (Modjaz et al., 2008; Metzger et al., 2017), favoring several scenarios that consider repeating FRBs to be produced by newly-born magnetars created in such events (see e.g. Margalit & Metzger, 2018; Piro & Gaensler, 2018). FRBs could thus be detectable at the sites of long GRBs, and the persistent source associated with FRB 121102 could be the longer-lived nebula following the afterglow of one of these events. In any case, FRBs are expected to be produced in relatively young objects ($\sim$ 10–100 yr) with possibly associated radio nebulae (Murase et al., 2016; Kashiyama & Murase, 2017; Omand et al., 2018).

Based on the properties of FRB 121102's persistent radio source and host galaxy, Ofek (2017) identified a number of similar sources in the Very Large Array (VLA) FIRST catalogue. Law et al. (2018b) showed that one of these sources, FIRST J141918.9+394036 (hereafter FIRST J1419+3940) is a slowly declining transient. Using archival observations, they showed that the source declined from $\sim 26\,\mathrm{mJy}$ (at 1.4 GHz) in 1993 to $\lesssim 0.4\,\mathrm{mJy}$ (at 3 GHz) in 2017. Both the light-curve and the inferred luminosities of $\nu L_\nu \gtrsim 3 \times 10^{38}\,\mathrm{erg\,s^{-1}}$ are consistent with the afterglow of a long GRB, requiring a released kinetic energy of $\sim 10^{51}\,\mathrm{erg}$ at the time of the explosion (estimated to be $\sim$ 25–30 yr ago). No convincing association with a previously detected GRB could be made, however (Law et al., 2018b).

FIRST J1419+3940 is associated with a small star-forming galaxy at redshift of $z \approx 0.01957$. Both sources, FIRST J1419+3940 and FRB 121102, show similar environments: both show compact and persistent radio emission with luminosities of $\sim 10^{38}\,\mathrm{erg\,s^{-1}}$ located inside star-forming regions with equivalent star formation rates in similar sized dwarf galaxies. Their

physical nature could thus also be similar, and FIRST J1419+3940 might be associated with a source capable of producing FRBs.

Here we present European VLBI Network (EVN) radio observations of FIRST J1419+3940 that provide the first constraints on the source compactness, coupled with simultaneous searches for millisecond-duration bursts. We present the observations and data reduction in Section 7.2. We describe the results in Section 7.3, and their implications for the nature of FIRST J1419+3940 in Section 7.4. Finally, we present our conclusions in Section 7.5.

7.2 Observations and data reduction

We observed FIRST J1419+3940 on 2018 September 18 between 12:00 and 19:00 UTC at 18 cm (1.6 GHz) with the EVN, involving a total of 12 stations: Jodrell Bank Mark2, Westerbork single-dish, Effelsberg, Medicina, Onsala 25-m, Tianma, Toruń, Hartebeesthoek, Sardinia, and three stations from e-MERLIN (Cambridge, Defford, and Knockin). The data were recorded with a total bandwidth of 128 MHz, and correlated in real time (e-EVN operational mode) at JIVE (The Netherlands) using the SFXC software correlator (Keimpema et al., 2015). The data were divided into eight subbands of 64 channels each, with full circular polarization products, and 1-s time averaging. We also buffered the baseband EVN data in parallel so that high-time-resolution correlations could be produced afterwards, if a millisecond-duration radio burst was detected.

Furthermore, we simultaneously observed FIRST J1419+3940 in the frequency range 1580–1736 MHz using the 100-m Effelsberg telescope and the PSRIX pulsar data recorder (Lazarus et al., 2016). We recorded with two summed linear polarizations, achieving a gain of 1.5 K Jy^{-1} and a receiver temperature of 25 K. The total bandwidth of 156 MHz was divided into 10 subbands — each one further divided into 64 channels and recorded with 32-bit time samples. The ultimate time and frequency resolution of the data were 40.96 µs and 0.2438 MHz, respectively. Before processing, the subbands were combined into a single band and the data were converted to 4-bit samples to ensure compatibility with the PRESTO pulsar analysis software suite (Ransom, 2001).

7.2.1 Interferometric data

We observed J1642+3948 as fringe finder and J1419+3821 (located at only 1.3° from FIRST J1419+3940) as phase calibrator. We scheduled a phase-referencing cycle of 4.5 min on the target and 1.5 min on the phase calibrator, achieving a total time of $\sim$ 4.5 h on FIRST J1419+3940.

The interferometric data were reduced using AIPS[1] (Greisen, 2003) and Difmap (Shepherd et al., 1994) following standard procedures. A-priori amplitude calibration was performed using the known gain curves and system temperature measurements recorded individually on each station during the observation. We used nominal system equivalent flux density

[1] The Astronomical Image Processing System (AIPS) is a software package produced and maintained by the National Radio Astronomy Observatory (NRAO).

(SEFD) values for the following stations: Jodrell Bank Mark2, Tianma, and the e-MERLIN stations. We manually flagged data affected by radio frequency interference (RFI) and then we fringe-fitted and bandpass-calibrated the data using the fringe finder and the phase calibrator. We imaged and self-calibrated the phase calibrator in Difmap to improve the final calibration of the data. The obtained solutions were then transferred to the target, which was subsequently imaged.

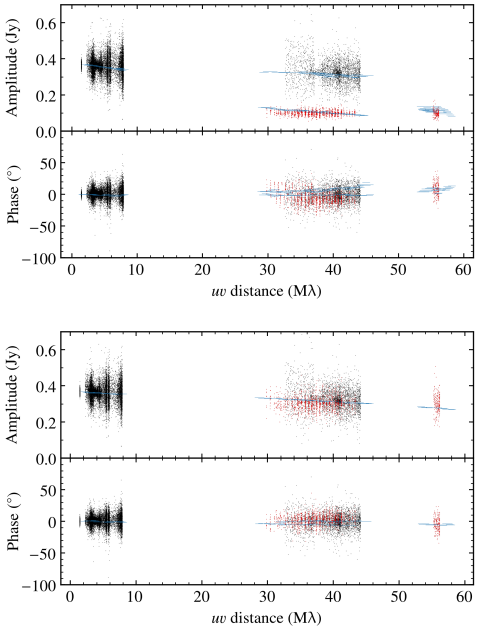

Figure 7.1: The obtained visibility data (amplitudes and phases) for the phase calibrator source, J1419+3821, after the original calibration (top) and in the alternate calibration where the gain calibration of the Tianma station was calibrated using a source model from only the stations with a robust amplitude calibration (bottom). See Sect. 7.2 for details. Red dots represent data from the baselines including the Tianma station. Blue lines represent the source model in each case.

We note that Tianma did not produce reliable system temperature values during the experiment. Most of these measurements failed and the existing ones exhibited a much larger scatter than usual. Therefore we used the nominal SEFD for amplitude calibration. This typically produces a satisfactory a-priori calibration that can be further improved during imaging and self-calibration. Tianma, however, provides the longest East-West baselines in our array with no equivalent baselines to compare with, and it also does not have short spacings to establish a reliable station calibration. In this case imaging and parametrization of source properties by model-fitting is complicated due to the fact that some source parameters may correlate with the Tianma station gain (Natarajan et al., 2017).

Figure 7.1 displays the visibility amplitudes and phases as a function of projected baseline length in units of observing wavelength. The top panel shows the initial calibration, with the Tianma data highlighted in red. The low amplitudes may be consistent with a source that is very compact in general, but well resolved in the East-West direction. The bottom panel shows the data after we apply an amplitude correction factor for Tianma, based on a source model obtained by only using the stations with robust calibration. The required scaling factor was about three, implying that the station could have been much less sensitive than expected.

Due to the uncertainty with the Tianma calibration, we decided to take the following procedure to analyze the data. Instead of fitting an elliptical-Gaussian model brightness distribution to the uv-data in model fitting, we assumed a circular-Gaussian brightness distribution. This is expected to be less sensitive to uncertainties in station gain calibration (Natarajan et al., 2017). In addition, we looked at the results derived from the following cases: Tianma removed from the data set, Tianma present with nominal gain calibration, and Tianma present but with its gain scaled to be in agreement with the most compact possible solution (as explained above). As we will see in Sect. 7.3, the fitted source sizes differ somewhat, but in all cases they support the same main conclusion: that our target is resolved on milliarcsecond scales.

7.2.2 High-time resolution data

The high-time-resolution Effelsberg data were analyzed to search for individual millisecond bursts or a periodic signal. First, using PRESTO's rfifind, we identified specific time samples and frequency channels contaminated by RFI. The regions highlighted by rfifind and the frequency range 1610–1631 MHz, associated with RFI from the Iridium satellites, were masked prior to conducting the analysis. We then dedispersed the 4-bit data using the PRESTO tool prepsubband for 2500 trial dispersion measures (DMs) in the range 0–1210.8 $\mathrm{pc\,cm^{-3}}$. The resulting dedispersed time series were then searched for single pulses above a 6-σ threshold using PRESTO's single_pulse_search.py, which applies a matched-filter technique using boxcar functions of various widths, and in our search was sensitive to burst durations in the range 40.96 $\mu\mathrm{s}$ and 0.02 s. Dynamic spectra of the identified single-pulse candidates were generated and inspected by eye to distinguish between astrophysical signals and RFI.

In addition, a Fourier-domain search was performed on each individual dedispersed time series using PRESTO's accelsearch, in order to search for periodic signals. Potential periodic signals were sifted using ACCEL_sift.py, and the remaining candidates were inspected by eye after folding using prepfold.

The RFI mitigation process was unable to remove all instances of RFI in the data. We calculate that of the $\sim$ 4.3-h Effelsberg on-source time, approximately 92.4% was examined for bursts and periodic signals. Note the discrepancy between the Effelsberg on-source time ($\sim$ 4.3 h) and the EVN on-source time ($\sim$ 4.5 h) which is due to Effelsberg's longer slew time compared with other antennas.

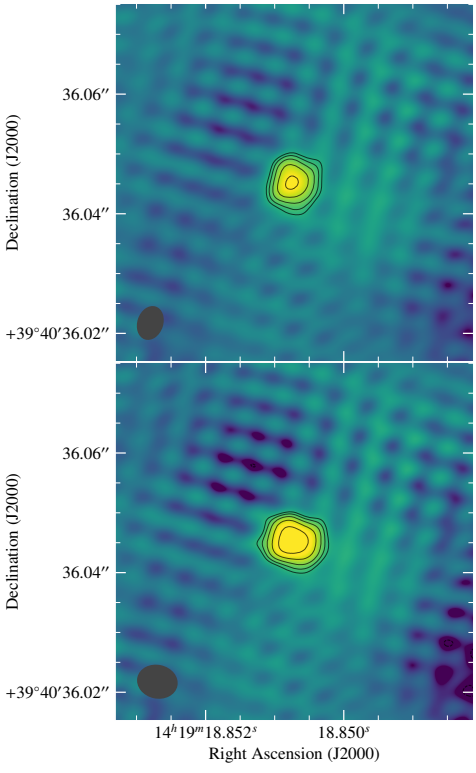

Figure 7.2: Images of FIRST J1419+3940 at 1.6 GHz with the EVN on 2018 September 18 derived from the two gain calibrations performed on Tianma data (original, top, and scaled, bottom). Contours start at a 3-σ rms noise level of 25 and 29 $\mu\mathrm{Jy\,beam}^{-1}$, respectively, and increase by factors of $\sqrt{2}$. The synthesized beams are represented by the dark gray ellipses at the bottom left corner of each image.

The aforementioned analysis strategy was verified using similar data targeting pulsar PSR B2020+28. We performed a blind search and detected both individual pulses and the known periodicity of this pulsar.

7.3 Results and discussion

7.3.1 On the persistent emission

FIRST J1419+3940 is detected on 2018 September 18 as a radio source that is compact on milliarcsecond scales (see Fig. 7.2), with a flux density of $620 \pm 20\,\mu\mathrm{Jy}$ at a position of:

$$\begin{aligned}\alpha(\mathrm{J2000}) &= 14^{\mathrm{h}}19^{\mathrm{m}}18.850722^{\mathrm{s}} \quad \pm 0.23\,\mathrm{mas}\\ \delta(\mathrm{J2000}) &= 39^{\circ}40'36.04520'' \quad \pm 0.23\,\mathrm{mas},\end{aligned}$$

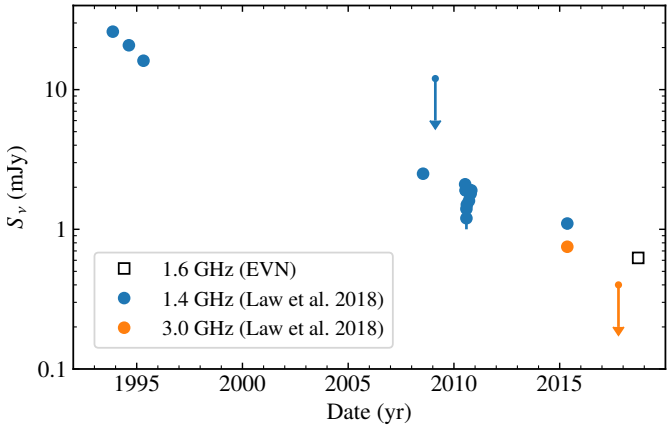

Figure 7.3: Light-curve of FIRST J1419+3940 during the last 25 yr at 1.4–1.6 GHz (blue circles and open square) and 3.0 GHz (orange circles). Errors bars represent 1-σ uncertainties (hidden by the size of the markers in most cases). Arrows represent 3-σ upper-limits.

Table 7.1: Properties of FIRST J1419+3940 measured following different imaging approaches.

	rms (μJy beam^{-1})	Peak brightness (μJy beam^{-1})	Flux Density (μJy)	size (mas)	synthesized beam (mas $\times$ mas, $^\circ$)
Default calibration	19	300	620 ± 20	4.3 ± 0.8	$5.5 \times 4.1,\ -18^\circ$
Without Tianma	30	510	630 ± 30	3.9 ± 0.9	$24 \times 5.3,\ 75^\circ$
Corrected Tianma	25	459	620 ± 30	3.4 ± 0.7	$6.6 \times 5.4,\ 78^\circ$

where the quoted uncertainties represent the 1-σ confidence interval and take into account the statistical uncertainties in the image (0.2 mas in both α and δ), the uncertainty in the phase calibrator position (0.1 mas; Beasley et al., 2002; Gordon et al., 2016), and the estimated uncertainties associated with the phase referencing technique (0.06 and 0.04 mas for α and δ, respectively; Pradel et al., 2006). The obtained position is consistent with the one reported from the FIRST survey (Law et al., 2018b), as well as the preliminary results published in Marcote et al. (2018). The measured flux density on 2018 September 18 follows the declining trend of the light-curve reported from observations with the Karl G. Jansky Very Large Array, VLA (see Fig. 7.3). Given the luminosity distance of 87 Mpc, the obtained flux density corresponds to an isotropic luminosity $\nu L_\nu = (9.4 \pm 0.3) \times 10^{36}\,\mathrm{erg\,s^{-1}}$. Together with the last published VLA observation at 3.0 GHz, and considering the same value for our epoch (i.e. no declining trend is assumed), we can place a conservative 3-σ upper limit on the spectral index between 1.6 and 3.0 GHz of $\alpha \lesssim -0.65$ (where $S_\nu \propto \nu^\alpha$).

FIRST J1419+3940 is significantly resolved in the obtained images given the size of the synthesized beam ($5.5 \times 4.1\,\mathrm{mas}^2$), as the measured size is larger than the minimum resolvable size by the array (see Martí-Vidal et al., 2012; Natarajan et al., 2017, for a detailed explanation). By fitting a circular Gaussian to the uv data we measure a source size of 4.3 ± 0.8 mas,

where the uncertainty has been estimated through a χ^2 test. However, we note that the gain calibration of Tianma constitutes a potential source of systematic errors in the size measurement. To provide a more reliable measurement, we produced images without this station. Despite having poorer resolution (synthesized beam of $24 \times 5.3\,\mathrm{mas}^2$), we obtained a size that is significant and consistent within uncertainties with the value quoted above ($3.9 \pm 0.9\,\mathrm{mas}$). Finally, we imaged the source with the gain correction applied to Tianma (as mentioned in the previous section), which provides the most stringent lower limit on the source size (i.e. assuming a point-like source during calibration). In this case we measured a source size of $3.4 \pm 0.7\,\mathrm{mas}$. The contribution of the longest baselines is therefore not critical as we obtain consistent results from all cases. We summarize the results of these different analyses in Table 7.1.

For comparison, the phase calibrator, J1419+3821, exhibits a main compact component with a measured size of 1.1–2.9 mas in all cases. The fact that the measured sizes are siginificantly different – while they are seen along almost the same Galactic line of sight – means that they are most likely intrinsic sizes, rather than due to scatter broadening. At the high Galactic latitudes of $\sim 67^\circ$ scatter broadening at GHz frequencies is almost negligible, and one would not expect strong variations of scattering size on small angular scales either (see e.g. Pushkarev & Kovalev, 2015).

We thus conclude that FIRST J1419+3940 is significantly resolved, with an angular size of $3.9^{+0.4+0.3}_{-0.5-0.2}\,\mathrm{mas}$, where the first uncertainties take into account the dispersion of the values from the different analyses, and the second ones consider the estimated statistical uncertainties on the value. Given that the angular diameter distance to the source is 83 Mpc (Law et al., 2018b), we derive a projected physical size of $1.6 \pm 0.3\,\mathrm{pc}$. This size also implies a brightness temperature of $T_b \sim 1.1 \times 10^7\,\mathrm{K}$, which clearly points to a non-thermal origin for the emission.

Law et al. (2018b) estimated that the putative GRB producing the observed afterglow likely took place around $\sim$ 25–30 yr ago. Considering an estimated central date for the explosion of $\sim$ 1993 and taking into account the given uncertainties, the afterglow must have a mean expansion velocity of $v = (3.0 \pm 0.6) \times 10^4\,\mathrm{km\,s^{-1}}$, or $(0.10 \pm 0.02)c$, consistent with a mildly relativistic expansion. We note that the calculated expansion velocity is an average over the whole lifetime, during which a significant deceleration has likely occurred.

7.3.2 On the single burst searches

We detected no astrophysical single pulses or periodic signals in the high-time-resolution Effelsberg data. We can estimate the expected dispersion measure (DM) towards FIRST J1419+3940 using Galactic electron density models (NE2001; Cordes & Lazio 2002, YMW16; Yao et al. 2017). For an extragalactic source, the observed DM can be divided into four components along the line of sight:

$$\mathrm{DM_{obs}} = \mathrm{DM_{MW}} + \mathrm{DM_{MW_{halo}}} + \mathrm{DM_{IGM}} + \mathrm{DM_{host}}. \quad (7.1)$$

The Milky Way contribution to the DM along the line of sight is divided into the disk and spiral arm component, $\mathrm{DM_{MW}}$, and the Galactic halo component, $\mathrm{DM_{MW_{halo}}}$. The former, $\mathrm{DM_{MW}}$, is 44 and 39 $\mathrm{pc\,cm^{-3}}$ calculated using the NE2001 and YMW16 models, respectively. The uncertainties in these contributions are not well quantified, but are likely on the order of 20%. Using this, we can derive an approximate range of: $30 \lesssim \mathrm{DM_{MW}} \lesssim 50\,\mathrm{pc\,cm^{-3}}$. We apply a Galactic halo contribution of $\sim$ 60–100 $\mathrm{pc\,cm^{-3}}$ to the DM (Prochaska & Zheng, 2019). Given that the redshift of FIRST J1419+3940 is 0.01957 (Law et al., 2018b), the mean intergalactic medium (IGM) contribution to the DM is $\mathrm{DM_{IGM}} \simeq 20\,\mathrm{pc\,cm^{-3}}$ (Ioka, 2003; Inoue, 2004). We assume that the DM contribution of the host galaxy of FIRST J1419+3940, $\mathrm{DM_{host}}$, is comparable to that of the host galaxy of FRB 121102: $55 \lesssim \mathrm{DM_{host}} \lesssim 225\,\mathrm{pc\,cm^{-3}}$ (Tendulkar et al., 2017). Combining all individual components using equation (7.1) results in the approximate range $160 \lesssim \mathrm{DM_{obs}} \lesssim 400\,\mathrm{pc\,cm^{-3}}$.

From the single pulse candidates reported using single_pulse_search.py, an astrophysical burst would be identifiable provided the signal-to-noise ratio exceeds ~ 10. We can estimate the fluence limit of our search using

$$F = (S/N)_{\mathrm{min}} \frac{T_{\mathrm{sys}}}{G} \sqrt{\frac{W_b}{n_{\mathrm{pol}}\,\Delta\nu}} \tag{7.2}$$

(following Cordes & McLaughlin, 2003), where $(S/N)_{\mathrm{min}}$ is our detection threshold of 10, T_{sys} is the system temperature, G is the telescope gain, n_{pol} is the number of recorded polarizations, $\Delta\nu$ is the total bandwidth, and W_b is the observed width of the burst. The observed width, W_b, accounts for broadening of the intrinsic width due to the finite time sampling of the data, intra-channel smearing, smearing due to DM-trial spacing, and scatter broadening. FRB 121102 has been shown to exhibit individual bursts with widths $\lesssim 30\,\mu\mathrm{s}$ (Michilli et al., 2018b) and there have been observations of FRBs with widths as large as $\sim$ 30 ms (Petroff et al., 2016)[2]. Taking a DM of $300\,\mathrm{pc\,cm^{-3}}$ and intrinsic widths 30 µs–30 ms, we find our fluence limit ranges from 0.1 Jy ms to 8 Jy ms.

7.4 Interpretation

7.4.1 Measured source size

In order to compare our measurements with the scenarios proposed by Law et al. (2018b), we need to compute the expected apparent size of the source. At the time of our observation, $t_{\mathrm{obs}} \sim 30\,\mathrm{yr} \sim 10^4$ d after the initial explosion, the external shock produced by the GRB jet upon deceleration into the interstellar medium (ISM) is expected to be non-relativistic, and to have become essentially spherical. Detailed, long term numerical relativistic hydrodynamics simulations (Zhang & MacFadyen, 2009) indeed show that the blast wave is well-described by the spherical, non-relativistic Sedov-Von Neumann-Taylor solution after a time $5t_{\mathrm{NR}} \approx 2 \times 10^3 E_{\mathrm{iso},53}^{1/3}\, n_1^{-1/3}$ d, where t_{NR} is the light-crossing time of the Sedov length associated to the jet. The initial relativistic expansion phase, however, can still have effects on the relation between observed time and projected size. For that reason, we compute

[2] All published FRBs and their properties can be found in the FRB Catalogue: http://www.frbcat.org.

the jet deceleration dynamics and spreading employing the "trumpet" model from Granot & Piran (2012), which has been shown to be in good quantitative agreement with results from numerical relativistic hydrodynamics simulations. The observed size is estimated as the maximum projected size of the equal-arrival-time surface, relativistic beaming of radiation being negligible in our late-time observations. Using the same jet parameters as Law et al. (2018b), namely an isotropic equivalent energy $E_{\rm iso} = 2 \times 10^{53}\,{\rm erg}$, an ISM number density $n = 10\,{\rm cm}^{-3}$ and a viewing angle $\theta_{\rm v} = 0.6\,{\rm rad}$, and further assuming a jet half-opening angle $\theta_{\rm j} = 0.1\,{\rm rad}$ (which implies a total jet energy $E_{\rm jet} \sim 10^{51}\,{\rm erg}$), we obtain the size evolution shown by the red solid line in Fig. 7.4, which is fully compatible with the measured one, assuming that the GRB took place in $\sim$ 1993. This disfavors the alternative scenario of a magnetar birth nebula, which would exhibit a significantly smaller size ($\lesssim 0.1\,{\rm pc}$), due to the much lower expansion velocity (Murase et al., 2016).

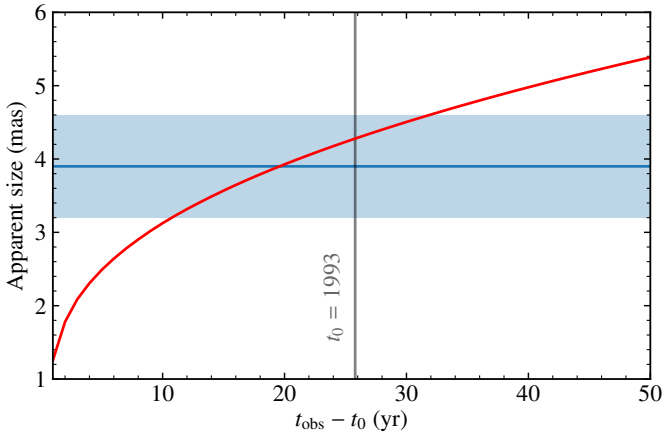

Figure 7.4: Apparent source size evolution. The red line shows the predicted apparent size evolution for a jet with parameters as those proposed by Law et al. (2018b). The blue line and the lighter blue band show our measured apparent size and its 1-σ uncertainty of $\theta_{\rm s} = 3.9 \pm 0.7\,{\rm mas}$. The grey vertical line marks the source age at the time of our observation, assuming that it originally exploded in 1993.

7

7.4.2 Flux density

While the measured size agrees well with the GRB scenario proposed by Law et al. (2018b), our measured flux density $S_{1.6\,{\rm GHz}} = 620 \pm 20\,\mu{\rm Jy}$ is low when compared to the extrapolation of their model. More precisely, adopting the same assumptions as Law et al. (2018b), namely quasi-isotropic, adiabatic expansion, Deep Newtonian regime and an electron power law index $p = 2.2$, the flux density should follow $S_\nu \propto \nu^{-0.6} t^{-0.96}$. Using the latest VLA detection as reference, which yielded a flux density of $1.1 \pm 0.1\,{\rm mJy}$ at $1.52\,{\rm GHz}$ on 2015 May 11, and assuming the GRB to have happened in 1993, we should have measured $S_{1.6\,{\rm GHz}} \approx 930 \pm 85\,\mu{\rm Jy}$ at the time of our observation, which is $\sim 3.5\sigma$ (summing the uncertainties in quadrature) above our measured flux density. As noted by Law et al. (2018b),

the latest VLASS non-detection $S_\nu < 400\,\mu\mathrm{Jy}$ at $3\,\mathrm{GHz}$ on 2017 October 11 already pointed to a faster decline after 2015. Several physical processes could lead to a steepening in the decay of the lightcurve, e.g.:

- The conditions in the shocked fluid could be changing as a consequence of the transition to the non-relativistic, Deep Newtonian phase, e.g. the fraction ϵ_e of shock energy given to electrons could decrease, or the electron momentum distribution power law index p could decrease from $p = 2.2$ towards ~ 2 (Sironi & Giannios, 2013). Both these effects would result in a steepening of the flux decay;
- Contrary to what is stated by Law et al. (2018b), the steepening could also be due to the shock crossing a dip in the ISM density. According to the argument by Law et al. (2018b), based on Nakar & Granot (2007) and Mimica & Giannios (2011), an ISM density drop would result only in a smooth, slow change in the lightcurve. This is essentially a consequence of the assumption that the shock is relativistic ($\Gamma \gg 1$), in which case the angular time scale $R/2\Gamma^2 c$ would be of the same order as the observer time t_obs, and therefore any change in the shock conditions would be smeared out over that time scale. In our case, conversely, the shock expansion speed is non-relativistic, and the angular time scale is $\sim R/2c << t_\mathrm{obs}$ (using our size measurement, we have $R/c \sim 2.5\,\mathrm{yr}$, which is significantly smaller than the explosion age $t_\mathrm{obs} \gtrsim 25\,\mathrm{yr}$), so that a drop in the ISM density at a radius slightly smaller than the observed size $\sim 1.6\,\mathrm{pc}$ may justify the flux deficit. Such a drop could mark the outer radius of the star-forming region where the GRB exploded. Let us caution, though, that this requires some fine-tuning. In order for the shock to entirely cross the outer edge of the star-forming region in a short enough time, the latter should be approximately spherical and nearly concentric to the shock. By using the same shock dynamics model as in the previous section, we estimate the current shock expansion velocity to be $v_\mathrm{s} \sim 0.03c \approx 9\,000\,\mathrm{km\,s^{-1}}$. The shock thus travelled a distance $\Delta R \sim 0.03\,\mathrm{pc}$ between the latest VLA detection at $1.5\,\mathrm{GHz}$ and our observation. The centers of the shock wave and the star-forming region, assumed spherical, should therefore be located less than ΔR away from each other. Since the flux deficit we observe amounts to a factor $\sim 2/3$ reduction with respect to the expected value, we can partially relax these requirements, allowing the outer edge of the star-forming region to have some structure – e.g. bumps, filaments, a non-spherical shape – as long as $\sim 1/3$ (in terms of solid angle) of the shock wave still experiences a sharp density drop in the required time. This leads us to conclude that, while the arguments against an ambient medium density drop proposed by Law et al. (2018b) do not hold in this case, this kind of explanation for the flux variation, while not impossible, remains rather unlikely.

Finally, we note that the flux deficit cannot be understood as due to scintillation-induced fluctuations, as the apparent size of the source is too large (Goodman, 1997).

7.4.3 Comparison with FRB 121102

The association of FRB 121102 with a persistent radio counterpart (Chatterjee et al., 2017; Marcote et al., 2017) led to the discovery of FIRST J1419+3940, the characteristics of which match those of the persistent source coincident with FRB 121102 (Ofek, 2017; Law et al., 2018b): i.e., a compact radio source with a similar luminosity and co-located with a star-forming region of a dwarf galaxy. It is, therefore, natural to compare FIRST J1419+3940 with the radio counterpart of FRB 121102.

The declining light curve of FIRST J1419+3940 contrasts with the persistent emission from FRB 121102 (Chatterjee et al., 2017; Plavin et al., 2022). Another discrepancy that arises is that the obtained source size of FIRST J1419+3940 is significantly larger than the one associated with FRB 121102 ($< 0.7\,\mathrm{pc}$; Marcote et al. 2017), implying a much higher expansion velocity. These differences can, naturally, be explained by a younger age of FIRST J1419+3940 ($\sim 30\,\mathrm{yr}$) when compared with FRB 121102 ($\sim 100\,\mathrm{yr}$; Metzger et al. 2017; Piro & Gaensler 2018). We note that although we conclude our observations are consistent with GRB jet expansion, we do not rule out the presence of a nebula driven by a highly magnetized neutron star contributing to a fraction of the radio emission observed. The presence of such nebula could cause the light curve to plateau at late-times.

It has been hypothesized that the birth of a millisecond magnetar can connect FRB 121102 with long GRBs or superluminous supernovae (SLSNe; Metzger et al., 2017). If we assume that millisecond magnetars can produce FRBs similar to what is observed in FRB 121102, and that a magnetized neutron star resides within the radio source FIRST J1419+3940, we might expect FRBs from this source. The comparable ages of FIRST J1419+3940 and FRB 121102 leads to our assumption that the compact object residing within FIRST J1419+3940 is emitting bursts with a comparable energy distribution and duty cycle to FRB 121102.

Bursts from the repeating FRB 121102 have been observed with fluences of $\sim 0.02\,\mathrm{Jy\,ms}$ (Gajjar et al., 2018) to $\gtrsim 7\,\mathrm{Jy\,ms}$ (Marcote et al., 2017) and widths ranging from $\lesssim 30\,\mu\mathrm{s}$ (Michilli et al., 2018b) to $\sim 8.7\,\mathrm{ms}$ (Spitler et al., 2016). Taking this range of fluence values at the luminosity distance of FRB 121102 ($972\,\mathrm{Mpc}$) and scaling to the luminosity distance of FIRST J1419+3940 ($87\,\mathrm{Mpc}$), gives an estimated fluence range of 2.5–870 $\mathrm{Jy\,ms}$. For bursts with widths exceeding $\sim 9\,\mathrm{ms}$, the fluence limit of our search increases beyond $2.5\,\mathrm{Jy\,ms}$ (see Section 7.3.2). Under the assumption that FIRST J1419+3940 is producing bursts with widths comparable to that of FRB 121102 and with an alignment (with respect to the observer) consistent with FRB 121102, single bursts from this source would be identifiable in the data.

The lack of short-duration bursts in our observation could imply that the source is in a quiescent state, similar to the behaviour observed in FRB 121102 (Scholz et al., 2016; Gajjar et al., 2018). Alternatively, the hypothesized central compact object could be producing bursts that do not cross our line-of-sight. To ensure our search was not affected by self-absorption, future observations of FIRST J1419+3940 at higher radio frequencies are required.

The potential connection of FRB 121102 with long GRBs or SLSNe has sparked targeted searches for millisecond-duration bursts and compact persistent radio sources at the positions of such events. In one such a search, Eftekhari et al. (2019) discovered a persistent radio source coincident with the SLSN PTF10hgi. An orphan GRB afterglow is explored as the potential origin of the emission, but is considered unlikely due to the high inferred isotropic jet energy, exceeding that of most observed long GRBs. Since the discovery of both this radio source and FIRST J1419+3940 were motivated by observations of FRB 121102 and its environment, we compare the inferred isotropic jet energy for both sources. The inferred properties of the radio source associated with PTF10hgi, assuming GRB jet expansion, is estimated as $E_{\rm iso} \sim (3\text{–}5) \times 10^{53}\,{\rm erg}$, $n = 10^{-3}\text{–}10^{2}\,{\rm cm}^{-3}$ (Eftekhari et al., 2019). Although this energy range is larger than the majority of observed long GRBs, it is comparable to that of FIRST J1419+3940 ($E_{\rm iso} = 2 \times 10^{53}\,{\rm erg}$, $n = 10\,{\rm cm}^{-3}$; Law et al. 2018b). The results shown in the work presented here support the scenario in which FIRST J1419+3940 is an orphan GRB afterglow. Whether this is the case for PTF10hgi as well is not clear at this point, but we argue that the inferred high isotropic jet energy in itself does not exclude an off-axis jet origin. The ultimate probe of this scenario is very high angular resolution VLBI observations. Accurately measuring the source size at the redshift of PTF10hgi (about five times more distant than FIRST J1419+3940) – and especially considering its low flux density of $\sim 50\,\mu{\rm Jy}$ – is very challenging, and may only be possible with a very sensitive future SKA-VLBI array (Paragi et al., 2015) observing at high frequencies ($\gtrsim 5\,{\rm GHz}$).

7.5 Conclusions

FIRST J1419+3940 was reported as a slowly fading radio transient source. We provide the first constraints on the source size, using EVN data. These measurements confirm the non-thermal emission of the source and are consistent with jet expansion from a putative orphan long GRB. The derived average expansion velocity is consistent with a mildly relativistic expansion, noting that a significant deceleration has likely happened during these $\sim 30\,{\rm yr}$ after the event. A flux density lower than expected is reported, suggesting a faster decline after 2015. This decay could be explained by a change in the post-shock microphysical parameters following the transition to the non-relativistic phase, or by a drop in the ISM density (e.g. due to the shock reaching the outer edge of the star-forming region where the GRB exploded). We exclude scintillation-induced fluctuations as the origin of the reported variability.

Finally, although FIRST J1419+3940 was discovered in a search for persistent radio sources similar to that associated with FRB 121102, we note significant differences between these sources (e.g. FIRST J1419+3940 shows a significantly larger extend, and stronger luminosity decay). Still, FIRST J1419+3940 could be a site of potential FRB production, although the burst searches conducted during the EVN observation reported null results. Future radio observations are required to provide better constraints on the possible presence of FRBs arising from this object, as well as to characterize the evolution of the light-curve and its accelerated decay.

Acknowledgements

We thank the annonymous referee for the useful comments and suggestions which helped to improve the paper. We thank H. J. van Langevelde for an internal review of the manuscript. K.N. would like to thank R. A. M. J. Wijers for helpful comments and discussions. O.S. wishes to thank G. Ghirlanda for valuable discussions and insights. The European VLBI Network is a joint facility of independent European, African, Asian, and North American radio astronomy institutes. Scientific results from data presented in this publication are derived from the following EVN project code: RM015. e-MERLIN is a National Facility operated by the University of Manchester at Jodrell Bank Observatory on behalf of STFC. We thank the directors and staff of all the EVN telescopes for making this target of opportunity observation possible. We thank the staff of the Effelsberg Radio Telescope, and in particular U. Bach, for his support with simultaneous pulsar recording. B.M. acknowledges support from the Spanish Ministerio de Economía y Competitividad (MINECO) under grants AYA2016-76012-C3-1-P and MDM-2014-0369 of ICCUB (Unidad de Excelencia "María de Maeztu"). J.W.T.H. acknowledges funding from an NWO Vidi fellowship and from the European Research Council under the European Union's Seventh Framework Programme (FP/2007-2013) / ERC Starting Grant agreement nr. 337062 ("DRAGNET"). E.P. acknowledges funding from an NWO Veni Fellowship. R.K. is supported by the ERC synergy grant "BlackHoleCam: Imaging the Event Horizon of Black Holes" (Grant No. 610058). This research made use of APLpy, an open-source plotting package for Python hosted at http://aplpy.github.com, Astropy, a community-developed core Python package for Astronomy (Astropy Collaboration et al., 2013), and Matplotlib (Hunter, 2007).

Appendix: No Radio Bursts Detected from FIRST J1419+3940 in Green Bank Telescope Observations

K. Nimmo, V. Gajjar, J. W. T. Hessels, C. J. Law, R. S. Lynch, A. D. Seymour, L. G. Spitler

Research Notes of the AAS, 2020, 4, 4, 50

Precise localisation of the first-known repeating fast radio burst source, FRB 121102 (Spitler et al., 2016; Chatterjee et al., 2017), led to its association with a star-forming region inside a low-metallicity dwarf host galaxy (Tendulkar et al., 2017). This host environment is similar to that typically associated with long gamma-ray bursts (GRB) and superluminous supernovae, potentially linking these astrophysical phenomena (Metzger et al., 2017). In addition, the bursting source is found to be spatially coincident with a compact (< 0.7 pc; Marcote et al. 2017), persistent radio source (Chatterjee et al., 2017). Ofek (2017) identified similar radio sources in the Very Large Array FIRST survey (Becker et al., 1995). One of these sources, FIRST J141918.9+394036 (hereafter FIRST J1419+3940), was identified as a radio transient decaying in brightness by a factor of ~ 50 over several decades (Law et al., 2018b). Very-long-baseline radio interferometric observations support the theory that FIRST J1419+3940 is the afterglow of a long GRB, based on the inferred physical size of the emission region (1.6 ± 0.3 pc; Marcote et al. 2019).

FIRST J1419+3940 and FRB 121102's persistent radio sources have similar properties and host galaxy type. Although FIRST J1419+3940 is declining in brightness, its peak luminosity ($\nu L_\nu > 3 \times 10^{38}$ erg s^{-1} at 1.4 GHz; Law et al. 2018b) is comparable to the mean luminosity of FRB 121102's persistent radio source ($\nu L_\nu \approx 3 \times 10^{38}$ erg s^{-1} at 1.7 GHz; Chatterjee et al. 2017). Possibly, their physical nature could be similar, and FIRST J1419+3940 could contain a source capable of producing millisecond-duration radio bursts. Above ~ 1.4 GHz, FIRST J1419+3940 is observed to have an optically-thin synchrotron spectrum (Law et al., 2018a). This, combined with the relatively close proximity of FIRST J1419+3940 (87 Mpc, about an order-of-magnitude closer than FRB 121102; Law et al. 2018b, Tendulkar et al. 2017), indicates that it should be possible to detect much lower energy bursts than those observed from FRB 121102, if FIRST J1419+3940 is producing FRBs. Marcote et al. (2019) reported the non-detection of bursts from FIRST J1419+3940 during 4.3 h of observations with the 100-m Effelsberg telescope at 1.7 GHz. Here, we report the non-detection of bursts from FIRST J1419+3940 using the 110-m Green Bank Telescope (GBT).

Table 7.2 summarises the observations. We observed FIRST J1419+3940 for a total duration of 3.1 h using the GBT and the Breakthrough Listen backend (MacMahon et al., 2018) on MJDs 58519 and 58529 — at both S-band (1.73–2.6 GHz) and C-band (3.95–8.0 GHz). The time and frequency resolutions were 349.5 μs and 0.366 MHz, respectively. In addition to the target scans, both noise diode and test pulsar (PSR B1508+55) scans were taken.

We searched for bursts using PRESTO[3] (Ransom, 2001). We identified and masked radio frequency interference (RFI) using PRESTO's rfifind and dedispersed using prepdata to create

[3] https://github.com/scottransom/presto

Table 7.2: Summary of observations and fluence upper limits.

Scan start time[1] (MJD)	Frequency range (GHz)	Duration (min)	$T_{sys} + T_{bg}$ [2] (K)	Gain (K/Jy)	Fluence limit[3] (Jy ms)
58519.4457	3.95–8.0	30.0	28	1.85	0.05
58519.4667	3.95–8.0	30.0	28	1.85	0.05
58519.5059	1.73–2.6	6.7	25	1.9	0.1
58529.1809	3.95–8.0	30.0	28	1.85	0.05
58529.2019	3.95–8.0	30.0	28	1.85	0.05
58529.2305	1.73–2.6	30.0	25	1.9	0.1
58529.2514	1.73–2.6	28.0	25	1.9	0.1

[1]Topocentric.
[2]System temperature (T_{sys}) are for typical GBT performance: http://www.gb.nrao.edu/~fghigo/gbtdoc/perform.html. Background temperature (T_{bg}) is a combination of the sky temperature (negligible in this case, using the 408 MHz all-sky map (Remazeilles et al., 2015) and extrapolating to our observing frequencies using a spectral index of −2.7; Reich & Reich 1988) and the cosmic microwave background ~ 3 K (Mather et al., 1994).
[3]Calculated following Cordes & McLaughlin (2003), assuming a 1-ms-wide burst with DM $= 300$ pc cm^{-3}, using the temperature and gain values listed, with a signal-to-noise detection threshold of 10.

timeseries with trial dispersion measures (DM) of $0 - 1000$ pc cm^{-3}. As is discussed in Marcote et al. (2019), the expected DM towards FIRST J1419+3940 is < 170 pc cm^{-3}, ignoring any contribution from the host galaxy. If we assume the host contribution is comparable to that of FRB 121102, then the expected DM is ~ 400 pc cm^{-3}. We then searched for single pulses above a 6σ threshold in the dedispersed time series using single_pulse_search.py. The single pulses due to RFI were filtered using an automated classifier (Michilli & Hessels, 2018). Our search was sensitive to bursts with widths between ~ 0.5 ms and 34.95 ms. The identified candidates were all deemed to be non-astrophysical after inspecting their dynamic spectra by eye. This analysis strategy was verified by performing a blind search for the test pulsar PSR B1508+55.

In this search, we were sensitive to 1-ms-wide bursts from FIRST J1419+3940 exceeding the fluence limits shown in Table 7.2, assuming DM ~ 300 pc cm^{-3}. Considering the weakest bursts observed from FRB 121102 (0.02 Jy ms; Gajjar et al. 2018) and scaling to the luminosity distance of FIRST J1419+3940 (87 Mpc; Law et al. 2018b), we find the corresponding fluence to be 2.5 Jy ms, well exceeding our detection threshold. We found no astrophysical bursts in these observations. If we assume there is a source associated with FIRST J1419+3940 that is producing FRBs, the lack of detection could indicate a quiescent state, as is often observed for FRB 121102 (e.g. Gajjar et al., 2018). Alternatively, the bursts could be beamed away from our line-of-sight. It is also possible that FIRST J1419+3940 does not contain a source capable of producing FRBs. Future searches are important to constrain the possible presence of an FRB-emitting source.

Bibliography

Abbott, B. P., Abbott, R., Abbott, T. D., et al. 2017, *Multi-messenger Observations of a Binary Neutron Star Merger*, ApJ, 848, L12

Ablimit, I. & Li, X.-D. 2015, *Formation of Binary Millisecond Pulsars by Accretion-induced Collapse of White Dwarfs under Wind-driven Evolution*, ApJ, 800, 98

Agarwal, D., Aggarwal, K., Burke-Spolaor, S., Lorimer, D. R., & Garver-Daniels, N. 2020, *FETCH: A deep-learning based classifier for fast transient classification*, MNRAS, 497, 1661

Alam, S., Albareti, F. D., Allende Prieto, C., et al. 2015, *The Eleventh and Twelfth Data Releases of the Sloan Digital Sky Survey: Final Data from SDSS-III*, ApJS, 219, 12

Anna-Thomas, R., Connor, L., Burke-Spolaor, S., et al. 2022, *A Highly Variable Magnetized Environment in a Fast Radio Burst Source*, arXiv e-prints, arXiv:2202.11112

Arzoumanian, Z., Nice, D. J., Taylor, J. H., & Thorsett, S. E. 1994, *Timing Behavior of 96 Radio Pulsars*, ApJ, 422, 671

Astropy Collaboration, Robitaille, T. P., Tollerud, E. J., et al. 2013, *Astropy: A community Python package for astronomy*, A&A, 558, A33

Backer, D. C. 1970, *Pulsar Nulling Phenomena*, Nature, 228, 42

Bannister, K. W., Deller, A. T., Phillips, C., et al. 2019, *A single fast radio burst localized to a massive galaxy at cosmological distance*, Science, 365, 565

Bassa, C. G., Tendulkar, S. P., Adams, E. A. K., et al. 2017, *FRB 121102 Is Coincident with a Star-forming Region in Its Host Galaxy*, ApJ, 843, L8

Beasley, A. J., Gordon, D., Peck, A. B., et al. 2002, *The VLBA Calibrator Survey-VCS1*, ApJS, 141, 13

Becker, R. H., White, R. L., & Helfand, D. J. 1995, *The FIRST Survey: Faint Images of the Radio Sky at Twenty Centimeters*, ApJ, 450, 559

Beloborodov, A. M. 2017, *A Flaring Magnetar in FRB 121102?*, ApJ, 843, L26

Beniamini, P. & Kumar, P. 2020, *What does FRB light-curve variability tell us about the emission mechanism?*, MNRAS, 498, 651

Beniamini, P., Wadiasingh, Z., & Metzger, B. D. 2020, *Periodicity in recurrent fast radio bursts and the origin of ultralong period magnetars*, MNRAS, 496, 3390

Bera, A. & Chengalur, J. N. 2019, *Super-giant pulses from the Crab pulsar: energy distribution and occurrence rate*, MNRAS, 490, L12

Bertin, E. & Arnouts, S. 1996, *SExtractor: Software for source extraction.*, A&AS, 117, 393

Bhandari, S., Heintz, K. E., Aggarwal, K., et al. 2022, *Characterizing the Fast Radio Burst Host Galaxy Population and its Connection to Transients in the Local and Extragalactic Universe*, AJ, 163, 69

Bhandari, S., Keane, E. F., Barr, E. D., et al. 2018, *The SUrvey for Pulsars and Extragalactic Radio Bursts - II. New FRB discoveries and their follow-up*, MNRAS, 475, 1427

Bhandari, S., Sadler, E. M., Prochaska, J. X., et al. 2020, *The Host Galaxies and Progenitors of Fast Radio Bursts Localized with the Australian Square Kilometre Array Pathfinder*, ApJ, 895, L37

Bhardwaj, M., Gaensler, B. M., Kaspi, V. M., et al. 2021a, *A Nearby Repeating Fast Radio Burst in the Direction of M81*, ApJ, 910, L18

Bhardwaj, M., Kirichenko, A. Y., Michilli, D., et al. 2021b, *A Local Universe Host for the Repeating Fast Radio Burst FRB 20181030A*, ApJ, 919, L24

Bij, A., Lin, H.-H., Li, D., et al. 2021, *Kinematics of Crab Giant Pulses*, ApJ, 920, 38

Blanton, M. R., Hogg, D. W., Bahcall, N. A., et al. 2003, *The Galaxy Luminosity Function and Luminosity Density at Redshift $z = 0.1$*, ApJ, 592, 819

Bochenek, C. D., Ravi, V., Belov, K. V., et al. 2020, *A fast radio burst associated with a Galactic magnetar*, Nature, 587, 59

Bray, J. C. & Eldridge, J. J. 2016, *Neutron star kicks and their relationship to supernovae ejecta mass*, MNRAS, 461, 3747

Brentjens, M. A. & de Bruyn, A. G. 2005, *Faraday rotation measure synthesis*, A&A, 441, 1217

Burke-Spolaor, S., Bailes, M., Ekers, R., Macquart, J.-P., & Crawford, Fronefield, I. 2011, *Radio Bursts with Extragalactic Spectral Characteristics Show Terrestrial Origins*, ApJ, 727, 18

Caleb, M., Heywood, I., Rajwade, K., et al. 2022a, *Discovery of a radio-emitting neutron star with an ultra-long spin period of 76 s*, Nature Astronomy

Caleb, M., Keane, E. F., van Straten, W., et al. 2018, *The SUrvey for Pulsars and Extragalactic Radio Bursts - III. Polarization properties of FRBs 160102 and 151230*, MNRAS, 478, 2046

Caleb, M., Rajwade, K., Desvignes, G., et al. 2022b, *Radio and X-ray observations of giant pulses from XTE J1810 - 197*, MNRAS, 510, 1996

Caleb, M., Stappers, B. W., Abbott, T. D., et al. 2020, *Simultaneous multi-telescope observations of FRB 121102*, MNRAS, 496, 4565

Camilo, F., Ransom, S. M., Halpern, J. P., & Reynolds, J. 2007, *1E 1547.0-5408: A Radio-emitting Magnetar with a Rotation Period of 2 Seconds*, ApJ, 666, L93

Camilo, F., Ransom, S. M., Halpern, J. P., et al. 2006, *Transient pulsed radio emission from a magnetar*, Nature, 442, 892

Cenko, S. B., Butler, N. R., Ofek, E. O., et al. 2010, *Unveiling the Origin of Grb 090709A: Lack of Periodicity in a Reddened Cosmological Long-Duration Gamma-Ray Burst*, AJ, 140, 224

Chatterjee, S., Cordes, J. M., Vlemmings, W. H. T., et al. 2004, *Pulsar Parallaxes at 5 GHz with the Very Long Baseline Array*, ApJ, 604, 339

Chatterjee, S., Law, C. J., Wharton, R. S., et al. 2017, *A direct localization of a fast radio burst and its host*, Nature, 541, 58

Chawla, P., Andersen, B. C., Bhardwaj, M., et al. 2020, *Detection of Repeating FRB 180916.J0158+65 Down to Frequencies of 300 MHz*, ApJ, 896, L41

CHIME/FRB Collaboration, Amiri, M., Andersen, B. C., et al. 2021, *The First CHIME/FRB Fast Radio Burst Catalog*, ApJS, 257, 59

Chime/Frb Collaboration, Amiri, M., Andersen, B. C., et al. 2020, *Periodic activity from a fast radio burst source*, Nature, 582, 351

CHIME/FRB Collaboration, Amiri, M., Bandura, K., et al. 2018, *The CHIME Fast Radio Burst Project: System Overview*, ApJ, 863, 48

CHIME/FRB Collaboration, Amiri, M., Bandura, K., et al. 2019a, *A second source of repeating fast radio bursts*, Nature, 566, 235

CHIME/FRB Collaboration, Amiri, M., Bandura, K., et al. 2019b, *Observations of fast radio bursts at frequencies down to 400 megahertz*, Nature, 566, 230

CHIME/FRB Collaboration, Andersen, B. C., Bandura, K., et al. 2019c, *CHIME/FRB Discovery of Eight New Repeating Fast Radio Burst Sources*, ApJ, 885, L24

CHIME/FRB Collaboration, Andersen, B. C., Bandura, K. M., et al. 2020, *A bright millisecond-duration radio burst from a Galactic magnetar*, Nature, 587, 54

Chime/Frb Collabortion. 2021, *Recent high activity from a repeating Fast Radio Burst discovered by CHIME/FRB*, The Astronomer's Telegram, 14497, 1

Cho, H., Macquart, J.-P., Shannon, R. M., et al. 2020, *Spectropolarimetric Analysis of FRB 181112 at Microsecond Resolution: Implications for Fast Radio Burst Emission Mechanism*, ApJ, 891, L38

Clauset, A., Rohilla Shalizi, C., & Newman, M. E. J. 2007, *Power-law distributions in empirical data*, arXiv e-prints, arXiv:0706.1062

Cognard, I., Shrauner, J. A., Taylor, J. H., & Thorsett, S. E. 1996, *Giant Radio Pulses from a Millisecond Pulsar*, ApJ, 457, L81

Colgate, S. A. 1975, *Electromagnetic pulse from supernovae.*, ApJ, 198, 439

Colgate, S. A. & Noerdlinger, P. D. 1971, *Coherent Emission from Expanding Supernova Shells*, ApJ, 165, 509

Condon, J. J., Cotton, W. D., Greisen, E. W., et al. 1998, *The NRAO VLA Sky Survey*, AJ, 115, 1693

Condon, J. J. & Ransom, S. M. 2016, Essential Radio Astronomy

Cordes, J. M. 1976, *Pulsar radiation as polarized shot noise.*, ApJ, 210, 780

Cordes, J. M., Bhat, N. D. R., Hankins, T. H., McLaughlin, M. A., & Kern, J. 2004, *The Brightest Pulses in the Universe: Multifrequency Observations of the Crab Pulsar's Giant Pulses*, ApJ, 612, 375

Cordes, J. M. & Chatterjee, S. 2019, *Fast Radio Bursts: An Extragalactic Enigma*, ARA&A, 57, 417

Cordes, J. M. & Lazio, T. J. 1991, *Interstellar Scattering Effects on the Detection of Narrow-Band Signals*, ApJ, 376, 123

Cordes, J. M. & Lazio, T. J. W. 2002, *NE2001.I. A New Model for the Galactic Distribution of Free Electrons and its Fluctuations*, arXiv e-prints, astro

Cordes, J. M. & McLaughlin, M. A. 2003, *Searches for Fast Radio Transients*, ApJ, 596, 1142

Cordes, J. M. & Wasserman, I. 2016, *Supergiant pulses from extragalactic neutron stars*, MNRAS, 457, 232

Cordes, J. M., Wasserman, I., Hessels, J. W. T., et al. 2017, *Lensing of Fast Radio Bursts by Plasma Structures in Host Galaxies*, ApJ, 842, 35

Cordes, J. M., Weisberg, J. M., & Boriakoff, V. 1985, *Small-scale electron density turbulence in the interstellar medium.*, ApJ, 288, 221

Crane, P. C. & Napier, P. J. 1989, *Sensitivity*, in Astronomical Society of the Pacific Conference Series, Vol. 6, Synthesis Imaging in Radio Astronomy, ed. R. A. Perley, F. R. Schwab, & A. H. Bridle, 139

Crawford, D. F., Jauncey, D. L., & Murdoch, H. S. 1970, *Maximum-Likelihood Estimation of the Slope from Number-Flux Counts of Radio Sources*, ApJ, 162, 405

Crawford, F., Kaspi, V. M., Manchester, R. N., et al. 2001, *Radio Pulsars in the Magellanic Clouds*, ApJ, 553, 367

Cruces, M., Spitler, L. G., Scholz, P., et al. 2021, *Repeating behaviour of FRB 121102: periodicity, waiting times, and energy distribution*, MNRAS, 500, 448

Day, C. K., Bhandari, S., Deller, A. T., Shannon, R. M., & Moss, V. A. 2021, *ASKAP localisation of the FRB 20201124A source*, The Astronomer's Telegram, 14515, 1

Day, C. K., Deller, A. T., Shannon, R. M., et al. 2020, *High time resolution and polarization properties of ASKAP-localized fast radio bursts*, MNRAS, 497, 3335

Deng, W. & Zhang, B. 2014, *Cosmological Implications of Fast Radio Burst/Gamma-Ray Burst Associations*, ApJ, 783, L35

Dopita, M. A., Kewley, L. J., Sutherland, R. S., & Nicholls, D. C. 2016, *Chemical abundances in high-redshift galaxies: a powerful new emission line diagnostic*, Ap&SS, 361, 61

Driessen, L. N., Janssen, G. H., Bassa, C. G., Stappers, B. W., & Stinebring, D. R. 2019, *Scattering features and variability of the Crab pulsar*, MNRAS, 483, 1224

Dyks, J., Harding, A. K., & Rudak, B. 2004, *Relativistic Effects and Polarization in Three High-Energy Pulsar Models*, ApJ, 606, 1125

Eatough, R. P., Falcke, H., Karuppusamy, R., et al. 2013, *A strong magnetic field around the supermassive black hole at the centre of the Galaxy*, Nature, 501, 391

Eftekhari, T. & Berger, E. 2017, *Associating Fast Radio Bursts with Their Host Galaxies*, ApJ, 849, 162

Eftekhari, T., Berger, E., Margalit, B., et al. 2019, *A Radio Source Coincident with the Superluminous Supernova PTF10hgi: Evidence for a Central Engine and an Analog of the Repeating FRB 121102?*, ApJ, 876, L10

Everett, J. E. & Weisberg, J. M. 2001, *Emission Beam Geometry of Selected Pulsars Derived from Average Pulse Polarization Data*, ApJ, 553, 341

Faber, S. M., Willmer, C. N. A., Wolf, C., et al. 2007, *Galaxy Luminosity Functions to $z\backsim1$ from DEEP2 and COMBO-17: Implications for Red Galaxy Formation*, ApJ, 665, 265

Falcke, H. & Rezzolla, L. 2014, *Fast radio bursts: the last sign of supramassive neutron stars*, A&A, 562, A137

Farah, W., Flynn, C., Bailes, M., et al. 2018, *FRB microstructure revealed by the real-time detection of FRB170827*, MNRAS, 478, 1209

Farah, W., Pollak, A. W., Siemion, A. P. V., et al. 2021, *A bright double-peaked radio burst from FRB20201124A detected with the Allen Telescope Array*, The Astronomer's Telegram, 14676, 1

Feng, Y., Li, D., Yang, Y.-P., et al. 2022, *Frequency-dependent polarization of repeating fast radio bursts—implications for their origin*, Science, 375, 1266

Fletcher, C. & Fermi GBM Team. 2020, *Fermi GBM observation of a bright flare from magnetar SGR 1935+2154*, GRB Coordinates Network, 27659, 1

Fomalont, E. B. & Perley, R. A. 1999, *Calibration and Editing*, in Astronomical Society of the Pacific Conference Series, Vol. 180, Synthesis Imaging in Radio Astronomy II, ed. G. B. Taylor, C. L. Carilli, & R. A. Perley, 79

Fong, W.-f., Dong, Y., Leja, J., et al. 2021, *Chronicling the Host Galaxy Properties of the Remarkable Repeating FRB 20201124A*, ApJ, 919, L23

Fonseca, E., Andersen, B. C., Bhardwaj, M., et al. 2020, *Nine New Repeating Fast Radio Burst Sources from CHIME/FRB*, ApJ, 891, L6

Force, M. M., Demorest, P., & Rankin, J. M. 2015, *Absolute polarization determinations of 33 pulsars using the Green Bank Telescope*, MNRAS, 453, 4485

Foreman-Mackey, D., Hogg, D. W., Lang, D., & Goodman, J. 2013, *emcee: The MCMC Hammer*, PASP, 125, 306

Freedman, W. L., Hughes, S. M., Madore, B. F., et al. 1994, *The Hubble Space Telescope Extragalactic Distance Scale Key Project. I. The Discovery of Cepheids and a New Distance to M81*, ApJ, 427, 628

Fujii, M. S. & Portegies Zwart, S. 2011, *The Origin of OB Runaway Stars*, Science, 334, 1380

Gaia Collaboration, Brown, A. G. A., Vallenari, A., et al. 2018, *Gaia Data Release 2. Summary of the contents and survey properties*, A&A, 616, A1

Gaia Collaboration, Brown, A. G. A., Vallenari, A., et al. 2016, *Gaia Data Release 1. Summary of the astrometric, photometric, and survey properties*, A&A, 595, A2

Gajjar, V., Perez, K. I., Siemion, A. P. V., et al. 2021, *The Breakthrough Listen Search For Intelligent Life Near the Galactic Center. I.*, AJ, 162, 33

Gajjar, V., Siemion, A. P. V., Price, D. C., et al. 2018, *Highest Frequency Detection of FRB 121102 at 4-8 GHz Using the Breakthrough Listen Digital Backend at the Green Bank Telescope*, ApJ, 863, 2

Gavriil, F. P., Kaspi, V. M., & Woods, P. M. 2004, *A Comprehensive Study of the X-Ray Bursts from the Magnetar Candidate 1E 2259+586*, ApJ, 607, 959

Gehrels, N., Ramirez-Ruiz, E., & Fox, D. B. 2009, *Gamma-Ray Bursts in the Swift Era*, ARA&A, 47, 567

Geyer, M., Serylak, M., Abbate, F., et al. 2021, *The Thousand-Pulsar-Array programme on MeerKAT - III. Giant pulse characteristics of PSR J0540-6919*, MNRAS, 505, 4468

Ghirlanda, G., Salafia, O. S., Paragi, Z., et al. 2019, *Compact radio emission indicates a structured jet was produced by a binary neutron star merger*, Science, 363, 968

Good, D. & Chime/Frb Collaboration. 2020, *CHIME/FRB Detection of Three More Radio Bursts from SGR 1935+2154*, The Astronomer's Telegram, 14074, 1

Goodman, J. 1997, *Radio scintillation of gamma-ray-burst afterglows*, New A, 2, 449

Gordon, D., Jacobs, C., Beasley, A., et al. 2016, *Second Epoch VLBA Calibrator Survey Observations: VCS-II*, AJ, 151, 154

Gordon, Y. A., Boyce, M. M., O'Dea, C. P., et al. 2020, *A Catalog of Very Large Array Sky Survey Epoch 1 Quick Look Components, Sources, and Host Identifications*, Research Notes of the American Astronomical Society, 4, 175

Gould, D. M. & Lyne, A. G. 1998, *Multifrequency polarimetry of 300 radio pulsars*, MNRAS, 301, 235

Gourdji, K., Michilli, D., Spitler, L. G., et al. 2019, *A Sample of Low-energy Bursts from FRB 121102*, ApJ, 877, L19

Granot, J. & Piran, T. 2012, *On the lateral expansion of gamma-ray burst jets*, MNRAS, 421, 570

Greisen, E. W. 2003, *AIPS, the VLA, and the VLBA*, in Astrophysics and Space Science Library, Vol. 285, Information Handling in Astronomy - Historical Vistas, ed. A. Heck, 109

Grossan, B. 2021, *Possible Periodic Windowed Behavior in SGR1935+2154 Bursts*, PASP, 133, 074202

Gruzinov, A. & Levin, Y. 2019, *Conversion Measure of Faraday Rotation-Conversion with Application to Fast Radio Bursts*, ApJ, 876, 74

Gu, W.-M., Dong, Y.-Z., Liu, T., Ma, R., & Wang, J. 2016, *A Neutron Star-White Dwarf Binary Model for Repeating Fast Radio Burst 121102*, ApJ, 823, L28

Guillochon, J., Parrent, J., Kelley, L. Z., & Margutti, R. 2017, *An Open Catalog for Supernova Data*, ApJ, 835, 64

Gusev, A. S. 2014, *Hierarchy and size distribution function of star formation regions in the spiral galaxy NGC 628*, MNRAS, 442, 3711

Haffner, L. M., Reynolds, R. J., Tufte, S. L., et al. 2003, *The Wisconsin Hα Mapper Northern Sky Survey*, ApJS, 149, 405

Hagstotz, S., Reischke, R., & Lilow, R. 2022, *A new measurement of the Hubble constant using fast radio bursts*, MNRAS, 511, 662

Hankins, T. H. & Eilek, J. A. 2007, *Radio Emission Signatures in the Crab Pulsar*, ApJ, 670, 693

Hankins, T. H., Eilek, J. A., & Jones, G. 2016, *The Crab Pulsar at Centimeter Wavelengths. II. Single Pulses*, ApJ, 833, 47

Hankins, T. H., Jones, G., & Eilek, J. A. 2015, *The Crab Pulsar at Centimeter Wavelengths. I. Ensemble Characteristics*, ApJ, 802, 130

Hankins, T. H., Kern, J. S., Weatherall, J. C., & Eilek, J. A. 2003, *Nanosecond radio bursts from strong plasma turbulence in the Crab pulsar*, Nature, 422, 141

Hardy, L. K., Dhillon, V. S., Spitler, L. G., et al. 2017, *A search for optical bursts from the repeating fast radio burst FRB 121102*, MNRAS, 472, 2800

Heiles, C. & Campbell, D. B. 1970, *Pulsar NP 0532: Properties and Systematic Polarization of Individual Strong Pulses at 430 MHz*, Nature, 226, 529

Heinke, C. O., Grindlay, J. E., Lugger, P. M., et al. 2003, *Analysis of the Quiescent Low-Mass X-Ray Binary Population in Galactic Globular Clusters*, ApJ, 598, 501

Heintz, K. E., Prochaska, J. X., Simha, S., et al. 2020, *Host Galaxy Properties and Offset Distributions of Fast Radio Bursts: Implications for Their Progenitors*, ApJ, 903, 152

Herrmann, W. 2021, *Extremely bright pulse from FRB20201124A observed with the 25-m Stockert Radio Telescope*, The Astronomer's Telegram, 14556, 1

Hessels, J., Possenti, A., Bailes, M., et al. 2015, *Pulsars in Globular Clusters with the SKA*, in Advancing Astrophysics with the Square Kilometre Array (AASKA14), 47

Hessels, J. W. T., Ransom, S. M., Stairs, I. H., et al. 2006, *A Radio Pulsar Spinning at 716 Hz*, Science, 311, 1901

Hessels, J. W. T., Spitler, L. G., Seymour, A. D., et al. 2019, *FRB 121102 Bursts Show Complex Time-Frequency Structure*, ApJ, 876, L23

Hewish, A., Bell, S. J., Pilkington, J. D. H., Scott, P. F., & Collins, R. A. 1968, *Observation of a Rapidly Pulsating Radio Source*, Nature, 217, 709

Hewitt, D. M., Snelders, M. P., Hessels, J. W. T., et al. 2021, *Arecibo observations of a burst storm from FRB 20121102A in 2016*, arXiv e-prints, arXiv:2111.11282

Hilmarsson, G. H., Michilli, D., Spitler, L. G., et al. 2021a, *Rotation Measure Evolution of the Repeating Fast Radio Burst Source FRB 121102*, ApJ, 908, L10

Hilmarsson, G. H., Spitler, L. G., Main, R. A., & Li, D. Z. 2021b, *Polarization properties of FRB 20201124A from detections with the Effelsberg 100-m radio telescope*, MNRAS, 508, 5354

Hobbs, G., Lorimer, D. R., Lyne, A. G., & Kramer, M. 2005, *A statistical study of 233 pulsar proper motions*, MNRAS, 360, 974

Hotan, A. W., van Straten, W., & Manchester, R. N. 2004, *PSRCHIVE and PSRFITS: An Open Approach to Radio Pulsar Data Storage and Analysis*, PASA, 21, 302

Houben, L. J. M., Spitler, L. G., ter Veen, S., et al. 2019, *Constraints on the low frequency spectrum of FRB 121102*, A&A, 623, A42

Hunter, J. D. 2007, *Matplotlib: A 2D graphics environment*, Computing In Science & Engineering, 9, 90

Huppenkothen, D., Bachetti, M., Stevens, A. L., et al. 2019, *Stingray: A Modern Python Library for Spectral Timing*, ApJ, 881, 39

Huppenkothen, D., Brewer, B. J., Hogg, D. W., et al. 2015, *Dissecting Magnetar Variability with Bayesian Hierarchical Models*, ApJ, 810, 66

Huppenkothen, D., Watts, A. L., Uttley, P., et al. 2013, *Quasi-periodic Oscillations and Broadband Variability in Short Magnetar Bursts*, ApJ, 768, 87

Inoue, S. 2004, *Probing the cosmic reionization history and local environment of gamma-ray bursts through radio dispersion*, MNRAS, 348, 999

Ioka, K. 2003, *The Cosmic Dispersion Measure from Gamma-Ray Burst Afterglows: Probing the Reionization History and the Burst Environment*, ApJ, 598, L79

Ioka, K. & Zhang, B. 2020, *A Binary Comb Model for Periodic Fast Radio Bursts*, ApJ, 893, L26

Israel, G. L., Belloni, T., Stella, L., et al. 2005, *The Discovery of Rapid X-Ray Oscillations in the Tail of the SGR 1806-20 Hyperflare*, ApJ, 628, L53

Israel, G. L., Esposito, P., Rea, N., et al. 2016, *The discovery, monitoring and environment of SGR J1935+2154*, MNRAS, 457, 3448

Israel, G. L., Romano, P., Mangano, V., et al. 2008, *A Swift Gaze into the 2006 March 29 Burst Forest of SGR 1900+14*, ApJ, 685, 1114

Jahns, J. N., Spitler, L. G., Nimmo, K., et al. 2022, *The FRB 20121102A November rain in 2018 observed with the Arecibo Telescope*, arXiv e-prints, arXiv:2202.05705

James, C. W., Ekers, R. D., Macquart, J. P., Bannister, K. W., & Shannon, R. M. 2019, *The slope of the source-count distribution for fast radio bursts*, MNRAS, 483, 1342

Jarrett, T. H., Cluver, M. E., Magoulas, C., et al. 2017, *Galaxy and Mass Assembly (GAMA): Exploring the WISE Web in G12*, ApJ, 836, 182

Jessner, A., Popov, M. V., Kondratiev, V. I., et al. 2010, *Giant pulses with nanosecond time resolution detected from the Crab pulsar at 8.5 and 15.1 GHz*, A&A, 524, A60

Josephy, A., Chawla, P., Fonseca, E., et al. 2019, *CHIME/FRB Detection of the Original Repeating Fast Radio Burst Source FRB 121102*, ApJ, 882, L18

Karachentsev, I. D., Dolphin, A. E., Geisler, D., et al. 2002, *The M 81 group of galaxies: New distances, kinematics and structure*, A&A, 383, 125

Karuppusamy, R., Stappers, B. W., & van Straten, W. 2010, *Giant pulses from the Crab pulsar. A wide-band study*, A&A, 515, A36

Kashiyama, K. & Murase, K. 2017, *Testing the Young Neutron Star Scenario with Persistent Radio Emission Associated with FRB 121102*, ApJ, 839, L3

Kaspi, V. M. & Beloborodov, A. M. 2017, *Magnetars*, ARA&A, 55, 261

Kauffmann, G., Heckman, T. M., Tremonti, C., et al. 2003, *The host galaxies of active galactic nuclei*, MNRAS, 346, 1055

Kaur, B., Kanekar, N., & Prochaska, J. X. 2022, *A fast radio burst progenitor born in a galaxy merger*, ApJ, 925, L20

Keane, E. F. 2018, *The future of fast radio burst science*, Nature Astronomy, 2, 865

Keane, E. F., Stappers, B. W., Kramer, M., & Lyne, A. G. 2012, *On the origin of a highly dispersed coherent radio burst*, MNRAS, 425, L71

Keimpema, A., Kettenis, M. M., Pogrebenko, S. V., et al. 2015, *The SFXC software correlator for very long baseline interferometry: algorithms and implementation*, Experimental Astronomy, 39, 259

Keith, M. J., Coles, W., Shannon, R. M., et al. 2013, *Measurement and correction of variations in interstellar dispersion in high-precision pulsar timing*, MNRAS, 429, 2161

Kennicutt, Robert C., J., Tamblyn, P., & Congdon, C. E. 1994, *Past and Future Star Formation in Disk Galaxies*, ApJ, 435, 22

Kewley, L. J. & Dopita, M. A. 2002, *Using Strong Lines to Estimate Abundances in Extragalactic H II Regions and Starburst Galaxies*, ApJS, 142, 35

Kewley, L. J., Dopita, M. A., Sutherland, R. S., Heisler, C. A., & Trevena, J. 2001, *Theoretical Modeling of Starburst Galaxies*, ApJ, 556, 121

Kilpatrick, C. D., Fong, W., Prochaska, J. X., et al. 2021, *A redshift for the putative host galaxy of FRB20201124A*, The Astronomer's Telegram, 14516, 1

Kirsten, F., Marcote, B., Nimmo, K., et al. 2022, *A repeating fast radio burst source in a globular cluster*, Nature, 602, 585

Kirsten, F., Ould-Boukattine, O. S., Nimmo, K., et al. 2021a, *Two bright bursts from FRB 20201124A with the Onsala 25-m telescope at 1.4 GHz, with no simultaneous emission detected at 330 MHz with Westerbork 25-m*, The Astronomer's Telegram, 14605, 1

Kirsten, F., Snelders, M. P., Jenkins, M., et al. 2021b, *Detection of two bright radio bursts from magnetar SGR 1935 + 2154*, Nature Astronomy, 5, 414

Kirsten, F., Vlemmings, W., Campbell, R. M., Kramer, M., & Chatterjee, S. 2015, *Revisiting the birth locations of pulsars B1929+10, B2020+28, and B2021+51*, A&A, 577, A111

Kokubo, M., Mitsuda, K., Sugai, H., et al. 2017, *Hα Intensity Map of the Repeating Fast Radio Burst FRB 121102 Host Galaxy from Subaru/Kyoto 3DII AO-assisted Optical Integral-field Spectroscopy*, ApJ, 844, 95

Kramer, M., Stappers, B. W., Jessner, A., Lyne, A. G., & Jordan, C. A. 2007, *Polarized radio emission from a magnetar*, MNRAS, 377, 107

Kremer, K., Piro, A. L., & Li, D. 2021, *Dynamical Formation Channels for Fast Radio Bursts in Globular Clusters*, ApJ, 917, L11

Kulkarni, S. R. 2020, *Dispersion measure: Confusion, Constants & Clarity*, arXiv e-prints, arXiv:2007.02886

Kumar, P., Lu, W., & Bhattacharya, M. 2017, *Fast radio burst source properties and curvature radiation model*, MNRAS, 468, 2726

Kumar, P., Shannon, R. M., Flynn, C., et al. 2021, *Extremely band-limited repetition from a fast radio burst source*, MNRAS, 500, 2525

Kumar, P., Shannon, R. M., Lower, M. E., et al. 2022, *Circularly polarized radio emission from the repeating fast radio burst source FRB 20201124A*, MNRAS, 512, 3400

Kumar, P., Shannon, R. M., Osłowski, S., et al. 2019, *Faint Repetitions from a Bright Fast Radio Burst Source*, ApJ, 887, L30

Lanman, A. E., Andersen, B. C., Chawla, P., et al. 2022, *A Sudden Period of High Activity from Repeating Fast Radio Burst 20201124A*, ApJ, 927, 59

Law, C., Tendulkar, S., Clarke, T., Aggarwal, K., & Bethapudy, S. 2021, *VLA/realfast localization and deep imaging of FRB 20201124A*, The Astronomer's Telegram, 14526, 1

Law, C. J., Abruzzo, M. W., Bassa, C. G., et al. 2017, *A Multi-telescope Campaign on FRB 121102: Implications for the FRB Population*, ApJ, 850, 76

Law, C. J., Bower, G. C., Burke-Spolaor, S., et al. 2018a, *realfast: Real-time, Commensal Fast Transient Surveys with the Very Large Array*, ApJS, 236, 8

Law, C. J., Butler, B. J., Prochaska, J. X., et al. 2020, *A Distant Fast Radio Burst Associated with Its Host Galaxy by the Very Large Array*, ApJ, 899, 161

Law, C. J., Connor, L., & Aggarwal, K. 2022, *On the Fast Radio Burst and Persistent Radio Source Populations*, ApJ, 927, 55

Law, C. J., Gaensler, B. M., Metzger, B. D., Ofek, E. O., & Sironi, L. 2018b, *Discovery of the Luminous, Decades-long, Extragalactic Radio Transient FIRST J141918.9+394036*, ApJ, 866, L22

Lazarus, P., Karuppusamy, R., Graikou, E., et al. 2016, *Prospects for high-precision pulsar timing with the new Effelsberg PSRIX backend*, MNRAS, 458, 868

Levin, L., Bailes, M., Bates, S., et al. 2010, *A Radio-loud Magnetar in X-ray Quiescence*, ApJ, 721, L33

Levin, Y., Beloborodov, A. M., & Bransgrove, A. 2020, *Precessing Flaring Magnetar as a Source of Repeating FRB 180916.J0158+65*, ApJ, 895, L30

Li, C. K., Tuo, Y. L., Ge, M. Y., et al. 2020, *Insight-HXMT X-ray and hard X-ray upper limits to the radio burst detected by FAST from SGR 1935+2154*, The Astronomer's Telegram, 13703, 1

Li, D., Wang, P., Zhu, W. W., et al. 2021, *A bimodal burst energy distribution of a repeating fast radio burst source*, Nature, 598, 267

Li, Y., Zhang, B., Nagamine, K., & Shi, J. 2019, *The FRB 121102 Host Is Atypical among Nearby Fast Radio Bursts*, ApJ, 884, L26

Loewenstein, M., Mushotzky, R. F., Angelini, L., Arnaud, K. A., & Quataert, E. 2001, *Chandra Limits on X-Ray Emission Associated with the Supermassive Black Holes in Three Giant Elliptical Galaxies*, ApJ, 555, L21

Lomb, N. R. 1976, *Least-Squares Frequency Analysis of Unequally Spaced Data*, Ap&SS, 39, 447

Lorimer, D. R., Bailes, M., McLaughlin, M. A., Narkevic, D. J., & Crawford, F. 2007, *A Bright Millisecond Radio Burst of Extragalactic Origin*, Science, 318, 777

Lorimer, D. R. & Kramer, M. 2004, Handbook of Pulsar Astronomy, Vol. 4

Lorimer, D. R., Yates, J. A., Lyne, A. G., & Gould, D. M. 1995, *Multifrequency flux density measurements of 280 pulsars*, MNRAS, 273, 411

Lower, M. E., Shannon, R. M., Johnston, S., & Bailes, M. 2020, *Spectropolarimetric Properties of Swift J1818.0-1607: A 1.4 s Radio Magnetar*, ApJ, 896, L37

Lu, W., Beniamini, P., & Kumar, P. 2022, *Implications of a rapidly varying FRB in a globular cluster of M81*, MNRAS, 510, 1867

Lu, W., Kumar, P., & Narayan, R. 2019, *Fast radio burst source properties from polarization measurements*, MNRAS, 483, 359

Luo, R., Wang, B. J., Men, Y. P., et al. 2020, *Diverse polarization angle swings from a repeating fast radio burst source*, Nature, 586, 693

Lyubarsky, Y. 2014, *A model for fast extragalactic radio bursts.*, MNRAS, 442, L9

Lyubarsky, Y. 2020, *Fast Radio Bursts from Reconnection in a Magnetar Magnetosphere*, ApJ, 897, 1

Lyutikov, M. 2013, *The Electromagnetic Model of Short GRBs, the Nature of Prompt Tails, Supernova-less Long GRBs, and Highly Efficient Episodic Accretion*, ApJ, 768, 63

Lyutikov, M. 2017, *Fast Radio Bursts' Emission Mechanism: Implication from Localization*, ApJ, 838, L13

Lyutikov, M. 2020, *Radius-to-frequency Mapping and FRB Frequency Drifts*, ApJ, 889, 135

Lyutikov, M. 2021, *Coherent Emission in Pulsars, Magnetars, and Fast Radio Bursts: Reconnection-driven Free Electron Laser*, ApJ, 922, 166

Lyutikov, M., Barkov, M. V., & Giannios, D. 2020, *FRB Periodicity: Mild Pulsars in Tight O/B-star Binaries*, ApJ, 893, L39

Lyutikov, M. & Popov, S. 2020, *Fast Radio Bursts from reconnection events in magnetar magnetospheres*, arXiv e-prints, arXiv:2005.05093

MacMahon, D. H. E., Price, D. C., Lebofsky, M., et al. 2018, *The Breakthrough Listen Search for Intelligent Life: A Wideband Data Recorder System for the Robert C. Byrd Green Bank Telescope*, PASP, 130, 044502

Macquart, J. P., Prochaska, J. X., McQuinn, M., et al. 2020, *A census of baryons in the Universe from localized fast radio bursts*, Nature, 581, 391

MAGIC Collaboration, Acciari, V. A., Ansoldi, S., et al. 2018, *Constraining very-high-energy and optical emission from FRB 121102 with the MAGIC telescopes*, MNRAS, 481, 2479

Magnier, E. A., Schlafly, E. F., Finkbeiner, D. P., et al. 2020, *Pan-STARRS Photometric and Astrometric Calibration*, ApJS, 251, 6

Mahony, E. K., Ekers, R. D., Macquart, J.-P., et al. 2018, *A Search for the Host Galaxy of FRB 171020*, ApJ, 867, L10

Main, R. A., Hilmarsson, G. H., Marthi, V. R., et al. 2022, *Scintillation time-scale measurement of the highly active FRB20201124A*, MNRAS, 509, 3172

Majid, W. A., Pearlman, A. B., Nimmo, K., et al. 2020, *A Dual-band Radio Observation of FRB 121102 with the Deep Space Network and the Detection of Multiple Bursts*, ApJ, 897, L4

Majid, W. A., Pearlman, A. B., Prince, T. A., et al. 2021, *A Bright Fast Radio Burst from FRB 20200120E with Sub-100 Nanosecond Structure*, ApJ, 919, L6

Manchester, R. N., Hobbs, G. B., Teoh, A., & Hobbs, M. 2005, *The Australia Telescope National Facility Pulsar Catalogue*, AJ, 129, 1993

Manchester, R. N. & Taylor, J. H. 1972, *Parameters of 61 Pulsars*, Astrophys. Lett., 10, 67

Mannings, A. G., Fong, W.-f., Simha, S., et al. 2021, *A High-resolution View of Fast Radio Burst Host Environments*, ApJ, 917, 75

Marcote, B., Kirsten, F., Hessels, J. W. T., et al. 2021, *VLBI localization of FRB 20201124A and absence of persistent emission on milliarcsecond scales*, The Astronomer's Telegram, 14603, 1

Marcote, B., Nimmo, K., Hessels, J. W. T., et al. 2020, *A repeating fast radio burst source localized to a nearby spiral galaxy*, Nature, 577, 190

Marcote, B., Nimmo, K., Salafia, O. S., et al. 2019, *Resolving the Decades-long Transient FIRST J141918.9+394036: An Orphan Long Gamma-Ray Burst or a Young Magnetar Nebula?*, ApJ, 876, L14

Marcote, B., Paragi, Z., & Hessels, J. W. T. 2018, *First EVN measurements of the transient FIRST J141918.9+394036 on milliarcsecond scales*, The Astronomer's Telegram, 12126, 1

Marcote, B., Paragi, Z., Hessels, J. W. T., et al. 2017, *The Repeating Fast Radio Burst FRB 121102 as Seen on Milliarcsecond Angular Scales*, ApJ, 834, L8

Margalit, B., Berger, E., & Metzger, B. D. 2019, *Fast Radio Bursts from Magnetars Born in Binary Neutron Star Mergers and Accretion Induced Collapse*, ApJ, 886, 110

Margalit, B. & Metzger, B. D. 2018, *A Concordance Picture of FRB 121102 as a Flaring Magnetar Embedded in a Magnetized Ion-Electron Wind Nebula*, ApJ, 868, L4

Margalit, B., Metzger, B. D., & Sironi, L. 2020, *Constraints on the engines of fast radio bursts*, MNRAS, 494, 4627

Martí-Vidal, I., Guirado, J. C., Jiménez-Monferrer, S., & Marcaide, J. M. 2010a, *Atmospheric turbulence in phase-referenced and wide-field interferometric images. Application to the Square Kilometre Array*, A&A, 517, A70

Martí-Vidal, I., Pérez-Torres, M. A., & Lobanov, A. P. 2012, *Over-resolution of compact sources in interferometric observations*, A&A, 541, A135

Martí-Vidal, I., Ros, E., Pérez-Torres, M. A., et al. 2010b, *Coherence loss in phase-referenced VLBI observations*, A&A, 515, A53

Masui, K., Lin, H.-H., Sievers, J., et al. 2015, *Dense magnetized plasma associated with a fast radio burst*, Nature, 528, 523

Mather, J. C., Cheng, E. S., Cottingham, D. A., et al. 1994, *Measurement of the Cosmic Microwave Background Spectrum by the COBE FIRAS Instrument*, ApJ, 420, 439

McHardy, I. M., Koerding, E., Knigge, C., Uttley, P., & Fender, R. P. 2006, *Active galactic nuclei as scaled-up Galactic black holes*, Nature, 444, 730

McLaughlin, M. A., Lyne, A. G., Lorimer, D. R., et al. 2006, *Transient radio bursts from rotating neutron stars*, Nature, 439, 817

McQuinn, M. 2014, *Locating the "Missing" Baryons with Extragalactic Dispersion Measure Estimates*, ApJ, 780, L33

Mereghetti, S., Savchenko, V., Ferrigno, C., et al. 2020, *INTEGRAL Discovery of a Burst with Associated Radio Emission from the Magnetar SGR 1935+2154*, ApJ, 898, L29

Metzger, B. D., Berger, E., & Margalit, B. 2017, *Millisecond Magnetar Birth Connects FRB 121102 to Superluminous Supernovae and Long-duration Gamma-Ray Bursts*, ApJ, 841, 14

Metzger, B. D., Margalit, B., & Sironi, L. 2019, *Fast radio bursts as synchrotron maser emission from decelerating relativistic blast waves*, MNRAS, 485, 4091

Michilli, D. & Hessels, J. W. T. 2018, *SpS: Single-pulse Searcher*

Michilli, D., Hessels, J. W. T., Lyon, R. J., et al. 2018a, *Single-pulse classifier for the LOFAR Tied-Array All-sky Survey*, MNRAS, 480, 3457

Michilli, D., Masui, K. W., Mckinven, R., et al. 2021, *An Analysis Pipeline for CHIME/FRB Full-array Baseband Data*, ApJ, 910, 147

Michilli, D., Seymour, A., Hessels, J. W. T., et al. 2018b, *An extreme magneto-ionic environment associated with the fast radio burst source FRB 121102*, Nature, 553, 182

Mignard, F., Klioner, S., Lindegren, L., et al. 2016, *Gaia Data Release 1. Reference frame and optical properties of ICRF sources*, A&A, 595, A5

Mimica, P. & Giannios, D. 2011, *Gamma-ray burst afterglow light curves from realistic density profiles*, MNRAS, 418, 583

Modjaz, M., Kewley, L., Kirshner, R. P., et al. 2008, *Measured Metallicities at the Sites of Nearby Broad-Lined Type Ic Supernovae and Implications for the Supernovae Gamma-Ray Burst Connection*, AJ, 135, 1136

Mooley, K. P., Deller, A. T., Gottlieb, O., et al. 2018, *Superluminal motion of a relativistic jet in the neutron-star merger GW170817*, Nature, 561, 355

Murase, K., Kashiyama, K., & Mészáros, P. 2016, *A burst in a wind bubble and the impact on baryonic ejecta: high-energy gamma-ray flashes and afterglows from fast radio bursts and pulsar-driven supernova remnants*, MNRAS, 461, 1498

Nakar, E. & Granot, J. 2007, *Smooth light curves from a bumpy ride: relativistic blast wave encounters a density jump*, MNRAS, 380, 1744

Nan, R., Li, D., Jin, C., et al. 2011, *The Five-Hundred Aperture Spherical Radio Telescope (fast) Project*, International Journal of Modern Physics D, 20, 989

Natarajan, I., Paragi, Z., Zwart, J., et al. 2017, *Resolving the blazar CGRaBS J0809+5341 in the presence of telescope systematics*, MNRAS, 464, 4306

Ng, C., Vanderlinde, K., Paradise, A., et al. 2017, *CHIME FRB: An application of FFT beamforming for a radio telescope*, in XXXII International Union of Radio Science General Assembly & Scientific Symposium (URSI GASS) 2017, 4

Nimmo, K., Hessels, J. W. T., Keimpema, A., et al. 2021, *Highly polarized microstructure from the repeating FRB 20180916B*, Nature Astronomy, 5, 594

Nimmo, K., Hessels, J. W. T., Kirsten, F., et al. 2022a, *Burst timescales and luminosities as links between young pulsars and fast radio bursts*, Nature Astronomy, 6, 393

Nimmo, K., Hewitt, D. M., Hessels, J. W. T., et al. 2022b, *Milliarcsecond Localization of the Repeating FRB 20201124A*, ApJ, 927, L3

Niu, C. H., Aggarwal, K., Li, D., et al. 2021, *A repeating fast radio burst associated with a persistent radio source*, arXiv e-prints, arXiv:2110.07418

Noll, C. E. 2010, *The crustal dynamics data information system: A resource to support scientific analysis using space geodesy*, Advances in Space Research, 45, 1421

Nomoto, K. & Kondo, Y. 1991, *Conditions for Accretion-induced Collapse of White Dwarfs*, ApJ, 367, L19

Ofek, E. O. 2017, *A Search for FRB 121102-like Persistent Radio-luminous Sources—Candidates and Implications for the FRB Rate and Searches*, ApJ, 846, 44

Omand, C. M. B., Kashiyama, K., & Murase, K. 2018, *Radio emission from embryonic superluminous supernova remnants*, MNRAS, 474, 573

Oostrum, L. C., Maan, Y., van Leeuwen, J., et al. 2020, *Repeating fast radio bursts with WSRT/Apertif*, A&A, 635, A61

Oppermann, N., Yu, H.-R., & Pen, U.-L. 2018, *On the non-Poissonian repetition pattern of FRB121102*, MNRAS, 475, 5109

Ould-Boukattine, O. S., Kirsten, F., Nimmo, K., et al. 2022, *Subsequent detection of three more bursts from FRB 20201124A using the Westerbork-RT1 25-m telescope*, The Astronomer's Telegram, 15192, 1

Palmer, D. M. 2020, *A Forest of Bursts from SGR 1935+2154*, The Astronomer's Telegram, 13675, 1

Paragi, Z., Godfrey, L., Reynolds, C., et al. 2015, *Very Long Baseline Interferometry with the SKA*, Advancing Astrophysics with the Square Kilometre Array (AASKA14), 143

Pastor-Marazuela, I., Connor, L., van Leeuwen, J., et al. 2021, *Chromatic periodic activity down to 120 megahertz in a fast radio burst*, Nature, 596, 505

Patterson, M. T., Walterbos, R. A. M., Kennicutt, R. C., Chiappini, C., & Thilker, D. A. 2012, *An oxygen abundance gradient into the outer disc of M81*, MNRAS, 422, 401

Pearlman, A. B., Majid, W. A., Prince, T. A., et al. 2020, *Multiwavelength Radio Observations of Two Repeating Fast Radio Burst Sources: FRB 121102 and FRB 180916.J0158+65*, ApJ, 905, L27

Perelmuter, J.-M., Brodie, J. P., & Huchra, J. P. 1995, *Kinematics and Metallicity of 25 Globular Clusters in M81*, AJ, 110, 620

Perelmuter, J.-M. & Racine, R. 1995, *The Globular Cluster System of M81*, AJ, 109, 1055

Petroff, E., Bailes, M., Barr, E. D., et al. 2015, *A real-time fast radio burst: polarization detection and multiwavelength follow-up*, MNRAS, 447, 246

Petroff, E., Barr, E. D., Jameson, A., et al. 2016, *FRBCAT: The Fast Radio Burst Catalogue*, PASA, 33, e045

Petroff, E., Hessels, J. W. T., & Lorimer, D. R. 2019, *Fast radio bursts*, A&A Rev., 27, 4

Petroff, E., Hessels, J. W. T., & Lorimer, D. R. 2022, *Fast radio bursts at the dawn of the 2020s*, A&A Rev., 30, 2

Philippov, A., Uzdensky, D. A., Spitkovsky, A., & Cerutti, B. 2019, *Pulsar Radio Emission Mechanism: Radio Nanoshots as a Low-frequency Afterglow of Relativistic Magnetic Reconnection*, ApJ, 876, L6

Pihlström, Y. M., Taylor, G. B., Granot, J., & Doeleman, S. 2007, *Stirring the Embers: High-Sensitivity VLBI Observations of GRB 030329*, ApJ, 664, 411

Pilia, M., Burgay, M., Possenti, A., et al. 2020, *The Lowest-frequency Fast Radio Bursts: Sardinia Radio Telescope Detection of the Periodic FRB 180916 at 328 MHz*, ApJ, 896, L40

Piro, A. L. & Gaensler, B. M. 2018, *The Dispersion and Rotation Measure of Supernova Remnants and Magnetized Stellar Winds: Application to Fast Radio Bursts*, ApJ, 861, 150

Piro, L., Bruni, G., Troja, E., et al. 2021, *The fast radio burst FRB 20201124A in a star-forming region: Constraints to the progenitor and multiwavelength counterparts*, A&A, 656, L15

Planck Collaboration, Aghanim, N., Akrami, Y., et al. 2020, *Planck 2018 results. VI. Cosmological parameters*, A&A, 641, A6

Platts, E., Weltman, A., Walters, A., et al. 2019, *A living theory catalogue for fast radio bursts*, Phys. Rep., 821, 1

Plavin, A., Paragi, Z., Marcote, B., et al. 2022, *FRB 121102: Drastic changes in the burst polarization contrasts with the stability of the persistent emission*, MNRAS, 511, 6033

Plavin, A. V., Kovalev, Y. Y., Pushkarev, A. B., & Lobanov, A. P. 2019, *Significant core shift variability in parsec-scale jets of active galactic nuclei*, MNRAS, 485, 1822

Pleunis, Z., Good, D. C., Kaspi, V. M., et al. 2021a, *Fast Radio Burst Morphology in the First CHIME/FRB Catalog*, ApJ, 923, 1

Pleunis, Z., Michilli, D., Bassa, C. G., et al. 2021b, *LOFAR Detection of 110-188 MHz Emission and Frequency-dependent Activity from FRB 20180916B*, ApJ, 911, L3

Pooley, D., Lewin, W. H. G., Anderson, S. F., et al. 2003, *Dynamical Formation of Close Binary Systems in Globular Clusters*, ApJ, 591, L131

Pradel, N., Charlot, P., & Lestrade, J. F. 2006, *Astrometric accuracy of phase-referenced observations with the VLBA and EVN*, A&A, 452, 1099

Prandoni, I., Murgia, M., Tarchi, A., et al. 2017, *The Sardinia Radio Telescope . From a technological project to a radio observatory*, A&A, 608, A40

Prochaska, J. X., Macquart, J.-P., McQuinn, M., et al. 2019, *The low density and magnetization of a massive galaxy halo exposed by a fast radio burst*, Science, 366, 231

Prochaska, J. X. & Zheng, Y. 2019, *Probing Galactic haloes with fast radio bursts*, MNRAS, 485, 648

Protassov, R., van Dyk, D. A., Connors, A., Kashyap, V. L., & Siemiginowska, A. 2002, *Statistics, Handle with Care: Detecting Multiple Model Components with the Likelihood Ratio Test*, ApJ, 571, 545

Pushkarev, A. B. & Kovalev, Y. Y. 2015, *Milky Way scattering properties and intrinsic sizes of active galactic nuclei cores probed by very long baseline interferometry surveys of compact extragalactic radio sources*, MNRAS, 452, 4274

Rajwade, K. M., Mickaliger, M. B., Stappers, B. W., et al. 2020, *Possible periodic activity in the repeating FRB 121102*, MNRAS, 495, 3551

Rand, R. J. 1996, *Diffuse Ionized Gas in Nine Edge-on Galaxies*, ApJ, 462, 712

Ransom, S. M. 2001, *New search techniques for binary pulsars*, PhD thesis, Harvard University, Massachusetts

Ravi, V. 2019, *The prevalence of repeating fast radio bursts*, Nature Astronomy, 3, 928

Ravi, V., Catha, M., D'Addario, L., et al. 2019, *A fast radio burst localized to a massive galaxy*, Nature, 572, 352

Ravi, V., Law, C. J., Li, D., et al. 2022, *The host galaxy and persistent radio counterpart of FRB 20201124A*, MNRAS, 513, 982

Ravi, V., Shannon, R. M., Bailes, M., et al. 2016, *The magnetic field and turbulence of the cosmic web measured using a brilliant fast radio burst*, Science, 354, 1249

Rees, M. J. 1977, *A better way of searching for black-hole explosions?*, Nature, 266, 333

Reich, P. & Reich, W. 1988, *Spectral index variations of the galactic radio continuum emission : evidence for a galactic wind.*, A&A, 196, 211

Reines, A. E., Condon, J. J., Darling, J., & Greene, J. E. 2020, *A New Sample of (Wandering) Massive Black Holes in Dwarf Galaxies from High-resolution Radio Observations*, ApJ, 888, 36

Remazeilles, M., Dickinson, C., Banday, A. J., Bigot-Sazy, M. A., & Ghosh, T. 2015, *An improved source-subtracted and destriped 408-MHz all-sky map*, MNRAS, 451, 4311

Remillard, R. A., McClintock, J. E., Orosz, J. A., & Levine, A. M. 2006, *The X-Ray Outburst of H1743-322 in 2003: High-Frequency QPOs with a 3:2 Frequency Ratio*, ApJ, 637, 1002

Ricci, R., Piro, L., Panessa, F., et al. 2021, *Detection of a persistent radio source at the location of FRB20201124A with VLA*, The Astronomer's Telegram, 14549, 1

Rickett, B. J. 1975, *Amplitude-modulated noise: an empirical model for the radio radiation received from pulsars.*, ApJ, 197, 185

Rickett, B. J. 1990, *Radio propagation through the turbulent interstellar plasma.*, ARA&A, 28, 561

Ridnaia, A., Golenetskii, S., Aptekar, R., et al. 2020, *Konus-Wind observation of hard X-ray counterpart of the radio burst from SGR 1935+2154*, GRB Coordinates Network, 27669, 1

Riess, A. G., Casertano, S., Yuan, W., Macri, L. M., & Scolnic, D. 2019, *Large Magellanic Cloud Cepheid Standards Provide a 1% Foundation for the Determination of the Hubble Constant and Stronger Evidence for Physics beyond ΛCDM*, ApJ, 876, 85

Ros, E., Schwarz, D. J., & Vocks, C. 2018, *Community Paper on Radio Astronomy Infrastructures*, arXiv e-prints, arXiv:1802.08467

Rosswog, S., Ramirez-Ruiz, E., & Davies, M. B. 2003, *High-resolution calculations of merging neutron stars - III. Gamma-ray bursts*, MNRAS, 345, 1077

Ryle, M. & Vonberg, D. D. 1946, *Solar Radiation on 175 Mc./s.*, Nature, 158, 339

Savitzky, A. & Golay, M. J. E. 1964, *Smoothing and differentiation of data by simplified least squares procedures*, Analytical Chemistry, 36, 1627

Scargle, J. D. 1982, *Studies in astronomical time series analysis. II. Statistical aspects of spectral analysis of unevenly spaced data.*, ApJ, 263, 835

Scholz, P., Bogdanov, S., Hessels, J. W. T., et al. 2017, *Simultaneous X-Ray, Gamma-Ray, and Radio Observations of the Repeating Fast Radio Burst FRB 121102*, ApJ, 846, 80

Scholz, P., Cook, A., Cruces, M., et al. 2020, *Simultaneous X-Ray and Radio Observations of the Repeating Fast Radio Burst FRB $\sim$ 180916.J0158+65*, ApJ, 901, 165

Scholz, P., Spitler, L. G., Hessels, J. W. T., et al. 2016, *The Repeating Fast Radio Burst FRB 121102: Multi-wavelength Observations and Additional Bursts*, ApJ, 833, 177

Sciama, D. W. 1964, *The Physical Structure of General Relativity*, Reviews of Modern Physics, 36, 463

Seebeck, J., Ravi, V., Connor, L., et al. 2021, *The Effects of Selection Biases on the Analysis of Localised Fast Radio Bursts*, arXiv e-prints, arXiv:2112.07639

Sell, P. H., Pooley, D., Zezas, A., et al. 2011, *Luminosity Functions and Point-source Properties from Multiple Chandra Observations of M81*, ApJ, 735, 26

Shepherd, M. C., Pearson, T. J., & Taylor, G. B. 1994, *DIFMAP: an interactive program for synthesis imaging.*, in Bulletin of the American Astronomical Society, Vol. 26, 987–989

Sironi, L. & Giannios, D. 2013, *A Late-time Flattening of Light Curves in Gamma-Ray Burst Afterglows*, ApJ, 778, 107

Smith, F. G. 1968, *Faraday Rotation of Radio Waves from the Pulsars*, Nature, 220, 891

Sobacchi, E., Lyubarsky, Y., Beloborodov, A. M., & Sironi, L. 2021, *Self-modulation of fast radio bursts*, MNRAS, 500, 272

Spitler, L. G., Cordes, J. M., Hessels, J. W. T., et al. 2014, *Fast Radio Burst Discovered in the Arecibo Pulsar ALFA Survey*, ApJ, 790, 101

Spitler, L. G., Scholz, P., Hessels, J. W. T., et al. 2016, *A repeating fast radio burst*, Nature, 531, 202

Staelin, D. H. 1970, *Observed Shapes of Crab Nebula Radio Pulses*, Nature, 226, 69

Staelin, D. H. & Reifenstein, Edward C., I. 1968, *Pulsating Radio Sources near the Crab Nebula*, Science, 162, 1481

Stephens, M. 1974, *EDF Statistics for Goodness of Fit and Some Comparisons.*, Journal of the American Statistical Association, 69, 730

Stratta, G., Dainotti, M. G., Dall'Osso, S., Hernandez, X., & De Cesare, G. 2018, *On the Magnetar Origin of the GRBs Presenting X-Ray Afterglow Plateaus*, ApJ, 869, 155

Tan, C. M., Bassa, C. G., Cooper, S., et al. 2018, *LOFAR Discovery of a 23.5 s Radio Pulsar*, ApJ, 866, 54

Tauris, T. M., Sanyal, D., Yoon, S. C., & Langer, N. 2013, *Evolution towards and beyond accretion-induced collapse of massive white dwarfs and formation of millisecond pulsars*, A&A, 558, A39

Tavani, M., Ursi, A., Verrecchia, F., et al. 2020, *AGILE detection of a hard X-ray burst in temporal coincidence with a radio burst from SGR 1935+2154*, The Astronomer's Telegram, 13686, 1

Taylor, J. H., Manchester, R. N., & Lyne, A. G. 1993, *Catalog of 558 Pulsars*, ApJS, 88, 529

Tendulkar, S. P., Bassa, C. G., Cordes, J. M., et al. 2017, *The Host Galaxy and Redshift of the Repeating Fast Radio Burst FRB 121102*, ApJ, 834, L7

Tendulkar, S. P., Gil de Paz, A., Kirichenko, A. Y., et al. 2021, *The 60 pc Environment of FRB 20180916B*, ApJ, 908, L12

The CHIME/FRB Collaboration, Andersen, B. C., Bandura, K., et al. 2021, *Sub-second periodicity in a fast radio burst*, arXiv e-prints, arXiv:2107.08463

Thompson, A. R. 1999, *Fundamentals of Radio Interferometry*, in ASP Conf. Ser., Vol. 180, Synthesis Imaging in Radio Astronomy II, ed. G. B. Taylor, C. L. Carilli, & R. A. Perley, 11

Thornton, D., Stappers, B., Bailes, M., et al. 2013, *A Population of Fast Radio Bursts at Cosmological Distances*, Science, 341, 53

Thulasiram, P. & Lin, H.-H. 2021, *Narrow-band giant pulses from the Crab pulsar*, MNRAS, 508, 1947

Tuccari, G., Alef, W., Bertarini, A., et al. 2010, *DBBC2 Backend: status and development plan.*, in Behrend D, Baver KD (eds) IVS 2010 General Meeting Proceedings, Vol. NASA/CP-2010-215864, 392–395

Vachaspati, T. 2008, *Cosmic Sparks from Superconducting Strings*, Phys. Rev. Lett., 101, 141301

van der Horst, A. J., Kouveliotou, C., Gorgone, N. M., et al. 2012, *SGR J1550-5418 Bursts Detected with the Fermi Gamma-Ray Burst Monitor during its Most Prolific Activity*, ApJ, 749, 122

van der Klis, M. 2006, in Compact stellar X-ray sources, Vol. 39, 39–112

van Straten, W. 2009, *The Statistics of Radio Astronomical Polarimetry: Bright Sources and High Time Resolution*, ApJ, 694, 1413

van Straten, W. & Bailes, M. 2011, *DSPSR: Digital Signal Processing Software for Pulsar Astronomy*, PASA, 28, 1

van Straten, W., Jameson, A., & Osłowski, S. 2021, *PSRDADA: Distributed Acquisition and Data Analysis for Radio Astronomy*, Astrophysics Source Code Library, record ascl:2110.003

van Straten, W., Manchester, R. N., Johnston, S., & Reynolds, J. E. 2010, *PSRCHIVE and PSRFITS: Definition of the Stokes Parameters and Instrumental Basis Conventions*, PASA, 27, 104

VanderPlas, J. T. 2018, *Understanding the Lomb-Scargle Periodogram*, ApJS, 236, 16

Vedantham, H. K. & Ravi, V. 2019, *Faraday conversion and magneto-ionic variations in fast radio bursts*, MNRAS, 485, L78

Wadiasingh, Z., Beniamini, P., Timokhin, A., et al. 2020, *The Fast Radio Burst Luminosity Function and Death Line in the Low-twist Magnetar Model*, ApJ, 891, 82

Wharton, R., Bethapudi, S., Gautam, T., et al. 2021a, *uGMRT detection of a persistent radio source coincident with FRB20201124A*, The Astronomer's Telegram, 14529, 1

Wharton, R., Bethapudi, S., Gautam, T., et al. 2021b, *uGMRT detection of a persistent radio source coincident with FRB20201124A*, The Astronomer's Telegram, 14529, 1

Wharton, R., Bethapudi, S., Marthi, V., et al. 2021c, *uGMRT localization of FRB20201124A*, The Astronomer's Telegram, 14538, 1

Whitney, A. 2004, *The Mark 5B VLBI Data System*, in European VLBI Network on New Developments in VLBI Science and Technology, 251–252

Whitney, A., Kettenis, M., Phillips, C., & Sekido, M. 2010, *VLBI Data Interchange Format (VDIF)*, in Sixth International VLBI Service for Geodesy and Astronomy. Proceedings from the 2010 General Meeting, ed. R. Navarro, S. Rogstad, C. E. Goodhart, E. Sigman, M. Soriano, D. Wang, L. A. White, & C. S. Jacobs, 192–196

Wright, E. L. 2006, *A Cosmology Calculator for the World Wide Web*, PASP, 118, 1711

Wu, Z., Verbiest, J. P. W., Main, R. A., et al. 2022, *Pulsar scintillation studies with LOFAR. I. The census*, arXiv e-prints, arXiv:2203.10409

Xu, H., Niu, J. R., Chen, P., et al. 2021, *A fast radio burst source at a complex magnetised site in a barred galaxy*, arXiv e-prints, arXiv:2111.11764

Xu, S. & Zhang, B. 2020, *Probing the Intergalactic Turbulence with Fast Radio Bursts*, ApJ, 898, L48

Yamasaki, S. & Totani, T. 2020, *The Galactic Halo Contribution to the Dispersion Measure of Extragalactic Fast Radio Bursts*, ApJ, 888, 105

Yao, J. M., Manchester, R. N., & Wang, N. 2017, *A New Electron-density Model for Estimation of Pulsar and FRB Distances*, ApJ, 835, 29

Ye, C. S., Kremer, K., Chatterjee, S., Rodriguez, C. L., & Rasio, F. A. 2019, *Millisecond Pulsars and Black Holes in Globular Clusters*, ApJ, 877, 122

Younes, G., Güver, T., Kouveliotou, C., et al. 2020, *NICER View of the 2020 Burst Storm and Persistent Emission of SGR 1935+2154*, ApJ, 904, L21

Yuan, Y., Beloborodov, A. M., Chen, A. Y., & Levin, Y. 2020, *Plasmoid Ejection by Alfvén Waves and the Fast Radio Bursts from SGR 1935+2154*, ApJ, 900, L21

Zanazzi, J. J. & Lai, D. 2020, *Periodic Fast Radio Bursts with Neutron Star Free Precession*, ApJ, 892, L15

Zhang, B. 2016, *Mergers of Charged Black Holes: Gravitational-wave Events, Short Gamma-Ray Bursts, and Fast Radio Bursts*, ApJ, 827, L31

Zhang, B. 2017, *A "Cosmic Comb" Model of Fast Radio Bursts*, ApJ, 836, L32

Zhang, B. 2018a, *Fast Radio Burst Energetics and Detectability from High Redshifts*, ApJ, 867, L21

Zhang, B. 2018b, *FRB 121102: A Repeatedly Combed Neutron Star by a Nearby Low-luminosity Accreting Supermassive Black Hole*, ApJ, 854, L21

Zhang, C. F., Jiang, J. C., Men, Y. P., et al. 2020, *A highly polarised radio burst detected from SGR 1935+2154 by FAST*, The Astronomer's Telegram, 13699, 1

Zhang, W. & MacFadyen, A. 2009, *The Dynamics and Afterglow Radiation of Gamma-Ray Bursts. I. Constant Density Medium*, ApJ, 698, 1261

Zhang, Y.-C. & Yang, X.-H. 2019, *Size distribution of galaxies in SDSS DR7: weak dependence on halo environment*, , 19, 006

Zhong, S.-Q. & Dai, Z.-G. 2020, *Magnetars from Neutron Star-White Dwarf Mergers: Application to Fast Radio Bursts*, ApJ, 893, 9

Zhong, S.-Q., Dai, Z.-G., Zhang, H.-M., & Deng, C.-M. 2020, *On the Distance of SGR 1935+2154 Associated with FRB 200428 and Hosted in SNR G57.2+0.8*, ApJ, 898, L5

Zhou, B., Li, X., Wang, T., Fan, Y.-Z., & Wei, D.-M. 2014, *Fast radio bursts as a cosmic probe?*, Phys. Rev. D, 89, 107303

Contribution from co-authors

The relative chapter contribution of each co-author is represented by their position in the author list, unless specified.

Chapter 2: Highly polarized microstructure from the repeating FRB 20180916B

K. Nimmo, J. W. T. Hessels, A. Keimpema, A. M. Archibald, J. M. Cordes, R. Karuppusamy, F. Kirsten, D. Z. Li, B. Marcote, Z. Paragi

Nature Astronomy, 2021, 5, 594

K.N. discovered the signals, led the data analysis, made the figures, and wrote the majority of the manuscript. J.W.T.H. guided the work and made important contributions to the writing and interpretation. A.K. performed pre-processing of the EVN voltage data. All other authors contributed significantly to aspects of the data acquisition, analysis strategy or interpretation.

Chapter 3: Burst timescales and luminosities as links between young pulsars and fast radio bursts

K. Nimmo, J. W. T. Hessels, F. Kirsten, A. Keimpema, J. M. Cordes, M. P. Snelders, D. M. Hewitt, R. Karuppusamy, A. M. Archibald, V. Bezrukovs, M. Bhardwaj, R. Blaauw, S. T. Buttaccio, T. Cassanelli, J. E. Conway, A. Corongiu, R. Feiler, E. Fonseca, O. Forssén, M. Gawroński, M. Giroletti, M. A. Kharinov, C. Leung, M. Lindqvist, G. Maccaferri, B. Marcote, K. W. Masui, R. Mckinven, A. Melnikov, D. Michilli, A. G. Mikhailov, C. Ng, A. Orbidans, O. S. Ould-Boukattine, Z. Paragi, A. B. Pearlman, E. Petroff, M. Rahman, P. Scholz, K. Shin, K. M. Smith, I. H. Stairs, G. Surcis, S. P. Tendulkar, W. Vlemmings, N. Wang, J. Yang, J. P. Yuan

Nature Astronomy, 2022, 6, 393

K.N. led the data analysis, made the figures, and wrote most of the manuscript. J.W.T.H. guided the work and made important contributions to the writing and interpretation. F.K. discovered the bursts and contributed to the analysis of the voltage data. A.K. adapted the SFXC code to created coherently dedispersed voltage data at the native time resolution. J.M.C. provided important insights into the data analysis strategy. M.P.S., D.M.H. and R.K. played supporting roles in the data acquisition and analysis. All other authors contributed significantly to laying the groundwork for this study, aspects of the data acquisition, or interpretation.

Chapter 4: A burst storm from the repeating FRB 20200120E in an M81 globular cluster

K. Nimmo, J. W. T. Hessels, M. P. Snelders, R. Karuppusamy, D. M. Hewitt, F. Kirsten, B. Marcote, U. Bach, A. Bansod, E. D. Barr, J. Behrend, V. Bezrukovs, S. Buttaccio, R. Feiler, M. P. Gawroński, M. Lindqvist, A. Orbidans, W. Puchalska, N. Wang, T. Winchen, P. Wolak, J. Wu, and J. Yuan

Monthly Notices of the Royal Astronomical Society, submitted, arXiv:2206.03759

Chapter 5: Milliarcsecond localization of the repeating FRB 20201124A

K. Nimmo, D. M. Hewitt, J. W. T. Hessels, F. Kirsten, B. Marcote, U. Bach, R. Blaauw, M. Burgay, A. Corongiu, R. Feiler, M. P. Gawroński, M. Giroletti, R. Karuppusamy, A. Keimpema, M. A. Kharinov, M. Lindqvist, G. Maccaferri, A. Melnikov, A. Mikhailov, O. S. Ould-Boukattine, Z. Paragi, M. Pilia, A. Possenti, M. P. Snelders, G. Surcis, M. Trudu, T. Venturi, W. Vlemmings, N. Wang, J. Yang, J. Yuan

The Astrophysical Journal Letters, 2022, 927, L3

C

Chapter 6: A repeating fast radio burst source localized to a nearby spiral galaxy

B. Marcote, **K. Nimmo**, J. W. T. Hessels, S. P. Tendulkar, C. G. Bassa, Z. Paragi, A. Keimpema, M. Bhardwaj, R. Karuppusamy, V. M. Kaspi, C. J. Law, D. Michilli, K. Aggarwal, B. Andersen, A. M. Archibald, K. Bandura, G. C. Bower, P. J. Boyle, C. Brar, S. Burke-Spolaor, B. J. Butler, T. Cassanelli, P. Chawla, P. Demorest, M. Dobbs, E. Fonseca, U. Giri, D. C. Good, K. Gourdji, A. Josephy, A. Yu. Kirichenko, F. Kirsten, T. L. Landecker, D. Lang, T. J. W. Lazio, D. Z. Li, H. -H. Lin, J. D. Linford, K. Masui, J. Mena-Parra, A. Naidu, C. Ng, C. Patel, U. L. Pen, Z. Pleunis, M. Rafiei-Ravandi, M. Rahman, A. Renard, P. Scholz, S. R. Siegel, K. M. Smith, I. H. Stairs, K. Vanderlinde, A. V. Zwaniga

Nature, 2020, 577, 190

B.M. is Principal Investigator of the EVN observing programme and led the radio imaging analysis of those data. K.N. discovered the radio bursts and led the time-domain analysis. J.W.T.H. guided the time-domain analysis and made major contributions to the writing of the manuscript. S.P.T. and C.B. led the optical imaging and spectroscopic analyses. Z.P. performed an independent analysis of the EVN data, and in previous years has pioneered the development of the EVN's capabilities for fast transient research. A.K. created the software used to correlate the EVN baseband data. M.B. analysed the chance coincidence probability. R.K. arranged the Effelsberg PSRIX observations. C.J.L. analysed the VLA imaging data. D.M. determined the CHIME/FRB baseband position. V.M.K. played a significant coordination role that enabled these results. All other co-authors contributed to the CHIME/FRB discovery of the source or the interpretation of the analysis results and the final version of the manuscript.

Chapter 7: Resolving the decades-long transient FIRST J141918.9+394036: an orphan long gamma-ray burst or a young magnetar nebula?

B. Marcote, **K. Nimmo**, O. S. Salafia, Z. Paragi, J. W. T. Hessels, E. Petroff, R. Karuppusamy

The Astrophysical Journal Letters, 2019, 876, L14

As an appendix to this chapter is a Research Note of the American Astronomical Society: No Radio Bursts Detected from FIRST J1419+3940 in Green Bank Telescope Observations

K. Nimmo, V. Gajjar, J. W. T. Hessels, C. J. Law, R. S. Lynch, A. D. Seymour, L. G. Spitler

Research Notes of the AAS, 2020, 4, 4, 50

Additional publications

A list of papers featuring K. Nimmo as a co-author, which are closely related to the work presented in this thesis. These papers have been published by, accepted by or submitted to a peer-reviewed journal, as indicated.

1. *FRB 121102: Drastic changes in the burst polarization contrasts with the stability of the persistent emission*
   A. Plavin, Z. Paragi, B. Marcote, A. Keimpema, J. W. T. Hessels, **K. Nimmo**, H. K. Vendantham, L. G. Spitler
   Monthly Notices of the Royal Astronomical Society, 2022, 511, 6033
2. *The FRB 20121102A November rain in 2018 observed with the Arecibo Telescope*
   J. N. Jahns, L. G. Spitler, **K. Nimmo**, D. M. Hewitt, M. P. Snelders, A. Seymour, J. W. T. Hessels, K. Gourdji, D. Michilli, G. H. Hilmarsson
   Submitted to Monthly Notices of the Royal Astronomical Society, arXiv:2202.05705
3. *A repeating fast radio burst source in a globular cluster*
   F. Kirsten, B. Marcote, **K. Nimmo**, J. W. T. Hessels, and 62 co-authors
   Nature, 2022, 602, 585
4. *Arecibo observations of a burst storm from FRB 20121102A in 2016*
   D. M. Hewitt, M. P. Snelders, J. W. T. Hessels, **K. Nimmo**, J. N. Jahns, L. G. Spitler, K. Gourdji, G. H. Hilmarsson, D. Michilli, O. S. Ould-Boukattine, P. Scholz, A. D. Seymour
   Accepted by Monthly Notices of the Royal Astronomical Society, arXiv:2111.11282
5. *Detection of two bright radio bursts from magnetar SGR 1935+2154*
   F. Kirsten, M. P. Snelders, M. Jenkins, **K. Nimmo**, J. van den Eijnden, J. W. T. Hessels, M. P. Gawroński, J. Yang
   Nature Astronomy, 2021, 5, 414
6. *LOFAR Detection of 110-188 MHz Emission and Frequency-dependent Activity from FRB 20180916B*
   Z. Pleunis, and 34 co-authors including **K. Nimmo**
   The Astrophysical Journal Letters, 2021, 911, L3

7. *The 60 pc Environment of FRB 20180916B*
   S. P. Tendulkar, and 20 co-authors including **K. Nimmo**
   The Astrophysical Journal Letters, 2021, 908, L12
8. *Rotation Measure Evolution of the Repeating Fast Radio Burst Source FRB 121102*
   G. H. Hilmarsson, D. Michilli, L. G. Spitler, R. S. Wharton, P. Demorest, G. Desvignes, K. Gourdji, S. Hackstein, J. W. T. Hessels, **K. Nimmo**, A. D. Seymour, M. Kramer, R. Mckinven
   The Astrophysical Journal Letters, 2021, 908, L10
9. *Multiwavelength Radio Observations of Two Repeating Fast Radio Burst Sources: FRB 121102 and FRB 180916.J0158+65*
   A. B. Pearlman, W. A. Majid, T. A. Prince, **K. Nimmo**, J. W. T. Hessels, C. J. Naudet, J. Kocz
   The Astrophysical Journal Letters, 2020, 905, L27
10. *Simultaneous X-Ray and Radio Observations of the Repeating Fast Radio Burst FRB 180916.J0158+65*
    P. Scholz, and 37 co-authors including **K. Nimmo**
    The Astrophysical Journal, 2020, 901, 165
11. *A Dual-band Radio Observation of FRB 121102 with the Deep Space Network and the Detection of Multiple Bursts*
    W. A. Majid, A. B. Pearlman, **K. Nimmo**, J. W. T. Hessels, T. A. Prince, C. J. Naudet, J. Kocz, S. Horiuchi
    The Astrophysical Journal Letters, 2020, 897, L4
12. *Periodic activity from a fast radio burst source*
    CHIME/FRB Collaboration: 72 co-authors including **K. Nimmo**
    Nature, 2020, 582, 351

English Summary

This thesis is focused on exploring the nature of FRB emission by studying the burst properties and local environments in detail. The main science questions considered are:

- What types of astrophysical objects are capable of producing fast radio transients?
- Are repeating and non-repeating FRBs coming from the same type of sources, but with varying levels of activity?
- Are all repeating FRBs the same type of object?
- What is the physical mechanism behind the FRB emission?

The thesis is divided into two parts. The first, "Zooming-in in time", details work using extremely high time resolution (from 30 ns to μs) single-dish Effelsberg observations (see §1.6.1) of repeating FRB sources. In the second, "Zooming-in in space", we use the EVN (see §1.6.2) to pinpoint repeating FRBs to milliarcsecond precision, identifying their host galaxies, probing their immediate surroundings and we study a radio transient with a potential link to FRBs on spatial scales of $\sim$ pc.

Zooming-in in time

In Chapter 2 we probe 1.4 GHz FRB 20180916B (§1.2.2) burst properties down to microsecond timescales using raw voltage data recorded with the 100-m Effelsberg telescope. We show that the bursts exhibit a range of timescales from milliseconds down to 3–4μs (Figure 2.1). These short timescales cast doubt on the non-magnetospheric emission models (§1.4), since they imply a small emission region ($\sim$km ignoring relativistic effects). Following Beniamini & Kumar (2020), the minimum observable timescale is

$$\delta t = \frac{r\epsilon^2}{2c\gamma^2},$$

which gives $\delta t \sim 10\mu$s for radial distance $r = 10^5$ km, radiative efficiency $\epsilon = 0.1$ and Lorentz factor $\gamma = 10$ (Kumar et al., 2017). Therefore, the microsecond burst structure we observed is most *naturally explained* in magnetospheric models (radial distance $< 10^5$ km). Additionally, we observe polarimetric properties akin to that of FRB 20121102A, but differing from the general non-repeater polarimetric properties, suggesting that repeating FRBs could have a characteristic polarimetric description. Specifically, FRB 20180916B bursts at 1.4 GHz

are $\sim$ 100% linearly polarised, and $\sim$ 0% circularly polarised, with a constant polarisation angle during and *between* bursts (Figure 2.5).

Diffractive scintillation in the Milky Way ISM causes scatter broadening on a timescale of $\sim$ 2.7 μs at 1.4 GHz along the line-of-sight to FRB 20180916B. This means that we are unable to probe timescales shorter than a few microseconds in the case of FRB 20180916B at 1.4 GHz. FRB 20200120E, however, is at much higher Galactic latitude than FRB 20180916B, meaning that the path through the Milky Way is "cleaner" and does not induce as large a scatter broadening effect on bursts from FRB 20200120E (Figure 3.6). In Chapter 3 we exploit this fact and probe down to timescales of tens of nanoseconds. Typically the bursts have durations of 100 μs, which is exceptionally narrow compared with other repeating FRBs. In one burst we see strong micro-structure which resolves down to 60 ns isolated shots of emission (Figure 3.1), analogous to the "micro-bursts" and "nano-shots" phenomenology seen from Crab pulsar giant pulses (Hankins & Eilek, 2007). The observed 60 ns timescales further constrain the size of the emission region to be on the order of 10 m (ignoring relativistic effects). Not only are the timescales generally shorter than typical for FRBs, but we find the luminosities to be a few orders-of-magnitude lower than the weakest FRBs (and even 1–2 orders of magnitude weaker than the FRB-like burst from SGR 1935+2154; see §1.2.4). The range of timescales and luminosities we measure from FRB 20200120E is bridging the gap in the transient phase space between Galactic neutron stars and extragalactic FRBs (Figure 1.2). In this work, we are probing a relatively unexplored parameter space in the extremely short-duration (ns–μs), high-luminosity regime. This highlights that potentially there are *ultra*-fast transients populating this parameter space that current FRB searches are insensitive to.

In addition to FRB 20200120E exhibiting atypically narrow burst durations and low luminosities, FRB 20200120E lives in a nearby globular cluster (in M81, with distance 3.63 Mpc; Kirsten et al. 2022), which is in stark contrast to the other well-localised repeating FRBs found in relative proximity to star-formation (see §1.2). However, we show in Chapter 3 that the bursts exhibit polarimetric properties which match the characteristic description for repeating FRBs described in Chapter 2. Furthermore, in Chapter 4 we present the first-detected "burst storm" (53 bursts discovered in a 40 minute time window) from FRB 20200120E, resembling the activity behaviour of other repeating FRBs (Figure 4.12). With a large burst sample, we also show that the burst energy distribution is consistent with a power law (with index -2.39 ± 0.12; Figure 4.16), the time *between* consecutive bursts follow a bi-modal distribution (Figure 4.13), and there is no underlying periodicity in the burst arrival times, all characteristic of repeating FRBs. Whether FRB 20200120E is the same type of object as these other highly active repeating FRBs is still up for discussion, but Chapters 3 and 4 highlight the importance of FRB 20200120E and other local Universe ($<$ 100 Mpc) sources of fast radio transients to bridge our knowledge from Galactic sources to the extremely distant FRBs.

Zooming-in in space

As mentioned in §1.6.2, the localisation precision with VLBI depends on the maximum separation of array elements, as well as the array configuration (number **and** orientation of array elements), time on source, the source's signal-to-noise ratio and how well calibrated the data is. FRBs, however, are ∼millisecond-duration transients, which is essentially a "snapshot" in VLBI (no time integration). The advantage of repeating FRBs is that they produce multiple bursts, so combining the data from multiple bursts improves the localisation accuracy (especially if they are separated by sufficient time such that the Earth has rotated causing the projected array configuration to significantly change)[1].

Due to the extremely high activity of FRB 20201124A (§1.2.3), we detected a total of 18 bursts during our VLBI campaign, at two separate observing epochs (Chapter 5). Using the full sample we determined the FRB position to 2.7 mas accuracy ($1\,\sigma$). Having such a large burst sample provided the opportunity to explore the astrometric accuracy as a function of burst brightness and number of telescopes, while having detections at multiple epochs allowed for an independent calibration to limit any systematic calibration uncertainties on the final FRB position. We find that for $\geq$ 7 array elements, single bursts can be localised to milliarcsecond precision, and that this drops to 0.1–1 arcsecond precision for 4 array elements. This is promising given that arcsecond localisation precision is sufficient to identify the FRB's host galaxy, while increasing to milliarcsecond precision will strongly constrain the local environment properties.

With the 2.7 mas localisation precision (Figure 5.2), we find that FRB 20201124A is embedded in a star-forming region (Piro et al., 2021) in a massive star-forming galaxy at a redshift of $z = 0.0979 \pm 0.0001$ (Fong et al., 2021; Ravi et al., 2022). It is interesting to consider whether FRB 20201124A's high bursting activity (compared with other repeaters) is related to its close proximity to active star formation. FRB 20121102A (§1.2.1) is also living within a star-forming region (Bassa et al., 2017) and has relatively high bursting activity (Li et al., 2021). The notable difference between FRB 20121102A and FRB 20201124A is that the former has a compact persistent radio counterpart, while we show in Chapter 5 that FRB 20201124A does not, down to a limit of 25 μJy beam^{-1} (a factor of $\sim$ 60 times weaker than the radio counterpart to FRB 20121102A; Figure 5.2). This work further establishes the fact that repeating FRBs live in a diversity of host galaxy types and local environments, a fact first established by the work presented in Chapter 6.

In Chapter 6 we precisely localise FRB 20180916B to a massive (stellar mass 10^{10} M$_\odot$) Milky Way-like spiral galaxy using the EVN (Figure 6.5). Not only does this host galaxy highlight that the low-metallicity dwarf galaxy origin of FRB 20121102A is not a requirement for a repeating FRB, but the lack of a comparably bright persistent radio source, and relatively low RM, shows that their environments differ greatly. Using the 8-m Gemini-North telescope, we determine a spectroscopic redshift of FRB 20180916B's host galaxy, $z = 0.0337 \pm 0.0002$ (luminosity distance 149.0 ± 0.9 Mpc), which, at the time of publication, was by far the

[1] Though with a large number of telescopes, optimally oriented, and good calibration, even single bursts can be localised to milliarcsecond precision using VLBI.

closest FRB known (compared with the typical ∼Gpc FRB distances). Additionally, using Gemini-North, we determine that FRB 20180916B is living at the apex of a "v-shaped" star-forming region[2]. This work shows that FRBs live in a diverse range of host galaxy types and local environments. Perhaps this could mean that different types of astrophysical objects can produce FRBs, or that a single FRB progenitor can live in many different environments.

Although Chapter 6 shows that not all repeating FRBs have luminous persistent radio sources, a second repeating FRB, FRB 20190520B, was found with a persistent radio counterpart, and other strikingly similar qualities to FRB 20121102A (§1.2.1; Niu et al. 2021). This highlights that FRB 20121102A is not a red herring, but instead that some repeating FRBs are associated with a persistent radio counterpart. As discussed in §1.2.1, the nature of the persistent emission is not yet understood, nor is the relationship between the FRB source and the persistent emission. Law et al. (2022) predict that as much as 1% of the compact radio sources in the local Universe could be these FRB persistent radio sources. In Chapter 7, we study a radio source, FIRST J141918.9+394036, sharing properties with the persistent radio counterpart of FRB 20121102A: specifically, host galaxy type, proximity to star-formation and luminosity (Ofek, 2017). Using the EVN, we measure the radio source to be 1.6 ± 0.3 pc in extent (Figure 7.2), which implies an expansion velocity of $(0.10 \pm 0.02)c$, assuming an explosion date in 1993 (from the first reported detection of FIRST J141918.9+394036; Law et al. 2018b). The slowly-decaying nature of the radio source, mildly relativistic expansion and lack of detected radio bursts in high-time-resolution observations (using both the 100-m Effelsberg telescope and the 110-m Green Bank Telescope) supports the hypothesis that FIRST J141918.9+394036 is related to jet expansion from a long gamma-ray burst, and disfavours the competing model of a magnetar wind nebula. Nonetheless, there is evidence for magnetar creation in some long gamma-ray bursts (Stratta et al., 2018), so perhaps radio bursts can be detected from FIRST J141918.9+394036 with sufficient follow-up time and sensitivity. The behaviour of the longer-lived radio emission (expanding in size, and decaying in luminosity), however, points at a fundamentally different origin from the FRB persistent radio emission (Plavin et al., 2022).

In this thesis we show that FRBs come in a variety of "shapes and sizes" in their timescales, luminosities and local environments. This diversity must be accommodated for in the progenitor and emission models of fast radio transients.

[2] By increasing the spatial resolution in optical follow-up using the *Hubble Space Telescope*, Tendulkar et al. (2021) show that FRB 20180916B is offset from the peak of a nearby star-forming knot by ~ 250 pc (Figure 1.7).

Nederlandse Samenvatting

Dit proefschrift is gericht op het onderzoeken van de aard van de emissie van snelle radioflitsen (Fast Radio Bursts, FRB's) door de flitseigenschappen en lokale omgevingen in detail te bestuderen. De belangrijkste wetenschappelijke vragen zijn:

- Welke soorten astrofysische objecten zijn in staat om FRB's te produceren?
- Zijn herhalende en niet-herhalende FRB's afkomstig van hetzelfde type bronnen, maar met verschillende activiteitsniveaus?
- Zijn alle herhalende FRB's afkomstig van hetzelfde type object?
- Wat is het fysieke mechanisme achter de FRB-emissie?

Het proefschrift is opgedeeld in twee delen. Het eerste deel, "Inzoomen in de tijd", beschrijft het werk met extreem hoge tijdsresolutie (van 30 ns tot μs) waarnemingen met de enkele schotel van de Effelsberg radiotelescoop (zie §1.6.1) van herhalende FRB-bronnen. In het tweede deel, "Inzoomen in de ruimte", gebruiken we de EVN (zie §1.6.2) om herhalende FRB's tot op milliboogseconden nauwkeurig te lokaliseren, hun gastheerstelsels te identificeren, de directe omgeving te onderzoeken en om een kortdurig radioverschijnsel met een potentieel link naar FRB's op een ruimtelijke schaal van ∼pc te bestuderen.

Inzoomen in de tijd

In hoofdstuk 2 onderzoeken we 1.4 GHz FRB 20180916B (§1.2.2) flitseigenschappen tot op microseconde tijdschalen met behulp van ruwe voltagedata opgenomen met de 100-m Effelsberg radiotelescoop. Wij laten zien dat de flitsen een bereik van tijdschalen vertonen van milliseconden tot 3-4 □s (Figuur 2.1). Deze korte tijdschalen geven twijfel over de niet-magnetosferische emissiemodellen (§1.4), omdat ze een klein emissiegebied impliceren (∼km, relativistische effecten buiten beschouwing gelaten). Naar aanleiding van Beniamini & Kumar (2020), is de minimaal waarneembare tijdschaal

$$\delta t = \frac{r\epsilon^2}{2c\gamma^2},$$

wat $\delta t \sim 10\mu$s geeft, voor radiale afstand $r = 10^5$ km, stralingsrendement $\epsilon = 0.1$ en Lorentzfactor $\gamma = 10$ (Kumar et al., 2017). Daarom is de microseconde flitsstructuur die we hebben waargenomen het meest natuurlijk verklaard in magnetosferische modellen (radi-

ale afstand $< 10^5$ km). Bovendien observeren we polarimetrische eigenschappen die lijken op die van FRB 20121102A, maar die verschillen van de algemene niet-herhalende FRB polarimetrische eigenschappen, wat suggereert dat herhalende FRB's een karakteristieke polarimetrische beschrijving kunnen hebben. In het bijzonder, zijn FRB 20180916B flitsen op 1.4 GHz ∼100% lineair gepolariseerd en ∼0% circulair gepolariseerd, met een constante polarisatiehoek tijdens en tussen flitsen (Figuur 2.5).

Diffractieve scintillatie in het Melkweg ISM veroorzaakt verbreding van het signaal door verstrooiing op een tijdschaal van ~ 2.7 µs op 1.4 GHz langs de zichtlijn naar FRB 20180916B. Dit betekent dat we geen tijdschalen kunnen onderzoeken die korter zijn dan een paar microseconden in het geval van FRB 20180916B op 1.4 GHz. FRB 20200120E bevindt zich echter op een veel hogere galactische breedtegraad dan FRB 20180916B, wat betekent dat het pad door de Melkweg "schoner" is en er een minder groot verbredend effect is op het signaal van flitsen van FRB 20200120E (Figuur 3.6) door verstrooiing. In hoofdstuk 3 benutten we dit feit en onderzoeken we tijdschalen van tientallen nanoseconden. Meestal hebben de flitsen een duur van 100 µs, wat uitzonderlijk smal is in vergelijking met andere herhalende FRB's. In één flits zien we een sterke microstructuur waar 60 ns geïsoleerde flitsen van emissie onderscheiden kunnen worden (Figuur 3.1), analoog aan de fenomenologie van "micro-bursts" en "nano-shots" van de Krabpulsar reuzepulsen (Hankins & Eilek, 2007). De waargenomen 60 ns tijdschalen beperken de grootte van het emissiegebied verder tot in de orde van 10 m (relativistische effecten buiten beschouwing gelaten). Niet alleen zijn de tijdschalen over het algemeen korter dan gewoonlijk is voor FRB's, maar we vinden ook dat de lichtsterktes een paar ordes van grootte lager zijn dan de zwakste FRB's (en zelfs 1–2 ordes van grootte zwakker dan de FRB-achtige flits van SGR 1935+2154; zie §1.2.4). Het bereik van tijdschalen en lichtsterkten die we meten van FRB 20200120E overbrugt de kloof in de parameterruimte tussen galactische neutronensterren en extragalactische FRB's (Figuur 1.2). In dit werk onderzoeken we een relatief onverkende parameterruimte in het extreem korte duur (ns–µs), hoge helderheid regime. Dit benadrukt dat er mogelijk *ultrasnelle* kortdurige radioverschijnselen zijn die deze parameterruimte vullen waar huidige FRB-zoektochten ongevoelig voor zijn.

Naast dat FRB 20200120E atypische korte flitsen en lage lichtsterkte laat zien, leeft FRB 20200120E in een nabijgelegen bolvormige sterrenhoop (in M81, op een afstand van 3.63 Mpc; Kirsten et al. 2022), wat in sterk contrast staat met de andere goed gelokaliseerde herhalende FRB's gevonden in relatieve nabijheid van stervorming (zie §1.2). In hoofdstuk 3 laten we echter zien dat de flitsen polarimetrische eigenschappen vertonen die overeenkomen met de karakteristieke beschrijving voor herhalende FRB's die beschreven zijn in hoofdstuk,2. Verder presenteren we in hoofdstuk,4 de eerst gedetecteerde "flitsstorm" (53 flitsen ontdekt in een tijdvenster van 40 minuten) van FRB 20200120E, wat lijkt op het activiteitsgedrag van andere herhalende FRB's (Figuur 4.12). Met een grote verzameling van flitsen, laten we ook zien dat de flits-energieverdeling consistent is met een machtsfunctie (met index -2.39 ± 0.12; Figuur 4.16), de tijd tussen opeenvolgende bursts volgt een bimodale distributie (Figuur 4.13) en er is geen onderliggende periodiciteit in de aankomsttijden van flitsen, allemaal kenmerkend voor herhalende FRB's. Of FRB 20200120E hetzelfde

type object is als deze andere zeer actieve herhalende FRB's staat nog steeds ter discussie, maar hoofdstuk 3 en 4 benadrukken het belang van FRB 20200120E en andere bronnen van snelle kortdurig radioverschijnselen in het lokale universum (< 100 Mpc) om onze kennis te overbruggen van galactische bronnen naar het extreem verre FRB's.

Inzoomen in de ruimte

Zoals vermeld in §1.6.2, hangt de lokalisatieprecisie met VLBI af van de maximale scheiding van interferometer-elementen, evenals de configuratie van de interferometer (het aantal **en** de oriëntatie van de elementen), tijd op de bron, de signaal-ruisverhouding van de bron en hoe goed de gegevens zijn gekalibreerd. FRB's zijn echter kortdurig radioverschijnselen van ∼milliseconden, wat in wezen een "momentopname" is in VLBI (zonder integratie in de tijd). Het voordeel van herhalende FRB's is dat ze meerdere flitsen produceren, dus het combineren van de gegevens van meerdere flitsen verbetert de lokalisatienauwkeurigheid (vooral als ze voldoende tijd van elkaar verwijderd zijn zodat de aarde is gedraaid waardoor de geprojecteerde configuratie van de interferometer aanzienlijk veranderd)[1].

Door de extreem hoge activiteit van FRB 20201124A (§1.2.3) hebben we in totaal 18 flitsen tijdens onze VLBI-campagne gedetecteerd, in twee afzonderlijke waarnemingsperioden (hoofdstuk 5). Met de volledige steekproef bepaalden we de FRB-positie tot een nauwkeurigheid van 2.7 mas ($1\,\sigma$). Zo'n grote flitsverzameling bood de mogelijkheid om de astrometrische nauwkeurigheid als functie te onderzoeken van flitshelderheid en het aantal telescopen, terwijl detecties in verschillende periodes een onafhankelijke kalibratie bieden om eventuele systematische kalibratie-onzekerheden op de definitieve FRB-positie te beperken. We vinden dat voor ≥ 7 interferometer-elementen enkele flitsen kunnen worden gelokaliseerd tot milliboogseconde precisie, en dat dit daalt tot 0.1–1 boogseconde precisie voor 4 interferometer-elementen. Dit is veelbelovend, aangezien de nauwkeurigheid van boogsecondelokalisatie voldoende is om het gastheerstelsel van de FRB te identificeren, terwijl het verhogen tot milliboogseconde precisie de lokale omgevingseigenschappen sterk zal afbakenen.

Met de lokalisatieprecisie van 2.7 mas (Figuur 5.2) vinden we dat FRB 20201124A is ingebed in een stervormingsgebied (Piro et al., 2021) in een massief stervormingsstelsel met een roodverschuiving van $z = 0.0979 \pm 0.0001$ (Fong et al., 2021; Ravi et al., 2022). Het is interessant om te overwegen of de hoge flitsactiviteit van FRB 20201124A (vergeleken met andere herhalende FRB-bronnen) is gerelateerd aan de nabijheid van actieve stervorming. FRB 20121102A (§1.2.1) leeft ook binnen een stervormingsgebied (Bassa et al., 2017) en heeft een relatief hoge flitsactiviteit (Li et al., 2021). Het opmerkelijke verschil tussen FRB 20121102A en FRB 20201124A is dat de eerste een compacte, persistente radiotegenhanger heeft, terwijl we in hoofdstuk 5 laten zien dat FRB 20201124A dit niet heeft, tot een limiet van 25 μJy beam^{-1} (∼60 keer zwakker dan de radiotegenhanger van FRB 20121102A; Figure 5.2). Dit werk stelt het feit verder vast dat herhalende FRB's in een diverse groep van

[1] Hoewel er met een groot aantal telescopen, optimale oriëntatie en goede kalibratie, zelfs enkele flitsen kunnen worden gelokaliseerd tot milliboogsecondenprecisie met behulp van VLBI.

gastheerstelsels en lokale omgevingen leven, een feit dat voor het eerst werd vastgesteld door het werk dat in hoofdstuk 6 wordt gepresenteerd.

In hoofdstuk 6 lokaliseren we FRB 20180916B nauwkeurig naar een massief (stellaire massa $10^{10}\,M_\odot$) Melkweg-achtig spiraalstelsel met behulp van de EVN (Figuur 6.5). Dit gastheerstelsels benadrukt niet alleen dat de oorsprong van FRB 20121102A in het laagmetalliciteits-dwergstelsel geen vereiste is voor een herhalende FRB-bron, maar het ontbreken van een vergelijkbaar heldere persistente radiobron, en een relatief lage RM, laat zien dat hun omgevingen sterk verschillen. Met behulp van de 8-m Gemini-North telescoop, bepalen we een spectroscopische roodverschuiving van het gastheerstelsel van FRB 20180916B, $z = 0.0337 \pm 0.0002$ (helderheidsafstand 149.0 ± 0.9 Mpc), die op het moment van publiceren verreweg de dichtstbijzijnde bekende FRB was (vergeleken met de typische $\sim$Gpc FRB-afstanden). Bovendien, met behulp van Gemini-North, stellen we vast dat FRB 20180916B aan de top van een "v-vormig" stervormingsgebied leeft[2]. Dit werk laat zien dat FRB's in een breed scala van gastheerstelsels en lokale omgevingen leven. Misschien zou dit kunnen betekenen dat verschillende soorten astrofysische objecten FRB's kunnen produceren, of dat een enkele FRB-voorganger in veel verschillende omgevingen kan leven.

Hoewel hoofdstuk 6 laat zien dat niet alle herhalende FRB's heldere persistente radiobronnen hebben, werd een tweede herhalende FRB, FRB 20190520B, gevonden met een persistente radiotegenhanger, en andere opvallend vergelijkbare eigenschappen zoals FRB 20121102A (§1.2.1; Niu et al. 2021). Dit benadrukt dat FRB 20121102A geen rode haring is, maar dat er enkele herhalende FRB's zijn met een persistente radiotegenhanger. Zoals besproken in §1.2.1, is de aard van de persistente emissie nog niet begrepen, evenmin als de relatie tussen de FRB-bron en de persistente emissie. Law et al. (2022) voorspellen dat maar liefst 1% van de compacte radiobronnen in het lokale universum deze FRB persistente radiobronnen zouden kunnen zijn. In hoofdstuk 7 bestuderen we een radiobron, FIRST J141918.9+394036, die eigenschappen deelt met de persistente radiotegenhanger van FRB 20121102A: specifiek het type gastheerstelsel, de nabijheid van stervorming en helderheid (Ofek, 2017). Met behulp van de EVN meten we dat de radiobron 1.6 ± 0.3 pc in omvang is (Figuur 7.2), wat een uitzettingssnelheid impliceert van $(0.10 \pm 0.02)c$, uitgaande van een explosiedatum in 1993 (vanaf de eerste gerapporteerde detectie van FIRST J141918.9+394036; Law et al. 2018b). De langzaam afvallende aard van de radiobron, de licht relativistische expansie en het ontbreken van gedetecteerde radioflitsen in observaties met hoge tijdresolutie (met zowel de 100-m Effelsberg radiotelescoop en de 110-m Green Bank Telescope) ondersteunt de hypothese dat FIRST J141918.9+394036 jetexpansie van een lange gammaflits betreft, en het concurrerende model van een magnetar windnevel is moeilijk te verklaren. Toch is er bewijs voor het ontstaan van een magnetar in sommige lange gammaflitsen (Stratta et al., 2018), dus misschien kunnen radioflitsen worden gedetecteerd van FIRST J141918.9+394036 met voldoende extra en gevoelige waarnemingen. Het gedrag van de langlevende radiostraling (toenemend in omvang, en afvallend

[2] Door het scheidend vermogen te verbeteren tijdens opvolgende optische observaties met behulp van de *Hubble Space Telescope*, hebben Tendulkar et al. (2021) laten zien dat FRB 20180916B $\sim$ 250 pc verschoven is ten opzichte van de piek van een nabijgelegen stervormingsknoop (Figuur 1.7).

in helderheid), wijst echter op een fundamenteel andere oorsprong dan de FRB persistente radio-emissie (Plavin et al., 2022).

In dit proefschrift laten we zien dat FRB's in verschillende "vormen en maten" in hun tijdschalen, helderheid en lokale omgevingen voorkomen. Met deze diversiteit moet rekening worden gehouden voor de oorsprong- en emissiemodellen van snelle kortdurige radioverschijnselen.

Acknowledgements

First of all, Jason, I'm sorry for almost killing you. I promise it's no reflection on my view of you as an advisor. It's been a genuine pleasure working with you. Thank you for your endless support and guidance, and for making your research group a big bundle of fun (just as fun as Disneyland). I've loved my last 4 years in Amsterdam, thanks in large part to you. You've allowed me to learn and grow as a scientist (though definitely not in height) while still staying true to who I am. I can't imagine a situation where I could have had a better PhD experience, so thank you. If I've learned one thing from you it's to always order the fruitiest cocktail on the menu (with the exception of the volcano, ALWAYS the volcano).

I would not have had such an amazing experience during my PhD without the entire Astroflash research group, old and new. To my "old colleague" Benito, thanks for your wisdom and showing me the VLBI ropes. From the foosball tables to the tiki bar, I've had such a fun time working with you and look forward to continuing to do so in the future (hopefully in other exotic locations). Hey look Danté, I made it! Hallelujah! It's been an impossible year, and this was meant to be our roaring 20s. With our high hopes, we've made it through the good, the bad and the dirty. The silver lining is that crazy equals genius and we've built a house of memories during these golden days. Go be victorious: keep office sunbathing, sampling everything in the supermarket and spotting the gargantuan birds. To my wee baguette Mark, thanks for the endless entertainment and brightness you bring to the group. Your energy is infectious. Should I keep going? Nee, bedankt. Omar, first of all, how dare you. Yer a belter o' ae laddae, but haud yer wheesht wae yer bletherin' or al deep fry yer sushi. My wee academic sis, Akshatha, you are a ray of sunshine. Speaking with you always brightens up my day. Lovely Franz, working with you is always so exciting. I'd like to also thank you for bringing the international holiday Happy Franz Week into our lives. Who knew it was possible to do so little work during a work visit. Steef (yes, you are a member of our research group), thank you for your absolutely beautiful and genuine presence that you bring to the API and to our office. Amruta, Nina, and Daniele, thank you for welcoming me so warmly into your academic family and for being incredible role models. Anne, Cees, Dany, Matt, Pragya, Ruben, Shivani, Teresa, and Zsolt, thank you for your time and advice, your fun and for bringing your support and enthusiasm every day. It's been an honour working in this research group and I look forward to interacting with you all in the many years to come.

My Cairo crew, Ben and Frank - thanks for the chaos! OG flatmates Inés and Maxwell, thanks for being such good friends over the years. I hope Maxwell is catching all the meese. Susan, Milena and Renee, interacting with you always makes me smile. To those at ASTRON and

API that I've encountered over the years: those I've had a close working relationship with; my office-mates; avid coffee drinkers and Oerknal attendees; travel buddies; or those that hover over the pineapple pizza – you've made my PhD experience so special and I have each and every one of you to thank for making my time so beautiful.

I'd like to thank the wonderful people in astronomy, outside my research group, that I've had the pleasure of working with through my PhD: Jim, Joel, Vicky, Dan, Aard, Jacco, Emily, Nathalie, Laura, Ziggy, Kelly, Eva, Phil, Silvia, and the many others. Thank you for answering my many questions and providing your advice when it comes to science and job applications.

My brilliant wee sis, Karis. Doing this without you would be like wearing a ski suit to climb Tinto in the middle of June: it just doesn't make sense. Here's to our next adventures. Thanks to my Gran and Papa for their support in my dreams ever since I was a little girl. Gran, I know Papa is super proud. Fiona, Kenny, Mhairi and Terry, ya'll are absolute rockstars. Thank you for the endless laughs and all of your kindness. I'm extremely lucky that you've welcomed me into your family wholeheartedly. Laura, Reece, Daniel, Lisa, Hannah, Saoirse, Caitlin, thank you all for being my cheerleaders for the longest time.

Last, but certainly not least, my home, my heart, my family: Gregor and Elliot. I genuinely could not have done this without you. Gregor, I'm struggling to put into words how thankful I am for you (shocker!). Thank you for your unconditional support and love, thanks for your patience listening to me harp on about my research, and for the thousands of words you've proof-read for me over the years. I know it can't have been easy dealing with me through the stressful deadlines, late nights in front of the laptop, "let's start from the beginning" out-loud proof reading, and "Hi, I'm Kenzie"'s. You've been by my side through everything. I love you more than I can articulate. Let's play some basketball.